Faculty of Science and Technology
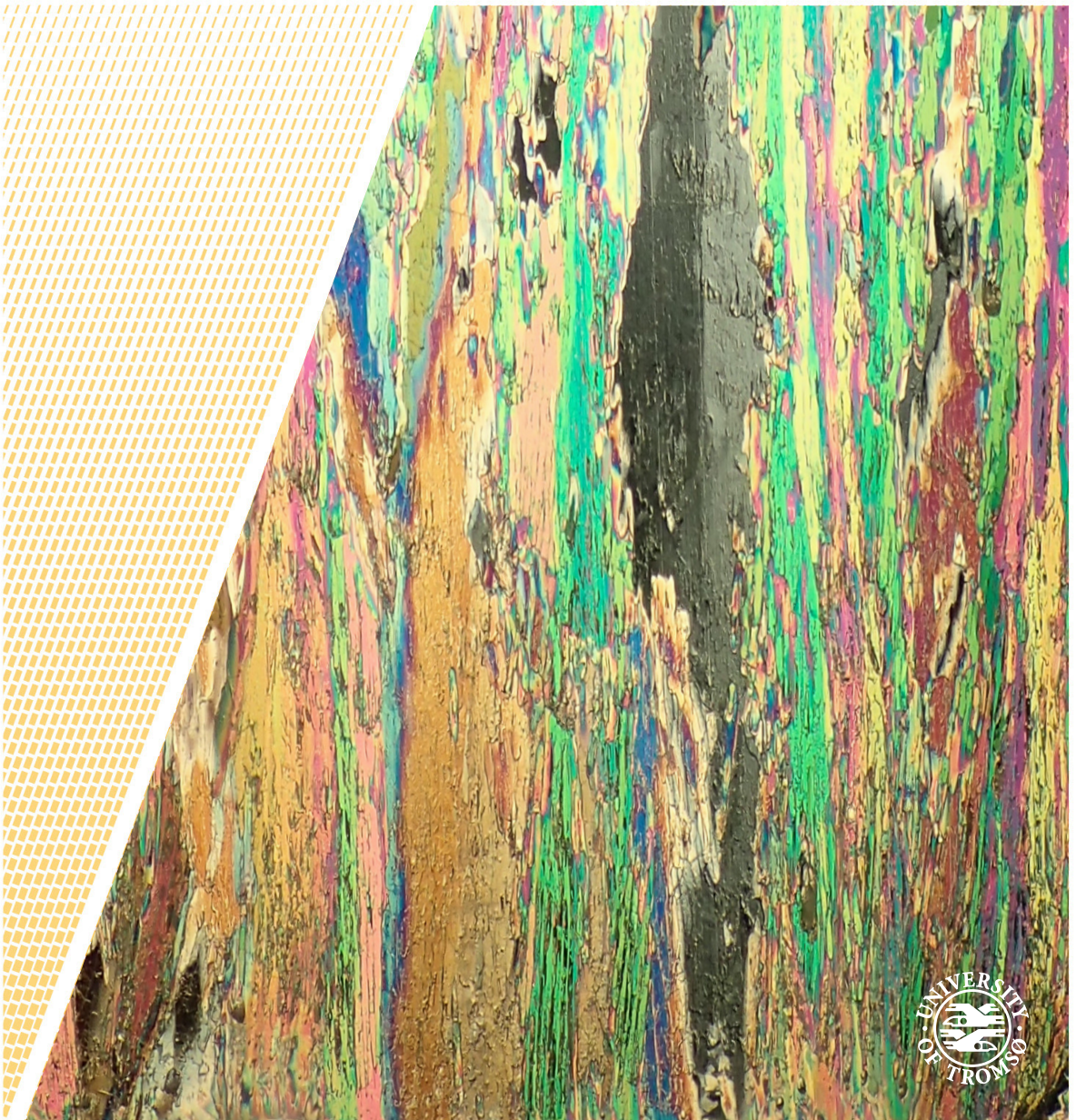Department of Physics and Technology

Multi-frequency radar remote sensing of sea ice

Modelling and interpretation of polarimetric multi-frequency radar signatures of sea ice

—

Jakob Grahn

A dissertation for the degree of Philosophiae Doctor – March 2018

Abstract

This thesis deals with polarimetric multi-frequency radar signatures of sea ice. It is divided into two parts. The first part presents a thorough background on the topic and the second part presents three case studies.

The first study presents a global sensitivity analysis of the fully polarimetric radar backscatter response from snow covered sea ice. The analysis is global in the sense that it takes into account the observed ranges of sea ice properties that are needed as input, and it attributes a quantitative sensitivity measure to each individual input parameter, such that the most influential one(s) can be identified. The considered model is configured with different snow layers and in particular the presence of brine-wetted snow is considered both in comparison and in combination with dry snow. Generally it can be concluded that parameters describing roughness of interfaces and dimensions of brine inclusions and snow grains, are more important than parameters describing bulk properties such as salinity, temperature and density. It is moreover found that parameters associated to the snow and upper part of the ice dominate at X- and C-band, while the roughness of the ice-water interface is important at L-band.

The second study complements the sensitivity analysis by showing that the considered backscatter model compare well to synthetic aperture radar (SAR) data at both C- and L-band, for ice identified as lead ice and ice floes (which presumably is first year ice). Generally, C-band data compare better than L-band data. Likewise, the ice identified as ice floes is better represented than ice types identified as lead ice. The model primarily deviates from the data in the co-polarised phase difference and the cross-polarised channel. Overall, the variance in model output is very large which can be explained by insufficient constraints on roughness and volumetric structure parameters.

The third study focuses on the backscatter from frazil and grease ice. A model for the dispersion relation of gravity waves in viscous ice slicks is considered and linked to a band ratio. This ratio provides the backscatter relative to a reference radar frequency and can readily be compared to data. The analysis concludes that under certain conditions, ice slicks have strong impact on the spectral be-

haviour of the radar backscatter. According to the numerical simulation, the damping due to ice slicks is strong at wavelengths relevant to radar remote sensing. Consequently, the wind speed presumably needs to be high in order to cause significant roughness of the ice slick surface and thus detectable amounts of Bragg scattering.

Acknowledgements

Contents

Acronyms

HJ-1-C   Huan Jing-1-C 13

IEM   Integral Equation Model 24, 44, 48, 51–53, 65, 101
IIEM   Improved Integral Equation Model vi, 50, 53, 70, 76, 91, 97, 147

JAXA   Japan Aerospace Exploration Agency 169
JPEG   Joint Photographic Experts Group 173

MIZ   Marginal Ice Zone 70, 176
MoM   Method of Moments 198
MR   Magnetic Resonance 33
MYI   Multi-Year Ice 3, 4, 81, 82, 123, 212

N-ICE 2015   Norwegian Young Sea Ice Cruise 2015 10, 38, 40, 41, 121–123, 141, 147, 148, 167, 168
N2M   Nghiem's 2-layer Model vi, 61, 62, 71, 76, 91, 92, 97, 101, 147
NESZ   Noise-equivalent Sigma Zero 127, 129, 138, 190
NFR   Norges Forskningsråd 169
NOAA   National Oceanic and Atmospheric Administration 11
NPI   Norwegian Polar Institute 40, 122
NRCS   Normalised Radar Cross Section 26
NSR   Northern Sea Route 8

POM   Physical Optics Model 50, 65

RCS   Radar Cross Section v, 25, 26, 171, 172, 182, 187, 189, 190, 192
RMS   Root Mean Square 44–49, 51, 54, 77, 79, 81, 82, 84, 88, 89, 93, 95, 98, 102, 145, 146, 168, 211
RT   Radiative Transfer 54, 55, 64, 65
RTE   Radiative Transfer Equation 54

SAR   Synthetic Aperture Radar i, 13, 15, 16, 121–124, 127, 141, 148, 167, 168, 172, 173, 196, 198, 199
SFT   Strong Fluctuation Theory vi, 55, 57–59, 61, 64, 65, 76–83, 97

Part I

Background

Chapter 1

Introduction

1.1 Sea ice

To many, sea ice may seem like a rarely occuring peculiarity that mainly is of interest to academics or the sparse population of the far north. However, the global sea ice extent is vast. While it is highly variable, on average sea ice covers about 20 to 25 million square kilometres of the Earth's oceans (Parkinson 2014), which is comparable to the size of North America.

Most of the global sea ice can be found in the Arctic Ocean[1] and the Southern Seas around Antarctica. Also seas at lower latitudes such as the Gulf of St. Lawrence, the Sea of Okhotsk, the Baltic Sea, the Caspian Sea, the Sea of Japan and the Bohai Sea can be important hosts in the winter time. In the Arctic, the sea ice normally reaches its maximum in early March and its minimum in September, while the situation is reversed for the Southern Seas. The average extent over a year is similar for both regions, although the Antarctic extent varies more from summer to winter.

The major differences between sea ice characteristics in the Arctic compared to the Antarctic relates to the fact that the Arctic Ocean is confined by land while the Southern Seas are not. The Arctic waters are consequently more affected by terrestrial fluxes of fresh water and contain more sediments and anthropogenic pollutants. Additionally, the Arctic sea ice is located at higher latitudes, with lower radiative input from the sun and also considerably lower heat flux from the ocean (Krishfield & Perovich 2005, Lytle et al. 2000). Another important difference that is currently in rapid change, is the significantly larger amount of multi-year ice (MYI) in the Arctic. This is ice that has survived at least one

---

[1] Including Baffin Bay, Barents Sea, Beaufort Sea, Chukchi Sea, East Siberian Sea, Greenland Sea, Hudson Bay, Hudson Strait, Kara Sea, Laptev Sea and White Sea.

melting season and is typically very fresh and thick. During the last decades however, the amount of MYI has rapidly decreased in the Arctic (Polyakov et al. 2012), making the age, salinity and thickness conditions between the two regions somewhat more similar than before.

Although many results of this thesis may be equally applicable to both polar regions, primarily Arctic sea ice is of consideration here. In figure 1.1 the Arctic sea ice extent is illustrated for March (maximum) and September (minimum) in 2017. The corresponding winter maximum and summer minimum extent as measured from 1981 to 2010 are also indicated. This map shows two remarkable features.

Firstly, the difference between the largest and smallest seasonal median extent is substantial (shown in figure 1.1 as blue and red dashed lines, respectively). During one season the ice in the Arctic can grow by about 10 million square kilometres, which is about the size of continental Europe. This variation is shown in more detail in figure 1.2 where the extent is plotted as a function of time of the year, for a the most recent 17 years. Sea ice is thus very dynamic over one season and the extent may fluctuate significantly from year to year. Also on short time scales, sea ice typically drifts (if not fastened to land or grounded icebergs) with speeds that can be up to tens of kilometres per day which causes local and regional changes of sea ice extent.

Secondly, during the year of 2017 (shown in figure 1.1) both the maximum and minimum extent were below the median. The minimum extent is especially small, which repeatedly has been observed over the last couple of decades, as also can be seen in figure 1.2. In fact, ever since satellite measurements became available in the late seventies, a clear decline in the summer extent has been observed (Cavalieri & Parkinson 2012, Fetterer et al. 2018). Estimates of earlier ice extents dating back to the late eighteen hundreds (based on data from historical sources such as ship logs and airplane surveys) indicate that the recent rate of change is unprecedented (Walsh et al. 2017). Model predictions, moreover, indicate that this trend will continue. It is expected that within a few decades, the Arctic may be ice free in the summer time (Overland & Wang 2013).

Apart from being an interesting, dynamic and versatile topic of research, knowledge about sea ice is important for a number of practical reasons. Generally sea ice plays a major role when modelling the climate, sea ice conditions need to be considered in local and regional weather forecasts, and the presence of sea ice affects the polar ecosystems. In addition, sea ice is of increasing interest to the industries involved in for example oil and gas, shipping, fishing and tourism. In the following sections, these items are discussed in more detail.

Figure 1.1: Map of the Arctic sea ice extent from March and September 2017 shown in blue and red, respectively. The corresponding median extent during the period 1981 to 2010 are highlighted as dashed lines. The map is based on the NSIDC Sea Ice Index (Version 3, for details see Fetterer et al. 2018).
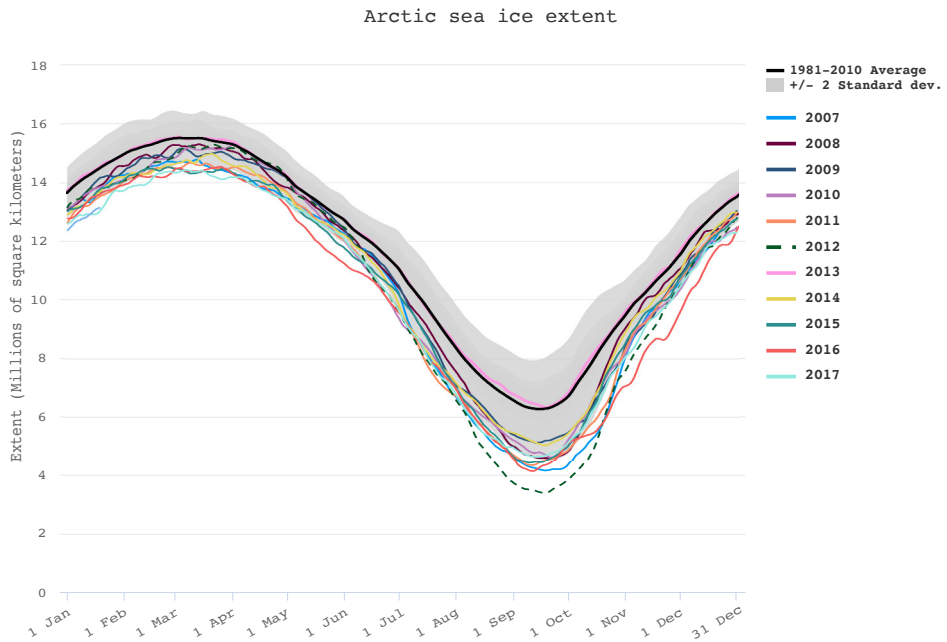
Figure 1.2: Graph of Arctic sea ice extent as a function of time of year, for the years 2007 to 2017 (coloured lines) and for the average from 1981 to 2010 (grey line). Year 2012, shown as a dashed line, was an extreme with regard to the minimum sea ice extent. The graph is based on data from the National Snow and Ice Data Center.

1.1.1 Weather and climate

Sea ice plays an intricate role in the weather and climate system. The implications and feedback mechanisms associated to changes in sea ice are not yet fully understood. Generally, sea ice:

1. has a high albedo and thus reflects significant amounts of the solar radiation back to space.

2. modulates the interactions between ocean and atmosphere, such as reducing fluxes of heat, momentum and gasses.

3. redistributes brine and fresh water which affects sea water density stratification and hence ocean circulation.

Much focus has been put on the sea ice in the Arctic due to its rapid decline, but also since the Arctic has suffered a much quicker warming over the past decades than any other parts of the Earth. The phenomenon is called the Arctic amplification and the decline in sea ice is believed to feed back on the rise in temperatures (Screen & Simmonds 2010, Kumar et al. 2010, Vihma 2014, Screen & Francis 2016). The ice thus plays a key role for understanding what the Arctic climate will be like in the future.

A decline in sea ice may also have an effect on climate over longer distances. Recent studies indicate for instance that the mid-latitudes may suffer colder winters as a result, since the sea ice decline may destabilise the polar jet stream, pushing cold air further south (Vihma 2014). A reduced sea ice cover may additionally contribute to North Atlantic freshening, which in turn could slow down thermohaline circulation (Serreze et al. 2007). This would have severe consequences for the climate in Northern Europe, since heat transport by the Gulf stream could decrease.

Arguably due to its rapid decline in the Arctic, sea ice has been one of the most recognized topics related to climate change. The manner of which sea ice interacts with the climate is however not yet fully understood and still gains considerable attention. It is far from a settled issue which calls for better and more detailed measurements. The two most important parameters are arguably the extent and thickness. The thickness is especially important for thin ice types, since a relatively thin ice layer (of only a few centimetres to decimetres) significantly changes the thermal heat flux between the ocean and atmosphere (Maykut 1978). Information about large scale deformation in terms of ridge statistics for instance, is important for estimating wind drag coefficients and momentum transfer (Guest & Davidson 1987, Garbrecht et al. 2002). Other important parameters include ice floe size distribution (Herman 2010, Zhang et al. 2015), ice salinity (Vancoppenolle et al. 2009) and age (Rigor & Wallace 2004).

1.1.2 Ecology

Since large parts of the Arctic consist of ocean regions, the species in the high north are predominantly marine and almost all are in one way or the other dependent on sea ice for their survival. Polar bears (see figure 1.3) are perhaps the most majestic and iconic of them all. Besides humans, they are the top predator of the food chain and are dependent on sea ice for hunting.

There is however much more to the Arctic ecosystem than just polar bears. Inside the porous structure of the sea ice, micro-organisms and algae thrive (see figure 1.4). These contribute significantly to the primary production and provide food for larger organisms such as various types of zooplankton, krill or shrimp. These in turn are eaten by various fish, squid or comb jellies, such as the one shown in figure 1.5. Further up this food chain are different kinds of sea bird, seals, walruses, whales and polar bears.

It is still unclear exactly how changes in ice cover will affect this ecosystem. The ice extent is clearly an important parameter for the species living directly on or inside the ice. Other parameters do also play a role, such as the fractional area of leads which determine the amount of light transmitted into the water, which in turn controls algae blooms (Assmy et al. 2017). Open leads are also important for seals and whales for breathing. Snow cover is another important parameter, which is needed for seals to build lairs to their cubs (Smith & Stirling 1975) and also affects the light transmission through the ice. Mapping of, not only sea ice extent, but also ice types and morphology are thus important for better understanding of the Arctic ecosystem and how changes in ice conditions will affect it.

1.1.3 Industry

Sea ice is one of the main reasons why the Arctic is relatively inaccessible to humans. The environment is harsh and it is difficult and expensive to operate in the region since ice breakers typically are needed. With a declining ice cover, industries involved in oil and gas, shipping, fishing, tourism and mining are however becoming increasingly interested in the region.

The cargo industry is for instance interested since shipping routes across the Arctic Ocean, from Europe to East Asian and North America, are significantly shorter than conventional ones via the Suez or Panama canal (Melia et al. 2016). Experimental test voyages aiming at commercial shipping have been carried out since the 1990s (Brubaker & Ragner 2010). In 2017, the first tanker sailed the northern sea route (NSR) (see figure 1.6) without aid of ice breakers. The journey took 19 days between Norway and South Korea. With further decline in sea ice, general cargo type vessels could reduce their sailing time to East Asia by about 10-13 days (a reduction of roughly 50%) when travelling the NSR instead of

Figure 1.3: Polar bear cubs photographed in the Fram Strait during a cruise in 2013. Although giving a cute impression as cubs, polar bears are notoriously dangerous and are the top predators of the Arctic (apart from humans). Photo: Jakob Grahn.
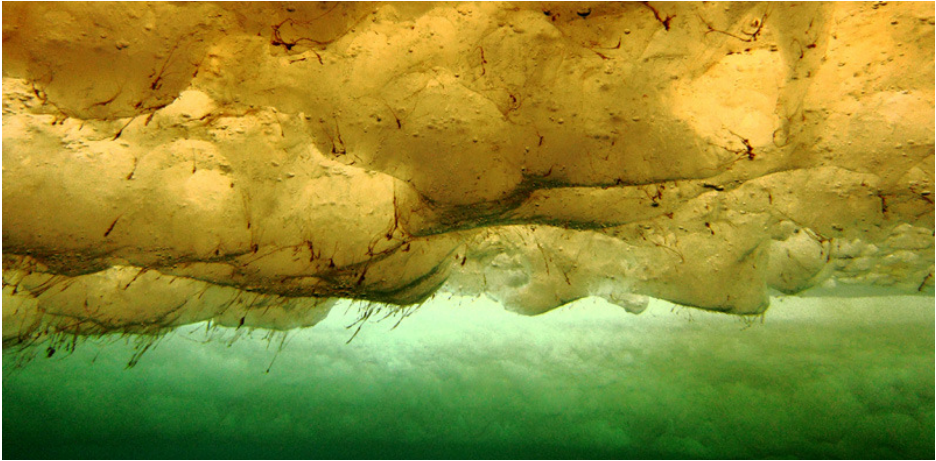
Figure 1.4: Algae growing inside the porous structures of the sea ice, seen from underneath the ice. These play a key role in the primary production of the Arctic Ocean. Image courtesy: Andrew Thurber.

Figure 1.5: A comb jelly observed under the sea ice in May during the Norwegian young sea ice cruise 2015 (N-ICE 2015). Image courtesy: Haakon Hop.
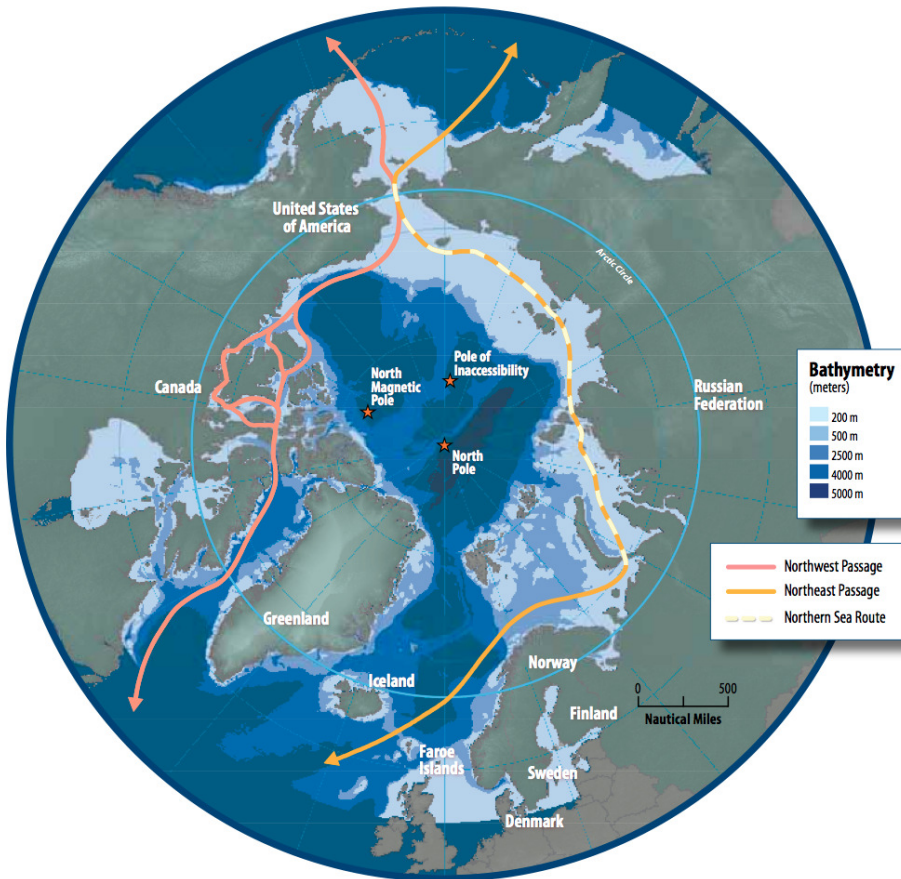
Figure 1.6: Map showing shipping routes through the Arctic. Since routes like these may significantly shorten travel from Europe to East Asia, there is an increasing interest in the observed changes of Arctic sea ice conditions from industries. Image courtesy: national oceanic and atmospheric administration (NOAA).

using the route through the Suez canal, and the time to North America could be reduced by about 4 days (Melia et al. 2016, Aksenov et al. 2017).

Depleting oil and gas reserves are also pushing the petroleum industries for exploring new sources. The United States geological survey (USGS) estimated the world's undiscovered oil and gas deposits and found that about 13% of the undiscovered oil and 30% of the undiscovered gas may be found north of the Arctic Circle, and most of it is likely located off-shore (Gautier et al. 2009). Also the fishing industry is moving north for similar reasons.

Industrial endeavours are however challenging in the Arctic environment, which is characterised by remoteness, low temperatures, bad visibility and darkness for several months of the year. Sea ice is a particularly critical hazard that needs to be monitored and permanently monitored by operational ice services. Rescue operations are difficult and costly, and incidents may quickly cost lives. Accidents involving oil production or shipping may moreover be devastating for the natural environment, since sea ice may complicate clean-up operations or even make them impossible.

There is thus an increased need for rapid and accurate systems for observations of sea ice. To this end, remote sensing may contribute significantly. This may include ice charts of sea ice types, thickness maps or estimates of ice hardness.

1.2   Radar remote sensing

Just considering the vast extent of the Earth's sea ice cover, combined with the remoteness and harsh environment of the polar regions, monitoring of sea ice is difficult. Not until satellites carrying microwave sensors became available was a global picture of the Earth's sea ice obtained.

Sensors operating in the microwave range of the electromagnetic spectrum (that is, with waves of a few millimetres to a metre in length) are arguably the most successful types of sensors for observing sea ice. There are two main reasons for this. Firstly, waves that are longer than some centimetre can penetrate clouds, which typically cover about 70-80% of the Arctic seas (Schweiger 2004). Secondly, solar illumination is not needed which is critical during the polar night. Either the microwaves emitted by the sea ice itself can be detected by so called passive sensors, or the illumination can be generated by a transmitter, in so called active sensors.

Passive microwave sensors, such as the scanning multichannel microwave radiometer (SMMR) or the special sensor microwave/imager (SSM/I), have been used successfully for large scale monitoring of sea ice extent, concentration and for discriminating between various sea ice types. Passive microwave sensors have provided data since the late 1970s, resulting in the longest consistent record of global sea ice extent that currently exists (on which both figures 1.1 and 1.2 are

based). They are characterised by a very large swath and can monitor the whole
Arctic in short time.

Active microwave sensors, such as radars, altimeters or scatterometers, in-
clude their own source of illumination by transmitting a pulse of microwaves that
scatters on the target of interest. The received pulse is measured and informa-
tion about the target can be retrieved. Since the radiation is generated, active
sensors enable more control over the measurement in contrast to passive sensors.
The radiation can in particular be polarised and coherent which can yield more
information about the target.

Synthetic aperture radars (SARs) in particular, utilise the coherent nature
of the transmitted pulse to significantly increase the spatial resolution. These
are, depending on their configuration, capable of resolving features on the size of
metres in contrast to the tens of kilometres that are typical for passive microwave
sensors. SARs can thus resolve important sea ice features like individual ice floes,
leads or ridges.

For a SAR, there is however a trade-off between spatial resolution and swath
width. The swath is therefore usually much narrower than for passive sensors. In
addition, the sensor can typically not be operated continuously due to high power
consumption. This makes mapping on pan-arctic or global scales difficult. During
the last two decades, there has however been a minor boom in the number of
satellites carrying SAR sensors. Current SAR equipped satellites include Sentinel
1a and 1b (C-band), Radarsat-2 (C-band), advanced land observing satellite 2
(ALOS-2) (L-band), ICEYE-X1 (X-band), TerraSAR-X (X-band), TanDEM-X
(X-band), Cosmo-SkyMed SG (X-band) and Huan Jing-1-C (HJ-1-C) (S-band).
Multiple future missions are planned and the increasing number of sensors will
likely enable better pan-arctic and global sea ice monitoring capabilities.

Conventionally, SARs operating with frequencies at C-band are used. This
frequency band is regarded as a sensible choice for good sea ice monitoring ca-
pabilities both in summer and winter. Relatively recently, space borne SARs
operating at other frequency bands have become available, in particular at X-
and L-band. These bands may be favourable for specific mapping tasks and
yield complementary information about sea ice compared to C-band. Dierking &
Busche (2006) conclude for instance that deformation features such as ice ridges,
rubble fields and brash are better characterised using L-band, while X- and C-
band may be favourable for thin ice types.

The full potential of using data acquired at multiple frequency bands have
however still not been properly clarified, and the diversity in frequency bands used
in recent and future satellite missions raises the interest in the multi-frequency
aspects of radar remote sensing of sea ice. There are still many unresolved or
only partly resolved issues, in particular in the basic understanding of how the
microwaves at different bands interact with the ice. This is critical for forward

and inverse modelling and designing new radar systems, in particular since in-situ measurements of sea ice are difficult to obtain which makes empirical approaches based on training data problematic.

1.3 Problem formulation

The major questions that this thesis is addressing can be formulated as:

1. Can the polarimetric radar signatures measured over Arctic sea ice be described in terms of idealised physical models, and is it better described at some frequency bands than at others?

2. What geophysical parameters of the sea ice have the largest influence on the radar backscatter and which ones can potentially be retrieved? Are some frequency bands better for certain parameters?

These are critical questions for assessing the full potential of radar remote sensing as a tool for science applications (for example monitoring the evolution of the Arctic ice cover) and for operational sea ice mapping.

Previous work on backscatter modelling has been extensive. Some of the earliest analytical models dedicated to sea ice appeared in the early eighties (for example Fung & Eom 1982, 1985, Lee & Kong 1985), but the topic is still subject to active research with new models being proposed (Albert et al. 2012, Komarov et al. 2014, are two relatively recent examples). What may at first appear surprising is the diversity of model descriptions. Some focus on the volumetric scattering from inclusions within the ice (Nghiem et al. 1990, 1995b, for instance), while others are pure surface scattering models (Fung 1994, Winebrenner et al. 1995). Considering on the other hand the dynamic and complex nature of sea ice, the diversity in model descriptions is perhaps necessary for describing the wide range of ice types that typically exists in the Arctic. At the same time, however, there is as per today no clear consensus on which models best suited for given ice conditions, which is a major problem when applying them.

Regarding model sensitivity, less work has been done. On the one hand, there are many existing studies that illustrate the sea ice backscatter sensitivity to particular parameters (for example Fung & Eom 1982, 1985, Kim et al. 1985, Soulis et al. 1989, Nghiem et al. 1990, 1993, 1995b, Tjuatja et al. 1992, Partington & Hanna 1994, Winebrenner et al. 1995, Kwok et al. 1995, Carlström 1997, Wakabayashi et al. 2004, Albert et al. 2012, Komarov et al. 2014). On the other hand, no studies (to my knowledge) compare the sensitivity of all model input parameters in a "global" sense, that is, providing quantitative measures of the relative influence of all model input parameters. Such information is critical in order to explain variations observed in data.

While previous work on modelling sea ice backscattering is rather extensive, in this thesis it is acknowledged that relatively few investigations are focused on (1) radar frequencies different from those at C-band (such as X- or L-band) and (2) the impact of brine wetted snow and (3) the backscatter from grease and frazil ice. With this in mind, the above questions are narrowed down to:

A. What input parameters are most important in a layered backscatter model (based on existing surface and volume scattering models) at X-, C- and L-band radar frequencies?

B. How does brine wetted snow affect model sensitivity?

C. Can a layered backscatter model generally be used to describe typical ice types observed at multiple frequency bands?

D. What is the multi-frequency backscatter characteristic of frazil and grease ice?

These questions constitute the main problem statements of the thesis.

1.4   Objectives

In light of the problem formulation in the previous section, this thesis has the following objectives:

1. Implement a layered backscatter model and conduct a global sensitivity analysis to identify the most influential geophysical parameters.

2. Assess the representativeness of the implemented model on SAR data acquired at multiple frequency bands in connection to field campaigns.

3. Characterise the backscatter response as a function of radar frequency for frazil and grease ice by considering wave dispersion and damping.

These objectives are attended in the second part of the thesis, specifically in chapters 5 to 7.

1.5   Thesis structure

This thesis is divided into two major parts. Part I, which includes this chapter, covers the general background of the thesis. In chapter 2, fundamental equations and definitions are stated for describing scattering of electromagnetic waves in dielectric media. These provide the principal starting point for physical backscattering models used later in the thesis. A general and important statement of the

chapter is that a contrast in permittivity is the cause for scattering, for instance at the interface between air and ice, or ice and brine. In chapter 3, the basic properties of sea ice are outlined. While sea ice is a complex medium, the main focus is on the properties that relate to its permittivity and structure. These are essential for understanding how the ice interacts with microwaves. Chapters 2 and 3 build up towards the last chapter of part I, which deals with backscatter models applicable to sea ice. The models presented in chapter 4 (together with relations from chapter 3) are used extensively in the rest of the thesis and contain the basic building blocks for the studies presented in part II.

Part II contains three chapters, each presenting a study of its own. Chapter 5 presents a sensitivity analysis of a composite backscatter model based on the models in chapter 4. This analysis highlights what input parameters are most important with regard to variations in the backscatter. The analysis is particularly focused on differences in sensitivity across different frequency bands, and a discussion of the basic scattering processes is also presented. In chapter 6, the same composite model is used in comparison to real data from satellite borne SAR sensors operating at X-, C- and L-band, accompanied with in-situ observations and meteorological data. While chapter 6 deals with multiple types of sea ice, the last chapter of part II (chapter 7) is focused particularly on grease and frazil ice. By modelling the dispersion relation of gravity waves propagating in slicks of frazil and grease ice, the effect on the radar backscatter is investigated as a function of operating frequency. A hypothesised band ratio is discussed and compared to observations from chapter 6 at C- and L-band.

Chapter 2

Electromagnetic waves and scattering

2.1 Maxwell's equations

The fundamental equations for describing electromagnetic waves classically, are Maxwell's equations. They read:

$$\nabla \times \mathbf{E} = -\frac{\partial}{\partial t}\mathbf{B} \tag{2.1a}$$

$$\nabla \times \mathbf{H} = \frac{\partial}{\partial t}\mathbf{D} + \mathbf{J} \tag{2.1b}$$

$$\nabla \cdot \mathbf{D} = \rho \tag{2.1c}$$

$$\nabla \cdot \mathbf{B} = 0 \tag{2.1d}$$

where $\nabla \times \ldots$ is the curl operator and $\nabla \cdot \ldots$ denotes divergence. $\mathbf{E}$ and $\mathbf{H}$ are the electric and magnetic fields, respectively, produced by sources realised through the current and charge densities, denoted $\mathbf{J}$ and ρ, respectively. $\mathbf{D}$ and $\mathbf{B}$ relates to the electric and magnetic field, respectively, in a manner that depends on the specific medium in question.

Maxwell's equations can alternatively be stated in terms of a frequency instead of time, assuming that the fields have harmonic time dependence, such that:

$$\mathbf{E}_\omega(t) = \mathbf{E}(\omega)\mathrm{e}^{-i\omega t} \tag{2.2}$$

17

and similarly for $\mathbf{D}$, $\mathbf{H}$ and $\mathbf{B}$. Equations 2.1 then read:

$$\boldsymbol{\nabla} \times \mathbf{E} = i\omega\mathbf{B} \tag{2.3a}$$

$$\boldsymbol{\nabla} \times \mathbf{H} = -i\omega\mathbf{D} + \mathbf{J} \tag{2.3b}$$

$$\boldsymbol{\nabla} \cdot \mathbf{D} = \rho \tag{2.3c}$$

$$\boldsymbol{\nabla} \cdot \mathbf{B} = 0 \tag{2.3d}$$

which are the spectral form of Maxwell's equations. These are assumed throughout the rest of the thesis.

2.1.1 Linear media

For a linear isotropic dielectric medium the $\mathbf{D}$ and $\mathbf{B}$ fields relate to the $\mathbf{E}$ and $\mathbf{H}$ fields as (Chew 1995, page 5):

$$\mathbf{D} = \varepsilon_0\varepsilon\mathbf{E} \tag{2.4a}$$

$$\mathbf{B} = \mu_0\mu\mathbf{H} \tag{2.4b}$$

where ε_0 and μ_0 are the permittivity and permeability for free space, respectively, while ε and μ are the corresponding relative permittivity and permeability of the medium. In this thesis, only non-magnetic media are considered for which $\mu = 1$.

If the medium is conductive, the conduction current $\mathbf{J}_c$ relates to the electric field as (Griffiths 2005, page 285):

$$\mathbf{J}_c = \sigma_c\mathbf{E} \tag{2.5}$$

where σ_c is the conductivity. By inserting equation 2.5 in the spectral form of Maxwell's equation, conduction can be included in an effective complex permittivity $\tilde{\varepsilon}$:

$$\tilde{\varepsilon} = \varepsilon - \frac{i}{\omega\varepsilon_0}\sigma_c \tag{2.6}$$

Waves that propagate through conductive media are attenuated due to the imaginary part of $\tilde{\varepsilon}$ (see).

If the medium is anisotropic, ε, μ and σ_c are in general tensors. Although this will be the case for sea ice, these quantities are written as scalars in this chapter for readability.

2.2 Wave equation

For linear media, the following wave equation can be derived from the spectral form of Maxwell's equations (Chew 1995, page 17):

$$\boldsymbol{\nabla} \times \boldsymbol{\nabla} \times \mathbf{E} - k^2\mathbf{E} = i\omega\mu_0\mathbf{J} \tag{2.7}$$

where the charge density ρ is neglected and the wave number k is:

$$k = \sqrt{\varepsilon}k_0 \tag{2.8}$$

with $k_0 = \omega\sqrt{\varepsilon_0\mu_0}$. An analogous wave equation can be found for the magnetic field $\mathbf{H}$. Both fields are however coupled such that, if $\mathbf{E}$ is known, $\mathbf{H}$ can be derived straightly from Maxwell's equations. It is thus sufficient to solve for only one of the two and conventionally the electric field $\mathbf{E}$ is considered, as will be done here.

2.2.1 Dyadic Green's function

A powerful and illustrative approach to solve the wave equation (equation 2.7) is by means of Green's function. Green's function is the impulse response of the wave equation, that is, the solution when the source is a point. When Green's function is found, the wave equation can be solved by convolving the source with Green's function.

Since the source in the wave equation is a vector, namely the current $\mathbf{J}$, the Green's function is a dyadic and will be referred to as the dyadic Green's function (DGF). This is a 3×3 matrix that transforms a vector at one position to a vector at another position. Convolving the source current $\mathbf{J}$ with the DGF $\bar{\mathbf{G}}(\mathbf{r}, \mathbf{r}')$ yields the electric field (Chew 1995, page 376):

$$\mathbf{E}(\mathbf{r}) = i\omega\mu_0 \int_V \mathrm{d}\mathbf{r}' \, \bar{\mathbf{G}}(\mathbf{r}, \mathbf{r}')\mathbf{J}(\mathbf{r}') \tag{2.9}$$

where $\mathrm{d}\mathbf{r}' = \mathrm{d}x'\,\mathrm{d}y'\,\mathrm{d}z'$ and V is a volume that contains the current $\mathbf{J}$. A useful interpretation of $\bar{\mathbf{G}}(\mathbf{r}, \mathbf{r}')$ is to view it as a propagator. Here it propagates the electric field from its source, that is the current at $\mathbf{r}'$ to the point of observation at position $\mathbf{r}$.

The DGF is further given as the solution to the point source wave equation (Chew 1995, page 376):

$$\boldsymbol{\nabla} \times \boldsymbol{\nabla} \times \bar{\mathbf{G}}(\mathbf{r}, \mathbf{r}') - k^2(\mathbf{r})\bar{\mathbf{G}}(\mathbf{r}, \mathbf{r}') = \bar{\mathbf{I}}\delta(\mathbf{r}-\mathbf{r}') \tag{2.10}$$

where the right hand side is the dyadic point source, with the Dirac delta function $\delta(\mathbf{r}-\mathbf{r}')$ and 3×3 unit dyadic $\bar{\mathbf{I}}$.

For unbounded homogeneous media, the DGF can be written in terms of the scalar Green's function $g(\mathbf{r}, \mathbf{r}')$ (Chew 1995, page 375-378):

$$\bar{\mathbf{G}}(\mathbf{r}, \mathbf{r}') = \left(\bar{\mathbf{I}} - k^{-2}\boldsymbol{\nabla}\boldsymbol{\nabla}\right) g(\mathbf{r}, \mathbf{r}') \tag{2.11}$$

where $g(\mathbf{r}, \mathbf{r}')$ is the solution to the simpler scalar wave equation:

$$\boldsymbol{\nabla}^2 g(\mathbf{r}, \mathbf{r}') + k^2 g(\mathbf{r}, \mathbf{r}') = \delta(\mathbf{r}-\mathbf{r}') \tag{2.12}$$

If the distance between $\mathbf{r}$ and $\mathbf{r}'$ is large, the scalar Green's function is (Ulaby et al. 1982, page 1022):

$$g_0^\infty(\mathbf{r}, \mathbf{r}') = -\frac{\mathrm{e}^{-ik|\mathbf{r}-\mathbf{r}'|}}{4\pi|\mathbf{r}-\mathbf{r}'|} \tag{2.13}$$

The corresponding DGF is:

$$\bar{\mathbf{G}}_0^\infty = (\bar{\mathbf{I}} - \hat{\mathbf{d}}\hat{\mathbf{d}})\frac{\mathrm{e}^{-ik|\mathbf{d}|}}{4\pi|\mathbf{d}|} \tag{2.14}$$

where $\mathbf{d} = \mathbf{r} - \mathbf{r}'$, $\hat{\mathbf{d}} = \mathbf{d}/|\mathbf{d}|$. Note that the factor $(\bar{\mathbf{I}} - \hat{\mathbf{d}}\hat{\mathbf{d}})$ implies that a vector multiplied by $\bar{\mathbf{G}}_0^\infty$ will be perpendicular to the radial direction $\hat{\mathbf{d}}$ and the second factor in 2.14 has the same spatial dependence as a spherical wave. In unbounded homogeneous media, the DGF can thus be seen as a spherical wave propagator if the observation point is far from the source point.

2.3   Representation of waves

2.3.1   Polarisation

From the far field Green's function in free space (equation 2.14) it was noted that point sources produce fields on the form of spherical waves. Moreover, being sufficiently far from the source, spherical waves can locally be treated as plane waves in a cartesian coordinate system.

Specifically, if a local cartesian coordinate system is chosen such that the z-axis points in the propagation direction, a plane wave can be fully described in the x-y-plane perpendicular to z. Conventionally, the x- and y-axes are chosen horizontally and vertically relativ to the ground and denoted h and v, respectively. In this coordinate system, a monochromatic plane wave takes the form (Lee & Pottier 2009, page 33):

$$\mathbf{E} = \begin{bmatrix} E_h \\ E_v \\ 0 \end{bmatrix} \mathrm{e}^{i(kz-\omega t)} \tag{2.15}$$

where E_h and E_v are complex valued amplitudes. These amplitudes constitute the so called Jones vector of the wave, denoted (Lee & Pottier 2009, page 37):

$$\tilde{\mathbf{E}} = \begin{bmatrix} E_h \\ E_v \end{bmatrix} \tag{2.16}$$

which completely describes the polarisation state of the wave. If the field is not a plane monochromatic wave, the Jones vector will be dependent on time and space. If the dependence is random, the wave is said to be depolarised. This can be quantified by considering the wave coherency, as will be described next.

2.3.2 Depolarisation

In order to describe partially polarised waves, consider the coherency matrix (Lee & Pottier 2009, page 47):

$$\bar{\mathbf{J}} = \langle \tilde{\mathbf{E}} \tilde{\mathbf{E}}^{\dagger} \rangle \tag{2.17}$$

where $\langle ... \rangle$ indicates ensemble average and † conjugate transpose. Denote the eigenvectors of this matrix by $\mathbf{u}_1$ and $\mathbf{u}_2$, with associated largest and smallest eigenvalues λ_1 and λ_2, respectively. For a polarised, unpolarised and partially polarised wave, the following conditions apply (Lee & Pottier 2009, page 49):

$$\text{Polarised: } \lambda_1 > \lambda_2 = 0$$
$$\text{Unpolarised: } \lambda_1 = \lambda_2$$
$$\text{Partially polarised: } \lambda_1 > \lambda_2 > 0$$

A measure of the degree of polarisation can accordingly be defined as (Lee & Pottier 2009, page 49):

$$D_p = \frac{\lambda_1 - \lambda_2}{\lambda_1 + \lambda_2} \tag{2.19}$$

such that:

$$\text{Polarised: } D_p = 1$$
$$\text{Unpolarised: } D_p = 0$$
$$\text{Partially polarised: } 1 > D_p > 0$$

An alternative measure of the degree of polarisation, which can more easily be generalised to scattering, is the wave entropy. It is defined in terms of the probability of a polarisation state being represented by the eigenvector $\mathbf{u}_i$:

$$P_i^{(w)} = \frac{\lambda_i}{\sum_j \lambda_j} \tag{2.21}$$

The wave entropy is then defined (Lee & Pottier 2009, page 49):

$$H^{(w)} = -\sum_{i=1}^{2} P_i^{(w)} \log_2 P_i^{(w)} \tag{2.22}$$

such that, for a polarised, unpolarised and partially polarised wave, it holds:

$$\text{Polarised: } H^{(w)} = 0$$
$$\text{Unpolarised: } H^{(w)} = 1$$
$$\text{Partially polarised: } 1 > H^{(w)} > 0$$
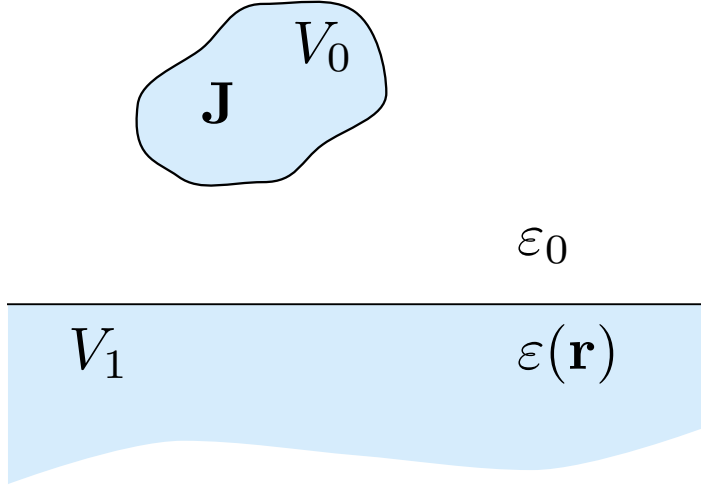
Figure 2.1: In the principal radar remote sensing setup, the source current is located in an antenna above ground. The resulting field is incident on the ground, where it is scattered whenever the permittivity fluctuates. The scattered field is the convolution of the DGF with the permittivity fluctuations of the ground (equation 2.27).

2.4 Scattering

The principal radar remote sensing setup is depicted in figure 2.1. An antenna is situated above ground, in free space, and accounts for the only active source of radiation through the current $\mathbf{J}$. The ground is characterised by a permittivity $\varepsilon(\mathbf{r})$, that may fluctuate arbitrarily with space. The antenna generates an electric field that propagates towards the ground, where it scatters.

2.4.1 Volume integral equation

To find the scattered field, the wave equation 2.7 must be solved with the appropriate boundary conditions. Note, however, that the wave equation can be rewritten such that the ground acts as an effective source:

$$\boldsymbol{\nabla} \times \boldsymbol{\nabla} \times \mathbf{E} - k_0^2 \mathbf{E} = i\omega\mu_0 \mathbf{J} + k_0^2(\varepsilon(\mathbf{r}) - 1)\mathbf{E} \qquad (2.24)$$

This is the free space wave equation, modified such that an additional source term is included on the right hand side, which accounts for scattering. As outlined in section 2.2.1, this can be solved using Green's function. In fact, the corresponding

Green's function is now the known $\bar{\mathbf{G}}_0$, as defined in equation 2.11. Convolving it with the source terms yields:

$$\begin{aligned}
\mathbf{E}(\mathbf{r}) =&\, i\omega\mu_0 \int_{V_0} d\mathbf{r}'\, \bar{\mathbf{G}}_0(\mathbf{r},\mathbf{r}')\mathbf{J}(\mathbf{r}') + \\
& k_0^2 \int_{V_1} d\mathbf{r}'\, \bar{\mathbf{G}}_0(\mathbf{r},\mathbf{r}')(\varepsilon(\mathbf{r}') - 1)\mathbf{E}(\mathbf{r}')
\end{aligned}$$

(2.25)

This is referred to as the volume integral equation (VIE) and is the basic equation for describing scattering in a great number of models and applications.

Some notes of physical insight can be made from equation 2.25. Firstly, the first term on the right hand side involves the source current $\mathbf{J}$ and is accordingly the field produced by the radar antenna. This will be referred to as the incident field and denoted:

$$\mathbf{E}_i(\mathbf{r}) = i\omega\mu_0 \int_{V_0} d\mathbf{r}'\, \bar{\mathbf{G}}_0(\mathbf{r},\mathbf{r}')\mathbf{J}(\mathbf{r}')$$

(2.26)

For the majority of radar remote sensing applications, this field can be assumed to take the form of a plane wave, since the antenna is small compared to the distance between antenna and ground.

The second term in equation 2.25 is the field produced by the target, i.e. the scattered field, denoted:

$$\mathbf{E}_s(\mathbf{r}) = k_0^2 \int_{V_1} d\mathbf{r}'\, \bar{\mathbf{G}}_0(\mathbf{r},\mathbf{r}')(\varepsilon(\mathbf{r}') - 1)\mathbf{E}(\mathbf{r}')$$

(2.27)

Note that the integrand contains the factor $\varepsilon(\mathbf{r}') - 1$. It is thus variations in permittivity relative to the background that is the source of scattering, and hence the source of information about the target in question. For a geophysical parameter to be measurable by means of radar remote sensing, it must in other words be linked to the spatial variation of permittivity in one way or the other.

2.4.2   Stratton Chu integral equation

If the considered volume in equation 2.27 is bounded by a surface S, it can be written as a surface integral equation using Green's vector theorem (Chew 1995, page 436):

$$\mathbf{E}_s(\mathbf{r}) = \int_S dS' \left(i\omega\mu_0\bar{\mathbf{G}}(\mathbf{r}-\mathbf{r}')\hat{\mathbf{n}} \times \mathbf{H}_s(\mathbf{r}') - (\boldsymbol{\nabla}' \times \bar{\mathbf{G}}(\mathbf{r}-\mathbf{r}'))\hat{\mathbf{n}} \times \mathbf{E}_s \right)$$

(2.28)

where $\hat{\mathbf{n}}$ is the normal unit vector of the surface. If the observation point is far from the surface, and the medium outside the surface is homogeneous, the corresponding homogeneous Greens function defined in equation 2.14 can be used.

This results in the famous Stratton Chu integral equation (Ulaby et al. 1982, page 1021-1023):

$$\mathbf{E}_s(\mathbf{r}) = -\frac{ik\mathrm{e}^{-ikr}}{4\pi r}\hat{\mathbf{r}} \times \int_S \mathrm{d}S' \left(\hat{\mathbf{n}} \times \mathbf{E}_s - \sqrt{\frac{\mu_0}{\varepsilon_0}}\hat{\mathbf{r}} \times (\hat{\mathbf{n}} \times \mathbf{H}_s)\right)\mathrm{e}^{ik\mathbf{r}\cdot\hat{\mathbf{r}}} \qquad (2.29)$$

Here $\hat{\mathbf{r}}$ is the unit vector pointing in direction of observation seen from the surface. This is the starting point of many popular surface scattering models, in particular the geometric optics model (GOM) and the integral equation model (IEM) (see sections 4.1.3 and 4.1.4, respectively).

2.4.3 Born series

Note that $\mathbf{E} = \mathbf{E}_s + \mathbf{E}_i$. Inserting this in the integrand of the VIE in equation 2.27 yields:

$$\mathbf{E}_s(\mathbf{r}) = k_0^2\Delta(\mathbf{r}')\bar{\mathbf{G}}_0(\mathbf{r}, \mathbf{r}')\mathbf{E}_i(\mathbf{r}') + k_0^2\Delta\bar{\mathbf{G}}_0(\mathbf{r}, \mathbf{r}')\mathbf{E}_s(\mathbf{r}') \qquad (2.30)$$

where integration is implicit over the primed positions. The permittivity contrast is expressed as $\Delta(\mathbf{r}') = \varepsilon(\mathbf{r}') - 1$. Note that the scattered field $\mathbf{E}_s$ appears both on the left-hand side and in the integrand on the right-hand side. The equation can thus be iterated to yield a series:

$$\begin{aligned}\mathbf{E}_s(\mathbf{r}) = \ & k_0^2\Delta(\mathbf{r}')\bar{\mathbf{G}}_0(\mathbf{r}, \mathbf{r}')\mathbf{E}_i(\mathbf{r}') + \\ & k_0^4\Delta(\mathbf{r}')\Delta(\mathbf{r}'')\bar{\mathbf{G}}_0(\mathbf{r}, \mathbf{r}')\bar{\mathbf{G}}_0(\mathbf{r}', \mathbf{r}'')\mathbf{E}_i(\mathbf{r}'') + \\ & \mathcal{O}(\Delta^3)\end{aligned} \qquad (2.31)$$

where again, integration over all primed positions is implicit. This is called a Born series and has a very useful interpretation. Specifically, the first term is the incident field propagated spherically from the permittivity contrast at $\mathbf{r}'$ to the observation point $\mathbf{r}$ and the field is scaled by the strength of the contrast. The second term is the incident field spherically propagated from the permittivity contrast at $\mathbf{r}''$ to the contrast at $\mathbf{r}'$, where it again propagates spherically to the observation point. The third term propagates through three permittivity contrasts and so on. Each term in the series thus represents the order of scattering. If only the first term is kept, single scattering of the incident field is described. This is called the first order Born approximation (FBA) and thus reads:

$$\mathbf{E}_s(\mathbf{r}) = k_0^2 \int \mathrm{d}\mathbf{r}'\bar{\mathbf{G}}_0(\mathbf{r}, \mathbf{r}')\Delta(\mathbf{r}')\mathbf{E}_i(\mathbf{r}') \qquad (2.32)$$

where now integration is explicit. An approximation of analogous form, namely the distorted Born approximation (DBA) discussed in section 4.2.1, will later be considered for volume scattering in snow and sea ice.

2.5   Representation of scatterers

2.5.1   Scattering vectors and matrices

If the antenna is far from the ground, the incoming wave at the ground as well as the scattered wave at the antenna can be treated as plane waves and can thus be represented by Jones vectors, denoted $\tilde{\mathbf{E}}_i$ and $\tilde{\mathbf{E}}_s$ respectively. The linear transformation between these two vectors characterises the target causing the scattered wave:

$$\tilde{\mathbf{E}}_s = \frac{\mathrm{e}^{-ikr}}{r}\bar{\mathbf{S}}\tilde{\mathbf{E}}_i \tag{2.33}$$

where the transformation matrix $\bar{\mathbf{S}}$ is referred to as the scattering matrix. The factor $\frac{\mathrm{e}^{-ikr}}{r}$, where r is the distance between the antenna and the target, accounts for propagation of the scattered wave from the ground to the antenna, which follows naturally from the far field Green's function in equation 2.13.

If expressed in terms of horizontally and vertically polarised basis vectors (called the lexicographic basis), the matrix elements can alternatively be expressed as a vector, specifically the so called lexicographic scattering vector:

$$\mathbf{k}_{L4} = \begin{bmatrix} S_{hh} \\ S_{hv} \\ S_{vh} \\ S_{vv} \end{bmatrix} \tag{2.34}$$

Most natural targets are reciprocal, such that $S_{hv} = S_{vh}$, in which case it can be reduced to a three element vector:

$$\mathbf{k}_{L3} = \begin{bmatrix} S_{hh} \\ \sqrt{2}S_{hv} \\ S_{vv} \end{bmatrix} \tag{2.35}$$

The scattering covariance matrix is further defined as:

$$\bar{\mathbf{C}} = \langle \mathbf{k}_{L3}\mathbf{k}_{L3}^{\dagger} \rangle \tag{2.36}$$

resulting in a 3×3 matrix under the assumption of reciprocity. Note the similarity to the wave coherency in equation 2.17.

2.5.2   Radar cross section

In terms of the incident and scattered Jones vectors, $\tilde{\mathbf{E}}_i$ and $\tilde{\mathbf{E}}_s$ respectively, the pq-polarised radar cross section (RCS) is defined as (Lee & Pottier 2009, page 54):

$$\sigma_{pq} = 4\pi r^2 \frac{|\tilde{\mathbf{E}}_s^p|^2}{|\tilde{\mathbf{E}}_i^q|^2} \tag{2.37}$$

where the incident wave is q-polarised, the scattered wave is p-polarised and r is the distance between the antenna and the target. Following from equation 2.33, the RCS can alternatively be written in terms of the scattering vector as (Lee & Pottier 2009, page 56):

$$\sigma_{pq} = |S_{pq}|^2 \tag{2.38}$$

In terms of the 3×3 scattering covariance matrix, the co- and cross-polarised RCS differ by a factor 1/2 (following from equation 2.35), specifically:

$$\sigma_{hh} = 4\pi|C_{11}| \tag{2.39}$$
$$\sigma_{hv} = 2\pi|C_{22}| \tag{2.40}$$
$$\sigma_{vv} = 4\pi|C_{33}| \tag{2.41}$$

For extended targets, illuminated by an area A, the normalised radar cross section (NRCS) is defined as:

$$\sigma^0{}_{pq} = \frac{\langle\sigma_{pq}\rangle}{A} \tag{2.42}$$

where $\langle\sigma\rangle$ is the average RCS over the area A.

2.5.3 Scattering entropy

Similarly to how the wave entropy (equation 2.22) could be defined from the eigenvalues of the wave coherency matrix (equation 2.17), a scattering entropy can be defined from the covariance matrix in equation 2.36, for describing wave depolarisation upon scattering. Let the eigenvectors of the scattering covariance matrix be denoted as $\mathbf{u}_i$ and the corresponding eigenvalues with λ_i, where $i = 1, 2, 3$. The probability of a scattering state being represented by the eigenvector $\mathbf{u}_i$ is then defined:

$$P_i = \frac{\lambda_i}{\sum_j \lambda_j} \tag{2.43}$$

The scattering entropy is further (Cloude 2010, page 97):

$$H = -\sum_{i=1}^{3} P_i \log_3 P_i \tag{2.44}$$

Chapter 3

Basic properties of sea ice

In order to interpret and model electromagnetic scattering from sea ice, a description of its dielectric characteristics is needed. This in turn is dependent on its physical and chemical composition. Being a result of sea water freezing, sea ice is mainly made up of pure ice, brine and solid salts. In addition, it may contain air as well as snow, sediments or algae. In particular the brine has a drastically different permittivity compared to the other components, making sea ice dielectrically very heterogeneous. In order to model radar signatures accurately, a description of the processes involved in shaping the ice is thus needed.

3.1 Components

Sea ice is mainly composed of the same basic ingredients as sea water. Primarily, these are pure water (H_2O) and a variety of salts. In sea ice, the water is frozen into pure ice, while the salts are either dissolved in water and trapped in small brine cells or crystallised in solid salts. This section contains some notes on key properties and relations regarding these basic ingredients that make up sea ice.

3.1.1 Pure ice

Most of the liquid water in sea ice contains large amounts of dissolved salts and is then denoted as "brine". Some amounts of relatively fresh water may also exist, in for instance melt ponds or in wet snow on top of the ice. For most types of sea ice, however, the majority of the water is in the form of pure ice (quantitative numbers about the relative amount of pure ice for typical sea ice can be found in section 3.2).
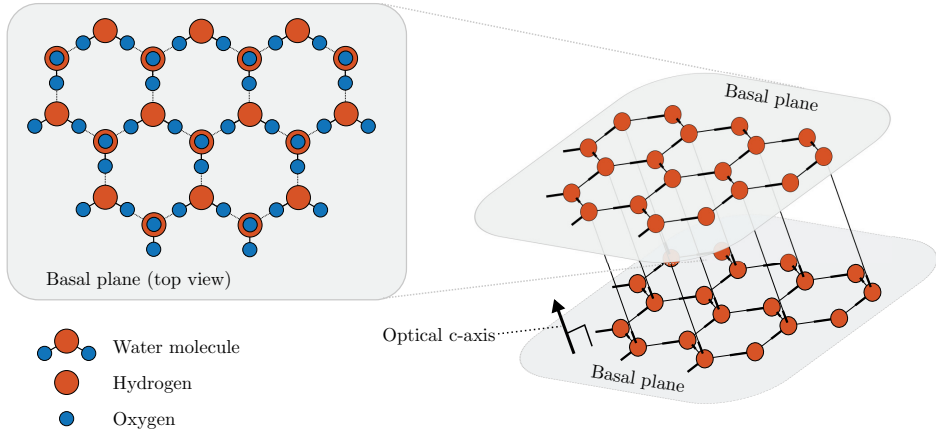
Figure 3.1: An illustration of the crystal lattice in ice I_h. The hydrogen and oxygen atoms form hydrogen bonds in a hexagonal pattern in the basal plane (see the left illustration). Half of the oxygen atoms will have a free hydrogen atom which bonds to an oxygen atom in another basal plane. The lattice thus takes the form of multiple parallel planes (see the right illustration). The axis perpendicular to the basal plane is called the optical c-axis.

Crystal structure of pure ice

Although salts make sea ice drastically different from pure ice, the basic ice formation process is the same. That is, at low enough temperatures H_2O solidifies into crystal lattices. The water molecules may solidify into a number of different crystal structures, depending on the temperature and pressure. However, at conditions typical for the biosphere, water freezes into so called ice I_h.

In ice I_h, the water molecules stick together with hydrogen bonds in a hexagonal pattern. This particular structure is favoured due to the six-fold symmetry of the H_20 molecule. The hexagonal pattern makes up the so called basal plane, of which the perpendicular axis is called the c-axis. The bonds in the basal plane involve 3/4 of the hydrogen atoms, the other 1/4 bond along the c-axis to another crystal plane. The full lattice thus consists of a stack of such crystal planes, as depicted in figure 3.1.

Density of pure ice

In contrast to many other naturally occurring substances, water has the peculiar property that it is less dense in its solid than in its liquid phase. Specifically, the density of pure ice, denoted ρ_{pi}, can be approximated as (Thomas & Dieckmann

2009):

$$\rho_{pi} = 917 - 0.1403T \qquad (3.1)$$

where T is the temperature.

Permittivity of pure ice

The relative permittivity for pure ice is weakly dependent on the temperature (Matzler & Wegmuller 1987):

$$\varepsilon_{pi} = 3.1884 + 0.00091T - i\left(\frac{A}{f \times 10^{-9}} + B(f \times 10^{-9})^C\right) \qquad (3.2)$$

where T is the temperature in °C, f is the frequency in Hz and A, B and C are temperature dependent constants. The constants were measured for -15°C and -5°C. For -15°C: A=0.0013, B=0.00012 and C=1.0. For -15°C: A=0.026, B=0.0023 and C=0.87. For other temperatures, linear interpolation will be used in the following chapters.

Despite the anisotropy of the ice crystals, the permittivity can be assumed isotropic. The crystal structure does however play an important role in shaping inclusions of brine, which can make the effective permittivity of sea ice anisotropic.

3.1.2   Sea water and brine

When salt is dissolved into water, the solution is called brine. In the literature, there is sometimes a distinction made between brine and sea water depending on the salinity. In this thesis, the distinction is made such that sea water embedded in sea ice or with a changed chemical composition due to ice formation, will be referred to as brine.

In Earth's oceans, sodium chloride (NaCl) is the most abundant salt and is dissolved into Na^+ and Cl^- ions (due to ion-dipole bonds with the water molecules). Other common salt ions are sulphate (SO_4^{2-}), magnesium (Mg^{2+}), calcium (Ca^-) and potassium (K^+) ions. Typically, however, these are at least one order of magnitude less abundant compared to the sodium chloride ions (Thomas & Dieckmann 2009).

When sea water and brine do freeze, the salt ions are separated from the ice crystals, since ion-dipole bonds cannot form with the crystal lattice (see section 3.1.1). This separation increases the salinity of the remaining brine and thus decreases its freezing point. In a closed system, both liquid brine and pure ice can thus coexists in thermal equilibrium.
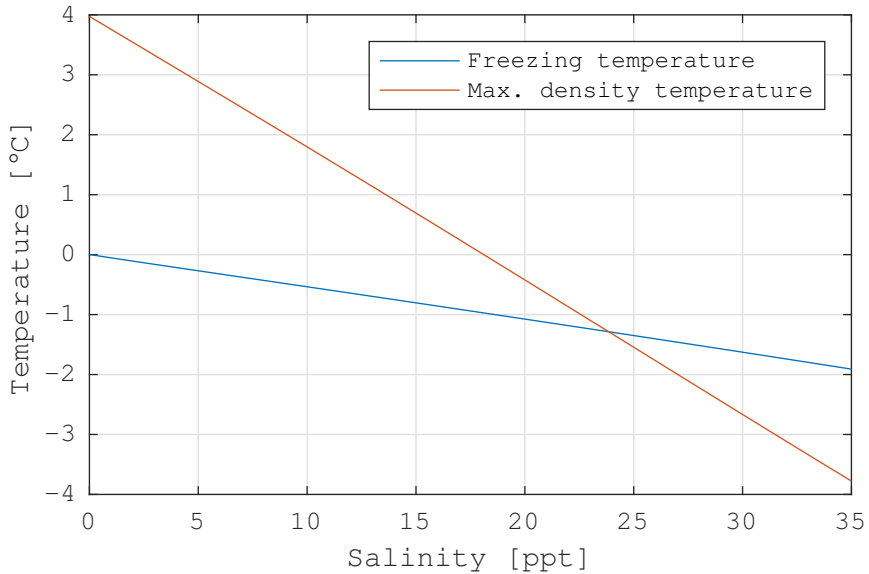
Figure 3.2: The freezing point of sea water compared to the temperature of maximum density plotted versus salinity. Above roughly a salinity of 24 ppt, sea water at its freezing point is heavier than warmer water. As water is cooled at the surface by the atmosphere, it will sink as it reaches its freezing point, resulting in a layer of supercooled water at the top of the water column.

Density of sea water

Pure water is most dense at about -4°C. As the salinity increases, the point of maximum density decreases roughly linearly, as illustrated in figure 3.2 (Mc-Dougall et al. 2003). As the salinity goes above about 24 ppt, the temperature of maximum density as a liquid is lower than the freezing point. In most oceans, the salinity is higher than this, in particular in the Arctic and Antarctic oceans. As sea water is cooled from the atmosphere it will become denser than the underlying water. An unstable density profile will form causing mixing in the top water layer. If the atmospheric cooling continues, the top layer may become supercooled. This allows for rapid ice growth and the formation of dendritic ice crystals. For open water, this results in an ice-water mix called frazil ice. Under consolidated ice, this can result in columnar ice.

Permittivity of brine

Since brine contains dissolved salt ions, a finite dielectric relaxation should be accounted for when calculating the permittivity. The single Debye relaxation equation has shown to be applicable for brine in the microwave frequencies (Stogryn & Desargant 1985), which is of the form:

$$\varepsilon_b = \varepsilon_\infty + \frac{\varepsilon_s - \varepsilon_\infty}{1 + i\omega\tau_r} - \frac{i\sigma_c}{\omega\varepsilon_0} \tag{3.3}$$

where the first two terms account for Debye relaxation and the last term accounts for conductive currents (as in equation 2.6). Specifically, ε_∞ and ε_s are the respective high frequency and static limits of the relative permittivity, τ_r is the relaxation time in seconds and σ_c is the conductivity.

   The single Debye relaxation equation 3.3 has shown to be applicable for brine in the microwave frequencies. Stogryn & Desargant (1985) fitted it to samples of brine extracted from sea ice, resulting in empirical and temperature dependent expressions for ε_∞, ε_s, τ_r and σ_c, which are stated in section B.2.

Permittivity of sea water

For sea water, the single Debye relaxation equation 3.3 has been shown inaccurate at high frequencies. A double Debye relaxation equation has been suggested by Meissner & Wentz (2004), valid for a wider range of frequencies:

$$\varepsilon_b = \varepsilon_\infty + \frac{\varepsilon_s - \varepsilon_1}{1 - i\omega\tau_r^{(1)}} + \frac{\varepsilon_1 - \varepsilon_\infty}{1 - i\omega\tau_r^{(2)}} - \frac{i\sigma_c}{\omega\varepsilon_0} \tag{3.4}$$

The corresponding permittivity limits ε_s, ε_1 and ε_∞, relaxation times $\tau_r^{(1)}$ and $\tau_r^{(2)}$ and conductivity σ_c are listed in section B.2.2. The relation is valid for salinities of 20 to 40 ppt.

3.1.3   Solid salts

At low temperatures, dissolved salt ions may crystallise into solid salts. Sodium chloride may for instance combine with water and form $NaCl \cdot 2H_2O$, or Na^+ ions may combine with sulphate and water, into $Na_2SO_4 \cdot 10H_2O$. Compared to pure ice, solid salts constitute only a small fraction of the sea ice. In particular, more than half of the water transforms into ice before any solid salts appear (Assur 1958). The solid salts are thus regarded as insignificant for wave propagation in microwave frequencies, thus their permittivities will not be stated here.

3.2   Phase relations and inclusions

In the previous section, the basic sea ice components are described, that is; pure
ice, brine and solid salts. In this section, the effect of temperature on the relative
fraction of single sea ice components is investigated in more detail. To this end,
sea ice phase relations are described.

   When making statements about the phase relations of sea ice, it is common
to assume that if melted, the sea ice would have the same chemical composition
as the sea water it originated from. This is called "standard" sea ice which was
introduced by Assur (1958). Although this assumption has been shown not to
be strictly correct in real sea ice samples, due to growth and depletion of frost
flowers (Rankin et al. 2002) or differential diffusion of salt ions through the ice
microstructure (Maus et al. 2011), it will be assumed valid for the purpose of
discussing electromagnetic wave interactions.

   Assuming "standard" sea ice, Assur (1958) compiled data from laboratory
grown samples (Nelson & Thompson 1954, Ringer 1928) and tabulated the frac-
tional weight of a number of components over a range of temperatures. Based on
this table, the fractional weights of brine, dissolved salts and pure ice are plotted
as solid lines in figure 3.3. The most abundant salt ions and solid salts are plotted
as dashed or dotted lines.

   As seen in figure 3.3, the amount of brine quickly decreases as the temper-
ature drops. Initially, this is almost only due to liquid water turning into pure
ice. The latter dominates the total weight soon after passing the freezing point
around -2°C. The first solid salt, $Na_2SO_4 \cdot 10H_2O$, appears around -8°C, but in
very small amounts. Considering the dominant salt ions, Na^+ and Cl^-, their
amounts remain relatively constant down to about -21°C, where they crystallise
into $NaCl \cdot H_2 0$. As the temperature decreases even further, other solid salts form,
but even at -40°C, they only account for 3% of the total weight. Note also that
liquid brine still exists at these low temperatures.

3.2.1   Volume fraction of brine

From the phase relations plotted in figure 3.3, the volume fraction of the different
components can be calculated. In terms of the dielectric properties of sea ice, the
volume fraction of brine is most important due to its relatively high permittivity.

   Based on the phase relations of Assur (1958), Frankenstein & Garner (1967)
found a simple relation between the volume fraction of brine V_b (as a fraction of
1), the sea ice bulk salinity S_{si} (in ppt) and temperature T (in °C):

$$V_b(T, S) = S_{si}(0.0532 - \frac{4.919}{T}) \times 10^{-2} \qquad (3.5)$$

which is stated to be valid for temperatures from $-22.9°C$ to $-0.5°C$. The density

of pure ice is assumed to be 926 kg/m^3. This is however weakly dependent on temperature, as was noted in equation 3.1. To account for this, Cox & Weeks (1983) later proposed the following relation, which allows for a variable ρ_{pi}:

$$V_b(T, S, \rho_{pi}) = \frac{\rho_{pi} S_{si}}{F_1(T) - \rho_{pi} S_{si} F_2(T)} \tag{3.6}$$

where $F_1(T)$ and $F_2(T)$ are polynomial functions of temperature (based on the data presented in Assur 1958) stated in section B.3. The relation is valid for temperatures from $-30°$C to $-2°$C. Note that if equation 3.1 is used for ρ_{pi}, equation 3.6 is a function of temperature and salinity only.

A comparison between equation 3.5 and 3.6 (using equation 3.1 for S_{si}) for a salinity of 10ppt is shown in figure 3.4. It is evident that the differences are small, with a maximum deviation of about 0.005 for the volume fraction of brine in the temperature range $-22°$C to $-2°$C. Note also the large sensitivity of the volume fraction to temperatures above $-5°$C. For example, the volume fraction is about twice as large at $-2°$C compared to $-5°$C.

3.2.2   Characteristics of brine inclusions

For an accurate description of the scattering from brine inclusions, the knowledge of only the volume fraction is not sufficient. Clearly, one large inclusion will scatter differently from ten small ones, even if they occupy the same fractional volume. Thus, a description of the sizes, shapes and orientations of the brine inclusions is also needed.

Traditionally, size measurements of brine inclusions are made by slicing ice cores into thin sections and estimating the inclusion sizes from photographs (Nakawo & Sinha 1984, Perovich & Gow 1996). The 2D-nature of such measurements may however hamper the ability to quantitively measure the inclusion sizes and shapes. More recently, magnetic resonance (MR) imaging (Eicken et al. 2000, Galley et al. 2015) and X-ray computed tomography (Golden et al. 2007) have been used to get a 3D-picture of the inclusion sizes, shapes and connectivity. Such measurements are however still rare which makes it difficult to provide a detailed and general description of the inclusions.

Studies indicate that the brine inclusions are on the order of a millimetre to fractions of a millimetre in size (Perovich & Gow 1991, 1996). When the inclusions get trapped in the sea ice, they typically become sandwiched in between the basal planes of the ice crystals. Initially, they tend to have a spherical shape (Galley et al. 2015) but later become elongated along the basal planes. Consequently their orientation is generally random in granular ice, but may have a preferred vertical alignment in columnar ice (Arcone et al. 1986, Weeks & Ackley 1986). Occasionally, they may have a preferred orientation also in the horizontal plane
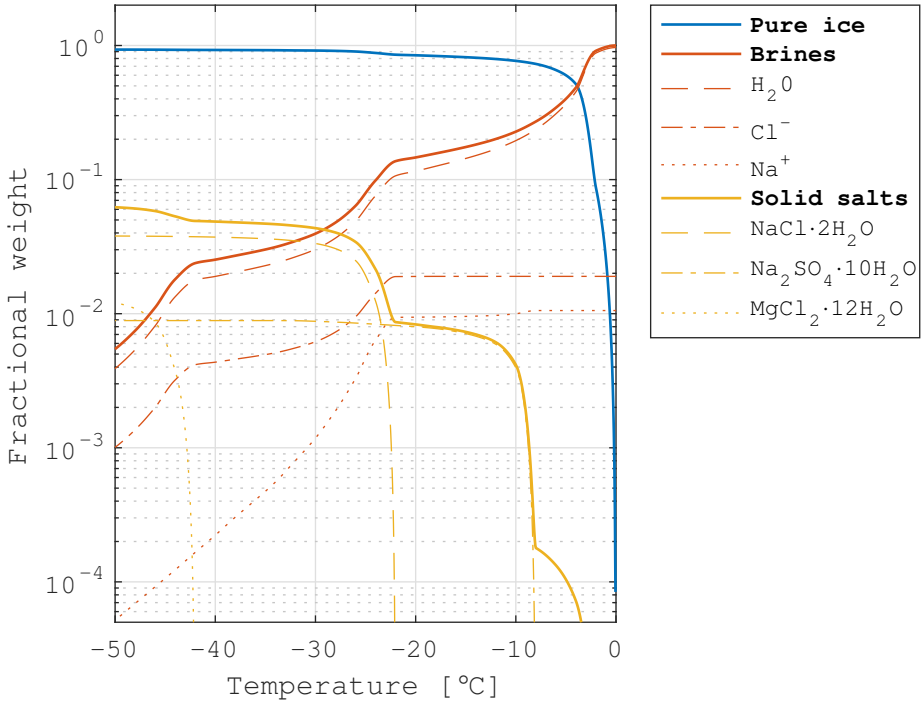
Figure 3.3: The phase relations between the different sea ice components plotted as fractional weights versus temperature. Plotted as solid lines, are the major components: pure ice, brine and solid salts. Solid salts and components of brine are plotted as dashed and dotted lines. The plot is based on table III in Assur (1958) corresponding to so called "standard" sea ice, with a salinity of 34.325 ppt at atmospheric pressure.

due to sea currents that align the ice crystals and thus also the brine inclusions (Weeks & Gow 1978, Nakawo & Sinha 1984), although generally no preferred horizontal orientation is observed.

3.3   Sea ice formation and structure

In this section, the spatial structure of these components is discussed in order to get an idea about what the sea ice permittivity configuration $\varepsilon(\mathbf{r})$ looks like, which determines the scattered electric field in equation 2.27. While the phase relations were simply a function of two parameters, that is temperature and salinity, the
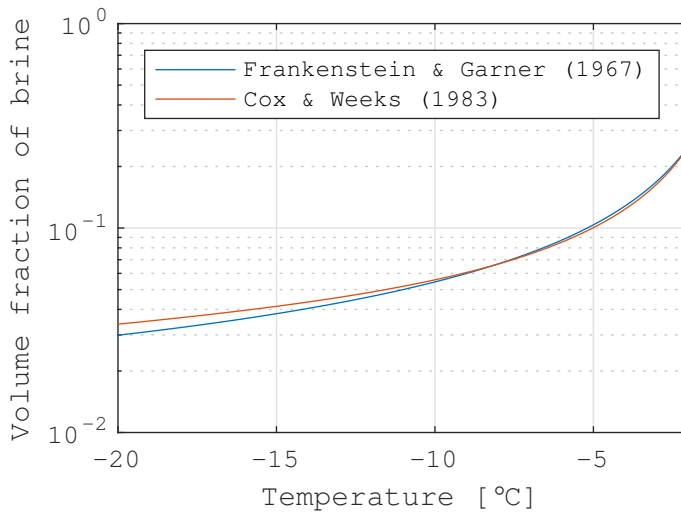
Figure 3.4: A comparison between the two expressions for the volume fraction of brine V_b shown in equation 3.5 by Frankenstein & Garner (1967) and equation 3.6 by Cox & Weeks (1983).

spatial structure is affected by a lot more factors, such as sea state, currents, winds and precipitation.

3.3.1 Frazil ice

Pure water is in its most dense state above the freezing point of 0°C. When salt is added, the temperature of maximum density goes down and if the salinity is higher than roughly 24 ppt, this temperature is below the freezing point, as illustrated in figure 3.2. This means that, when sea water is cooled from the atmosphere, the top of the water column becomes denser than deeper water, resulting in vertical mixing. Warm water will thus continually replace the colder water at the surface until the whole mixing layer is cooled. Studies show that this continues beyond the freezing point and the layer becomes supercooled (Katsaros 1973, Katsaros & Liu 1974, Tsang et al. 1985, Ushio & Wakatsuchi 1993).

Eventually, the water crystallises. Since the water is supercooled, the growth is dendritic and it is mainly confined to the basal plane of the crystal lattice. Initially, the crystals take the form of hexagonally shaped discs. After reaching a certain size, needle shaped spicules grow radially outwards in the basal plane. The spicules easily break off from the discs, resulting in a collection of discs and needle shaped spicules, referred to as frazils. These typically are a few to a couple

of tens of millimetres in length, but less than a millimetre in thickness (Thomas & Dieckmann 2009) and collectively make up so called frazil ice.

Under calm conditions, the frazil ice will form a thin layer at the sea surface and consolidate into an ice layer. If the water is turbulent, however, the frazils will be kept suspended in the water and eventually accumulate into a viscous layer, called grease ice. A characteristic feature of grease ice is that it dampen short surface waves, as seen in the photograph in figure 3.5.

3.3.2   Granular ice

If the sea state is turbulent, wave motion disturbs the ice growth process. Instead of forming a consolidated ice layer, frazil ice tends to transform into a smooth viscous soup, called grease ice. This may further consolidate into nilas, but then as so called granular ice. In this case the ice crystals and consequently also the brine inclusions do not have a preferred orientation. Continued ice growth can however be in the form of congelation growth. In fact, a transition from a granular to columnar structure is often found at some depth of a sea ice layer.

If the sea state is too turbulent for nilas to consolidate, grease ice tends to form collections of pancake-like ice plates instead, referred to as pancake ice. The ice pancakes eventually freeze together into one solid ice layer of young ice (YI), from which again congelation growth can proceed.

3.3.3   Columnar ice

Under calm conditions, the frazil ice consolidates to a thin elastic ice layer, called nilas. As the ice continues to grow, brine is rejected into the water column. As the brine mixes with the less saline sea water, the freezing point of the latter increases and it may become supercooled. This enables rapid dendritic-like ice growth into the supercooled water, called congelation growth that results in vertical lamellar ice structures. In particular, crystals with their basal planes oriented vertically will grow faster than those with more horizontally oriented planes (Perey & Pounder 1958, Weeks & Gow 1978), a phenomenon called geometric selection.

Brine will further be trapped in between the lamellar structures, as they freeze together into so called columnar ice. The brine inclusions are typically found to be elliptical in shape and vertically oriented, parallel with the basal plane of the ice crystals. The preferred orientation of the brine inclusions may further lead to a strong anisotropy of the permittivity of columnar ice.

In summary, depending on the sea state during ice formation, young sea ice typically consists of a granular ice layer at the top and of columnar ice further down. In figure 3.6 an example is shown. Specifically, vertical thin sections of the top and bottom of an ice core is viewed through cross polarised filters. The

Figure 3.5: A photograph of grease ice (to the left) in open water (to the right), in the Bering Sea. The matte and oily appearance of the grease ice is due to the damping of short surface waves. Image courtesy: U.S. Fish and Wildlife Service.
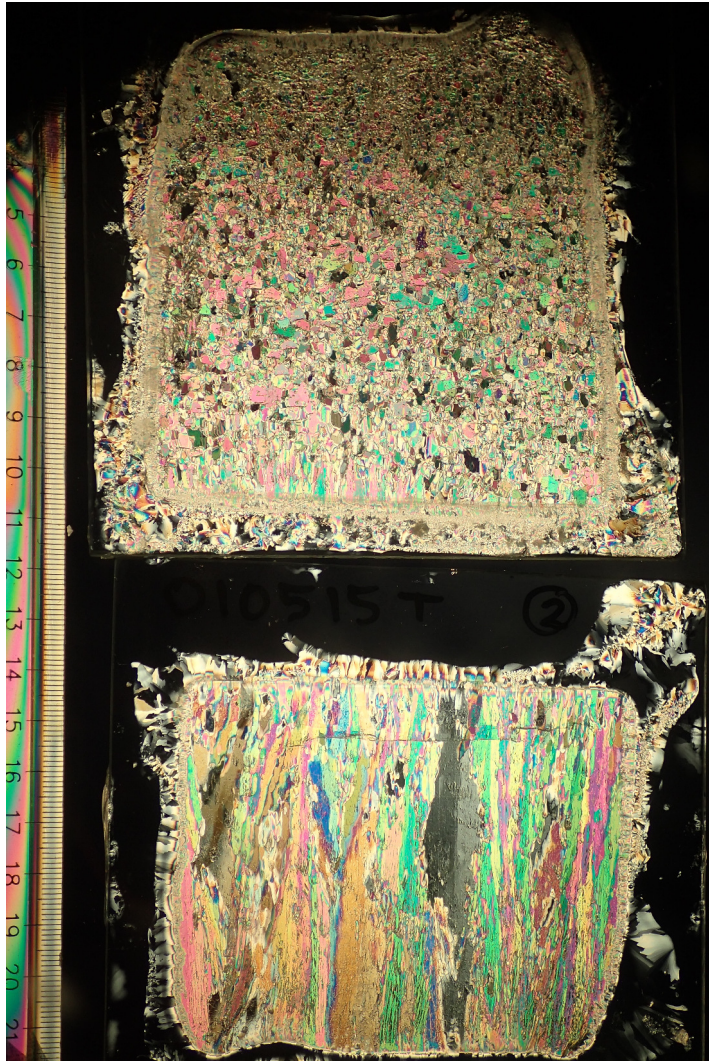
Figure 3.6: Thin vertical sections of the top and bottom part of an ice core collected during the N-ICE 2015 campaign. The top part is identified as granular ice, with randomly oriented rounded ice crystals. The bottom part is identified as columnar ice, with vertical elongated ice crystals. Courtesy: Martine Espeseth, UiT.

different colours relate to the orientation of the c-axis in the ice crystals. It can
be seen that the top consists of a granular crystal structure and the bottom is
characterised by columnar crystal structures.

3.3.4   Surface features

The characteristics of the sea ice surface are very important for microwave scat-
tering. A number of weathering and deformation processes affect the surface. The
large scale roughness features are mainly caused by ice deformation. Specifically,
rafting and ridging may cause significant deformation.

Small scale roughness of the ice surface is in addition governed by factors like
the sea state and temperature during the ice formation process, precipitation,
melt or wind. A notable example of small scale roughness features are so called
frost flowers (see figure 3.8). These are relatively large ice crystals with high salt
content that grow at the sea ice surface at specific atmospheric conditions (Style
& Worster 2009) and may play an important role to the backscattering response
of the surface (Isleifson et al. 2014).

It is difficult to make general statements about typical roughness characteris-
tics, partly due to their dynamic nature and partly due to lack of measurements
covering large regions. The deformation features on the order of decimetres to
metres can be mapped with helicopters, airplanes and satellites (Yitayew et al.
2018, Dierking et al. 2017). Measurements of the small scale characteristics are
however usually done using ground based laser scanners or other types of profilers
(Johansson 1988, Drinkwater 1989, Paterson et al. 1991, Onstott 1992, Dierking
1999, Landy et al. 2015) with limiting coverage. Johansson (1988) and Drinkwa-
ter (1989) find that the height distribution is Gaussian. Regarding the correlation
function, some indicate that an exponential correlation function is realistic for
undeformed sea ice (Kim et al. 1985, Johansson 1988, Dierking 1999). Even
less is known about the surface features of the ice-water interface. It is however
reasonable to believe that this is smoother than the upper surface, as shown in
figure 3.7.

3.3.5   Snow

Snow is of great importance to the microwave response in several ways. A layer
of snow will change the angle of incidence of the waves hitting the ice surface
and cause volume scattering. If the snow is dry, volume scattering mainly occurs
at relatively high frequencies. If the snow is wet, the liquid content will also
scatter, which can be significant even at lower frequencies. The liquid water also
attenuates the electromagnetic (EM) waves which depending on frequency, may
decrease the total volume scattering response from the snow as well as from the
sea ice under the snow.

Figure 3.7: Underwater photographs showing the interface between sea ice and sea water. The roughness of the interface may play an important role to microwave scattering for wavelengths that can penetrating through the sea ice. The images are taken during the N-ICE 2015 campaign. The top and bottom image are from the 10th and 18th May, respectively. In general, litttle is however known about typical roughness conditions of the ice-water interface. Image courtesy: Haakon Hop, norwegian polar institute (NPI)

Figure 3.8: A close up photograph of frost flowers on sea ice. Frost flowers grow under cold low wind conditions and may be up to a few centimetres in height. Since they typically are very saline and rough, they may contribute significantly to microwave scattering. Image is used under the public domain.

Figure 3.9: A close up photograph of a thin brine wetted snow layer on top of young ice. The image was taken on the 8th of May during the N-ICE 2015 campaign. The high permittivity of brine makes such snow layers important to microwave scattering. Image courtesy: Martine Espeseth, UiT.

Snow is typically assumed dry in cold condition. However, brine being expelled from the sea ice may also cause wetting, even at low temperatures. This affects the bottom of the snow layer and occurs on relatively relatively young and saline ice types (see an example in figure 3.9). Several studies have indicated that brine wetted snow plays a significant role to the scattering response from sea ice (Barber & Nghiem 1999, Nandan et al. 2017).

Large snow loads may also cause flooding of sea water on top of the ice, greatly changing the dielectric properties of its surface.

Chapter 4

Backscatter modeling

Radar backscattering from sea ice has been the topic of research for many decades, resulting in a wide variety of backscattering models (excellent summaries of some models can be found for instance in Winebrenner et al. (1992), Dierking (1992)). Common to most models is the treatment of sea ice as a random medium. This means that the geometry of the medium is described in terms of random variables and the modelled backscatter is the ensemble average over geometrical realisations. Moreover, most models regard sea ice as a layered medium, resulting in scattering from layer interfaces as well as from inhomogeneities within the layer volumes. In particular, brine and air inclusions are important for the latter.

In this chapter, the scattering models used later in the thesis are highlighted. Although there is in principal not a clear distinction between scattering from layer interfaces and volume inhomogeneities in terms of the integral equation (equation 2.27), the problem is greatly simplified by treating surface and volume scattering separately. Accordingly, section 4.1 deals with surface scattering and section 4.2 with volume scattering. Based on these models, a semi-coherent layered backscatter model representing sea ice is described in section 5.2.

4.1   Surface scattering

Surface scattering denotes scattering resulting from a single horizontal interface between two media of different permittivity. If the boundary is perfectly flat, the incident wave is only reflected into the so called specular direction, such that the incident and scattered angles are the same. For backscattering to occur, the boundary needs to be rough.

There are many approximate solutions to the backscattering problem from rough surfaces (an extensive review can be found in Elfouhaily et al. (2004)).

Historically, two approximations, stand out in popularity: the small perturbation model (SPM) and the stationary phase approximation of the Kirchoff model, also referred to as the GOM. These approximations result in closed form expressions for the backscattering coefficient, but are limited to small and large roughness scales, respectively. Many approaches have been suggested to bridge the gap in validity between the SPM and GOM, of which the integral equation model (IEM) is one of the most popular.

In the following, the concept of surface roughness is first presented. Then, the SPM, GOM and IEM are introduced with according validity ranges.

4.1.1 Surface roughness

Surface roughness can be modelled as random but correlated vertical height variations, denoted $z(x, y)$. Normally, the variations can be assumed Gaussian distributed and the coordinate system can be chosen in a way that the mean is zero, such that $z(x, y) \sim \mathcal{N}(0, \sigma_z^2)$. The standard deviation σ_z is referred to as the root mean square (RMS) height of the surface. The smoothness of the surface is realised though the correlation of the height variations along x and y, which is typically modelled with some idealised correlation function.

Before considering a few correlation functions in more detail, it is worth noting that most correlation functions are parameterised by a correlation length l. Thus, given a specific correlation function, the roughness of a surface is fully described by only two parameters: the RMS height σ_z and the correlation length l.

Surface correlation

The (normalised) correlation function tells how the vertical heights $z(x, y)$ at two displaced positions along the surface are correlated and is defined as:

$$\rho(x, y) = \lim_{S \to \infty} \frac{1}{S} \int \int_S \frac{z(x', y')z(x' - x, y' - y)}{\sigma_z^2} \, \mathrm{d}x' \, \mathrm{d}y' \qquad (4.1)$$

where x and y are the displacements. Often, the correlation function can be assumed isotropic, such that it only depends on the radial variable $r = \sqrt{x^2 + y^2}$. It is then sufficient to consider the one sided radial correlation function defined as:

$$\rho(r) = \lim_{R \to \infty} \frac{2\pi}{R} \int_0^R \frac{z(r')z(r' - r)}{\sigma_z^2} \, \mathrm{d}r' \qquad (4.2)$$

In this thesis, all surfaces are assumed isotropic. Specifically, the following three radial correlation functions are considered: the Gaussian, the exponential and the generalised power law (GPL) correlation function. These are defined as (Fung

1994, Li et al. 2002):

Gaussian: $\qquad \rho(r) = \mathrm{e}^{-r^2/l^2}$ (4.3a)

Exponential: $\qquad \rho(r) = \mathrm{e}^{-|r|/l}$ (4.3b)

GPL: $\qquad \rho(r) = \dfrac{1}{2^{p-2}\Gamma(p-1)} \left(\dfrac{2b_p r}{a_p l}\right)^{p-1} K_{p-1}\left(\dfrac{2b_p r}{a_p l}\right)$ (4.3c)

where $\Gamma(\cdot)$ is the Gamma function, $K_\nu(\cdot)$ is the ν:th order modified Bessel function of the second kind and the coefficients a_p and b_p are defined in equations B.19 and B.20 (appendix B).

The Gaussian and exponential correlation functions are clearly mathematically simpler. The GPL correlation function is less simple, but more general in the sense that the other two functions are special cases of it. Specifically, for $p = 1.5$, the GPL correlation function reduces to the exponential one and as $p \to \infty$ it approaches the Gaussian one (Li et al. 2002).

In figure 4.1(a), the three correlation functions are plotted versus the radius r. In figure 4.2, corresponding random surfaces are generated, using identical RMS heights, correlation lengths and random seeds. The profiles that are highlighted across the surfaces are shown in figure 4.1(c).

Roughness spectrum

Regarding surface scattering, the Fourier transform of the correlation function plays an important role (see sections 4.1.2 and 4.1.4). Specifically, the Fourier transform of the n:th power of the correlation functions is:

$$W_n(k) = \int_0^\infty \rho^n(r) J_0(kr) r \, \mathrm{d}r \tag{4.4}$$

where $J_0(\cdot)$ is the 0:th order Bessel function of the first kind. For the above mentioned correlation functions this yields (Fung 1994, Li et al. 2002):

Gaussian: $\qquad W_n(k) = \dfrac{l^2}{2n} \mathrm{e}^{-(kl)^2/4n}$ (4.5a)

Exponential: $\qquad W_n(k) = \dfrac{l^2 n}{((kl)^2 + n^2)^{3/2}}$ (4.5b)

GPL: $\qquad W_n(k) \approx \left(\dfrac{l}{n^{f_p}}\right)^2 \dfrac{p-1}{2} \dfrac{a_p^2}{b_p^2} \left(1 + \dfrac{1}{4} \dfrac{a_p^2}{b_p^2} \left(\dfrac{kl}{n^{f_p}}\right)^2\right)^{-p}$ (4.5c)

where f_p is defined in equation B.21 (appendix B). Note that for $n = 1$, these yield the power spectra of the surfaces, also referred to as the surface roughness

(a)

(b)

(c)
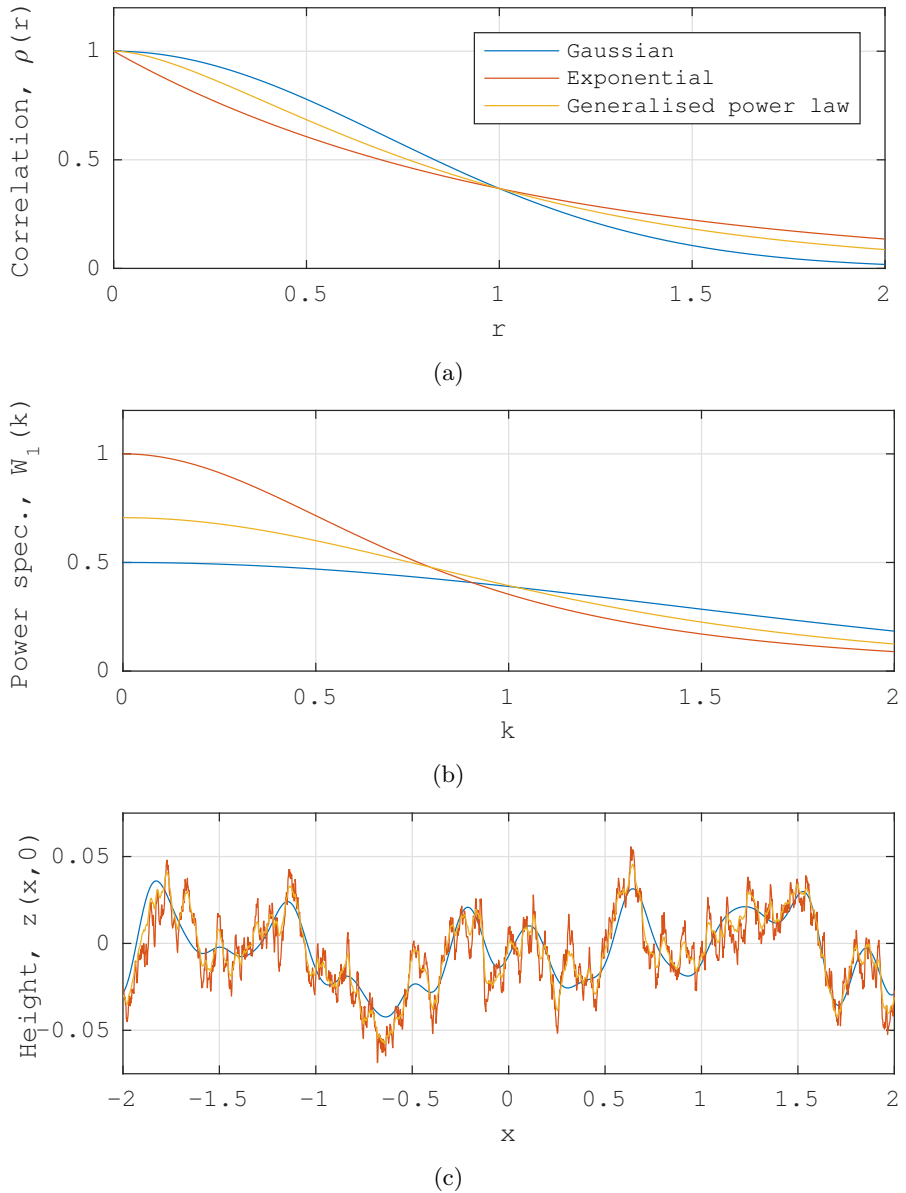
Figure 4.1: The Gaussian, exponential and generalised power law (GPL) (with $p = 2.1$) correlation functions plotted in (a), with corresponding power spectra in (b) and generated horizontal profiles in (c) (see corresponding surfaces in figure 4.2). The RMS height is $\sigma_z = 0.3$ and correlation length is $l = 1$.
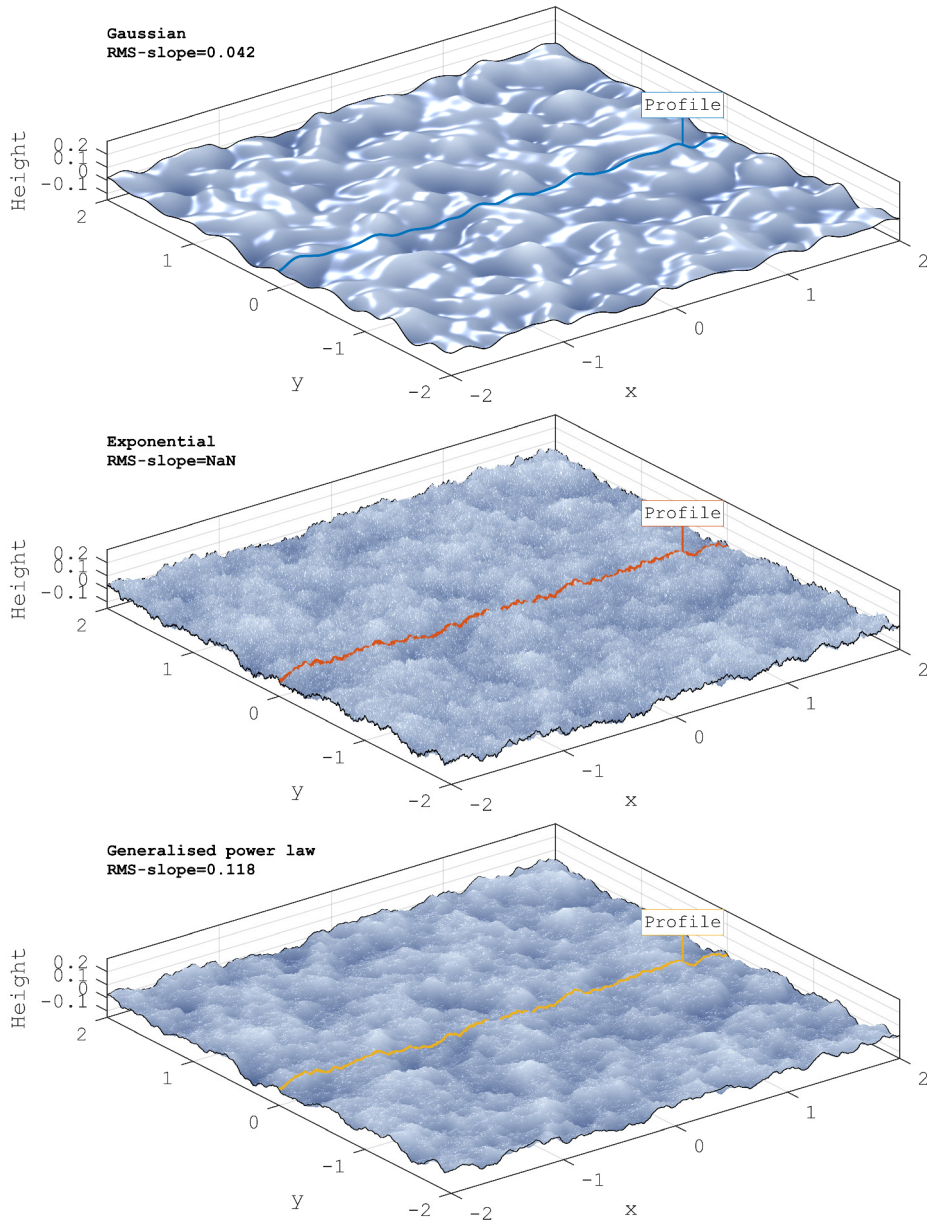
Figure 4.2: Three surfaces generated using the Gaussian (top), exponential (middle) and GPL with $p = 2.1$ (bottom) correlation functions, using the RMS height $\sigma_z = 0.3$ and correlation length $l = 1$. The surfaces have been shaded in order to enhance the small scale roughness.

spectra. Note further that the GPL spectrum is given as an approximation of the true Fourier transform (see Li et al. (2002) for details). In figure 4.1(b), the three roughness spectra are plotted versus the wave number k.

RMS surface slope

The RMS slope of a random rough surface is an important parameter, partly because it enters explicitly into the GOM (equation 4.13), but also because it indicates if multiple surface scattering is significant. Specifically, if the surface has very large slopes, multiple scattering typically needs to be considered. The RMS slope σ_s is defined as (Ulaby et al. 1982, page 1012):

$$\sigma_s = \sigma_z \left(-\frac{\mathrm{d}^2 \rho(r)}{\mathrm{d}r^2} \bigg|_{r=0} \right)^{1/2} \tag{4.6}$$

which for the above mentioned correlation functions yields (Fung 1994, Li et al. 2002):

Gaussian: $\qquad\qquad \sigma_s = \frac{\sigma_z}{l} \sqrt{2}$ $\hfill$ (4.7a)

Exponential: $\qquad\quad \sigma_s$ is undefined $\hfill$ (4.7b)

GPL: $\qquad\qquad\quad \sigma_s = \frac{\sigma_z}{l} \sqrt{\frac{2}{p-2}} \frac{b_p}{a_p} \qquad$ for $p > 2$ $\hfill$ (4.7c)

For the exponential correlation function, the derivative at the origin is not defined thus neither is the RMS slope. This is also the case for the GPL correlation function for $p \leq 2$. Note however the similarity between the exponential correlation function and the GPL with $p = 2.1$ in the generated profiles and corresponding surfaces in figures 4.1(c) and 4.2, respectively, where the latter does have a well defined RMS slope.

Average radius of surface curvature

The average radius of curvature of a random rough surface is a key parameter in the Kirchhoff approximation which is the basis for both the GOM and IEM. If the RMS slope is small, such that $\sigma_s \ll 1$, the average radius of curvature Γ_c is approximately given as (Ulaby et al. 1982, page 1013):

$$\Gamma_c \approx \frac{1}{\sigma_z} \left(-\frac{2}{\pi} \frac{\mathrm{d}^4 \rho(r)}{\mathrm{d}r^4} \bigg|_{r=0} \right)^{-1/2} \tag{4.8}$$

For the considered correlation functions, this yields:

Gaussian: $\qquad\qquad \Gamma_c \approx \dfrac{l^2}{\sigma_z}\sqrt{\dfrac{\pi}{24}}$ $\qquad\qquad\qquad\qquad\qquad\qquad$ (4.9a)

Exponential: $\qquad\;\; \Gamma_c$ is undefined $\qquad\qquad\qquad\qquad\qquad\qquad\qquad$ (4.9b)

GPL: $\qquad\qquad\quad \Gamma_c \approx \dfrac{l^2}{2\sigma_z}\dfrac{a_p^2}{b_p^2}\sqrt{\dfrac{\pi}{6}\left(6-5p+p^2\right)}$ $\qquad$ for $p > 3$ $\qquad$ (4.9c)

As for the RMS slope, curvature cannot be derived for the exponential function. The expression for the GPL average radius of curvature is derived in section A.1 in appendix A.

4.1.2 Small perturbation model (SPM)

The SPM (also referred to as the Bragg model) dates back to work on sound waves by Lord Rayleigh in the late nineteenth century, but was formulated for dielectric surface scattering by Rice (1951). There are many ways to derive the model (see Elfouhaily et al. 2004, for an overview), but popularly it is derived from the wave equation 2.7 rather than the surface integral equation 2.29.

In this case, the derivation can be carried out using Rayleigh's hypothesis. The scattered field at the surface is then assumed to be a superposition of upgoing plane waves of unknown amplitudes, thus this requires small surface slopes relative to the EM wavelength to be valid. By imposing appropriate boundary condition at the surface, the amplitudes can be determined and the incident and scattered fields can be expressed as power series with respect to the RMS height relative to the wavelength, that is $k\sigma_z$. If $k\sigma_z$ is sufficiently small, the series can be truncated to yield an approximate closed form solution.

Truncation to first order results in (Ulaby et al. 1982, page 961):

$$C_{ijkl}(k,\theta,\varepsilon_r,\sigma_z,\rho) = 4(k\cos\theta)^4 \sigma_z^2 W(-2k\sin\theta,0)\alpha_{ij}\alpha_{kl}^* \qquad (4.10)$$

where the indices i,j,k,l indicate polarisation and:

$$\begin{aligned}
\alpha_{hh} &= \frac{(\mu_r-1)(\mu_r\varepsilon_r + \sin^2\theta(\mu_r-1)) + {\mu_r}^2(\varepsilon_r-1)}{|\mu_r\cos\theta + q|^2}R_{hh} \\
\alpha_{vv} &= \frac{(\varepsilon_r-1)(\mu_r\varepsilon_r + \sin^2\theta(\varepsilon_r-1)) + {\varepsilon_r}^2(\mu_r-1)}{|\varepsilon_r\cos\theta + q|^2}R_{vv} \qquad (4.11) \\
\alpha_{hv} &= \alpha_{vh} = 0
\end{aligned}$$

The range of validity of the first order SPM is (Ulaby et al. 1982, page 966):

$$\begin{aligned}
k\sigma_z &< 0.3 \\
\sigma_s &< 0.3
\end{aligned} \qquad (4.12)$$

Truncation to second order will result in a non-zero cross polarised channel, that is $\alpha_{hv} = \alpha_{vh} \neq 0$. The second order terms are however very complicated (Valenzuela 1967) and therefore not considered here.

4.1.3 Geometric optics model (GOM)

The GOM is another widely used surface scattering model. Its starting point is the Stratton Chu integral equation (equation 2.27), where the surface is approximated locally as a tangent plane when evaluating the surface fields in the integral. This is known as the Kirchhoff approximation and is valid if the curvature and correlation length of the surface is large compared to the wavelength.

If the tangent planes are assumed infinite, referred to as the stationary phase approximation, the integral can be evaluated analytically resulting in the GOM (Ulaby et al. 1982, page 936):

$$C_{ijkl}(\theta, \varepsilon_r, \sigma_s) = \begin{cases} \mathrm{e}^{-(\sigma_s \tan \theta)^2/2} \left(2\sigma_s{}^2 \cos^4 \theta\right)^{-1} |R_0|^2 & \text{if } i{=}j{=}k{=}l \\ 0 & \text{else} \end{cases} \quad (4.13)$$

where i, j, k, l indicate polarisation and $R_0 = R_{hh}(0) = R_{vv}(0)$ is the fresnel reflectivity at zero degree incidence angle (see equation B.4). The GOM is thus independent of polarisation, yet the full covariance matrix notation is kept here for consistency with the other models.

The GOM is valid if (Dierking 1992):

$$\begin{aligned} k\sigma_z &> \frac{\pi/2}{\cos \theta} \\ kl &> 2\pi \\ k\Gamma_c &> 2\pi \end{aligned} \quad (4.14)$$

An alternative to the stationary phase approximation that results in the GOM, is a small roughness approximation which results in a power series that can be truncated. This is known as the scalar approximation and yields the so called physical optics model (POM). As indicated in Tsang et al. (2004), however, the POM is less accurate compared to the SPM and will not be considered here.

4.1.4 Improved integral equation model (IIEM)

In figure 4.3, the validity ranges of the SPM and GOM are plotted in purple and yellow respectively, using the GPL correlation function for different values of p (recall that $p = 1.5$ and $p = \infty$ yields the exponential and Gaussian correlation functions, respectively). The validity for the respective model is constrained by the inequalities in equation 4.12 and 4.14. Clearly, there is a wide range of
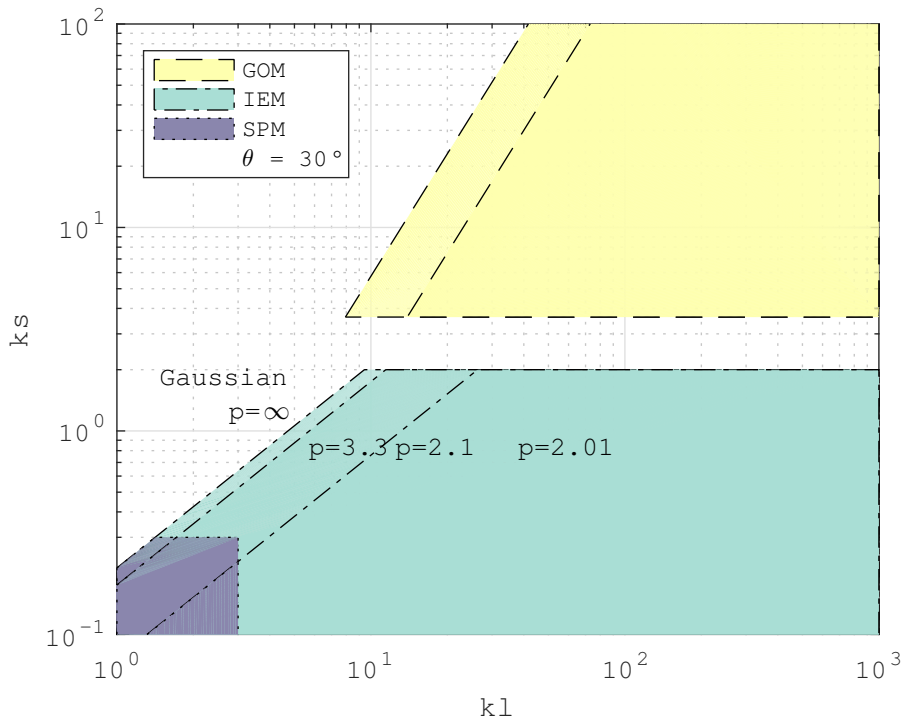
Figure 4.3: The validity domains illustrated in terms of normalised RMS heights ($k\sigma_z$) and correlation lengths (kl), for the three surface scattering models: SPM, IEM and GOM. The generalised power law correlation function is considered for varying values of the parameter p, as indicated in the figure. Note that only the cases where $p > 3$ are shown for the GOM, when the mean radius of curvature is well defined (see equation 4.9c). The incidence angle is 30°.

roughness conditions for which neither model is valid. A great number of unifying methods trying to bridge the gap between the SPM and GOM has been proposed (see e.g. Elfouhaily et al. 2004, and references therein). A group of models that has gained a lot of popularity are the IEMs. The derivation of these models are more involved than for the SPM and GOM, yet the key steps are highlighted below.

The IEMs are based on a second iteration Kirchhoff approximation of the surface fields in the Stratton Chu integral equation (see equation 2.29). Specifically, the electric surface field resulting from the Kirchhoff approximation, call it $(\hat{\mathbf{n}} \times \mathbf{E})_k$, is separated form the total unknown surface field $\hat{\mathbf{n}} \times \mathbf{E}$, as:

$$\hat{\mathbf{n}} \times \mathbf{E} = (\hat{\mathbf{n}} \times \mathbf{E})_k + (\hat{\mathbf{n}} \times \mathbf{E})_c \qquad (4.15)$$

where the rest term $(\hat{\mathbf{n}} \times \mathbf{E})_c$ is called the complementary field. The same is done for the the magnetic surface field, but the approach is the same and therefore left out here.

The main approximation of the IEMs is to apply the Kirchhoff approximation on the complementary field. After a set of further simplifications of the Kirchhoff approximation, restricting the incident and scattered fields to be either horizontally or vertically polarised (see section III in Fung et al. 1992, for details), the Stratton Chu integral can be split up into two parts (note that by simply inserting equation 4.15 into the Stratton Chu integral equation 2.29, does not generally result in two separate integrals), each corresponding to a component of the total scattered field:

$$\mathbf{E}_{qp}^s = (\mathbf{E}_{qp}^s)_k + (\mathbf{E}_{qp}^s)_c \qquad (4.16)$$

where the indices qp indicate polarisation. As it turns out, $(\mathbf{E}_{qp}^s)_k$ only depends on the Kirchhoff surface field $(\hat{\mathbf{n}} \times \mathbf{E})_k$ and $(\mathbf{E}_{qp}^s)_c$ only depends on the complementary surface field $(\hat{\mathbf{n}} \times \mathbf{E})_c$. Specifically, these scattered field components can be written as integrals over the so called Kirchhoff and complementary field coefficients, denoted f_{qp} and F_{qp}, respectively (Fung et al. 1992).

Thus, if the field coefficients f_{qp} and F_{qp} are found (which depend on the Kirchhoff and complementary surface fields, respectively), they can be integrated and summed to give the total scattered field and thus the scattering covariance matrix:

$$\left.\begin{array}{ccc} f_{qp} & \rightarrow & (\mathbf{E}_{qp}^s)_k \\ F_{qp} & \rightarrow & (\mathbf{E}_{qp}^s)_c \end{array}\right\} \rightarrow \mathbf{E}_{qp}^s \rightarrow C_{ijkl} \qquad (4.17)$$

The first derivation of the field coefficients, f_{qp} and F_{qp}, was carried out by Fung et al. (1992) and is rather long and intricate. A particular approximation that is made, is that the local incidence angle in the Fresnel reflection coefficients, which appears in both field coefficients, is approximated with the (global) incidence angle if the roughness is small to intermediate and as the specular angle if the

roughness is large (validity range of GOM). Doing so, the integral reduces to the GOM in the large scale limit (Fung et al. 1992). In the small to intermediate scale, the integral becomes what is normally referred to as the original IEM. This can further be reduced to the SPM if the roughness is sufficiently small.

A semi-empirical approximation thought to be more valid for intermediate roughness scales was suggested by Wu et al. (2001), introducing modified Fresnel reflection coefficients containing a transition function which smoothly bridges the gap between the two limiting angle approximations. As stated in (Fung & Chen 2010, page 164), the suggested transition function is an estimation and may not be correct for all roughness, angle and frequency conditions. Nevertheless, the transition function described in Wu et al. (2001) is considered in this thesis. Moreover, it is only applied to the Kirchhoff field coefficient f_{pp} here, and not to the complementary field coefficient F_{qp} (according to Fung & Chen 2010, this appears to be adequate).

In addition to the transition function suggested by Wu et al. (2001), various other modifications of the field coefficients have been suggested and resulted in a variety of different IEMs (see Hsieh et al. 1997, Chen et al. 2000, Álvarez-Pérez 2001, Fung et al. 2002, Liu et al. 2003, Wu et al. 2008, for example). In this thesis, the model described in Fung et al. (2002) and Fung & Chen (2010) is considered, which hereafter will be referred to as the improved integral equation model (IIEM) (also referred to as the IEM-B or I^{2}EM, by some authors). Ignoring multiple scattering, the IIEM does not predict a cross polarised backscatter and the co-polarised elements of the covariance matrix are:

$$C_{ppqq}(k, \theta, \varepsilon_r, \sigma_z, \rho) = \frac{k^2}{4\pi} e^{-2(k\cos\theta\sigma_z)^2} \sum_{n=1}^{\infty} I_{pp}(n) I_{qq}^*(n) \frac{W^{(n)}(2k\sin\theta, 0)}{n!} \quad (4.18)$$

where:

$$I_{pp}(n) = (2k\sigma_z \cos\theta)^n f_{pp} + \frac{\sigma_z}{4}(k\sigma_z \cos\theta)^n F_{pp} \quad (4.19)$$

and the expressions for f_{pp} and F_{pp} can be found in Fung & Chen (2010).

The validity range of the single scattering IIEM is (Fung & Chen 2010):

$$\begin{aligned} k\sigma_z &< 2 \\ \sigma_s &< 0.3 \end{aligned} \quad (4.20)$$

In figure 4.3, the corresponding region of validity is shown in green. The model thus overlaps the SPM and it's region of validity is considerably closer to the region of the GOM for the plotted case (using the GPL correlation function and 30° incidence angle).

4.1.5   Shadowing

Shadowing is considered by multiplying the backscatter coefficients by a factor f_{shdw} that depends on the RMS slope and incidence angle (Fung & Chen 2010, page 12):

$$f_{shdw} = \left(1 + \frac{1}{2}\left(\frac{\mathrm{e}^{-a^2}}{\sqrt{\pi}a} - \mathrm{erfc}(a)\right)\right)^{-1} \qquad (4.21)$$

where $\mathrm{erfc}(\cdot)$ is the complementary error function and:

$$a = \frac{\cot(\theta)}{\sigma_s\sqrt{2}} \qquad (4.22)$$

where σ_s is the RMS slope and θ is the incidence angle.

4.2   Volume scattering

Volume scattering is caused by permittivity contrasts within the bulk of a medium. In sea ice, such contrasts are typically attributed to the brine or air being trapped between crystalline ice (see section 3.2.2). In dry snow, the snow crystals account for the contrasts, while if the snow is wet, liquid water or brine droplets are important.

All theoretical volume scattering models are in one way or the other approximate solutions to the volume integral equation (VIE) (equation 2.27). The particular approximations distinguish the models from one another. Common to most sea ice models is that they are one dimensional, such that material properties vary only as a function of depth and typically in terms of discrete layers. Other distinguishing features are to what extent the models account for polarisation of the EM waves, material anisotropy, multiple backscattering and coherent interactions within the media. The latter include interference between the bulk permittivity fluctuations such as brine pockets or ice crystals, called dense medium effects, as well as interference between layer boundaries, such as between the snow-ice and ice-water interface in sea ice.

Two general classes of models can be identified: (1) those formulated in terms of the VIE, called wave theory models, and (2) those formulated in terms of the radiative transfer equation (RTE), called radiative transfer (RT) models. Although both types of models in principal provide an approximate solution to the basic wave equation, the RTE was initially motivated by phenomenological arguments rather than being derived from first principles. Later, however, the RTE has been derived from the VIE under certain assumptions (Mishchenko 2008), which makes the separation between wave theory and RT models somewhat misleading.

Nevertheless, a key difference is that wave theory models solve for the EM field while RT models solve for the intensity or stokes vector. As such, wave theory models are intrinsically coherent, although limiting approximations are typically needed. Specifically, all wave theory models of volume scattering in sea ice that can be found in the literature are based on the distorted Born approximation (DBA) and as such, do not account for multiple backscattering (Lee & Kong 1985, Nghiem et al. 1990, 1993, 1995b). Some RT models on the other hand include effects of multiple incoherent backscattering (Fung & Eom 1982) and can be modified to account for dense medium effects as well (Fung & Eom 1985, Tjuatja et al. 1992, Tonboe et al. 2011, Albert et al. 2012), although most of them do not account for interference between layer interfaces, except a modified RT model presented by Lee & Kong (1988).

At present, there is no analytical sea ice model that includes all aspects of volume scattering mentioned above. In this thesis, the wave theory model described in Nghiem et al. (1990, 1993) is considered. This is based on strong fluctuation theory (SFT) accompanied with the DBA. The model (1) is fully polarimetric (that is, it calculates the full scattering covariance matrix), (2) allows for anisotropic media resulting from elongated brine inclusions with a preferred alignment and (3) accounts for coherent interaction between planar layer interfaces.

4.2.1   Strong fluctuation theory (SFT)

This section outlines the SFT described in Nghiem et al. (1990, 1993) which mainly builds on the theory of Tsang & Kong (1981) and work referenced therein.

Inclusions of permittivity ε_i are embedded in a background permittivity ε_b, such that the permittivity randomly fluctuates between the two:

$$\varepsilon(\mathbf{r}) = \begin{cases} \varepsilon_i & \text{if } \mathbf{r} \in \text{inclusion} \\ \varepsilon_b & \text{if } \mathbf{r} \in \text{background} \end{cases} \tag{4.23}$$

The probability of $\varepsilon(\mathbf{r}) = \varepsilon_i$ corresponds to the volume fraction of the inclusions, denoted V_i. The spatial smoothness of the permittivity fluctuations are described in terms of a correlation function, which here is assumed exponential, that is:

$$\rho_\varepsilon(\mathbf{r}) = \mathrm{e}^{-\left|\bar{\mathbf{L}}^{-1}\mathbf{r}\right|} \tag{4.24}$$

where the matrix $\bar{\mathbf{L}}$ contains the correlation lengths in x, y and z on the diagonal:

$$\bar{\mathbf{L}} = \begin{bmatrix} l_x & 0 & 0 \\ 0 & l_y & 0 \\ 0 & 0 & l_z \end{bmatrix} \tag{4.25}$$
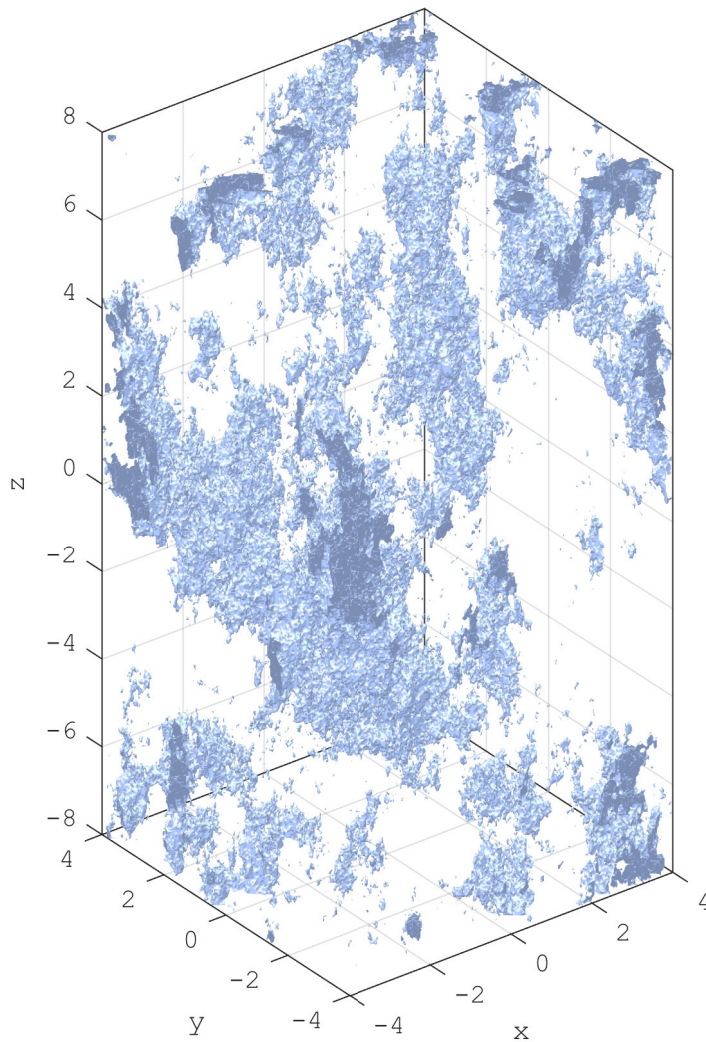
Figure 4.4: An exponentially correlated randomly fluctuating permittivity is visualised in terms of permittivity-iso-surfaces showing the boundary between the background and inclusions. Here the volume fraction of inclusions is 5% and the correlation lengths are $l_x = l_y = 1$ and $l_z = 2$.

In figure 4.4, a realisation of such a randomly fluctuating permittivity is visualised. The figure shows the iso-permittivity surfaces, that is, the surfaces at the boundary between the inclusions and the background. It is easy to recognise that electric field in this geometry will be rather complex. However, it can be decomposed into two parts; a mean field and a randomly fluctuating field with zero mean. SFT provide approximate expressions for these in terms of integral equations.

In the following, the mean field and its propagation through the random medium by the mean dyadic Green's function (DGF) will be discussed. These will be used to describe the scattered field under the distorted Born approximation.

Mean wave propagation

The starting point for finding the mean field is the VIE (equation 2.27), which reads:

$$\mathbf{E}(\mathbf{r}) = \mathbf{E}_g(\mathbf{r}) + k_0^2 \int \mathrm{d}\mathbf{r}' \, \bar{\mathbf{G}}_0(\mathbf{r}, \mathbf{r}')\bar{\mathbf{Q}}\mathbf{E}(\mathbf{r}') \tag{4.26}$$

where the permittivity contrast is introduced in the dyad:

$$\bar{\mathbf{Q}}(\mathbf{r}) = \varepsilon(\mathbf{r})\bar{\mathbf{I}} - \bar{\varepsilon}_g \tag{4.27}$$

where $\varepsilon(\mathbf{r})$ is the randomly fluctuating permittivity and $\bar{\varepsilon}_g$ is a homogeneous permittivity that will be specified shortly.

Note first that to obtain the mean field within the medium, the DGF needs to be integrated over $\mathbf{r} = \mathbf{r}'$ where it is singular. This can be treated by integrating around an exclusion volume centred at the singularity, which is let to approach zero in size. The shape of the exclusion volume corresponds to an iso-surface of the correlation function. For the exponential correlation function in equation 4.24, this shape is an ellipsoid. Formally, this is done by expressing the Green's function in terms of a principal value part and a Dirac delta part:

$$\bar{\mathbf{G}}_g(\mathbf{r}, \mathbf{r}') = PV\,\bar{\mathbf{G}}_g(\mathbf{r}, \mathbf{r}') - \delta(\mathbf{r} - \mathbf{r}')k_0^{-2}\bar{\mathbf{S}} \tag{4.28}$$

where the dyad $\bar{\mathbf{S}}$ depends on the shape of the exclusion volume (Nghiem et al. 1990).

Next, it turns out to be convenient to express the electric field in terms of the so called external field, defined as:

$$\mathbf{F}(\mathbf{r}) = \left(\bar{\mathbf{I}} + \bar{\mathbf{S}}\bar{\mathbf{Q}}(\mathbf{r})\right)\mathbf{E}(\mathbf{r}) \tag{4.29}$$

and the permittivity contrasts in terms of:

$$\bar{\xi}(\mathbf{r}) = \bar{\mathbf{Q}}(\mathbf{r})\left(\bar{\mathbf{I}} + \bar{\mathbf{S}}\bar{\mathbf{Q}}(\mathbf{r})\right)^{-1} \tag{4.30}$$

Equation 4.26 then becomes:

$$\mathbf{F}(\mathbf{r}) = \mathbf{E}_g(\mathbf{r}) + k_0^2 \int \mathrm{d}\mathbf{r}' \, \bar{\mathbf{G}}_0(\mathbf{r}, \mathbf{r}') \bar{\xi}(\mathbf{r}') \mathbf{F}(\mathbf{r}') \tag{4.31}$$

The homogeneous permittivity $\bar{\varepsilon}_g$ is now chosen such that $\langle \bar{\xi} \rangle = 0$.

The mean field $\langle \mathbf{F}(\mathbf{r}) \rangle$ can next be expressed in terms of a path integral in the so called Dyson's equation. This essentially means that at any point in space, the mean field is a weighted average over fields that have propagated to that point through all possible scattering paths. However, as it turns out, Dyson's equation contains an infinite series (the so called mass operator) that must be approximated to give a closed form solution for the mean field.

In SFT, the so called bi-local approximation is applied (also referred to as the Bourret or first order smoothing approximation). In the bi-local approximation, the paths that visit a unique scatterer only once are kept (formally, this is obtained by expressing the mass operator in terms of a series of Feynman diagrams, where only the first diagram is kept). The analytical expression for Dyson's equation under the bi-local approximation reads (Tsang & Kong 2004, page 181):

$$\langle \mathbf{F}(\mathbf{r}) \rangle = \mathbf{E}_g(\mathbf{r}) + \int \int \mathrm{d}\mathbf{r}_1 \mathrm{d}\mathbf{r}_2 \bar{\mathbf{G}}_g(\mathbf{r}, \mathbf{r}_1) \bar{\mathbf{G}}_g(\mathbf{r}_1, \mathbf{r}_2) \langle \mathbf{F}(\mathbf{r}_2) \rangle \rho_\varepsilon(\mathbf{r}_1 - \mathbf{r}_2) \tag{4.32}$$

Next, propagation of the mean external field through the random medium can be describe in terms of the mean DGF $\langle \bar{\mathbf{G}}(\mathbf{r}, \mathbf{r}') \rangle$. Similarly to the mean field in equation 4.32, the mean DGF can be derived under the bi-local approximation as (Tsang & Kong 2004, page 167):

$$\langle \bar{\mathbf{G}}(\mathbf{r}, \mathbf{r}') \rangle = \bar{\mathbf{G}}_g(\mathbf{r}, \mathbf{r}') + \int \int \mathrm{d}\mathbf{r}_1 \mathrm{d}\mathbf{r}_2 \bar{\mathbf{G}}_g(\mathbf{r}, \mathbf{r}_1) \bar{\mathbf{G}}_g(\mathbf{r}_1, \mathbf{r}_2) \langle \bar{\mathbf{G}}(\mathbf{r}_2, \mathbf{r}') \rangle \rho_\varepsilon(\mathbf{r}_1 - \mathbf{r}_2)$$
$$\tag{4.33}$$

Both the mean field and the mean DGF will be used to calculate the radar backscatter through the DBA (in section 4.2.1 below).

Interpretation of the bi-local approximation

Since the mean DGF $\langle \bar{\mathbf{G}}(\mathbf{r}, \mathbf{r}') \rangle$ is in the integrand in equation 4.33, the equation can be iterated to expand in a series (similarly to the Born series in section 2.4.3). One iteration yields:

$$\langle \bar{\mathbf{G}}(\mathbf{r}, \mathbf{r}') \rangle = \bar{\mathbf{G}}_g(\mathbf{r}, \mathbf{r}') + ...$$
$$\bar{\mathbf{G}}_g(\mathbf{r}, \mathbf{r}_1) \bar{\mathbf{G}}_g(\mathbf{r}_1, \mathbf{r}_2) \bar{\mathbf{G}}_g(\mathbf{r}_2, \mathbf{r}') \rho_\varepsilon(\mathbf{r}_1 - \mathbf{r}_2) + ...$$
$$\bar{\mathbf{G}}_g(\mathbf{r}, \mathbf{r}_1) \bar{\mathbf{G}}_g(\mathbf{r}_1, \mathbf{r}_2) \bar{\mathbf{G}}_g(\mathbf{r}_2, \mathbf{r}_3) \bar{\mathbf{G}}_g(\mathbf{r}_3, \mathbf{r}_4) \langle \bar{\mathbf{G}}(\mathbf{r}_4, \mathbf{r}') \rangle \rho_\varepsilon(\mathbf{r}_1 - \mathbf{r}_2) \rho_\varepsilon(\mathbf{r}_3 - \mathbf{r}_4)$$
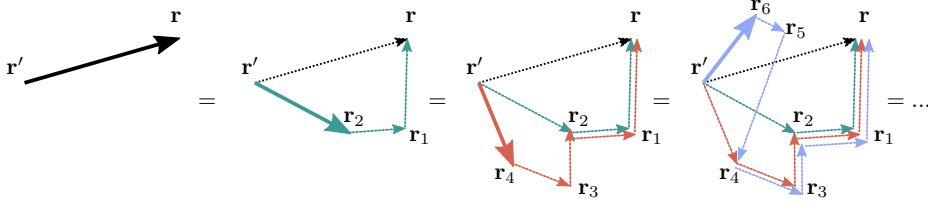$$\tag{4.34}$$

Figure 4.5: An illustration of the series expansion of the mean DGF under the bi-local approximation. Solid lines indicate propagation by the mean DGF $\langle \bar{\mathbf{G}} \rangle$ and dotted lines indicate non-scattered propagation in a homogeneous medium of permittivity ε_g governed by $\bar{\mathbf{G}}_g$. By iterating Dyson's equation, new paths going through the integration variables $\mathbf{r}_i$ for $i = 1, 2, 3...$ are obtained. Under the bi-local approximation, these paths only go through a unique scatterer once. Repeated scattering between inclusions are thus not considered in the approximation.

where the integration signs are omitted for readability (integration goes over all $\mathbf{r}_i$ for $i = 1, 2, 3...$). This iteration can be continued indefinitely to form an infinite series. The physical interpretation of this series is that it represents a weighted average of infinitely many propagation paths, all starting at $\mathbf{r}'$ and ending at $\mathbf{r}$.

Graphically, the series expansion can be illustrated as in figure 4.5. Solid lines indicate propagation by the mean DGF and dotted lines indicate non-scattered propagation by the homogeneous DGF $\bar{\mathbf{G}}_g(\mathbf{r}, \mathbf{r}')$. The first graph shows the mean DGF propagating the field from $\mathbf{r}'$ to $\mathbf{r}$. The second graph shows Dyson's equation under the bi-local approximation as written in equation 4.33. Here, one of an infinite number of position pairs $\mathbf{r}_1$ and $\mathbf{r}_2$ involved in integration is shown. By iterating Dyson's equation once, the third graph which corresponds to the right hand side of equation 4.34 is obtained, with new integration variables $\mathbf{r}_4$ and $\mathbf{r}_5$. By iterating once more, the forth graph is obtained. By imagining this iteration to continue an infinite number of times, it becomes clear that the propagation of the mean DGF is an average of an infinite number of different propagation paths through the medium, where the paths start at $\mathbf{r}'$, go through the positions $\mathbf{r}_1, \mathbf{r}_2, \mathbf{r}_3, ...$, and end at $\mathbf{r}$.

Being subject to the bi-local approximation, SFT thus accounts for multiple scattering in the mean dyadic Green function $\langle \bar{\mathbf{G}}(\mathbf{r}, \mathbf{r}') \rangle$ and corresponding mean field $\langle \mathbf{F}(\mathbf{r}) \rangle$.

Effective permittivity

A consequence of the bi-local approximation is that the mean field behaves as if the medium was homogeneous with an effective permittivity. Considering the mean electric field $\langle \mathbf{E} \rangle$, it can be shown that under the bi-local approximation, a plane wave with wave number $\mathbf{k}$ satisfies:

$$\langle \mathbf{D}(\mathbf{k}) \rangle = \bar{\varepsilon}_{eff}(\mathbf{k}) \langle \mathbf{E}(\mathbf{k}) \rangle \qquad (4.35)$$

where $\bar{\varepsilon}_{eff}(\mathbf{k})$ is the so called effective permittivity. An analytical expression for $\bar{\varepsilon}_{eff}(\mathbf{k})$ can be found if the frequency is assumed low, for which it becomes a function of the background and inclusion permittivities ε_b and ε_i, respectively, the volume fraction of the inclusions V_i and the correlation function ρ_ε (Tsang & Kong 1981, 2004, Nghiem et al. 1990).

Even if ε_b and ε_i are real numbers, that is, represent lossless media, the effective permittivity has in general an imaginary part that accounts for scattering losses. In addition, although ε_b and ε_i may be not dependent of $\mathbf{k}$, the effective permittivity will in general be so.

Moreover, if the correlation function is anisotropic, so is the effective permittivity. Horizontally and vertically polarised waves will thus propagate with different velocities through the medium resulting in different phase delays. In addition, transmission and refraction at the ice interfaces will be different between the two polarisations, a phenomenon called birefringence.

Backscattering

The backscattered field is solved with the DBA, which reads:

$$\mathbf{E}_s(\mathbf{r}) = k_0^2 \int d\mathbf{r}' \langle \bar{\mathbf{G}}(\mathbf{r}, \mathbf{r}') \rangle \bar{\xi}(\mathbf{r}') \langle \mathbf{F}(\mathbf{r}') \rangle \qquad (4.36)$$

Note the similarity to the first order Born approximation (FBA) in equation 2.32. The backscattered field is thus the sum of the mean field $\langle \mathbf{F}(\mathbf{r}') \rangle$ being backscattered by all the inclusions $\bar{\xi}(\mathbf{r}')$ and propagated back through the medium by the mean DGF $\langle \bar{\mathbf{G}}(\mathbf{r}, \mathbf{r}') \rangle$. The corresponding scattering covariance matrix is obtained through the ensemble average over the random permittivity fluctuations.

Since both the mean field and the mean DGF involve multiple scattering and the DBA involve single backscattering, models based on equation 4.36 are sometimes referred to as "multiple-forward-scatter, single-backscatter models" (Winebrenner et al. 1992). Note however that, while the DBA may seem limiting in that it only accounts for single backscattering, it is consistent with the bi-local approximation in Dyson's equation which assumes that the field is only scattered by a unique scatterer once. If multiple backscattering would be included, this assumption would break, since the integral in equation 4.36 goes over all scatterers (see for example Stogryn 1983, for a formal derivation).

4.2.2   Nghiem's 2-layer Model (N2M)

A solution to equation 4.36 for a geometrical configuration consisting of two and
three planar layers was developed by Nghiem et al. (1990, 1993). In the two layer
version, which from now on will be referred to as Nghiem's 2-layer Model (N2M),
an anisotropic heterogeneous media is sandwiched in between two homogeneous
media (see figure 4.6). This two layer version will later be used for volume
scattering calculations in section 5.2 and is therefore stated here in more detail.

For the sandwiched anisotropic media, the exponential correlation function
stated in equation 4.24 is used and restricted to be azimuthally symmetric, such
that $l_x = l_y = l_\rho$:

$$\bar{\mathbf{L}} = \begin{bmatrix} l_\rho & 0 & 0 \\ 0 & l_\rho & 0 \\ 0 & 0 & l_z \end{bmatrix} \tag{4.37}$$

The corresponding effective permittivity tensor is calculated through SFT and
takes the shape:

$$\bar{\varepsilon} = \begin{bmatrix} \varepsilon_\rho & 0 & 0 \\ 0 & \varepsilon_\rho & 0 \\ 0 & 0 & \varepsilon_z \end{bmatrix} \tag{4.38}$$

This is allowed to be rotated around one of the horizontal axes, say the x-axis,
by an angle ψ:

$$\bar{\varepsilon}(\psi) = \begin{bmatrix} 1 & 0 & 0 \\ 0 & \cos\psi & \sin\psi \\ 0 & -\sin\psi & \cos\psi \end{bmatrix} \begin{bmatrix} \varepsilon_\rho & 0 & 0 \\ 0 & \varepsilon_\rho & 0 \\ 0 & 0 & \varepsilon_z \end{bmatrix} \begin{bmatrix} 1 & 0 & 0 \\ 0 & \cos\psi & \sin\psi \\ 0 & -\sin\psi & \cos\psi \end{bmatrix}^{-1} \tag{4.39}$$

The rotation makes the medium azimuthally non-symmetric. However, the hori-
zontal alignment is assumed uniformly distributed in the ensemble averaging such
that the averaged target will still be vertically uniaxial.

A characteristic feature of the model is that it generally predicts a phase
shift between the co-polarised channels. This is caused by the anisotropy of
the layer, which causes different phase delays between the h- and v-polarised
waves. Moreover, stronger anisotropy leads to larger phase shifts, as illustrated
in figure 4.7(a) (see caption for parameter settings). In the figure, the co-polarised
phase difference is plotted versus the ratio l_z/l_ρ which here is referred to as the
elongation of the inclusions and is a measure of the anisotropy. The inclusions
are assumed vertically aligned (that is $\psi = 0$), with a permittivity of $\varepsilon_i = 38 - 41i$
(brine) in a background permittivity $\varepsilon_b = 3.15 - 0.002i$ (pure ice). The cross-
polarised backscatter is moreover also caused by the anisotropy of the medium, as
shown in figure 4.7(b). Specifically, the cross-polarised channel is only significant
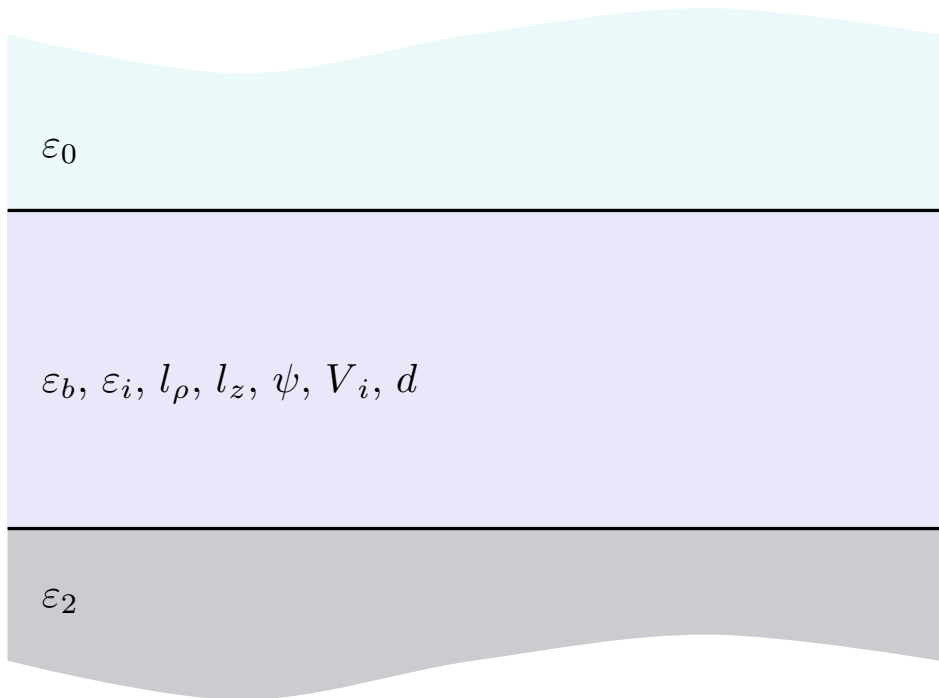if the inclusions are tilted in their local frame of reference, such that $\psi \neq 0$.

Figure 4.6: In the Nghiem's 2-layer Model (N2M) model, an anisotropic medium is sandwiched between two homogeneous non-scattering media as depicted above. The associated model input parameters are shown for the respective media.
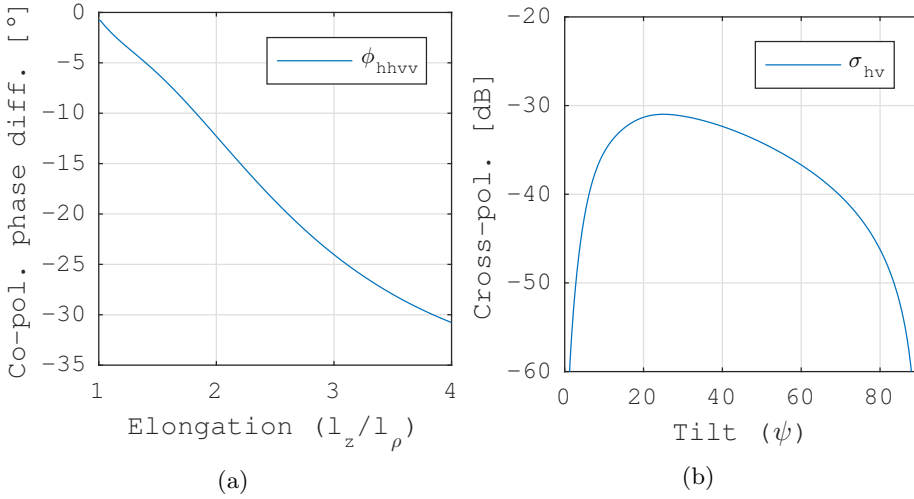
Figure 4.7: The co-polarised phase difference is plotted versus the elongation of the inclusions in (a) (with $\psi = 0$) and the cross polarised channel is plotted versus the tilt of the inclusions in (b) (with $l_\rho = 0.5$ mm and $l_z = 1$ mm). The frequency is 5.4 GHz, the incidence angle is 30° and $\varepsilon_0 = 1$, $\varepsilon_b = 3.15 - 0.002i$, $\varepsilon_i = 38 - 41i$, $\varepsilon_2 = 45 - 40i$, $V_i = 0.03$ and $d = 1$ m.
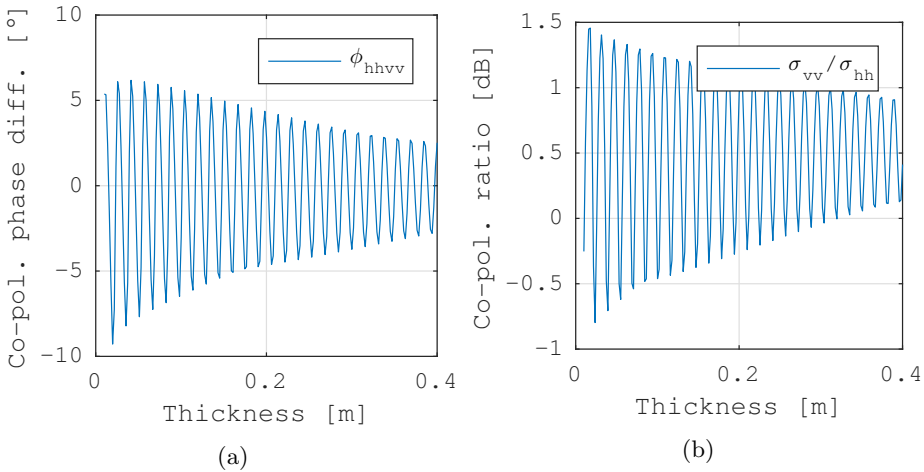
Figure 4.8: Co-polarised phase difference in (a) and co-polarised ratio in (b), plotted versus layer thickness, using $\psi = 0$, $l_\rho = 0.5$ mm, $l_z = 1$ mm and the other parameters are the same as in figure 4.7 (see figure caption).

Another associated and important feature is that the model is sensitive to variations in the layer thickness, as illustrated in figure 4.8 where the co-polarised phase difference and the co-polarised ratio is plotted versus the layer thickness. Firstly, both plots show a strong high-frequency oscillation which is caused by interference between the top and bottom interfaces. With regard to sea ice, such effects are unlikely to observe in real data, since the layer thickness typically vary on scales similar to the radar wavelength within the resolution cell. However, even if the high frequency interference were to be smoothened out, there is a trend in the signal as a function of thickness, in particular for the co-polarised channel (Kwok et al. 1995).

4.3   Overview of sea ice models

Based on the different ways of modelling surface and volume scattering mentioned above, an array of sea ice models can be found in the literature. Since the volume of the ice is generally more complicated than the surface, the treatment of volume scattering is generally what distinguishes them. A number of different models are summarised in chronological order, in table 4.1.

Some of the earliest models appeared in the late seventies and early eighties. An early example is Fung & Eom (1982) which treats a single ice layer using the GOM and classical RT theory. A later model by the same authors (Fung & Eom 1985) includes dense medium effects. In the mid eighties, an early model appeared using DBA for volume scattering (Lee & Kong 1985). This was later combined with SFT in Nghiem et al. (1990, 1995b). A model based on dense medium radiative transfer (DMRT) appeared at roughly the same time (Tjuatja et al. 1992). Later DMRT models include the one by (Albert et al. 2012). Recently, a model allowing for multiple rough interfaces was presented in Komarov et al. (2014).

Generally speaking, the main focus has been on models of level ice. For heavily deformed ice and ridges, the study by Carlström (1997) is an exceptions. No explicit models treating frazil or grease ice has been found. Also, relatively little attention has been payed on snow layers that have been wetted by melt, brine expulsion or flooding.

Reference	Surface model	Volume model	Lay-ers	Polari-metric	Aniso-tropic	Dense media	Coh. layers
Fung & Eom (1982)	GOM	RT	2	Semi	No	No	No
Fung & Eom (1985)	-	DMT	2	Semi	No	Yes	No
Lee & Kong (1985)	GOM	DBA	3	Yes	Yes	No	Yes
Kim et al. (1985)	POM	RT	3	No	No	No	No
Soulis et al. (1989)	POM	RT	3	No	No	No	No
Nghiem et al. (1990, 1993)	SPM	SFT+DBA	3	Yes	Yes	Semi	Yes
Tjuatja et al. (1992)	IEM	DMRT	3	Semi	No	Yes	No
Partington & Hanna (1994)	POM	RT	3	No	No	No	No
Nghiem et al. (1995b)	GOM/SPM	SFT+DBA	3	Yes	Yes	Semi	Yes
Winebrenner et al. (1995)	SPM[†]	-	-	Yes	No	No	-
Carlström (1997)	GOM/IEM	-	-	Yes	No	No	-
Albert et al. (2012)	IEM	DMPACT	3	Semi	No	Yes	No
Komarov et al. (2014)	SPM[††]	-	N	Yes	No	No	Yes

[†] This is an extension of the original SPM with a variable permittivity profile. The notion of discrete interfaces beneath the top interface is not applicable for this model.

[††] This is an extension of the original SPM which allows for multiple interfaces.

Table 4.1: A summarising table of analytical sea ice backscatter models found in the literature.

Part II

Studies

Chapter 5

Global model sensitivity analysis of the radar backscatter from snow covered sea ice

The sensitivity of a model tells how much the output vary, when one or more input parameters are changed. It is an important feature of a model, since it indicates the causes of variation in measurements and thus what actually can be estimated from radar remote sensing data. Knowledge about what physical aspects the measurement is most sensitive to is thus imperative for parameter retrieval by means of model inversion, as well as for making appropriate design choices when developing new measurement systems (such as selecting radar frequency or polarisation mode).

In this chapter, combination of the backscatter models described in chapter 4 is considered in a variance based global sensitivity analysis. The analysis is probabilistic in the sense that the model input parameters are sampled randomly and the resulting variance in the model output is decomposed into fractions associated to the respective input parameters. These fractions are interpreted as quantities of model sensitivity.

5.1   Motivation and objectives

While backscatter models for sea ice have been developed for several decades (see section 4.3 for an overview of analytical models), there is still an active debate about what sea ice parameters are actually measurable.

A good example is the sea ice thickness, which also is one of the most important parameters for a wide range of applications (see the section 1.1 for examples). Winebrenner et al. (1995), for instance, show that there may be a sensitivity to thickness by extending the small perturbation model (SPM) to allow for a permittivity profile beneath the surface. Indeed, also the model described in section 4.2.2 by Nghiem et al. (1990) shows a sensitivity to the layer thickness (see figure 4.8). In contrary to the surface scattering model by Winebrenner et al. (1995), the one by Nghiem et al. (1990) is however a pure volume scattering model. Moreover, Wakabayashi et al. (2004) and Nakamura et al. (2005) show by measurements that there is a significant thickness dependence in radar data (at least for the marginal ice zone (MIZ) in the Sea of Okhotsk), but argue that this relates to the ice salinity, since thicker ice typically is less saline than thinner ice. The basic description of the thickness dependence in these studies is thus very different and in order to apply correct model assumptions for thickness retrieval, uncertainties like these need to be clarified.

In contrast to ice thickness, there is a clear consensus that surface roughness on the scales of the radar wavelengths is important. It is however less clear which surface is contributing the most, wether it is the air-snow, snow-ice or ice-water interface. Or, if possibly rough interfaces or volume structures within the ice or snow are dominant. General effects of surface features like skims of brine (Nghiem et al. 1995b,a) or frost flowers (Nghiem et al. 1997, Isleifson et al. 2014) are also uncertain as per today.

The main objective of this chapter is to identify what physical parameters of the sea ice are most important for the radar measurement.

5.2   Model composition

Common to most sea ice backscatter models, is the treatment of the ice as a stratified random medium. Largely depending on the radar frequency and the amount of brine present in the sea ice or snow, scattering is attributed to roughness at the interfaces between discrete layers and to inhomogeneities due to brine and air inclusions between the interfaces. A complete description of the radar backscatter would thus involve rough surface scattering from multiple interfaces, multiple volume scattering and scattering between interfaces and volume elements.

In this section, a layer-stacking approach that covers some of these aspects is examined. Each layers may have a rough top surface, described by the improved

integral equation model (IIEM) or geometric optics model (GOM) (depending on roughness scale) and a two-phase fluctuating volume described by the Nghiem's 2-layer Model (N2M). The surface and volume scattering responses are computed separately and added incoherently. For each layer, transmission effects through the above layers are accounted for. The resulting layer backscattering responses are then added incoherently.

This approach is flexible considering that it is not limited to a certain number of layers. The incoherent nature of the layer-stacking is however dismissing coherent effects between layers. Coherence within each layer is however still accounted for through the N2M, although such effects are seldom observed in measurements (Nghiem et al. 1995a). It also limits a fully polarimetric description if anisotropic layers are included.

5.2.1   Propagation through a layer

Note that the N2M assumes a vertically uniaxial anisotropic layer, thus wave propagation can be decomposed into an ordinary (o) and an extraordinary (e) direction. Recall that the model describes the layering setup as shown in figure 5.1, where the top medium is denoted by 0, the middle medium by 1 and the bottom medium by 2. Downward and upward transmission through the 0-1 interface and medium 1 can be described by the 2×2 matrices (Nghiem et al. 1995b):

$$\bar{\mathbf{D}} = \left(\bar{\mathbf{I}} - \bar{\mathbf{R}}_{10}\bar{\mathbf{R}}_{12}\right)^{-1}\bar{\mathbf{T}}_{01} \tag{5.1a}$$
$$\bar{\mathbf{U}} = \bar{\mathbf{T}}_{10} \tag{5.1b}$$

As illustrated in figure 5.1, $\bar{\mathbf{D}}$ operates on an incident field $\mathbf{E}_i$ located just above the 0-1 interface and propagates it down to just above the 1-2 interface. $\bar{\mathbf{U}}$ takes a scattered field $\mathbf{E}_s$ located just above the 1-2 interface and propagates it upwards to just above the 0-1 interface. The matrices $\bar{\mathbf{T}}_{ij}$ and $\bar{\mathbf{R}}_{ij}$ are transmission and reflection matrices containing Fresnel coefficients and propagation delays and losses. Full expressions for $\bar{\mathbf{T}}_{ij}$ and $\bar{\mathbf{R}}_{ij}$ can be found in Nghiem et al. (1990). The factor $\left(\bar{\mathbf{I}} - \bar{\mathbf{R}}_{10}\bar{\mathbf{R}}_{12}\right)^{-1}$ account for multiple reflections between the layers. For vertical uniaxial media, both $\bar{\mathbf{D}}$ and $\bar{\mathbf{U}}$ are diagonal, that is:

$$\bar{\mathbf{D}} = \begin{bmatrix} D_{oh} & D_{ov} \\ D_{eh} & D_{ev} \end{bmatrix} = \begin{bmatrix} D_o & 0 \\ 0 & D_e \end{bmatrix} \tag{5.2a}$$

$$\bar{\mathbf{U}} = \begin{bmatrix} U_{oh} & U_{ov} \\ U_{eh} & U_{ev} \end{bmatrix} = \begin{bmatrix} U_o & 0 \\ 0 & U_e \end{bmatrix} \tag{5.2b}$$

where the indices o and e indicate ordinary and extraordinary directions, respectively and the subscripts h and v are dropped on the right hand side. The trans-

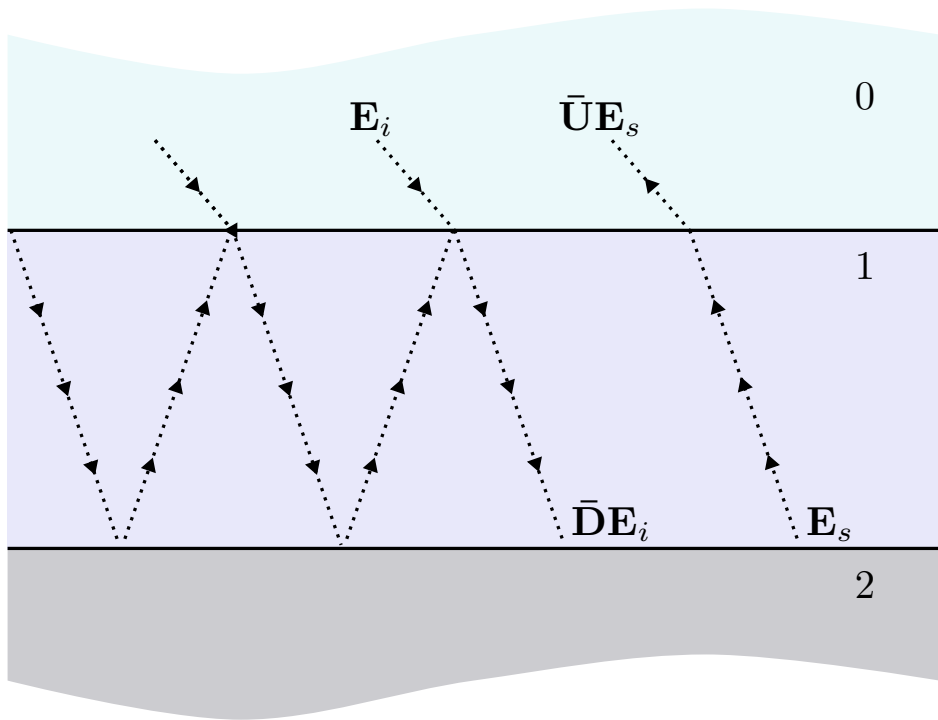Figure 5.1: Illustration of the transmission operators $\bar{\mathbf{D}}$ and $\bar{\mathbf{U}}$ in equation 5.1. $\bar{\mathbf{D}}$ operates on an incident field $\mathbf{E}_i$ located just above the 0-1 interface and propagates it down to just above the 1-2 interface. $\bar{\mathbf{U}}$ takes a scattered field $\mathbf{E}_s$ located just above the 1-2 interface and propagates it upwards to just above the 0-1 interface.

mission of the ordinary and extraordinary polarised wave that passes through a layer downwards or upwards can thus be written:

$$D_p = |D_p| \mathrm{e}^{-i\phi_p} \tag{5.3a}$$

$$U_p = |U_p| \mathrm{e}^{-i\phi_p} \tag{5.3b}$$

where the subscript p is either o or e and propagation losses and phase delays are realised through the complex phases (Nghiem et al. 1995b, equation 21):

$$\phi_o = k_\rho \rho_o + k_z^o d \tag{5.4a}$$

$$\phi_e = k_\rho \rho_e - k_z^e d \tag{5.4b}$$

where

$$
\begin{aligned}
k_\rho &= \text{Lateral wave number} \\
k_z^o &= \text{Vertical (downward) wave number for the ordinary wave} \\
k_z^e &= \text{Vertical (downward) wave number for the extraordinary wave} \\
\rho_o &= \text{Lateral distance travelled by the ordinary wave} \\
\rho_e &= \text{Lateral distance travelled by the extraordinary wave}
\end{aligned}
$$

Definitions of the wave numbers can be found in Nghiem et al. (1990) and the lateral distances are:

$$\rho_o = d\frac{\text{Re}(k_\rho)}{\text{Re}(k_z^o)} \tag{5.5a}$$

$$\rho_e = -d\frac{\text{Re}(k_\rho)}{\text{Re}(k_z^e)} \tag{5.5b}$$

Unless the layer is isotropic, the distances are different to eachother. The ordinary and extraordinary waves will thus arrive at the bottom of the layer at different incidence angles, specifically:

$$\theta_o = \arctan\left(\frac{\rho_o}{d}\right) = \arctan\left(\frac{\text{Re}(k_\rho)}{\text{Re}(k_z^o)}\right) \tag{5.6a}$$

$$\theta_e = \arctan\left(\frac{\rho_e}{d}\right) = \arctan\left(-\frac{\text{Re}(k_\rho)}{\text{Re}(k_z^e)}\right) \tag{5.6b}$$

The ordinary and extraordinary waves will also propagate through the medium according to the permittivities:

$$\varepsilon_o = \frac{k_\rho^2 + k_z^{o\,2}}{k_0^2} \tag{5.7a}$$

$$\varepsilon_e = \frac{k_\rho^2 + k_z^{e\,2}}{k_0^2} \tag{5.7b}$$

In summary, when the anisotropy is vertically uniaxial, the horizontally and vertically polarised waves will couple to the ordinary and extraordinary directions in the media, respectively. Considering the h-polarised wave as an example, it will be transmitted downwards through the layer interface according to D_o. At the bottom of the layer it will arrive at an incidence angle θ_o and at the interface it will behave as if the current layer has a permittivity ε_o.

The transmission coefficients in equation 5.3 together with the angles in equation 5.6 and permittivities in equation 5.7 will next be considered for initiating scattering model below a layer and thus enabling stacking of multiple layers.

5.2.2   Scattering from underneath a layer

Assume that the backscattering from a layer is described by a scattering matrix with elements S_{pq}. If another layer is introduced above this layer, S_{pq} can be modified to account for transmission and propagation through the above layer as:

$$S_{pq}^{(t)} = U_p D_q S_{pq} \tag{5.8}$$

where U_p and D_q are the transmission coefficients for the layer above, given in equation 5.3. The corresponding scattering covariance matrix elements are:

$$
\begin{aligned}
C_{ijkl}^{(t)} = \left\langle S_{ij}^{(t)} S_{kl}^{(t)*} \right\rangle = \left\langle U_i D_j S_{ij} \left[U_k D_l S_{kl} \right]^* \right\rangle = \\
U_i D_j \left[U_k D_l \right]^* \left\langle S_{ij} S_{kl}^* \right\rangle = U_i D_j \left[U_k D_l \right]^* C_{ijkl}
\end{aligned}
\tag{5.9}
$$

Denoting:

$$T_{ijkl} = U_i D_j \left[U_k D_l \right]^* \tag{5.10}$$

equation 5.9 reads:

$$C_{ijkl}^{(t)} = T_{ijkl} C_{ijkl} \tag{5.11}$$

which is the scattering covariance matrix elements that accounts for transmission through the layer located above.

Note that if a layer is anisotropic, the h- and v-polarised waves will decouple and propagate differently through the layer. This is illustrate in figure 5.2, where media 0 is isotropic and media 1 is anisotropic. As the waves reach the 1-2 interface, both the permittivity contrast and incidence angle at the interface will consequently be different for the h- and v-polarisations. This decoupling should in general be accounted for in the models describing the layers below the anisotropic layer. With regard to sea ice, this is however a minor issue. Anisotropy is mainly expected in the ice layers of an air-snow-ice-water configuration. For the water layer located below the ice, surface scattering is expected to dominate which mainly yield a co-polarised response anyways.
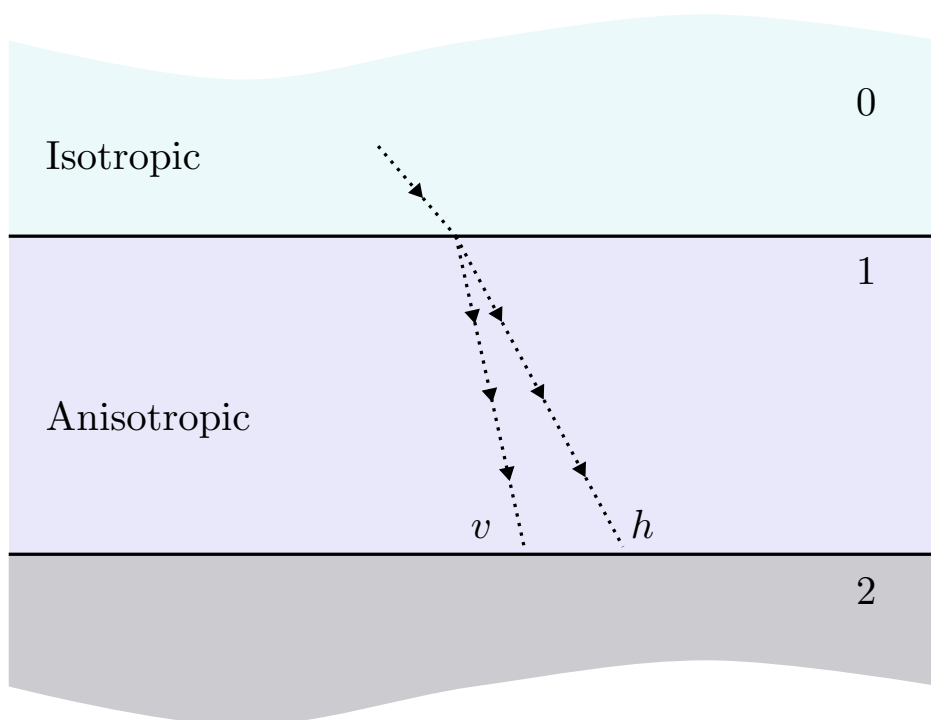
Figure 5.2: Illustration of the different propagation paths the h- and v-polarised waves take in an anisotropic layer.

5.2.3   Incoherent layer-stacking

Considering a stack of layers, it follows from equation 5.11 that the backscattering response from layer n is:

$$C_{ijkl}^{(t),n} = T_{ijkl}^0 T_{ijkl}^1 ... T_{ijkl}^{n-1} C_{ijkl}^n = \prod_{m=1}^{n} T_{ijkl}^{m-1} C_{ijkl}^n \qquad (5.12)$$

where C_{ijkl}^n is the covariance matrix element in absence of the layers above. The total backscattering response is formed as the sum over all layer responses:

$$C_{ijkl}^{tot} = \sum_{n=1}^{N} C_{ijkl}^{(t),n} = \sum_{n=1}^{N} \prod_{m=1}^{n} T_{ijkl}^{m-1} C_{ijkl}^n \qquad (5.13)$$

where T_{ijkl}^{m-1} is given in equation 5.10.

The incoherent layer-stacking approach in equation 5.13 will be used for calculating the backscatter from multi-layer sea ice configurations. Volume and surface scattering will be assumed uncorrelated such that:

$$C_{ijkl}^n = C_{ijkl}^{n(srf)} + C_{ijkl}^{n(vol)} \qquad (5.14)$$

In the following, volume scattering will be computed with the N2M (described in section 4.2.2) and the IIEM and GOM will be used for surface scattering (described in sections 4.1.3 and 4.1.4, respectively).

5.3   Layer parametrisation

In this section, the parametrisation of the layers describing sea ice, dry snow, brine-wetted snow and sea water is stated. All layers except sea water are assumed heterogeneous such that the N2M applies. The bulk of these layers are thus described by the basic strong fluctuation theory (SFT) parameters:

$$
\begin{aligned}
\varepsilon_b &= \text{Background permittivity} \\
\varepsilon_i &= \text{Inclusion permittivity} \\
l_\rho &= \text{Minor correlation length} \\
l_z &= \text{Major correlation length} \\
\psi &= \text{Inclusion tilt angle} \\
V_i &= \text{Inclusion volume fraction}
\end{aligned}
$$

Moreover, the top surfaces of the layers are assumed rough and described by the generalised power law (GPL) correlation function. Each layer surface is thus defined by:

$$\sigma_z = \text{RMS-height}$$
$$\sigma_s = \text{RMS-slope}$$
$$p = \text{GPL p-value}$$

Here, the σ_s is chosen as the independent parameter instead of the correlation length in order to make sampling easier (the validity domain of the input parameters will be a square region instead of a triangle). The correlation length is related to the RMS-slope through equation 4.7.

In the following subsections, the layer specific parameterisations of these basic model input parameters are stated.

5.3.1 Dry snow

Dry snow is modelled as an air background with isotropic inclusions of pure ice. Specifically, the permittivity of air is assumed to be the same as vacuum and the empirical relation stated in equation 3.2 is used for the permittivity of pure ice. The volume fraction if pure ice is assumed ρ_{ds}/ρ_{pi} with ρ_{ds} being the density of the dry snow and ρ_{pi} the density of pure ice as is given by equation 3.1. In summary:

$$\varepsilon_b = \text{Air background permittivity equal to 1}$$
$$\varepsilon_i = \text{Pure ice inclusion permittivity from equation 3.2}$$
$$V_i = \text{Pure ice volume fraction from } \rho_{ds}/\rho_{pi}$$

Using this parametrisation, ε_b, ε_i and V_i are determined by the temperature T and density ρ_{ds}. As for sea ice, the temperature is derived from the neighbouring layers assuming that the thermal conductivity is given by (Fukusako 1990, see table I, line number 11):

$$\kappa_{ds} = 10^{-1.25+2.12\times10^{-3}\rho_{ds}} \tag{5.15}$$

The effective permittivity is calculated using SFT. An example is shown in figure 5.3 where the SFT results are compared to the empirical relations by Hallikainen et al. (1986) and Tiuri et al. (1984) which read:

$$\varepsilon'_{ds} = \begin{cases} 1 + 1.9 \times 10^{-3}\rho_{ds} & \text{if } \rho_{ds} \leq 500\text{kg/m}^3 \\ 0.51 + 2.88 \times 10^{-3}\rho_{ds} & \text{if } \rho_{ds} > 500\text{kg/m}^3 \end{cases} \tag{5.16a}$$

$$\varepsilon''_{ds} = 1.59 \times \left(0.52 \times 10^3 \rho_{ds} + 0.62\rho_{ds}^2\right) \times \left(f^{-1} + 1.23 \times 10^{-14}\sqrt{f}\right) \times e^{0.036T} \tag{5.16b}$$

where the temperature is given in degrees centigrades and the frequency f in Hz. Equation 5.16a is based on data at frequencies between 3-37 GHz and equation 5.16b based on data below 13 GHz. As seen in the figure, the SFT results fit remarkably well to the empirical relations.
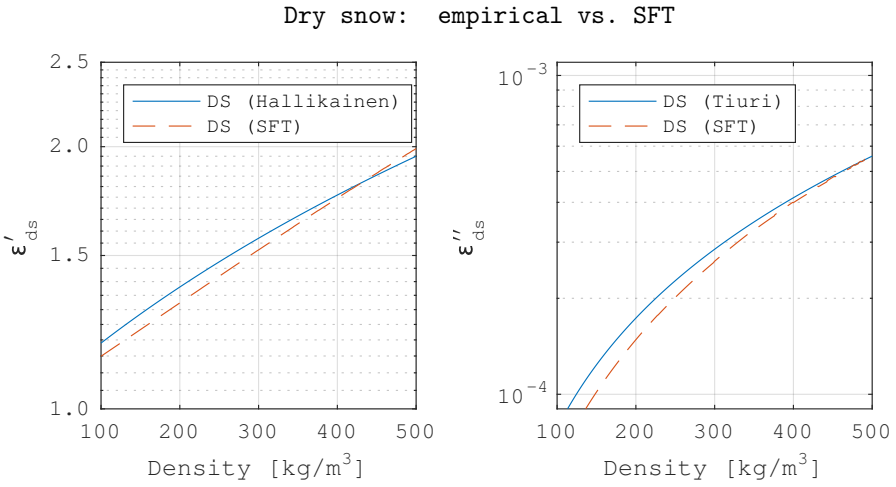
Figure 5.3: The relative permittivity of dry snow, $\varepsilon_{ds}=\varepsilon'_{ds}-i\varepsilon''_{ds}$, at 5.4GHz (C-band) is computed with the empirical relation in equation 5.16 (solid blue line) and with SFT (dashed red line). In the SFT calculation, the snow is modelled as pure ice inclusions in an air background, letting both the minor and major correlation lengths be 0.1 mm. The pure ice permittivity is given by equation 3.2 with the temperature set to -7°C.

As for sea ice, the correlation of the top surface is assumed close to exponential with a GPL p-value of 2.1. In summary, the following independent parameters are:

ρ_{ds} = Dry snow density
l_{ds} = Snow grain correlation length
$\sigma_{z,ds}$ = Surface RMS-height
$\sigma_{s,ds}$ = Surface RMS-slope
d_{ds} = Snow thickness

5.3.2 Brine-wetted snow

Brine-wetted snow is modelled as a dry snow background with inclusions of brine. Consequently, scattering from snow grains is ignored. This is a crude approximation, but is assumed to be adequate for the purpose of this thesis considering the relatively high permittivity of brine compared to air and pure ice. The permittivity of dry snow is calculated from the empirical relation in equation 5.16. equation 3.3 is used for the permittivity of brine. The volume fraction of brine is calculated as (Drinkwater & Crocker 1988, equation 4):

$$V_i = \frac{\rho_{bs} V_b}{(1 - V_b)\rho_{pi} + V_b \rho_b} \tag{5.17}$$

where ρ_{bs}, ρ_{pi}, ρ_b are the densities of the brine-wetted snow, pure ice and brine respectively. The latter two are given by equation 3.1 and equation 3.3, respectively. V_b is the volume fraction of brine relative to the pure ice volume. This is calculated assuming that the phase relation between pure ice and brine behaves as in standard sea ice and thus can be approximated by equation 3.6. Again, the temperature is derived from the above and below layers assuming the thermal conductivity being the same as for dry snow (equation 5.15).

An example of the resulting effective permittivity as a function of density and temperature according to SFT is shown in figure 5.4. The calculations are compared to the empirical equations for dry snow by Hallikainen et al. (1986) and Tiuri et al. (1984). Overall, both the real and imaginary parts are higher in the brine-wetted snow as compared to the empirical equations for dry snow. Both the real and imaginary part deviate most from the dry snow case at high temperatures, due to relatively high volume fractions of brine.

As for dry snow and sea ice, the correlation of the top surface is assumed close to exponential with a GPL p-value of 2.1. In summary, the following independent parameters are:
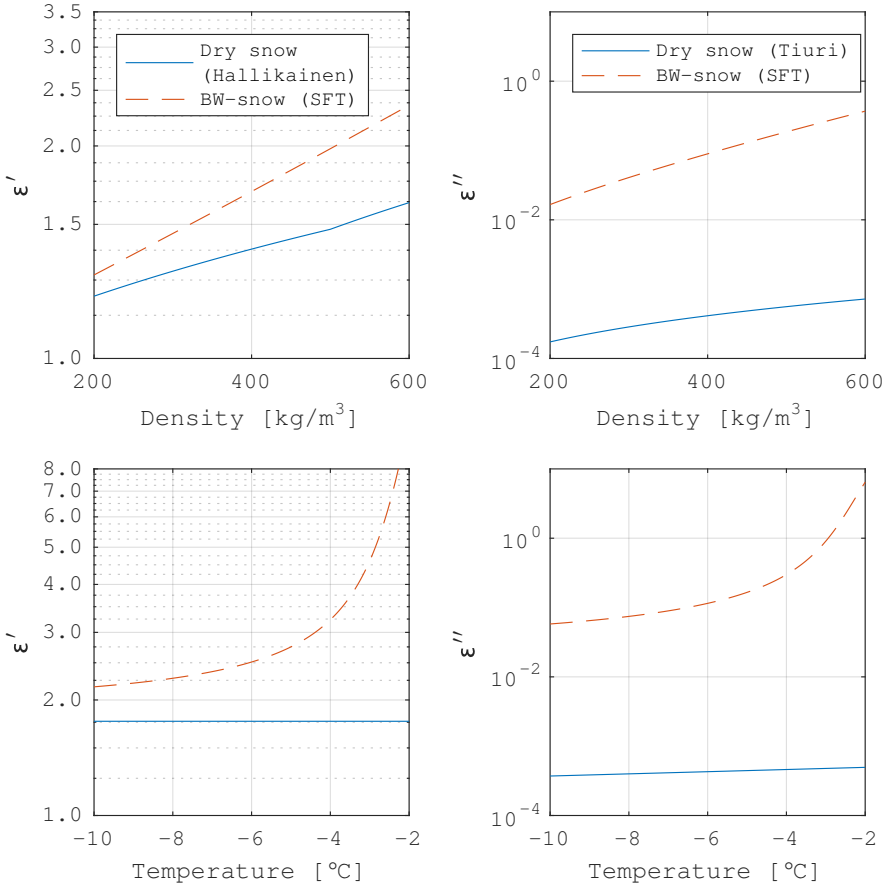
Figure 5.4: The relative permittivity of dry and brine-wetted snow ($\varepsilon = \varepsilon' - i\varepsilon''$) plotted as a function of snow density for the top two plots and snow temperature for the bottom two plots. The dry snow (solid blue line) is computed with the empirical relation in equation 5.16 and for the brine-wetted snow (dashed red line) the SFT is used with brine inclusions in a dry snow background. The frequency is 5.4 GHz (C-band), both the minor and major correlation lengths are 0.5 mm, the salinity of the brine-wetted snow is 40 ppt. For the top plots the temperature is -7°C and for the bottom ones the density is 400 kg/m^3.

ρ_{bs} = brine-wetted snow density
S_{bs} = brine-wetted snow salinity
l_{bs} = Brine droplet correlation length
$\sigma_{z,bs}$ = Surface RMS-height
$\sigma_{s,bs}$ = Surface RMS-slope
d_{bs} = Snow thickness

5.3.3 Sea ice

Sea ice is modelled as a two phase medium consisting of a pure ice background with inclusions of liquid brine. As such, scattering from air filled structures such as bubbles or empty drainage channels is ignored. This is a reasonable approximation for sea ice with a relatively high salinity, due to the considerably larger permittivity difference between brine and pure ice compared to air and pure ice (see section 3.1). For low saline ice, such as multi-year ice (MYI) or ice formed in brackish water such as the Baltic, inclusions of air are significant. In this thesis, such ice types are however not considered.

The single Debye relaxation relation stated in equation 3.3 is used for the permittivity of brine and the empirical relation stated in equation 3.2 is used for the permittivity of pure ice. The volume fraction of brine is calculated assuming standard sea ice (see section 3.2) using the relation in equation 3.6. In summary:

ε_b = Pure ice background permittivity from equation 3.2
ε_i = Brine inclusion permittivity from equation 3.3
V_i = Brine volume fraction from equation 3.6

Using this parametrisation, ε_b, ε_i and V_i are determined by the temperature T and salinity S. The temperature is calculated from the layers located above and beneath the current layer, using the thermal conductivity (Thomas & Dieckmann 2009, equation 2.14, page 48):

$$\kappa_{si} = \kappa_{pi} + 0.13\frac{S_{si}}{T^2} \tag{5.18}$$

where S_{si} is the salinity of the sea ice and T is the temperature in °C and the pure ice thermal conductivity is given by (Thomas & Dieckmann 2009, equation 2.11, page 48):

$$\kappa_{pi} = 1.16\times(1.91 - 8.66\times10^{-3}T + 2.97\times10^{-5}T^2) \tag{5.19}$$

The effective permittivity is calculated using SFT. An example is shown in figure 5.5 where the SFT results are compared to the empirical relation by Vant

et al. (1978):

$$\varepsilon'_{si} = a_0 + a_1 V_b \tag{5.20a}$$
$$\varepsilon''_{si} = b_0 + b_1 V_b \tag{5.20b}$$

where $a_{0,1}$ and $b_{0,1}$ are empirically determined coefficients (see B.4) and V_b is the volume fraction of brine. The coefficients are given for first-year ice (FYI) and MYI, separately. With equations 3.1 and 3.6 for V_b and the pure ice density ρ_{pi}, the empirical sea ice permittivity becomes a function of the sea ice salinity S_{si} and temperature T. Note that the empirical relation does not account for anisotropy in the sea ice.

Overall, the SFT results are similar to the empirical relation. The real part of the permittivity ε'_{si} is generally higher according to SFT, while the imaginary part ε''_{si} is lower. The deviation in the real part is higher at high salinities, while the imaginary part deviate more at lower salinities. This may be a result of neglecting air inclusions which have a low permittivity (thus lowers the real part) but scatter (thus increases the imaginary part).

Regarding the roughness of the ice surface, systematic measurements on scales relevant for microwaves are scarce. Johansson (1988) and Drinkwater (1989) however find that the assumption of a Gaussian height distribution is accurate. Kim et al. (1985), Johansson (1988) and Dierking (1999) indicate that the exponential correlation function is realistic for undeformed sea ice. Here, the GPL correlation function is therefore used with $p = 2.1$. The surface is then close to the exponential ($p = 2$) but has a well defined RMS-slope (see section 4.1 for details).

In summary, this results in the following independent model parameters for the sea ice layer:

$$
\begin{aligned}
S_{si} \quad &= \quad \text{Bulk salinity} \\
l_{\rho,si} \quad &= \quad \text{Brine minor correlation length} \\
E_{si} \quad &= \quad \text{Brine elongation } (= l_{z,si}/l_{\rho,si}) \\
\psi_{si} \quad &= \quad \text{Brine inclusion tilt angle} \\
\sigma_{z,si} \quad &= \quad \text{Surface RMS-height} \\
\sigma_{s,si} \quad &= \quad \text{Surface RMS-slope} \\
d_{si} \quad &= \quad \text{Ice thickness}
\end{aligned}
$$

5.3.4   Sea water

Sea water is assumed homogeneous with a permittivity described by the double Debye relaxation relation in equation 3.4. In contrast to the snow and sea ice surfaces, the sea water top surface is assumed correlated according to the gaussian correlation function. This makes the sea water medium parameterised by:
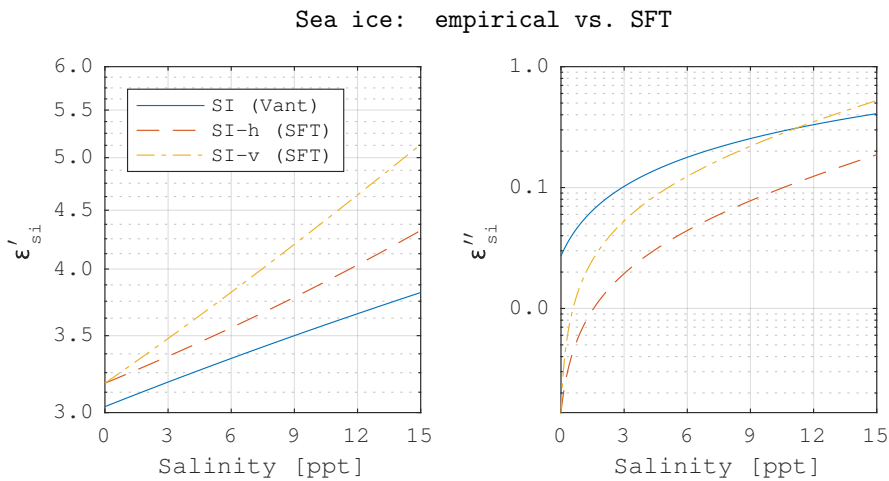
Figure 5.5: The relative permittivity of sea ice, $\varepsilon_{si} = \varepsilon'_{si} - i\varepsilon''_{si}$, at 5.4GHz (C-band) is computed with the empirical relation in equation 5.20 (solid blue line) and with SFT (dashed red and yellow lines). Equation 3.6 is used to relate the sea ice salinity to volume fraction of brine, where the sea ice temperature is set to -7°C. For the SFT calculations, the inclusions are non-tilted with horizontal and vertical correlation lengths of $l_\rho = 0.5$ mm and $l_z = 0.8$mm, respectively.

$$
\begin{aligned}
T_{sw} &= \text{Sea water temperature} \\
S_{sw} &= \text{Sea water salinity} \\
\sigma_{z,sw} &= \text{Surface RMS-height} \\
\sigma_{s,sw} &= \text{Surface RMS-slope}
\end{aligned}
$$

In the subsequent layer configurations the bottom layer will always be sea water. Consequently, the termperatures are not derived from other layers, but are treated as an independent model variable and will together with the air temperature determine the temperatures of the other layers.

5.4   Sobol indices

For different model configurations, a variance based global sensitivity analysis which gives an overview of the most influential model input parameters is conducted. Specifically, the first order and total effect Sobol indices are considered (Sobol 1993). These assume that the input variables, denoted X_i, are uniformly distributed in a cube in the input space. The distribution of a corresponding output variable, call it Y, will have a variance denoted $V(Y)$, that is a measure of the sensitivity of the model to all the input variables. Now, if one input variable X_i is fixed at some value, the expectation of the output variable is denoted $E(Y|X_i)$. If the fixed input variable is randomly varied, this expectation will have a variance denoted $V\left[E(Y|X_i)\right]$. This is a measure of how much the model is sensitive to the input parameter X_i alone. By normalising this variance with $V(Y)$, the so called first order Sobol index is defined:

$$
S_i^{(1)} = \frac{V\left[E(Y|X_i)\right]}{V(Y)} \tag{5.21}
$$

which will take a value between 0 and 1. This is a measure of the sensitivity of the output variable Y, due to variations in the input variable X_i.

Since the first order Sobol index only contains the expectation conditioned on X_i, it does not contain information about coupling between input variables. Since the backscatter models considered in this chapter are layered and non-linear, such couplings are likely. For instance, the sensitivity to surface roughness at an ice-snow interface will be strongly coupled to how much the snow layer on top attenuates the electromagnetic (EM) waves. An index that contains all conditional expectations, thus incorporates coupling between all input variables is the total effect Sobol index, defined as:

$$
S_i^{(tot)} = 1 - \frac{V\left[E(Y|X_{\sim i})\right]}{V(Y)} \tag{5.22}
$$

where $E(Y|X_{\sim i})$ denotes the expectation of the output variable Y, when all input variables except X_i are held fixed at some value. For instance, if the considered
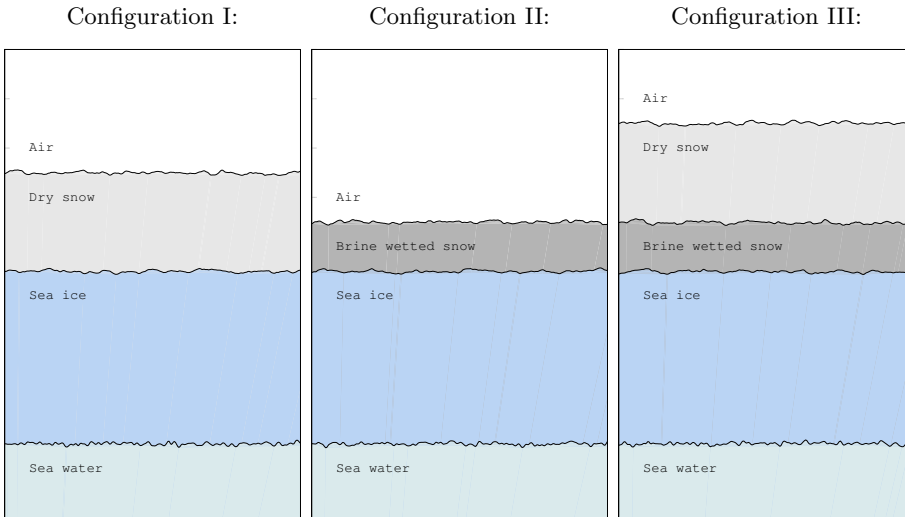
Figure 5.6: Illustrations of the model configurations considered in this chapter (see table 5.1 for details). The layer thicknesses and roughness parameters are set to the default values as listed in table 5.2.

model has the four input variables X_1, X_2, X_3, X_4, the total effect Sobol index for the second input variable is:

$$S_2^{(tot)} = 1 - \frac{V\left[E(Y|X_1, X_3, X_4)\right]}{V(Y)} \tag{5.23}$$

It should be noted that these indices are most appropriate if the distribution of Y is not highly skewed or contains multiple pronounced modes (Pianosi & Wagener 2015).

5.5   Results

The first order and total effect Sobol indices ($S^{(1)}$ and $S^{(tot)}$, resectively) are calculated using Monte Carlo sampling according to the method described in Saltelli et al. (2008). This method involves $N \times (2 + k)$ samples, where k is the number of input variables and N is a large enough number for the Monte Carlo approach to give good estimates of the distribution of Y. In the following, $N = 5 \times 10^4$ is assumed sufficient. After Monte Carlo sampling, the index calculations

Configuration I:
Dry snow cover

Layer	Effective medium	Top surface correlation	Background medium	Inclusion medium	Inclusion shape
0	Air	-	Air	-	-
1	Dry snow	GPL	Air	Pure ice	Spherical
2	Sea ice	GPL	Pure ice	Brine	Ellipsoidal
3	Sea water	Gaussian	Sea water	-	-

Configuration II:
brine-wetted snow cover

Layer	Effective medium	Top surface correlation	Background medium	Inclusion medium	Inclusion shape
0	Air	-	Air	-	-
1	brine-wetted snow	GPL	Dry snow	Brine	Spherical
2	Sea ice	GPL	Pure ice	Brine	Ellipsoidal
3	Sea water	Gaussian	Sea water	-	-

Configuration III:
Dry and brine-wetted snow cover

Layer	Effective medium	Top surface correlation	Background medium	Inclusion medium	Inclusion shape
0	Air	-	Air	-	-
1	Dry snow	GPL	Air	Pure ice	Spherical
2	Sea ice (granular)	GPL	Pure ice	Brine	Spherical
3	Sea ice (columnar)	GPL	Pure ice	Brine	Ellipsoidal
4	Sea water	Gaussian	Sea water	-	-

Table 5.1: Above are the three considered layer configurations for this chapter. The tables indicate which correlation function is used for characterising the top interface of each layer and which background and inclusion materials are considered (see sections 5.3.1 to 5.3.4 for details about these). See figure 5.6 for graphical illustrations.

are done using the SAFE toolbox (Pianosi et al. 2015) where confidence intervals are estimated with the bootstrapping method.

The Sobol indices are calculated for the three model configurations:

Configuration I: Sea ice covered by dry snow.

Configuration II: Sea ice covered by brine-wetted snow.

Configuration III: Sea ice covered by dry and brine-wetted snow.

The respective configuration is summarised in table 5.1 and illustrated in figure 5.6. The sampling limits of the input parameters for the corresponding snow, ice and water layers are listed in table 5.2. These limits are somewhat arbitrary, but correspond to what typically is observed in Arctic sea ice (for a more detailed discussion about typical limits for sea ice in the Fram Strait, see section 6.4). The indices are calculated for X-, C- and L-band radar frequencies separately.

It should be pointed out that the method for computing the Sobol indices used here (Saltelli et al. 2008) requires that the input parameters are independent. This may in extreme cases lead to somewhat unphysical parameter settings. For example, some samples may represent thin ice covered by very thick and dense snow, which most likely would cause flooding of the ice in practice. This is however not an effect that is incorporated in the considered backscatter model.

Since the Sobol indices assume output distributions that are not highly skewed, some polarimetric output parameters may not be suitable. For the considered model configurations, it is found that the co-polarised correlation coefficient ρ_{hhvv} is such a parameter, which typically has a very pronounced and left-skewed peak close to 1. Here, it is therefore proposed to use the "un-correlation" expressed in decibels, that is $10 \log_{10}(1 - \rho_{hhvv})$. Variations in ρ_{hhvv} close to 1 will then be emphasised and it is found that the corresponding distribution is considerably less skewed. It is moreover also found that the Sobol indices are generally very similar for both the co-polarised channels. The vv-channel will therefore be disregarded in the following analysis and differences between the two co-polarised channels will be discussed in terms of the co-polarised ratio. In total, the following output parameters will be considered for X-, C- and L-band separately:

$$Y = \begin{cases} 10 \log_{10}(\sigma_{hh}) \\ 10 \log_{10}(\sigma_{vv}/\sigma_{hh}) \\ 10 \log_{10}(\sigma_{hv}) \\ 10 \log_{10}(1 - \rho_{hhvv}) \\ \phi_{hhvv} \end{cases} \quad (5.24)$$

This set of parameters describes the full scattering covariance matrix (assuming reflection symmetry and reciprocity of the target, see for example Lee & Pottier

2009, for details) and thus represents a fully polarimetric single frequency radar measurement. The resulting Sobol indices are analysed in terms of box plots in figures 5.11 to 5.25. The median values (of the Sobol index samples obtained by bootstrapping) are indicated as red horizontal lines. The boxes indicate the intervals between the 25th and 75th percentiles, for the first order index $S_i^{(1)}$ in blue and the total effect index $S_i^{(tot)}$ in yellow. The whiskers (thin lines) extend to the extreme points in the respective bootstrapping distributions. In the following sections, these plots are discussed in more detail.

5.5.1   Configuration I: Dry snow cover

This is a 3-layer configuration representing an anisotropic sea ice layer covered by an isotropic dry snow layer (see table 5.1 and figure 5.6 for details and table 5.2 for corresponding input sampling limits). The resulting Sobol indices are shown in figures 5.11 to 5.15 and in the following paragraphs, the polarimetric output parameters in equation 5.24 are discussed one by one.

Co-polarised channels

Considering the hh-channel in figure 5.11, all frequency bands indicate sensitivity in terms of the first order index for the RMS slope at the snow-ice interface. This parameter is most dominant at C-band, indicating penetration through the dry snow without significant attenuation. This is consequently also the case for the longer waves at L-band, where indeed the first order index for the ice surface RMS slope is relatively high. However, the index for the RMS height at the ice-water interface is of similar magnitude.

At L-band, also the sea ice salinity indicates sensitivity since it controls the amount of brine in the ice and thus the penetration to the ice-water interface. The situation is illustrated in more detail in figure 5.7, where the hh-channel is plotted as a function of sea ice salinity and frequency (keeping the other input parameters set to the default values listed in table 5.2). The figure indicates that for low frequencies such as at L-band, the ice-water interface becomes dominant if the sea ice salinity is low enough, given that the ice-water interface is rough. In the shown scenario, this is the case below a salinity of 7 ppt.

For the hh-channel at X-band in figure 5.11, the first order index is high for both the ice surface RMS slope as well as the snow grain correlation length. The latter indicates significant volume scattering from the snow at X-band, which is not the case for C- or L-band. This can also be seen for the special case shown in figure 5.7(b), where the radar cross section for the snow layer dominates above roughly 7 GHz.

Model input parameter	Symbol	Default	Min.	Max.	Unit
Air:					
Temperature	T_{air}	-10	-20	-5	$^\circ$C
Dry snow:					
Thickness	d_{ds}	40	10	80	cm
Density	ρ_{ds}	300	200	400	kg/m^3
Snow grain cor. length	l_{ds}	0.5	0.1	1	mm
RMS height	$\sigma_{z,ds}$	5	0.1	10	mm
RMS slope	$\sigma_{s,ds}$	0.15	0	0.3	-
GPL p-value	p_{ds}	2.1	fixed		-
brine-wetted snow:					
Thickness	d_{bs}	20	1	30	cm
Density	ρ_{bs}	400	300	500	kg/m^3
Salinity	S_{bs}	40	20	60	ppt
Brine droplet cor. length	l_{bs}	0.5	0.01	1	mm
RMS height	$\sigma_{z,bs}$	5	0.1	10	mm
RMS slope	$\sigma_{s,bs}$	0.15	0	0.3	-
GPL p-value	p_{bs}	2.1	fixed		-
Sea ice:					
Thickness	d_{si}	70	20	200	cm
Salinity	S_{si}	7	1	15	ppt
Brine pocket cor. length	l_{si}	0.5	0.1	1	mm
Brine pocket elongation	E_{si}	2	1.5	4	-
Brine pocket tilt	ψ_{si}	10	0	90	$^\circ$
RMS height	$\sigma_{z,si}$	5	0.1	100	mm
Surface slope	$\sigma_{s,si}$	0.15	0	0.3	
GPL p-value	p_{si}	2.1	fixed		-
Sea water:					
Temperature	T_{sw}	-2	fixed		$^\circ$C
Salinity	S_{sw}	32	fixed		ppt
RMS height	$\sigma_{z,sw}$	5	0.1	100	mm
Surface slope	$\sigma_{s,sw}$	0.1	0	0.3	
GPL p-value	p_{sw}	∞	fixed		-
Radar:					
Incidence angle	θ	30	fixed		$^\circ$

Table 5.2: The model parameter sampling limits used for the configurations listed in table 5.1 to produce the Sobol sensitivity indices.

Configuration I: **Dry snow cover**

(a)   (b)
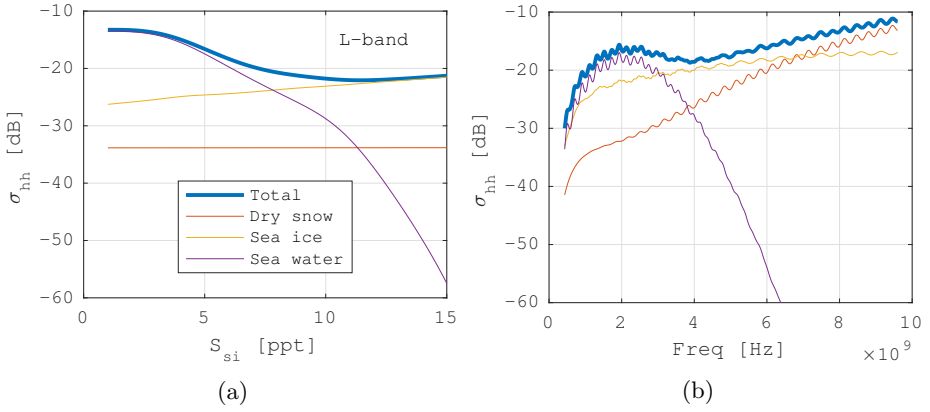
Figure 5.7: Plots showing sensitivity of the hh-channel to sea ice salinity at L-band in (a) and frequency in (b). The non-variable input parameters are fixed to the default values in table 5.2.
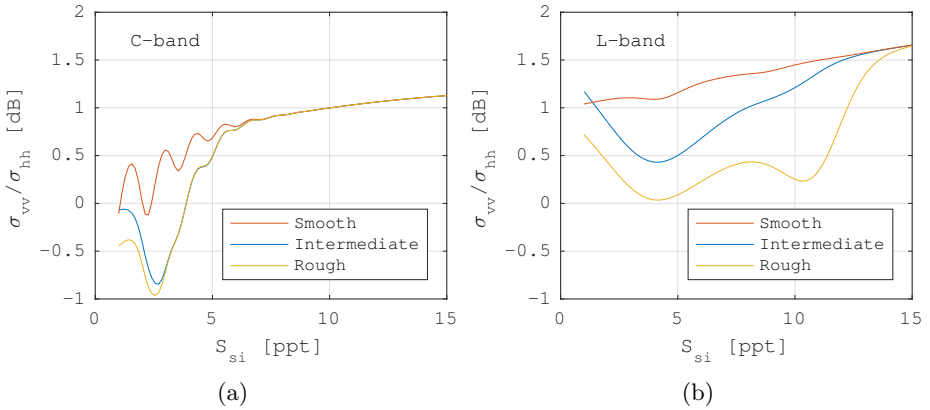
Configuration I: **Dry snow cover**

(a)   (b)

Figure 5.8: Plots showing sensitivity of the co-polarised ratio to sea ice salinity at C-band in (a) and L-band in (b) for varying roughness of the ice-water interface. The non-variable input parameters are fixed to the default values in table 5.2.

Configuration I: **Dry snow cover**
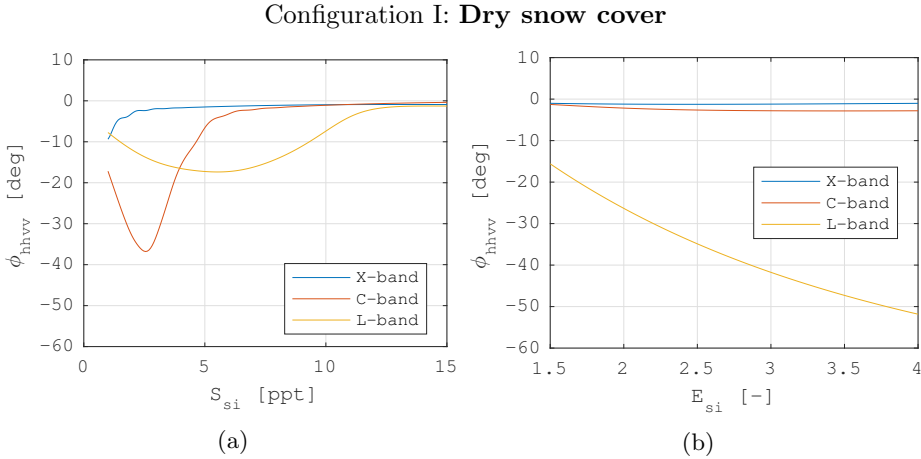
Figure 5.9: Plots showing sensitivity of the co-polarised phase difference to sea ice salinity in (a) and brine pocket elongation in (b). The non-variable input parameters are fixed to the default values in table 5.2.

Co-polarised ratio

Regarding figure 5.12, both C- and L-band indicate a sensitivity to the salinity, in particular for the total effect index $S^{(tot)}$. In both bands, this sensitivity is partly related to the ice-water interface as illustrated in figure 5.8. The figure shows the sensitivity to sea ice salinity for different roughness conditions of the ice-water interface, for C-band in figure 5.8(a) and for L-band in figure 5.8(b). Specifically, the figures indicate that the salinity modulates the impact of the ice-water interface and that the sensitivity to salinity cannot in general be attributed to the snow-ice interface only. Considering figure 5.12 again, the snow grain correlation length is most important at X-band. However, the total variance in the co-polarised ratio is relatively low here.

Cross-polarised channel

For the considered configuration the hv-channel is much lower than the co-polarised channels, typically below -30dB with relatively little variance in total. Note that neither the IIEM nor the GOM predicts a cross-polarised channel. In addition, the N2M only has a non-zero hv-signal for anisotropic layers with non-vertical tilt of the inclusions (see for example figure 4.7(b)). In this configuration, the snow is isotropic and consequently it may not come as a surprise that the brine correlation length and tilt are the most important parameters in all bands,

as can be seen in figure 5.13.

Co-polarised (un)correlation

The sensitivity to the co-polarised correlation expressed as the un-correlation parameter $10 \log_{10}(1 - \rho_{hhvv})$ is shown in figure 5.14. As for the cross-polarised response, this parameter is mainly affected by tilted brine inclusions in the anisotropic sea ice layer. It is thus balanced by surface scattering and isotropic volume scattering from the snow that on the one hand increases the co-polarised correlation, and volume scattering from the ice on the other hand that lowers it. The sensitivity plots are however more complex than for the cross-polarised channel.

The brine pocket correlation length is significant at all bands, while the brine pocket tilt is significant at X- and C-band but not so much at L-band. At X-band, the dry snow correlation length is important as well. At L-band, the sea ice salinity has a relatively high total effect index yet low first order index, likely due to strong coupling to the surface scattering response at the ice-water interface.

Co-polarised phase difference

Regarding the co-polarised phase difference ϕ_{hhvv}, the situation is similar to the results for the hv-channel. The surface scattering models predict very small phase shifts, which is also the case for isotropic layers in the N2M (that is the snow layers). Phase shifts thus mainly result from propagation through the anisotropic ice layer. Strong isotropic volume scattering from the snow or dominant surface scattering may thus mask phase shifts resulting from the ice. For this reason, X-band yields small shifts as the waves scatter in the snow and attenuates quickly in the sea ice layer. The largest phase shifts occur at C- and L-band, as illustrated in figure 5.9. In figure 5.9(a), the phase shift is plotted versus sea ice salinity for the three frequency bands. At salinities below 5 ppt, C-band yield significantly larger shifts than L-band. The attenuation is small enough for the waves to propagate through the layer and scatter back but the anisotropy of the brine inclusions is significant enough to cause phase delays between the h- and v-polarisations. As the salinity increases, the wave attenuates more rapidly resulting in smaller phase shifts. The same situation holds for L-band, although the salinities must be higher for the brine to have an effect, due to the longer wavelength in relation to the brine inclusions.

Considering the sensitivity indices for the co-polarised phase difference in figure 5.15, the above description is manifested in that all bands show a relatively high total effect index on the sea ice salinity and brine tilt. C- and X-band have some sensitivity to the sea ice roughness, which reduces the shifts. At X-band, suppression of phase shifts is however mainly attributed to the snow grain

correlation length and thus volumes scattering in the snow. At L-band, the RMS-height of the ice-water interface has a large total effect index, attributed to the propagation through the ice layer. It is however interesting to note that the sea ice thickness does not show a strong sensitivity in any band.

5.5.2 Configuration II: Brine-wetted snow cover

In section 3.3.5 it was mentioned that, even at low temperatures the snow cover on sea ice is not necessarily dry since brine may be expelled upwards from the ice. The effect of such a brine-wetted snow layer is examined in this model configuration. The configuration is identical to the one in the last section (configuration I), except that the dry snow is replaced with a thinner layer of brine-wetted snow, which enable easy comparison to the dry snow case. An illustration of the configuration can be seen in figure 5.6 and sampling limits of the involved input variables are listed in table 5.2. The resulting Sobol indices are plotted as box plots in figures 5.16 to 5.20 and discussed in detail below.

Co-polarised channels

The Sobol indices for the hh-channel are shown in figure 5.16. Considering X-band, the correlation length of the brine droplets dominates (in contrast to that of the snow grain in configuration I). The sensitivity to the sea ice RMS-slope is lower, even though the brine-wetted snow layer is on average thinner than the dry snow.

In configuration I, the sensitivity to the RMS-slope at the snow-ice interface was dominating at C-band. In this configuration, the situation is more complicated. No parameters stands out significantly in figure 5.16. The Sobol indices for the RMS-slope and the brine droplet correlation length are somewhat larger than the other input parameters, but there is a relatively large overlap in confidence intervals. At C-band, scattering from the brine-wetted snow can in other words not be neglected to the same extent as for dry snow.

The indices for L-band are generally very similar to the dry snow case in configuration I. The sea ice salinity and the sea ice RMS-height are however not as dominant. For the brine-wetted snow case, mainly the roughness at the ice-water interface dominates.

Co-polarised ratio

Considering the co-polarised ratio at X-band (figure 5.17), the main difference to configuration I is that the values for the roughness parameters for the snow-ice interface are lower while those for the air-snow interface are increased. This can be explained by: (1) the real part of the permittivity is higher for the wetted snow

(see figure 5.4) which makes the contrast stronger at the air-snow interface but weaker at the snow-ice interface and (2) the X-band waves are strongly attenuated by the liquid brine in the wetted snow.

At C-band, the roughness parameters at the air-snow interface are also slightly higher than in configuration I. The sensitivity to the sea ice salinity is slightly lower in both the first oder and total effect index, while the air temperature and snow thickness have slightly higher sensitivities. Overall, no single parameter stand out in the box plot.

The box plot for L-band is very similar to that of configuration I. The indices for the roughness parameters of the snow-ice and ice-water interfaces are generally highest. The indices for the brine pocket tilt and elongation are slightly increased as well as the roughness parameters of the brine-wetted snow.

Cross-polarised channel

As for configuration I, all cross-polarised responses originate from tilted and elongated brine inclusions in the sea ice layer. As seen in figure 5.18, the indices for the sea ice salinity and the brine pocket tilt are thus also here significant. However, for the shorter waves at X- and C-band attenuation through the brine snow is important and which suppresses the sensitivity to the ice and sea water parameters. For X-band in particular, the indices for the air temperature, snow thickness, snow density and snow salinity are relatively high, which all are associated to attenuation. The L-band plot is however very similar to the dry snow case.

Co-polarised (un)correlation

Compared to the dry snow case, the sensitivity for the co-polarised correlation (figure 5.19) is somewhat similar for C- and L-band, while at X-band the brine-wetted snow has a strong impact. The brine-wetted snow scatter and attenuates the shorter waves too strongly for the anisotropic sea ice layer to have an effect.

The C-band plot indicate a slightly increased total effect index but decreased first order index on the sea ice salinity as well as lower indices for the brine pocket correlation length and tilt as compared to the dry snow case. At L-band, the first order index for the sea ice salinity and thickness is increased.

Co-polarised phase difference

For the co-polarised phase difference plotted in figure 5.20, the situation is similar to configuration I. At X-band, the correlation length for the brine droplets in the wet snow is however slightly lower compared to the correlation length of the snow grains in the dry snow case.

At C-band, the situation is also similar to configuration I. The sensitivities to the correlation length and thickness of the brine-wetted snow are slightly lower than the corresponding parameters for the dry snow. Also the sea ice surface roughness parameters are somewhat lower, due to the reduced permittivity contrast between the ice and snow.

The situation for L-band is generally similar to the dry snow case. The largest first order indices are found for the brine pocket tilt and the RMS-height of the the ice-water interface.

5.5.3 Configuration III: Dry and brine-wetted snow cover

This configuration represents sea ice with a snow cover that is dry on the top and wetted by brine at the bottom. The layer setup is shown in table 5.1 and also illustrated in figure 5.6. The corresponding input sample limits are listed in table 5.2. The resulting Sobol indices are shown in figures 5.16 to 5.20 and will be discussed more thoroughly below.

Co-polarised channels

The results for the HH-channel can be seen in figure 5.21. At X-band, the plot is dominated by the correlation length of the dry snow grains. There is a slight sensitivity to the correlation length of the brine droplets in the wetted snow, but this is significantly lower compared to that of the dry snow. As in configuration I, there is also a slight sensitivity to the dry snow thickness. The sea ice parameters play an insignificant role indicating that the response from the ice essentially is shielded by the snow.

The situation for C-band is in this configuration similar to that of X-band. The correlation length of the dry snow has the highest sensitivity followed by the brine droplet correlation length in the wetted snow. In contrast to the previous two configurations, there is only a very low sensitivity to the sea ice in terms of the RMS slope.

For L-band, the plot is more complicated than for the previous two configurations, where very little sensitivity was attributed to the snow. As before, the first order indices are relatively high for the roughness parameters at the ice-water and snow-ice interface as well as for the sea ice salinity. However, these are not at all as dominant as in configuration I and II. Also the air temperature, brine-wetted snow salinity, density and roughness indicate some sensitivity.

Co-polarised ratio

The sensitivity for the co-polarised ratio are shown in figure 5.22. Considering X-band, the indices are considerably larger for the correlation length of the dry

snow that the other parameters. There is a small sensitivity also to the brine-wetted snow parameters. The situation is thus simpler here than for the previous configurations where in configuration I, the sea ice was not negligible and in configuration II, the brine-wetted snow dominated.

At C-band, the situation is somewhat complicated with no clear dominant parameter. The sea ice salinity has a significantly larger total effect index. For the first order indices, no parameter stands out indicating strong coupling between parameters.

The situation is on the other hand more similar to the previous configurations for L-band. The first order indices are highest for the roughness at the snow-ice and ice-water interfaces. The sea ice salinity has a relatively high total effect index.

Cross-polarised channel

The sensitivity for the cross-polarised channel is shown in figure 5.23. As for the previous configurations, this channel is in principal only affected by the anisotropic sea ice layer. The snow thus acts to reduce the cross-polarised channel and most so at higher frequencies. Indeed, X- and C-band indicate no, or very little sensitivity to the sea ice parameters. In fact, the air temperature as well as brine snow salinity and density indicate largest sensitivity. It should however be noted that the response in absolute terms at these bands are extremely low, below -30 db and would thus be close to the noise floor for conventional satellite sensors.

Co-polarised (un)correlation

For this configuration, the reduction of the co-polarised ratio due to the brine pockets in the sea ice layer is masked even mover by the snow cover than in the previous configurations. Generally, the co-polarised correlation is relatively close to 1 for most samples in all three configurations and the confidence intervals are relatively wide, especially for the total effect indices.

As expected, the masking due to snow is however strongest at X-band where both snow layers yield strong scattering and the brine-wetted snow attenuates the waves significantly before reaching brine pockets. Consequently, the snow parameters are dominant in the X-band plot.

At C-band, no single parameter stand out from the other. The brine pocket correlation length and tilt still indicate sensitivity, but the air temperature, dry snow thickness and salinity of both the sea ice and brine-wetted snow have first order indices of similar magnitude.

At L-band, the situation is somewhat similar to configuration II (brine-wetted snow cover), where the sea ice salinity and thickness yielded highest first order

indices. Here, the sea ice brine pocket elongation and correlation length are however of similar magnitude. The sea ice salinity has a again a relatively high total effect index.

Co-polarised phase difference

In figure 5.25, the Sobol indices for the co-polarised phase difference are shown. As for the cross-polarised channel, in this configuration mainly the sea ice layer contribute to phase shifts due to its anisotropy. Consequently, at X-band the total variance in phase shift is very small since the signal originating from the sea ice is very weak due to attenuation in the two snow layers. No first order indices show significant sensitivity.

At C-band, the attenuation in the snow is weaker and consequently a sensitivity is seen in the sea ice salinity as well as brine pocket tilt. The total effect index is not negligible for some of the dry snow parameters as well as the air temperature, similarly to configuration I.

Also at L-band, the situation is similar to the previous configurations. The sea ice tilt, salinity and the roughness parameters at the ice-water interface have relatively large first order indices compared to the other parameters.

5.6   Summary and discussion

The above sections present the (to my knowledge) first global sensitivity analysis of the fully polarimetric radar backscatter response from snow covered sea ice. The response is modelled by an incoherent layer-stacking approach where each layer is characterised by a rough top surface and a volume containing ellipsoidal inclusions. Scattering from the surfaces are modelled by the IIEM and GOM (depending on the roughness scale relative to the radar wavelength) while scattering from the volume is modelled by the N2M which is based on SFT.

The model is set up in terms of three different configurations, distinguished by the properties of the snow layer. Configuration I is ice with dry snow on top, configuration II ice with a wet snow cover, and in configuration III the snow cover consists of a layer of wet snow with a dry-snow layer on top of it. By comparing the results for the configurations, the impact of the snow can be determined. The analysis is performed for X-, C- and L-band radar frequencies.

A summary of the sensitivity analysis is shown in table 5.3 based on the first order Sobol indices in the box plots of figures 5.11 to 5.25. Each cell in the table specifies up to three of the model input parameters that yield the largest sensitivity index (symbols for the input parameters are listed in table 5.2). Each row corresponds to a polarimetric model output parameter and each column corresponds to one of the three model configurations, run at either X-, C- or

L-band. Cells containing input parameters that are all associated to a single layer, are highlighted by a colour. The colour corresponds to the layer as shown in the illustrations at the top of the table (dry snow = light grey, brine-wetted snow = dark grey, sea ice = blue and sea water = green). Cases where many input parameters are significant or where the confidence intervals are too large to separate them from each other, are marked with the letter M(any). If the total variance is very low (that is, no significant sensitivity could be estimated for any input parameter) the letter N(one) is used.

Comparing the configurations

A general conclusion that instantly can be made from table 5.3, is that the polarimetric backscatter response to snow covered sea ice is complex. There is no single input parameter that stands out across all configurations and frequency bands. Not even when restricted to only one frequency band, there is a single input parameter that dominates across all configurations.

Considering configuration I however, it is clear that the sea ice layer dominates at C-band (judging by the blue colour along most of the column). In particular, the hh-channel is dominantly sensitive to the surface roughness at the snow-ice interface (specifically the RMS-slope). On the contrary, at X-band the dry snow is important. Particularly the correlation length of the snow grains yields high sensitivities for both the co- and cross-polarised channels as well as the co-polarised ratio. At L-band, most output parameters are most influenced by the roughness of the ice-water interface. Thus, the bottom side of the ice cannot in general be neglected when modelling signatures at L-band.

By introducing the brine-wetted snow layer in configuration II, the situation becomes somewhat more complicated than in configuration I. At X-band, the direct influence of the snow is most substantial. At C-band, the hh-channel and co-polarised ratio are not dominated exclusively by sea ice parameters as in configuration I. Also at L-band, some sea ice parameters have a reduced influence. For the hh-channel in particular, the RMS-slope of the ice-water interface becomes more important than that of the snow-ice interface.

By considering both a dry and wet snow layer as in configuration III, the impact of the sea ice naturally becomes even weaker than in configuration I and II. Particularly the hh-channel is dominated by the dry snow correlation length at both X- and C-band. At C-band, only the co-polarised phase difference is dominated by only sea ice parameters. At L-band, all output parameters show a relatively complicated sensitivity with multiple input parameters being important.

Considering all configurations, an interesting note can moreover be made about the co-polarised phase difference ϕ_{hhvv} at L-band. Together with the RMS-slope of the ice-water interface, the sensitivity to the tilt of the brine pockets in

	Configuration I			Configuration II			Configuration III		
	X	C	L	X	C	L	X	C	L
σ_{hh} (in dB)	l_{ds} $\sigma_{s,si}$	$\sigma_{s,si}$	$\sigma_{z,sw}$ $\sigma_{s,si}$	l_{bs}	M	$\sigma_{z,sw}$ $\sigma_{s,sw}$	l_{ds}	l_{ds}	M
σ_{vv}/σ_{hh} (in dB)	l_{ds}	S_{si} $\sigma_{z,si}$ ψ_{si}	M	l_{bs} $\sigma_{z,bs}$ $\sigma_{s,bs}$	M	M	l_{ds}	M	M
σ_{hv} (in dB)	l_{si} ψ_{si}	l_{si} ψ_{si}	l_{si} ψ_{si}	T_{air} d_{bs} S_{bs}	l_{si} ψ_{si}	l_{si} ψ_{si}	T_{air} ρ_{bs} S_{bs}	T_{air} ρ_{bs} S_{bs}	M
$1-\rho_{hhvv}$ (in dB)	ψ_{si} l_{si} l_{ds}	M	M	M	l_{si} ψ_{si}	M	M	M	M
ϕ_{hhvv}	M	M	ψ_{si} $\sigma_{z,sw}$	M	M	ψ_{si} $\sigma_{z,sw}$	N	S_{si}	S_{si} ψ_{si} $\sigma_{z,sw}$

Table 5.3: Summary of the most influential model input parameters, considering the five polarimetric output parameters (rows) as well as the different model configurations and frequency bands (columns). If more than three parameters dominate or the confidence intervals overlap significantly, the letter M(any) is used. If no significant sensitivity to any input parameter were observed, the letter N(one) is used. The cases where the dominant parameter(s) are all associated to a specific layer, are indicated with a colour. The colour corresponds to the layer as shown in the illustrations at the top of the table (the ice layer is for instance blue).

the ice is significant for all three configurations. This suggests that measurements of ϕ_{hhvv} at L-band could potentially be used to infer information about the brine inclusions even when dry or brine-wetted snow is present (assuming that the snow can be treated as isotropic).

Effects of brine-wetted snow

The above analysis shows clearly that a snow layer that is fully or partially soaked by brine can have a significant impact on the polarimetric radar return at all frequency bands considered. As a final example of this effect, consider figure 5.10 where the hh-channel is plotted for the three different configurations versus the radar frequency (keeping all other input parameters at their "default" values as listed in table 5.2). The figure shows the backscatter decomposed per layer. For L-band in the dry snow case (top plot), the sea water interface and sea ice yield the highest backscatter. By replacing the dry snow with brine-wetted snow (middle plot), the total response is almost unaffected, yet the response from the sea ice is drastically reduced while the ice water interface is still of similar magnitude. If the snow cover consists of a wet and a dry layer (bottom plot) the response from the sea ice layer is further reduced and is more than 10 dB below the total response. At X- and C-band, the ice-water interface never dominates, but a similar trend in the heavily reduced influence of the sea ice layer due to the brine-wetted snow can be seen. The general effect of the brine-wetted snow layer can in summary be attributed to the following conditions:

1. The real part of the effective permittivity is closer to the one of sea ice (see figures 5.4 and 5.5) making the permittivity contrast weaker at the snow-ice interface, thus reducing the interface scattering contribution. This is particularly the case if the temperature and salinity of the snow is high.

2. The imaginary part of the effective permittivity is considerably higher than for dry snow. In particular, if the temperature and salinity is high, it becomes even higher than for sea ice. Attenuation is then significant, particularly at higher frequencies such as X- or even C-band.

Note that the strong temperature dependence of the brine-wetted snow permittivity also makes a potential dry snow cover important. In particular, if the air temperature is low, such a snow cover can significantly insulate the brine-wetted snow from the air, thus influencing its permittivity.

Comments on ice thickness

It is furthermore worth to note that none of the considered output parameters reveal a dominant sensitivity to the sea ice thickness. Although it is clearly shown

in figure 4.8 that the N2M used in the model configurations is sensitive to the layer thickness, this sensitivity is evidently weak in relation to other input parameters. Unless detailed knowledge about other more significant input parameters is at hand, thickness retrieval through model inversion appears difficult for the considered model setup.

On the other hand, Kwok et al. (1995) concludes that thin sea ice thickness in the range from 0 to 10 cm can be retrieved at C- and L-band. In their study, a fully coherent 3-layer version of the N2M (see Nghiem et al. 1995b) is used and inverted by an artificial neural network (ANN). The top layer represents a few millimetres thick and highly saline surface skim, the middle layer represents sea ice and the bottom layer is sea water. Both the brine skim and sea ice layer are modelled as a pure ice background with brine inclusions. The brine skim is isotropic and does not include volume scattering, while the sea ice is anisotropic and include volume scattering using the distorted Born approximation (DBA). The model output is moreover averaged over distribution of ice thicknesses to remove unrealistic interference patterns (as shown in figure 4.8). Surface scattering is modelled with the SPM. The model is thus different to the configurations considered here in a number of ways and it is at this stage unclear if the apparent contradiction in conclusions is due to such differences.

It is also interesting to highlight the sensitivity for the co-polarised ratio in relation to sea ice thickness. The co-polarised ratio is particularly interesting since the influence of the roughness is suppressed for slightly rough surfaces, which makes it relatively sensitive to changes in the permittivity contrast at the interface. To this end, the ratio is sometimes considered for inferring information about parameters that relate to the dielectric properties, such as the moisture of soil for example (Oh et al. 1992, Dubois et al. 1995).

For sea ice, the ratio has for similar reasons been considered for explaining thickness dependencies observed in data at L-band. Specifically, Wakabayashi et al. (2004) and Nakamura et al. (2005) use empirical equations that relate the ice permittivity to ice salinity, which is further linked to ice thickness. Assuming a single ice surface (modelled by the integral equation model (IEM)), they continue to show a clear thickness sensitivity on the co-polarised ratio. Table 5.3 however indicates that if multiple layers are included in the model, the situation becomes more complicated. The sea ice salinity is indeed significant at C-band in configuration I, but other parameters are also important. Across all configurations, the snow layers are most important at X-band. With the exception of C-band at configuration I, multiple layers and parameters are significant at both C- and L-band. While this is not strictly conflicting the results of Wakabayashi et al. (2004) and Nakamura et al. (2005), it suggests that detailed knowledge about other parameters such as inclusion correlation lengths, brine pocket tilt and elongation are potentially needed for understanding and quantifying the link

between ice thickness and co-polarised ratio.

Model limitations

In the above discussion, it is important to keep in mind the limitations of the backscatter model. The main limitations include:

1. The model is described in terms of discrete layers. This means that it disregards large scale deformation features due to ridging or rafting.

2. Coherent interactions between layers are disregarded.

3. A number of properties are assumed homogeneous across the layers. Specifically, the layer thicknesses as well as inclusion and background properties (tilt, permittivity, size and shape) are described by single values rather than distributions as would be expected in reality.

4. Only one inclusion type is considered per layer. Consequently, the model neglects backscattering from air bubbles in the sea ice and from ice crystals in the brine-wetted snow.

5. Multiple backscattering is not accounted for due to the DBA.

6. The roughness scales at the layer interfaces is constrained. In particular, multiple surface scattering is disregarded since the RMS-slope is limited to low values.

7. The roughness at the layer interfaces as well as the volume inclusions are described by means of simple correlation function (the GPL and exponential correlation function, respectively). In reality, such functions may be over-simplistic.

Models with other constraints could potentially yield different results. Direct comparison of models is however difficult, due to mathematical and/or numerical complexity but perhaps most importantly, because of differences in parametrisation. Moreover, there are many existing models in the literature but little apparent consensus about which one to pick in general. In order to assess what effect model limitations, detailed laboratory measurements are therefore needed.

5.7   Conclusions

While there are many existing studies that, in one way or the other, illustrate the sea ice backscatter sensitivity to particular parameters (Fung & Eom 1982, 1985, Kim et al. 1985, Soulis et al. 1989, Nghiem et al. 1990, 1993, 1995*b*, Tjuatja et al.
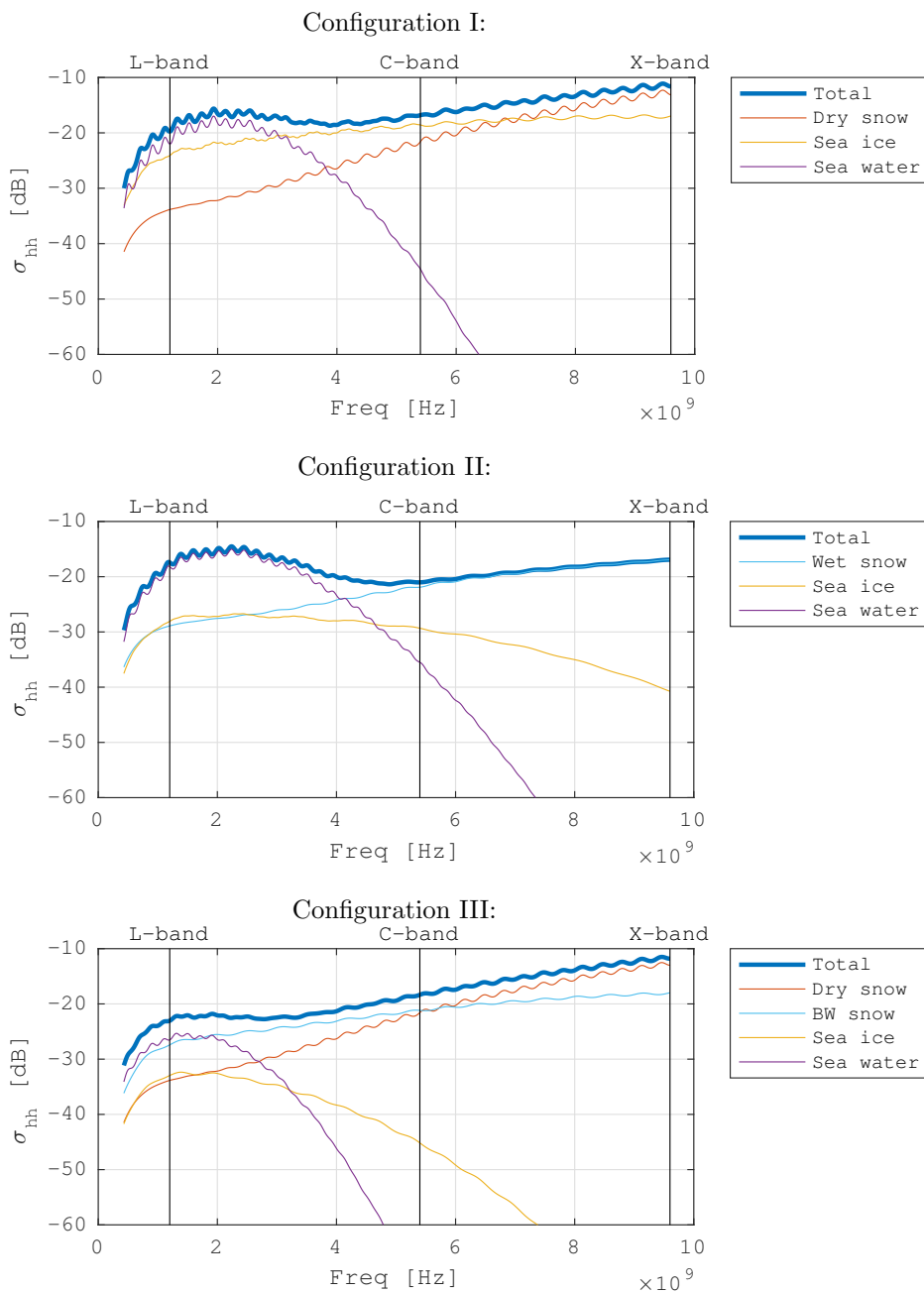
Figure 5.10: Comparison of the hh-channel as a function of radar frequency (keeping all other input parameters at their "default" value listed in table 5.2) for the three different configurations.

1992, Partington & Hanna 1994, Winebrenner et al. 1995, Kwok et al. 1995, Carlström 1997, Wakabayashi et al. 2004, Albert et al. 2012, Komarov et al. 2014, just to mention a few), this chapter presents the first (to my knowledge) global sensitivity analysis that enable a readable comparison of the sensitivity to different model input parameters. Such information is critical in order to explain variations in measured data and assess the feasibility of parameter retrieval by means of model inversion.

By analysing different snow cover, it is concluded that snow can have a significant impact on what model parameters yield highest sensitivity, even for low radar frequencies such as L-band. The results indicate a rather complex situation, where generally multiple input parameters dominate and that these may differ depending on snow cover. Overall, it is found that:

- Brine-wetted snow generally suppresses the relative impact of the snow-ice interface and the ice volume, even at L-band.

- Roughness at the ice-water interface is significant at L-band regardless of snow cover.

- The sea ice dominate the sensitivity at C-band if the snow is dry, but the situation becomes relatively complex if a brine-wetted snow layer is introduced.

- The snow is generally important at X-band, specifically the correlation lengths of grains and brine droplets in snow is significant.

While these general conclusions are relatively well known, the presented analysis is unique in that it provides detailed and quantitative information about the relative importance of different sea ice parameters.

Finally, it should be emphasised that the results may depend on the particular limitations of the considered model. Other models, distinguished by other limitations, could potentially yield different results. The number of existing models is however quite large and there is no apparent consensus about which one to pick in general. In order to assess the effect of model limitations, detailed laboratory measurements that can provide validation data at variable sea ice conditions are therefore greatly desired. Although such measurements are difficult and expensive to perform, their importance still needs to be emphasised.

Configuration I: **Dry snow cover**
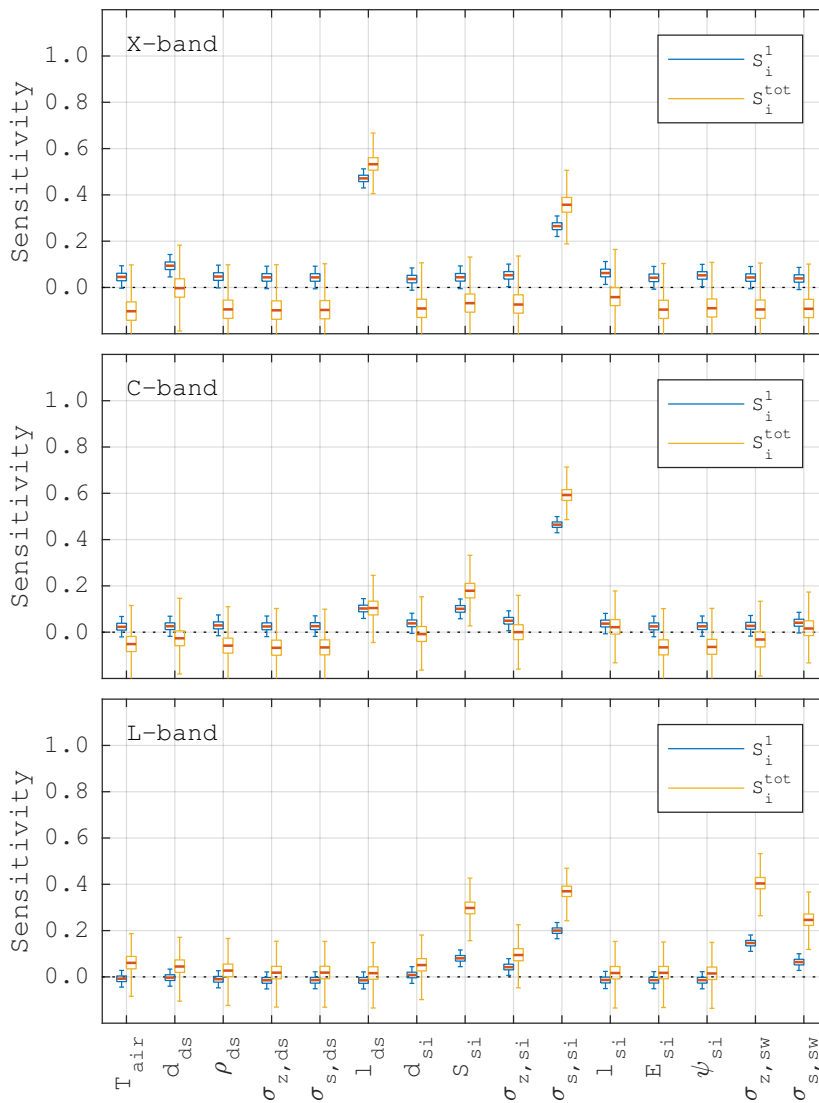
$$Y = 10\log_{10}(\sigma_{hh})$$

Figure 5.11: A box plot for Sobol indices $S^{(1)}$ and $S^{(tot)}$ for the output variable $Y = 10\log_{10}(\sigma_{hh})$ for "sea ice covered by dry snow" (see table 5.1). The indices are shown for X-, C- and L-band, respectively, for an incidence angle of $30°$. Input sampling limits are listed in table 5.2.
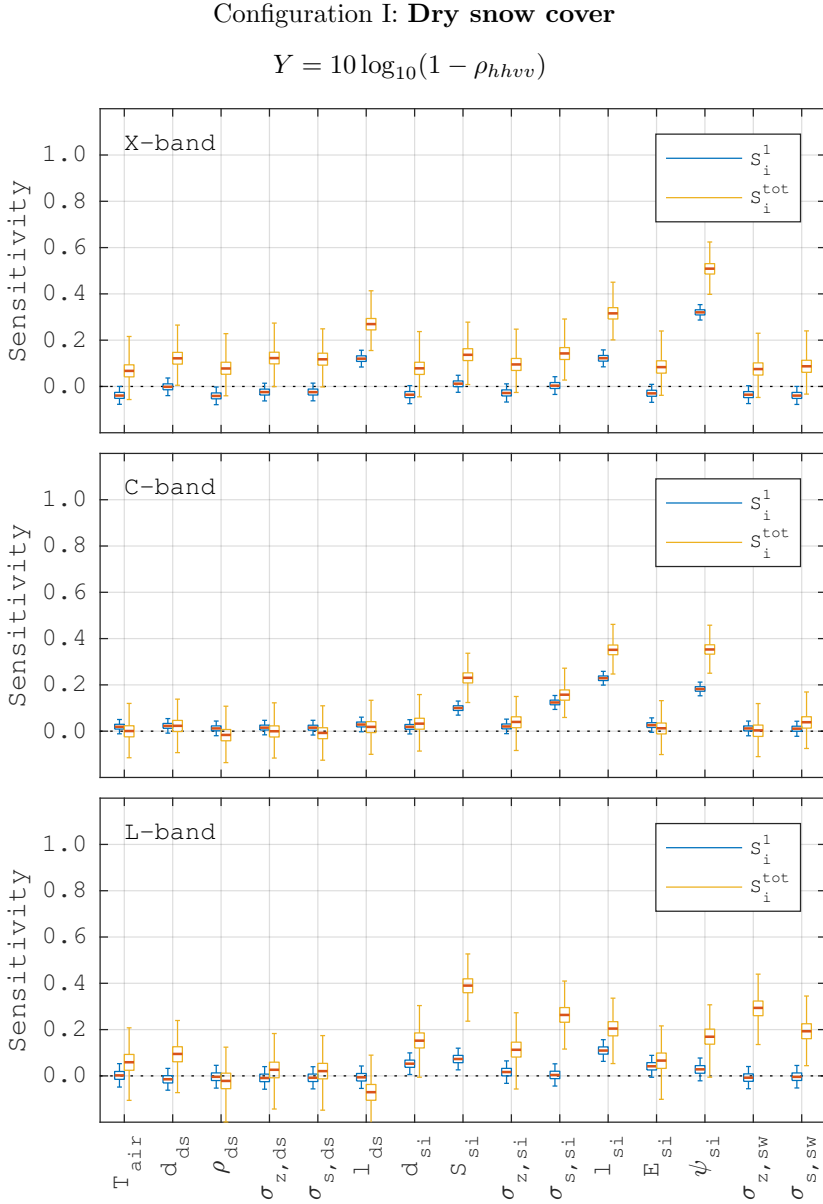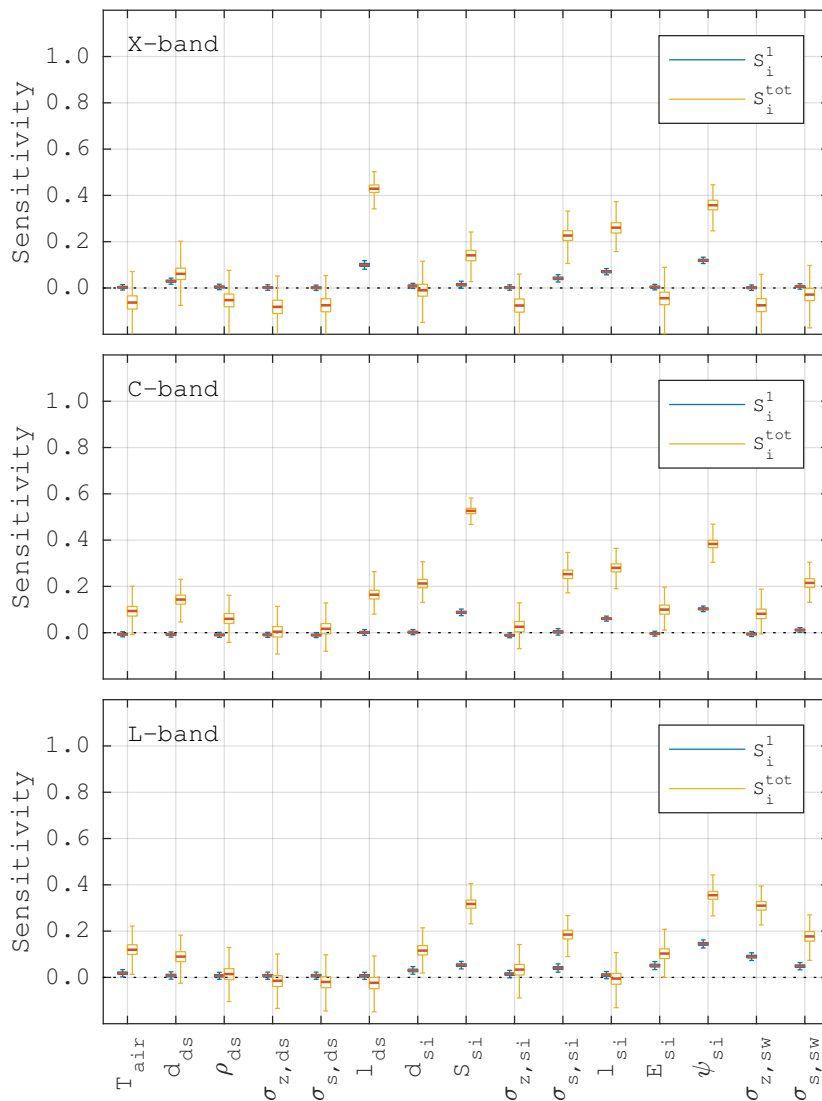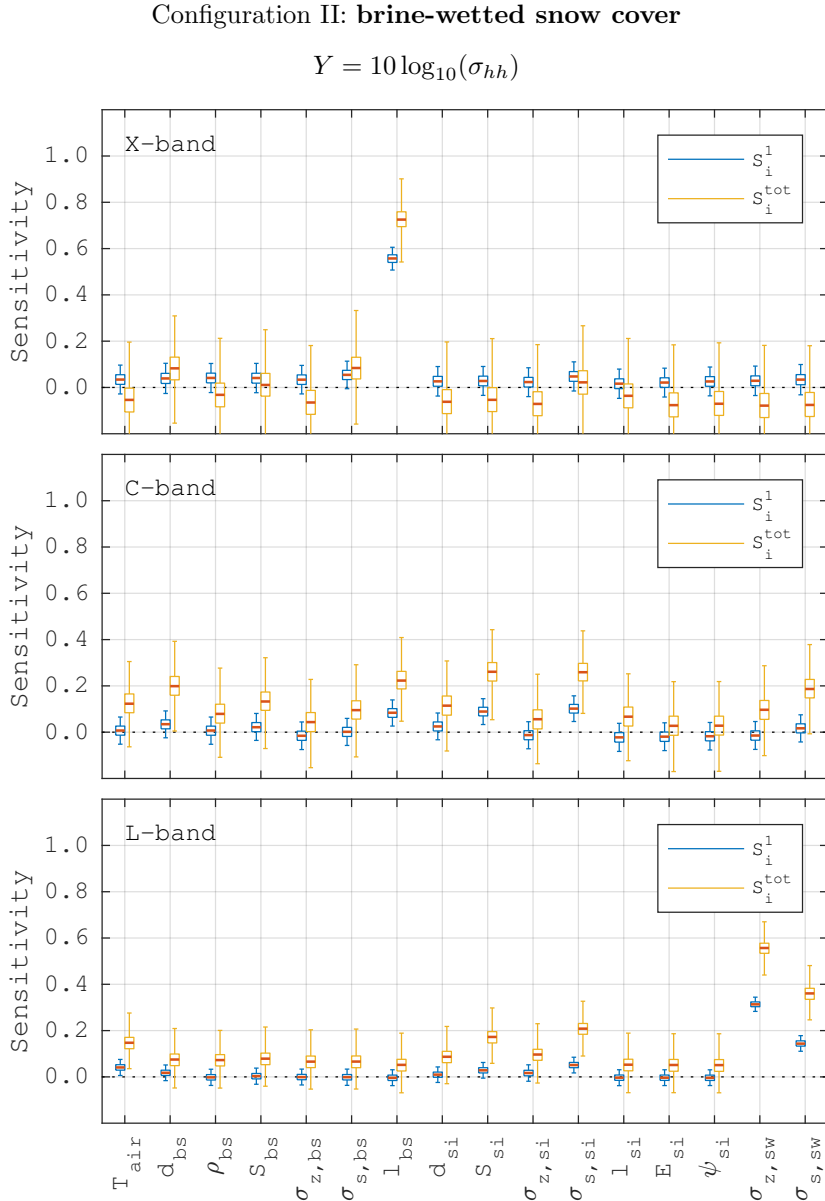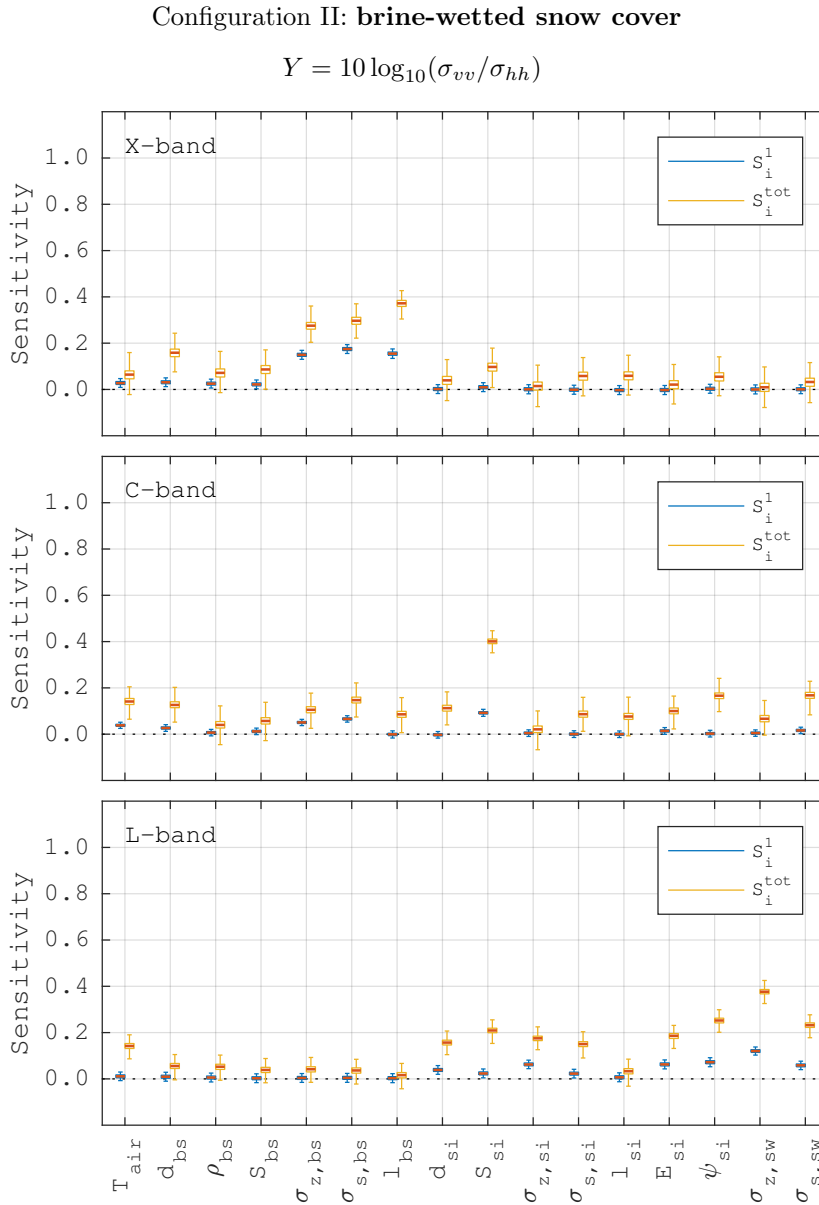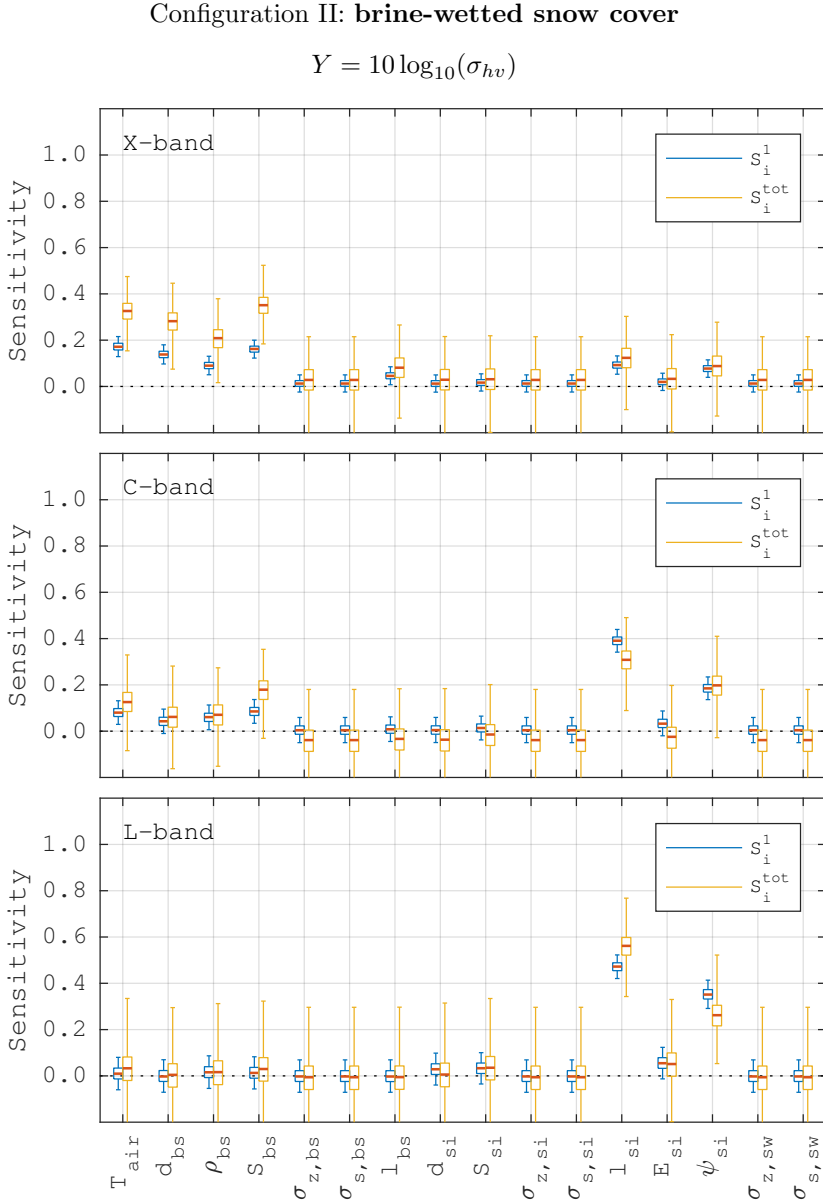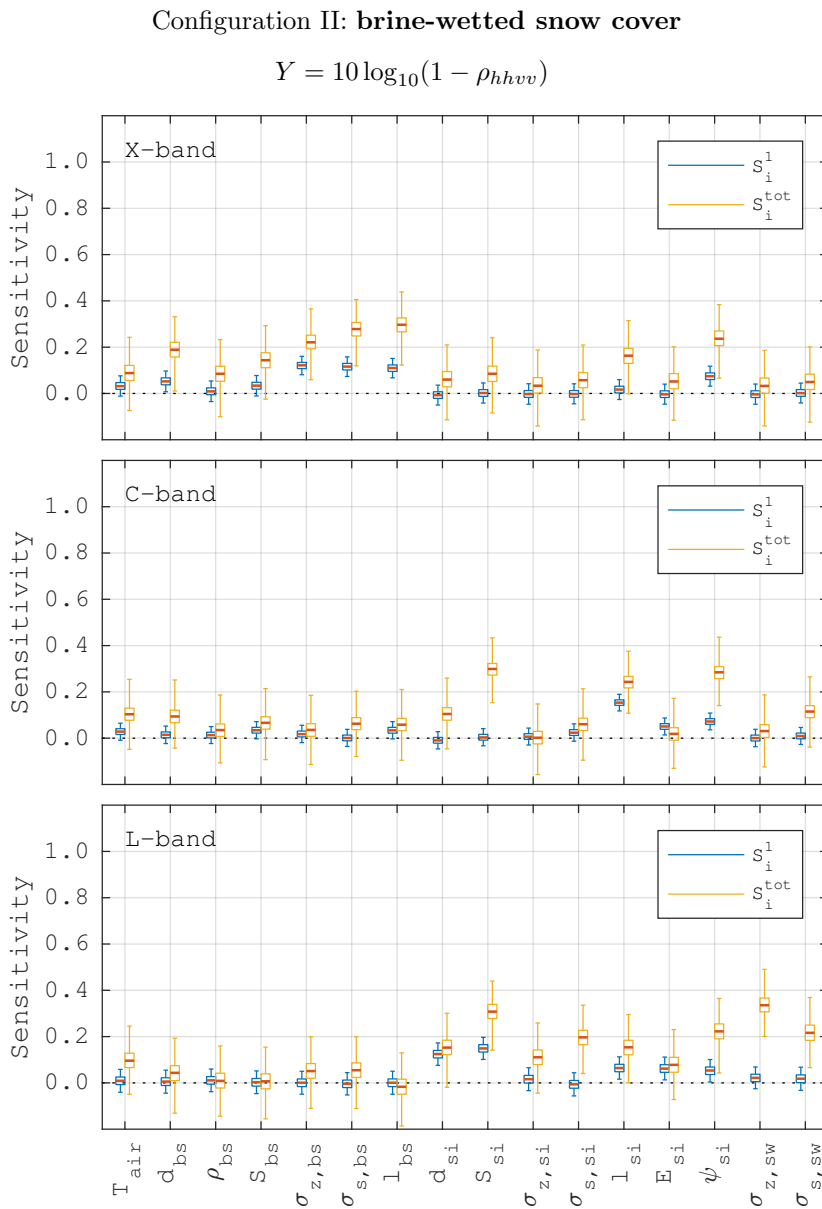
Configuration I: **Dry snow cover**
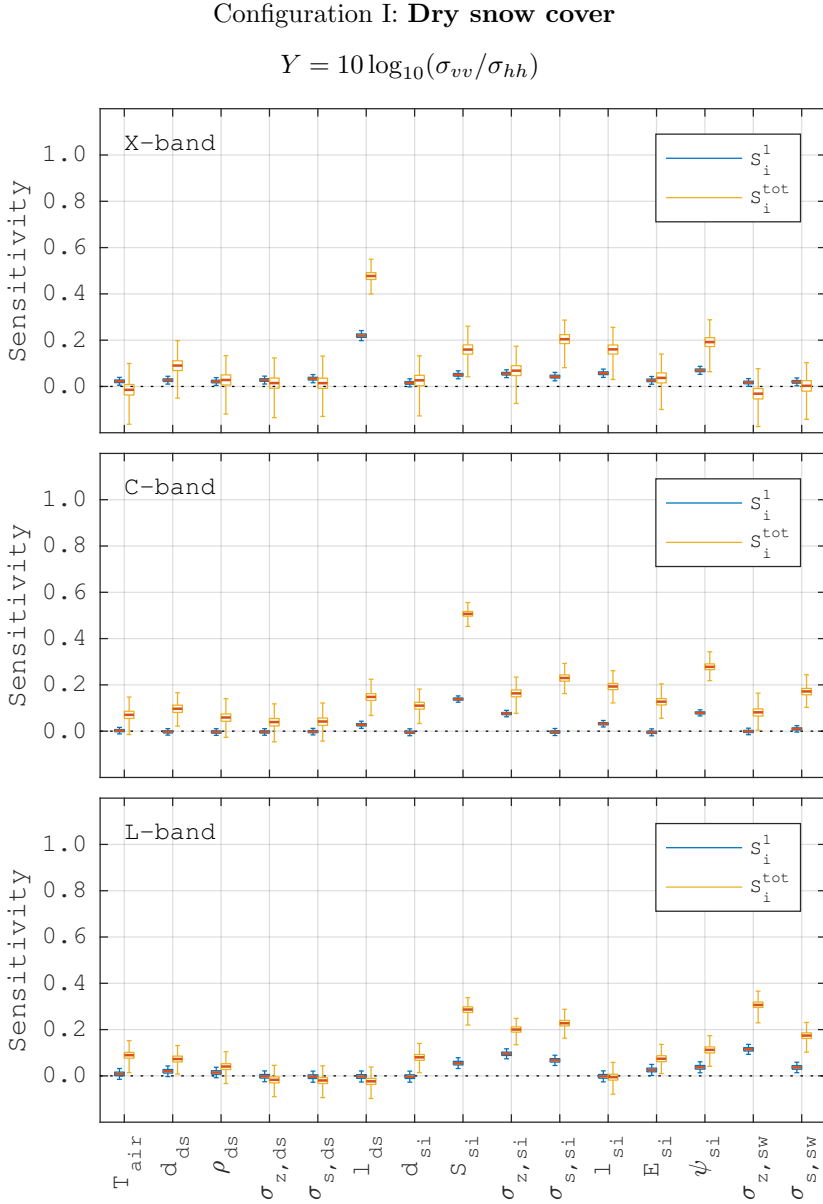
$$Y = 10 \log_{10}(\sigma_{vv}/\sigma_{hh})$$

Figure 5.12: A box plot for Sobol indices $S^{(1)}$ and $S^{(tot)}$ for the output variable $Y = 10 \log_{10}(\sigma_{vv}/\sigma_{hh})$ for "sea ice covered by dry snow" (see table 5.1). The indices are shown for X-, C- and L-band, respectively, for an incidence angle of 30°. Input sampling limits are listed in table 5.2.
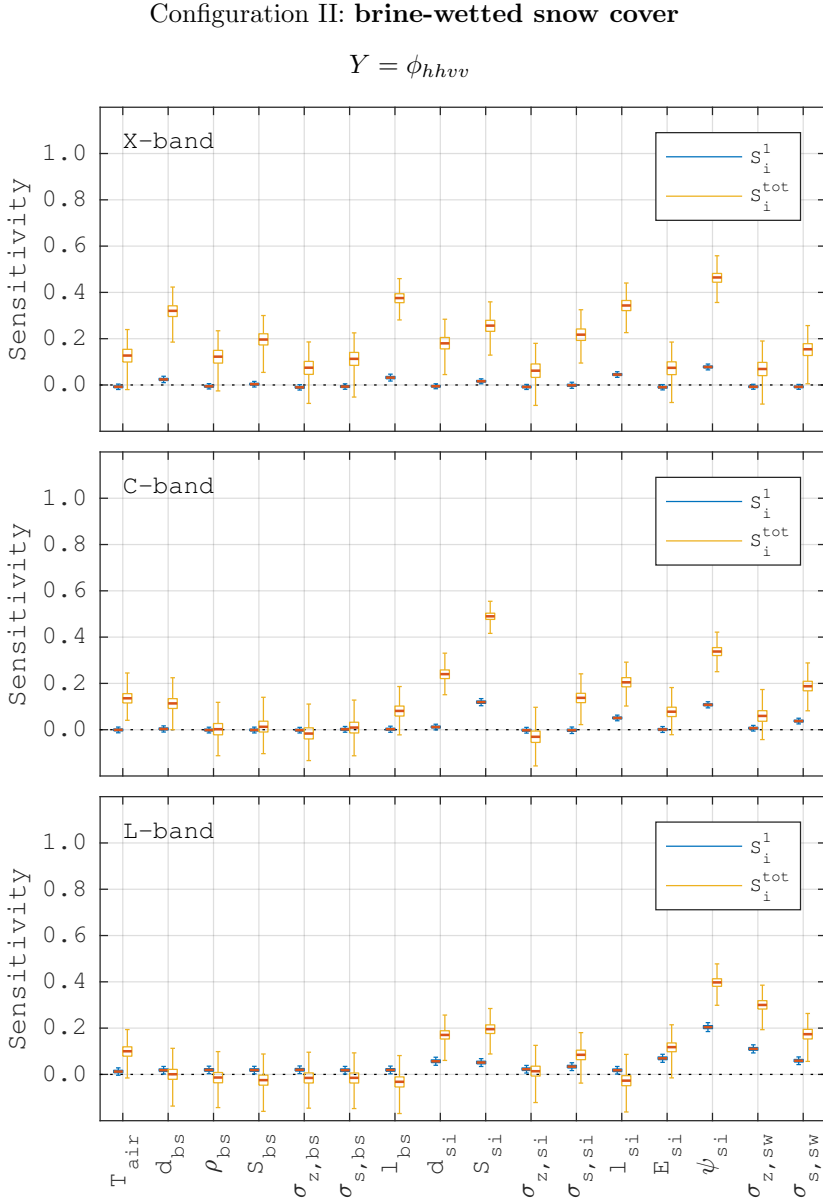
Configuration I: **Dry snow cover**
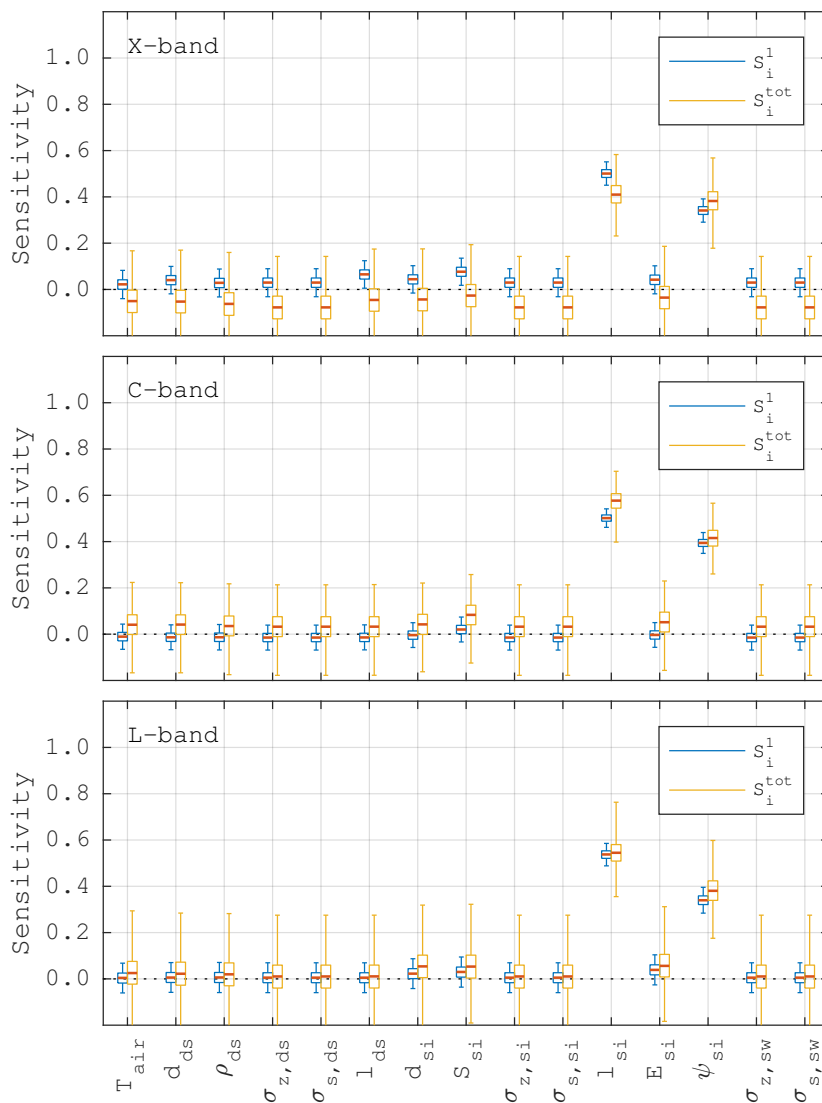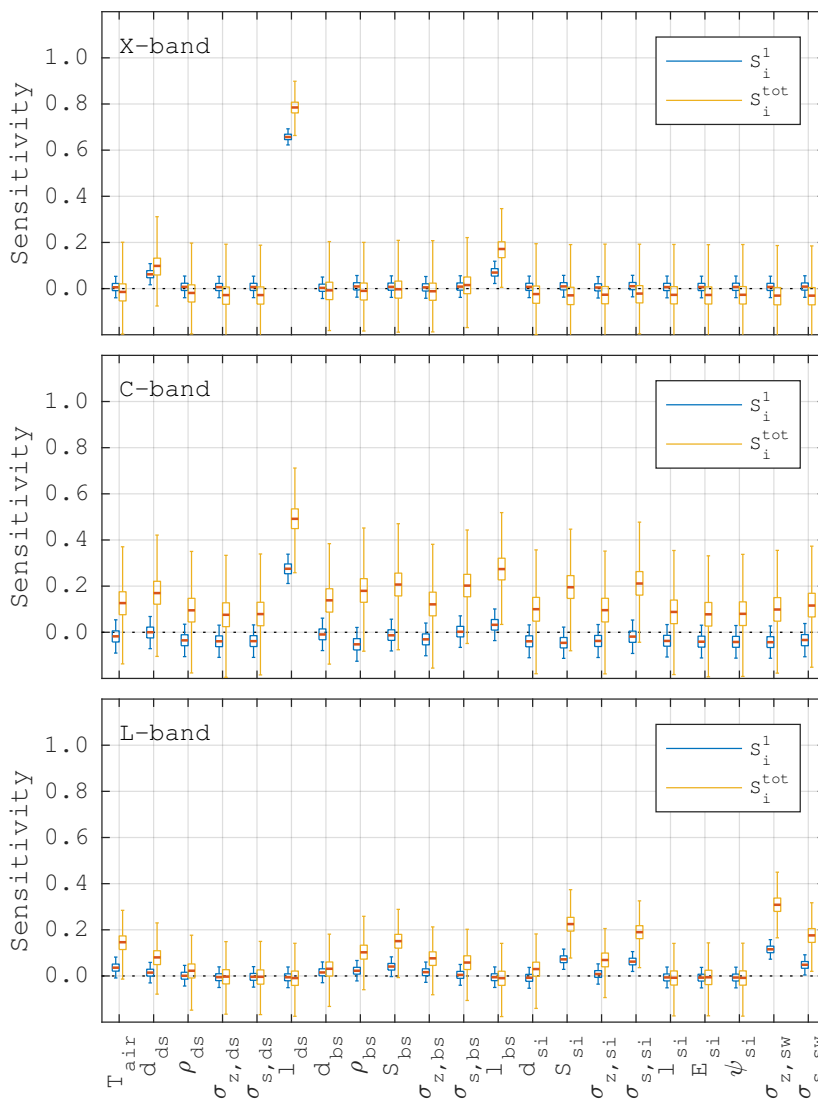
$$Y = 10 \log_{10}(\sigma_{hv})$$

Figure 5.13: A box plot for Sobol indices $S^{(1)}$ and $S^{(tot)}$ for the output variable $Y = 10 \log_{10}(\sigma_{hv})$ for "sea ice covered by dry snow" (see table 5.1). The indices are shown for X-, C- and L-band, respectively, for an incidence angle of 30°. Input sampling limits are listed in table 5.2.

Configuration I: **Dry snow cover**

$$Y = 10 \log_{10}(1 - \rho_{hhvv})$$

Figure 5.14: A box plot for Sobol indices $S^{(1)}$ and $S^{(tot)}$ for the output variable $Y = 10 \log_{10}(1 - \rho_{hhvv})$ for "sea ice covered by dry snow" (see table 5.1). The indices are shown for X-, C- and L-band, respectively, for an incidence angle of 30°. Input sampling limits are listed in table 5.2.

Configuration I: **Dry snow cover**

$$Y = \phi_{hhvv}$$

Figure 5.15: A box plot for Sobol indices $S^{(1)}$ and $S^{(tot)}$ for the output variable $Y = \phi_{hhvv}$ for "sea ice covered by dry snow" (see table 5.1). The indices are shown for X-, C- and L-band, respectively, for an incidence angle of 30°. Input sampling limits are listed in table 5.2.

Configuration II: **brine-wetted snow cover**

$$Y = 10 \log_{10}(\sigma_{hh})$$

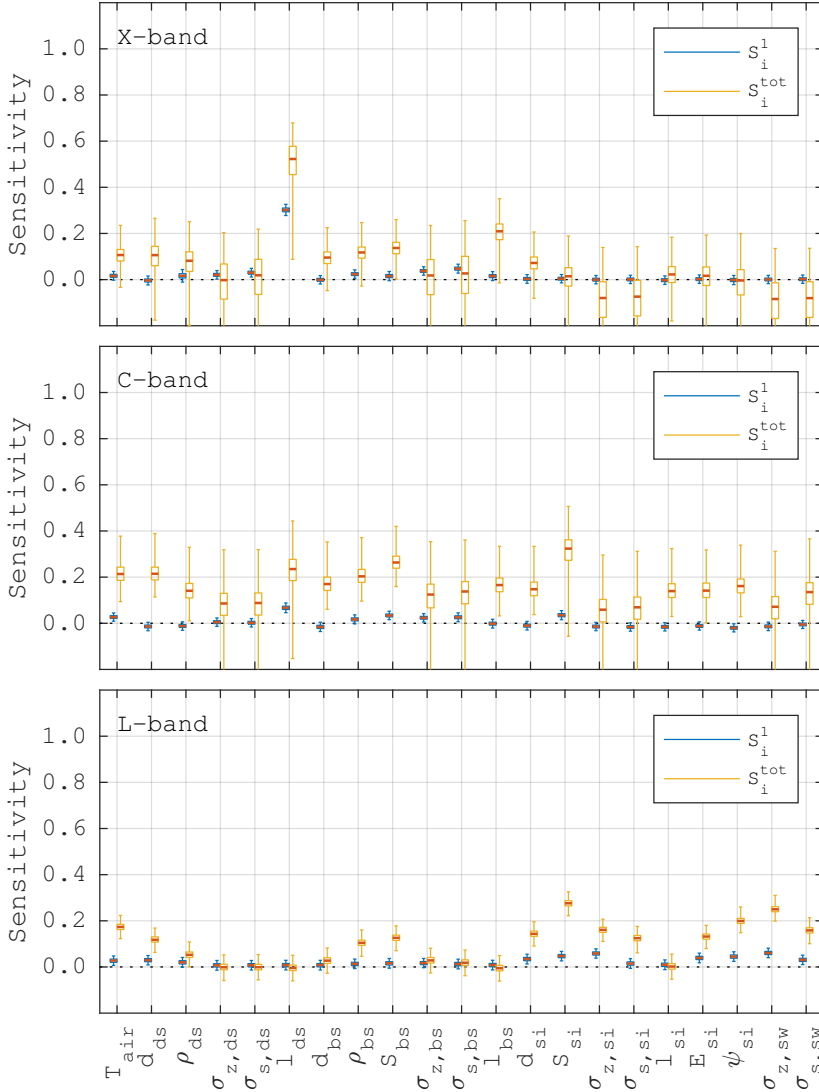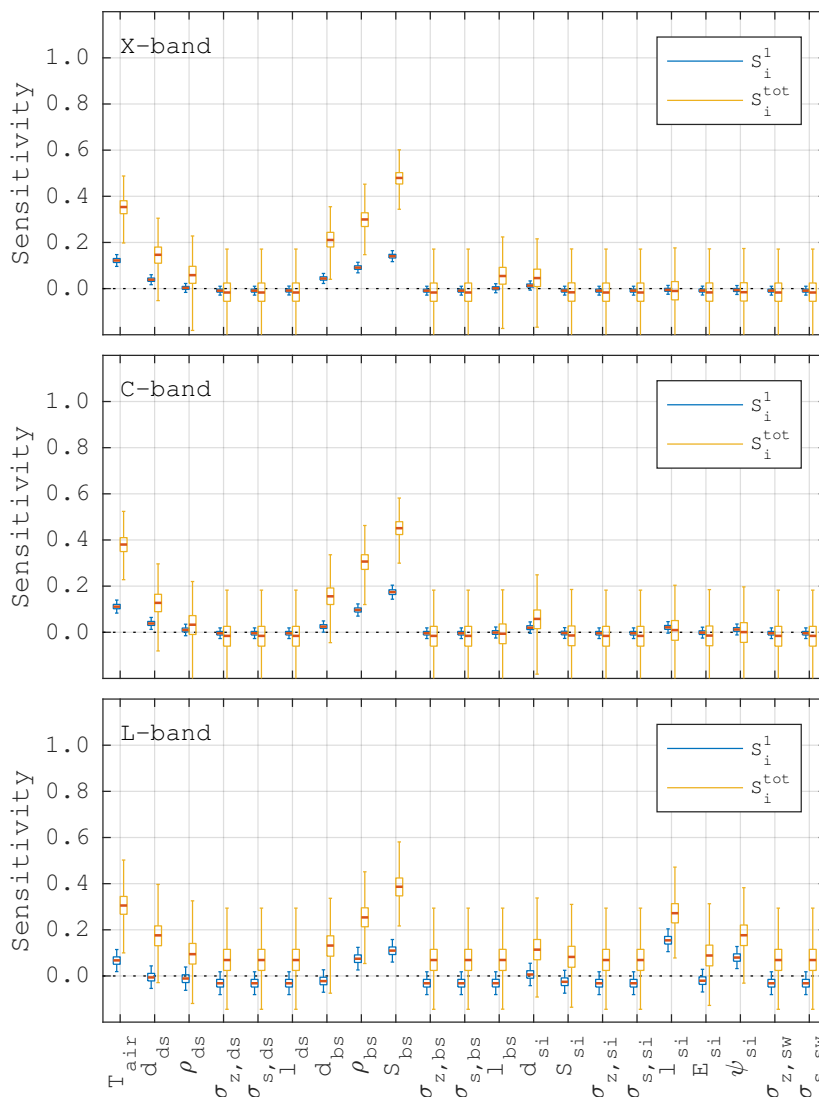

Figure 5.16: A box plot for Sobol indices $S^{(1)}$ and $S^{(tot)}$ for the output variable $Y = 10 \log_{10}(\sigma_{hh})$ for "sea ice covered by brine-wetted snow" (see table 5.1). The indices are shown for X-, C- and L-band, respectively, for an incidence angle of $30°$. Input sampling limits are listed in table 5.2.

Configuration II: **brine-wetted snow cover**

$$Y = 10 \log_{10}(\sigma_{vv}/\sigma_{hh})$$

Figure 5.17: A box plot for Sobol indices $S^{(1)}$ and $S^{(tot)}$ for the output variable $Y = 10 \log_{10}(\sigma_{vv}/\sigma_{hh})$ for "sea ice covered by brine-wetted snow" (see table 5.1). The indices are shown for X-, C- and L-band, respectively, for an incidence angle of $30°$. Input sampling limits are listed in table 5.2.

Configuration II: **brine-wetted snow cover**

$$Y = 10 \log_{10}(\sigma_{hv})$$

Figure 5.18: A box plot for Sobol indices $S^{(1)}$ and $S^{(tot)}$ for the output variable $Y = 10 \log_{10}(\sigma_{hv})$ for "sea ice covered by brine-wetted snow" (see table 5.1). The indices are shown for X-, C- and L-band, respectively, for an incidence angle of 30°. Input sampling limits are listed in table 5.2.

Configuration II: **brine-wetted snow cover**
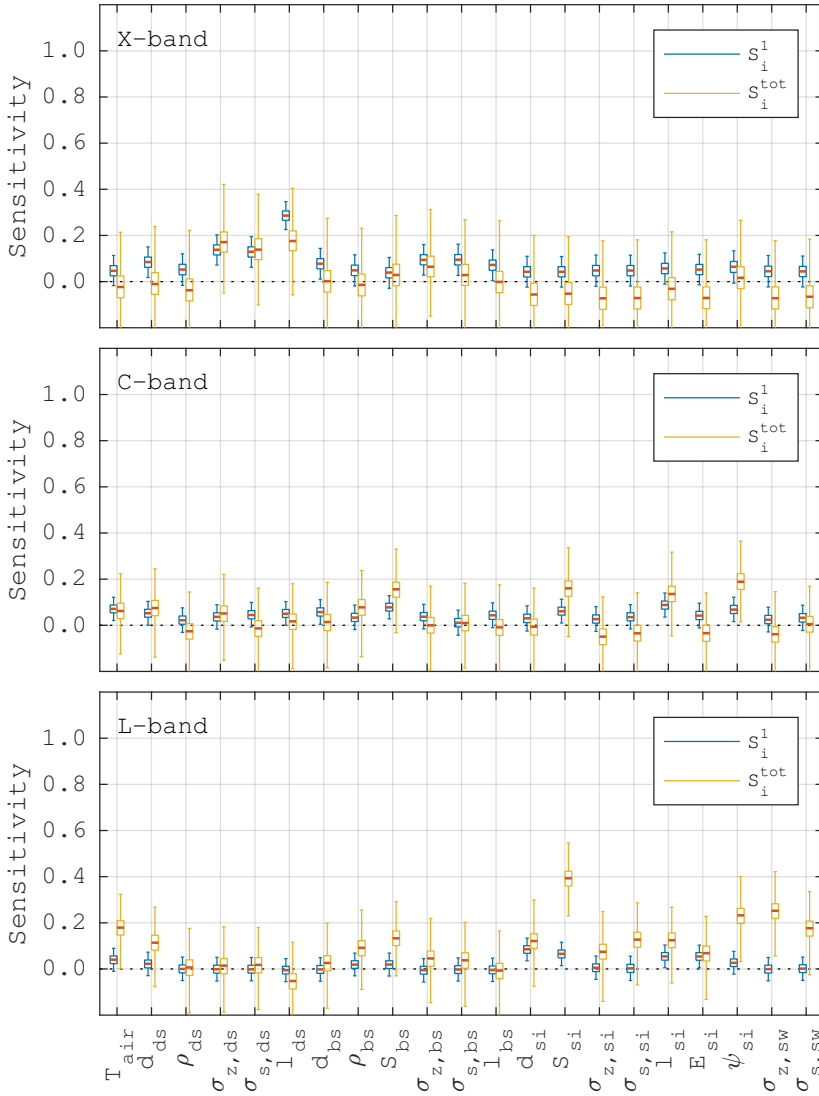
$$Y = 10 \log_{10}(1 - \rho_{hhvv})$$

Figure 5.19: A box plot for Sobol indices $S^{(1)}$ and $S^{(tot)}$ for the output variable $Y = 10 \log_{10}(1 - \rho_{hhvv})$ for "sea ice covered by brine-wetted snow" (see table 5.1). The indices are shown for X-, C- and L-band, respectively, for an incidence angle of $30°$. Input sampling limits are listed in table 5.2.

Configuration II: **brine-wetted snow cover**
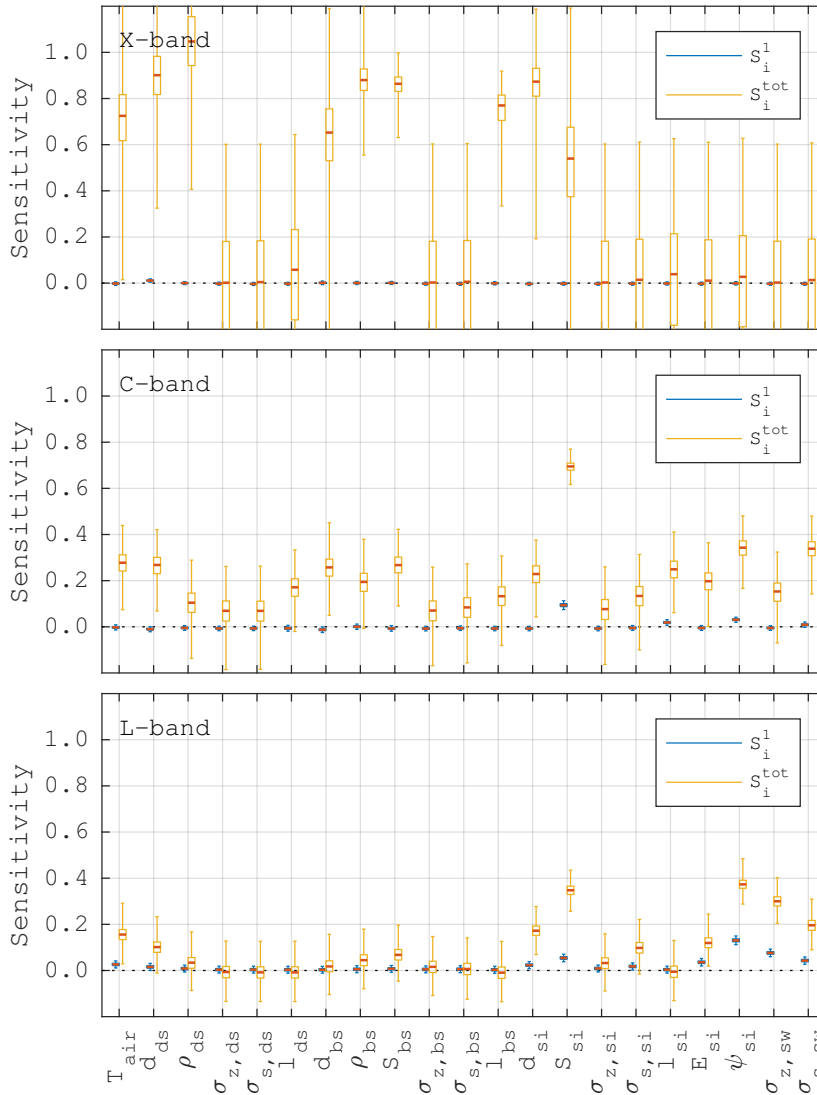
$$Y = \phi_{hhvv}$$

Figure 5.20: A box plot for Sobol indices $S^{(1)}$ and $S^{(tot)}$ for the output variable $Y = \phi_{hhvv}$ for "sea ice covered by brine-wetted snow" (see table 5.1). The indices are shown for X-, C- and L-band, respectively, for an incidence angle of 30°. Input sampling limits are listed in table 5.2.

Configuration III: **Dry and brine-wetted snow cover**

$$Y = 10\log_{10}(\sigma_{hh})$$

Figure 5.21: A box plot for Sobol indices $S^{(1)}$ and $S^{(tot)}$ for the output variable $Y = 10\log_{10}(\sigma_{hh})$ for "sea ice covered by brine-wetted snow" (see table 5.1). The indices are shown for X-, C- and L-band, respectively, for an incidence angle of $30°$. Input sampling limits are listed in table 5.2.

Configuration III: **Dry and brine-wetted snow cover**

$$Y = 10 \log_{10}(\sigma_{vv}/\sigma_{hh})$$

Figure 5.22: A box plot for Sobol indices $S^{(1)}$ and $S^{(tot)}$ for the output variable $Y = 10 \log_{10}(\sigma_{vv}/\sigma_{hh})$ for "sea ice covered by brine-wetted snow" (see table 5.1). The indices are shown for X-, C- and L-band, respectively, for an incidence angle of 30°. Input sampling limits are listed in table 5.2.

Configuration III: **Dry and brine-wetted snow cover**

$$Y = 10 \log_{10}(\sigma_{hv})$$

Figure 5.23: A box plot for Sobol indices $S^{(1)}$ and $S^{(tot)}$ for the output variable $Y = 10 \log_{10}(\sigma_{hv})$ for "sea ice covered by brine-wetted snow" (see table 5.1). The indices are shown for X-, C- and L-band, respectively, for an incidence angle of $30°$. Input sampling limits are listed in table 5.2.

Configuration III: **Dry and brine-wetted snow cover**

$$Y = 10 \log_{10}(1 - \rho_{hhvv})$$

Figure 5.24: A box plot for Sobol indices $S^{(1)}$ and $S^{(tot)}$ for the output variable $Y = 10 \log_{10}(1 - \rho_{hhvv})$ for "sea ice covered by brine-wetted snow" (see table 5.1). The indices are shown for X-, C- and L-band, respectively, for an incidence angle of $30°$. Input sampling limits are listed in table 5.2.

Configuration III: **Dry and brine-wetted snow cover**

$$Y = \phi_{hhvv}$$

Figure 5.25: A box plot for Sobol indices $S^{(1)}$ and $S^{(tot)}$ for the output variable $Y = \phi_{hhvv}$ for "sea ice covered by brine-wetted snow" (see table 5.1). The indices are shown for X-, C- and L-band, respectively, for an incidence angle of 30°. Input sampling limits are listed in table 5.2.

Chapter 6

Models compared to SAR data of sea ice in the Fram Strait

While the previous chapter was focusing on the sensitivity of a backscatter model, this chapter deals with the representativeness of such a model. While the sensitivity is critical for identifying the parameters that can be retrieved from data, the representativeness is critical for selecting a realistic model in the first place.

Specifically, model predictions are compared to synthetic aperture radar (SAR) data collected in conjunction with the Norwegian young sea ice cruise 2015 (N-ICE 2015). By considering meteorological data as well as in-situ observations of the sea ice in the region, model input parameters can be partly constrained. Within these constraints, the ability of the model to represent certain ice types can be assessed.

The assessment suggests that a relatively simple composite backscatter model (based on incoherent layer-stacking as described in chapter 5) can typically be fitted well to SAR data at both C- and L-band, for ice types tagged as lead ice or ice floes. Generally, C-band data is better represented by the considered models than L-band data. Likewise, the ice identified as ice floes is better represented than ice types identified as lead ice. The model primarily deviates from the data in the co-polarised phase shift and the cross-polarised channel. Overall, the range of plausible model predictions is however very wide, which is explained by insufficiently constraints on roughness and volumetric structure parameters (which seldom are known).

6.1 Motivation and objectives

Throughout the years, a great number of models have been proposed for describing the radar backscatter from sea ice (see table 4.1 for an overview). In fact, even though more than half a century has passed since some of the first sea ice mapping experiments were conducted with imaging radars (Anderson 1966, Rouse 1969), forward modelling of the radar backscatter from sea ice is still an active research topic.

While the past development of models is both impressive and important for the general understanding, a consensus on which models to use under what circumstances seems to be lacking. Moreover, few models have found their way to operational applications. Considering geophysical parameter retrieval through model inversion, one arguable reason for this is their complexity and high dimensionality. It is therefore desirable to identify ice types and sensor configurations for which relatively simple models with few input parameters do appear representative to the data.

With this in mind, the objective of this chapter is to assess what types of sea ice and what radar configurations are well described by a relatively simple scattering model. The assessment is focused on sea ice in the Fram Strait during the late winter and early spring, with data mainly containing new, young and first year ice. The backscatter simulations are based on the composite model used in the sensitivity analysis of chapter 5 (see section 5.2 for details).

6.2 SAR data

The data considered in this chapter were acquired in the Arctic ocean north of Svalbard, in conjunction with the N-ICE 2015 campaign. N-ICE 2015 was an research expedition lasting from 12 January to 24 June in 2015 and was lead by the norwegian polar institute (NPI). In the expedition, the NPI research vessel RV Lance was positioned at approximately 83°N 21°E and was let to drift with the sea ice. The ship was repositioned three times, resulting in four periods of passive drift. In figure 6.1, the ship track of RV Lance is shown as a grey dotted line and the drift periods are highlighted as blue solid lines.

During drift, a research camp was established on the ice floe next to the ship, enabling extensive in-situ data collection including continuous meteorological measurements. A large amount of remote sensing data was also collected. In particular, multiple SAR scenes were acquired from the satellites advanced land observing satellite 2 (ALOS-2), Radarsat-2, TerraSAR-X and Sentinel-1. In this section, the selected SAR data is presented.

6.2.1 Selected scenes

From the large amount of remote sensing data aquired coincident with the N-ICE 2015 campaign, a subset of overlapping SAR scenes has been selected based on the criteria:

(i) The overlapping scenes are acquired at different radar frequencies.

(ii) The overlapping scenes contain the same sea ice.

(iii) The maximum time difference between the overlapping scenes does not exceed 24 hours.

This resulted in a total of 26 individual SAR scenes from the satellites ALOS-2, Radarsat-2 and TerraSAR-X, constituting 5 overlapping scene sets. The footprints of the scenes are shown in figure 6.1 and the acquisition times and radar configurations are listed per overlapping scene set in table 6.1. The time separation between the overlapping scenes range from 1 minute to 14 hours. As an example, the scenes of overlap number 1 (see table 6.1) are displayed on top of each other in figure 6.2 and separately in figure 6.3. Yellow polygons indicate regions of interest, which are discussed next.

6.2.2 Regions of interest

Four types of regions are identified in the overlapping scenes and labeled as "open water", "lead ice", "ice floe" or "ridge or brash". These types are primarily defined by their shape and motion characteristics. In particular:

Open water is defined as a region of homogeneous radar signature found in linear openings in the ice pack, that may change in size and shape over relatively short time and may have drifting ice features within them.

Lead ice is defined as a homogeneous region found in lead like features within the ice pack, with a shape that does not change considerably over short time.

Ice floe is defined as a homogeneous region within the ice pack that does not resemble a lead or crack and does not change in size over time. These presumably corresponds to level FYI or similar (very little MYI was observed during N-ICE 2015).

Ridge or brash is defined as a region of considerably higher backscatter than the surrounding area. Ridges are typically identified by their elongated shape. Brash ice, that is ice fragments of centimetres to decimetres in size, are typically located between individual ice floes.
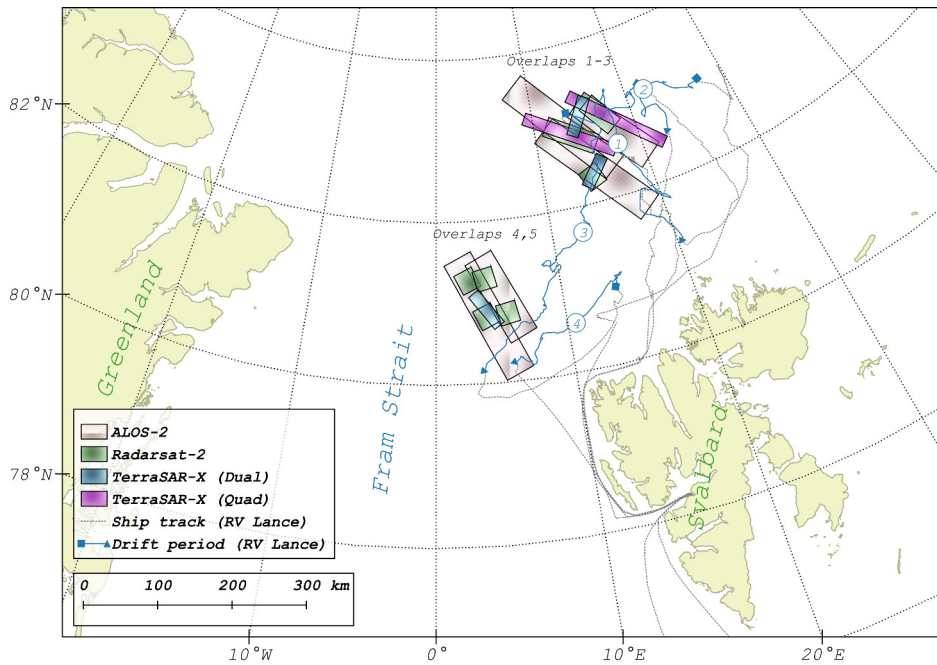
Figure 6.1: Map showing the area of interest, including footprints of the 18 SAR scenes considered in this chapter and the track of RV Lance traced out during N-ICE 2015. The ship track for the whole expedition is depicted as a grey dotted line while the four drift periods are highlighted as solid blue lines. The drift periods are labeled according to their duration of drift, specifically as: (1) 15 Jan. - 21 Feb., (2) 24 Feb. - 19 Mar., (3) 18 Apr. - 5 June and (4) 7 - 22 June.
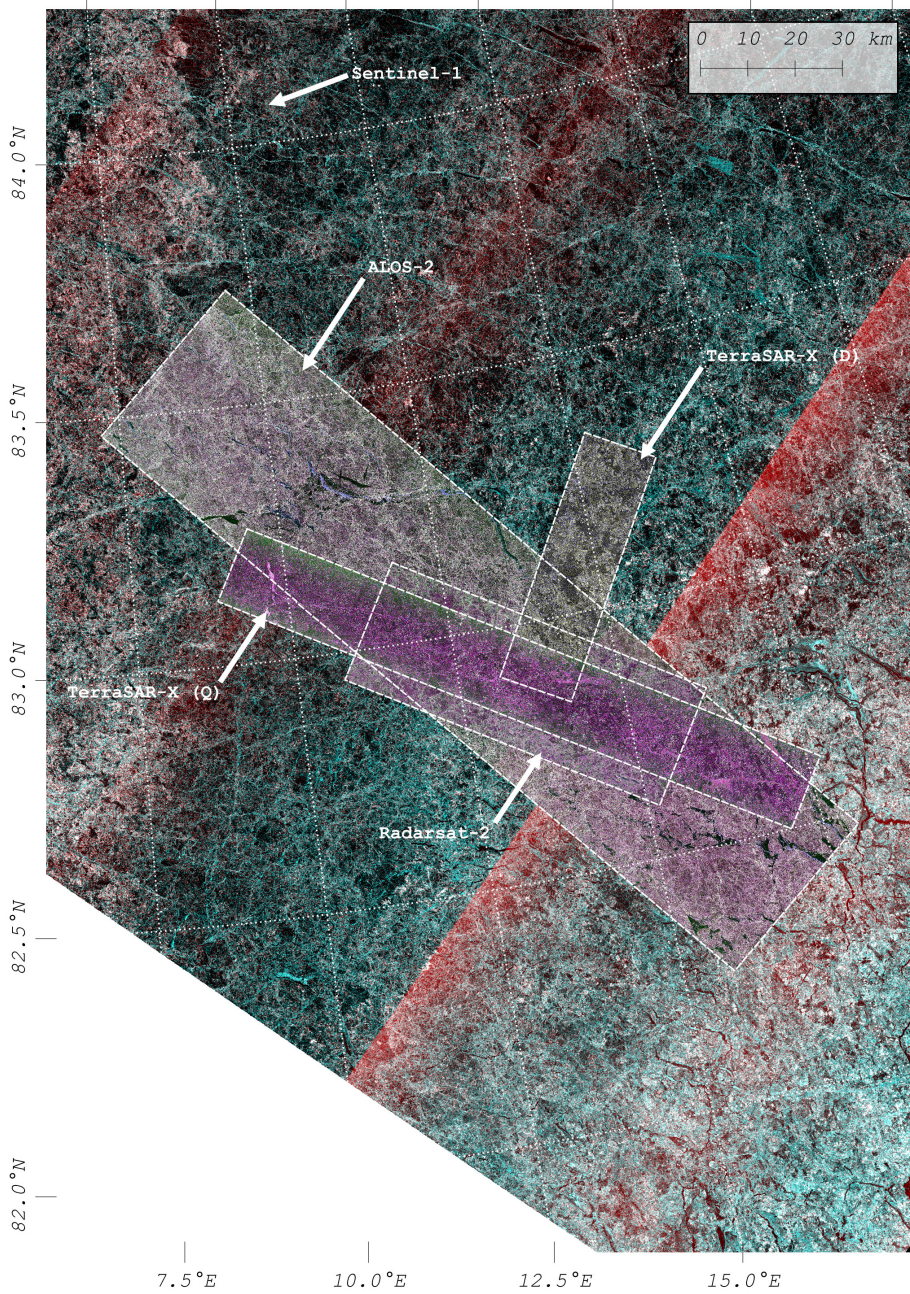
Figure 6.2: All scenes of overlap number 1 acquired on the 19 April 2015 (see table 6.1 for details). A Sentinel-1 scanSAR scene is included in the background as an overview.

Over-lap	Date	UTC	Satellite	SAR mode	Freq. band	Wave-len.	Polari-sation	Incidence angle	Resolu-tion [m]
1	2015-04-19	20:32	ALOS-2	Strip	L	24.2cm	Quad	32.4-35.3°	2.9×3.2
		13:19	RS-2	Strip	C	5.6cm	Quad	20.9-22.8°	4.7×5.4
		13:18	TS-X	Strip	X	3.1cm	Quad	17.3-19.1°	0.9×2.1
		07:01	TS-X	Strip	X	3.1cm	hh,vv	42.7-43.9°	0.9×2.9
		08:02	S-1A	Scan	C	5.6cm	hh,hv	18.9-46.4°	40×40
2	2015-04-23	20:18	ALOS-2	Strip	L	24.2cm	Quad	32.4-35.3°	2.9×3.2
		14:42	RS-2	Strip	C	5.6cm	Quad	36.5-38.0°	4.7×5.5
		13:43	TS-X	Strip	X	3.1cm	Quad	27.4-29.0°	0.9×2.2
3	2015-04-28	20:25	ALOS-2	Strip	L	24.2cm	Quad	29.5-32.6°	2.9×3.1
		15:37	RS-2	Strip	C	5.6cm	Quad	42.0-43.4°	4.7×5.0
		07:35	TS-X	Strip	X	3.1cm	hh,vv	30.9-32.4°	0.9×2.4
4	2015-05-26	22:02	ALOS-2	Strip	L	24.2cm	Quad	37.7-40.3°	2.9×3.1
		17:00	RS-2	Strip	C	5.6cm	Quad	48.4-49.5°	4.7×5.1
5	2015-05-31	22:08	ALOS-2	Strip	L	24.2cm	Quad	37.7-40.3°	2.9×3.1
		16:14	RS-2	Strip	C	5.6cm	Quad	37.5-39.0°	4.7×5.0
		15:26	TS-X	Strip	X	3.1cm	hh,vv	26.3-27.9°	0.9×2.4

Table 6.1: An overview of the overlapping sets of scenes with corresponding acquisition times, satellite missions and radar configurations. For consecutive scenes acquired along the same orbit track, only the first scene is included in the table. The scenes of overlap number 1 are further shown in figures 6.2 and 6.4.

Corresponding polygons were drawn manually on map projected RGB composites of the SAR scenes. In total, 943 individual polygons were drawn in the overlapping scenes (table C.1 shows an overview of the number of polygons per satellite sensor and overlapping scene set). In figure 6.4, a few examples are further shown for an ALOS-2 scene from overlap 2. Polygons that corresponding to the same sea ice or water area, but observed with different sensors, are referred to as polygon pairs.

6.2.3   Processing

To get an overview of the data, each polygon is processed in the the slant range radar geometry according to the following steps:

1. Cropping:
   In the radar geometry (slant range and azimuth), the rectangular region that bounds the polygon is cropped out into a sub-image.

2. Multi-looking:
   The 3×3 scattering covariance matrix is formed by multi-looking the sub-image with a 4×4 averaging filter.

3. Cutting:
   The pixels within the polygon are extracted. If the pixels are fewer than 10, the polygon is dismissed and not considered further.

4. Feature extraction:
   Polarimetric features are extracted.

5. Averaging:
   The median value of all pixels is taken.

This will reduce each polygon to one data sample in the polarimetric feature space of choice. All the SAR scenes were calibrated using the sentinel application platform (SNAP) version 3.0.3, apart from the quad polarised TerraSAR-X scenes that were calibrated by Deutsches zentrum für luft- und raumfahrt (DLR).

6.2.4   Sensor noise

The system noise level is strongly dependent on the sensor, in what mode the sensor is operated and on incidence angle (Slade 2011, Mittermayer et al. 2010). Estimates for the noise-equivalent sigma zero (NESZ) are provided in the metadata of Radarsat-2 and TerraSAR-X. For the Radarsat-2 scenes used in this chapter, the NESZ at the polygons vary from -37.4 to -31.1 dB. For TerraSAR-X, the noise level is higher and is moreover significantly different between the
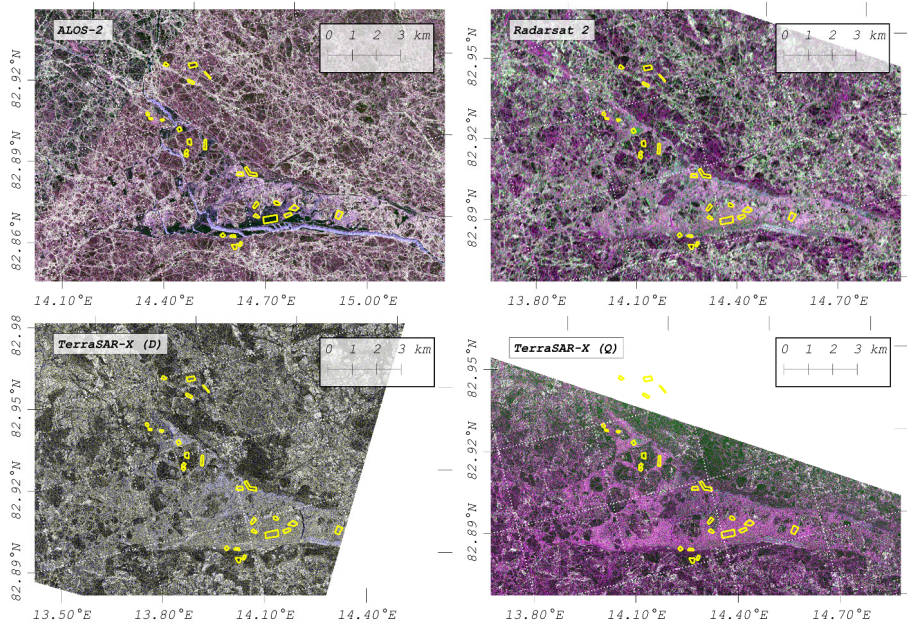
Figure 6.3: The scenes of overlap number 1 (see table 6.1 for details). The manually selected regions of interest are highlighted as yellow polygons.
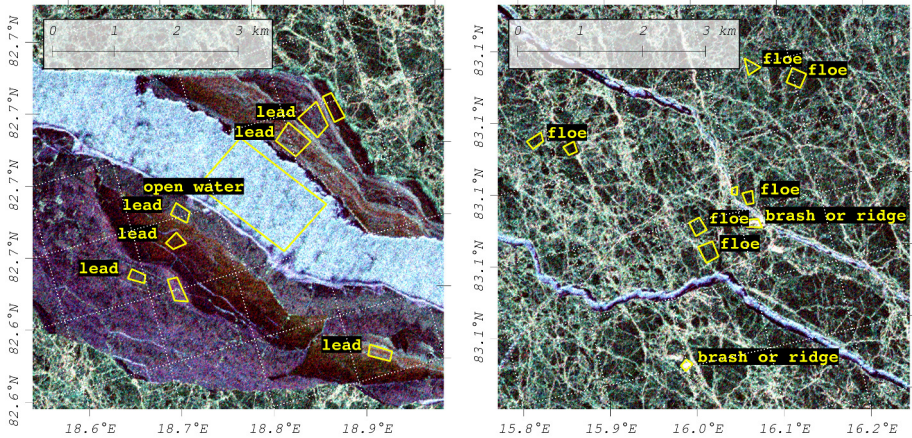
Figure 6.4: Example polygons for an ALOS-2 scene in overlap 2, labeled as "open water" and "lead ice" in the left image and "floe" and "ridge or brash" in the right image.

dual- and quad-polarised modes and vary from -25.7 to -17.0 dB. The NESZ is unfortunately not provided for ALOS-2. By analysing the darkest pixels in the considered ALOS-2 scenes, it is however here roughly estimated to be around -35 dB. This value will be used regardless of incidence angle, for all ALOS-2 polygons.

In the following analysis, the signal-to-noise ratio (SNR) of a polygon is moreover considered as the average power of the channels involved in the considered polarimetric parameter, relative to the NESZ at the centre position of the polygon. For instance, the co-polarised phase difference involve only the co-polarised channels, thus $\text{SNR} = 0.5(\sigma_{hh} + \sigma_{vv})/\sigma_{\text{NESZ}}$. The largest circle is indicated when $10\log_{10}(\text{SNR}) = 0$ dB and no circle is indicated if $10\log_{10}(\text{SNR}) > 10$ dB.

6.2.5   Polygon overview

An overview of all polygons as a function of incidence angle is shown in figures 6.5 to 6.8 for "open water", "lead ice", "ice floe" and "ridge or brash", respectively. The SNR is indicated by circles around the markers. Specifically, the largest circle is indicated if $10\log_{10}(\text{SNR}) \leq 0$ dB and no circle is indicated if $10\log_{10}(\text{SNR}) > 10$ dB.

In order to further compare the sensors, the polygon pairs are plotted in difference plots in figures 6.9 to 6.12. The polygons from the ALOS-2 scenes are indicated along the x-axis and the corresponding polygons from the Radarsat-2 and TerraSAR-X scenes are indicated along the y-axis. Here, the circles around the markers show the difference in incidence angle between the paired polygons, rather than SNR. Such differences will increase the spreading of the points in the plot. In particular, the difference in incidence angle vary from less than a degree for some pairs, up to 12.6° in the most extreme case. It should also be noted that there are differences in acquisition time between the polygon pairs as well (see table 6.1).

Open water

In figure 6.5, the polygons tagged as open water are displayed. Regarding all sensors, the radar cross sections vary significantly. Specifically, σ_{hh} range from -29 to -10 dB, σ_{hv} from -36 to -22 dB and σ_{vv} from -29 to -9 dB. This variability is expected considering differences in fetch and wind conditions between the polygons.

Considering the radar cross sections in the difference plots in figure 6.9, it is evident that the TerraSAR-X polygons yield higher σ_{hh} than ALOS-2 in all cases except two, while σ_{vv} is more similar. The Radarsat-2 polygons are more similar to ALOS-2 in σ_{hh} than in σ_{vv}.

A few polygons are particularly noticeable in that σ_{vv} is considerably lower for Radarsat-2 than for ALOS-2, despite similar incidence angles. This could
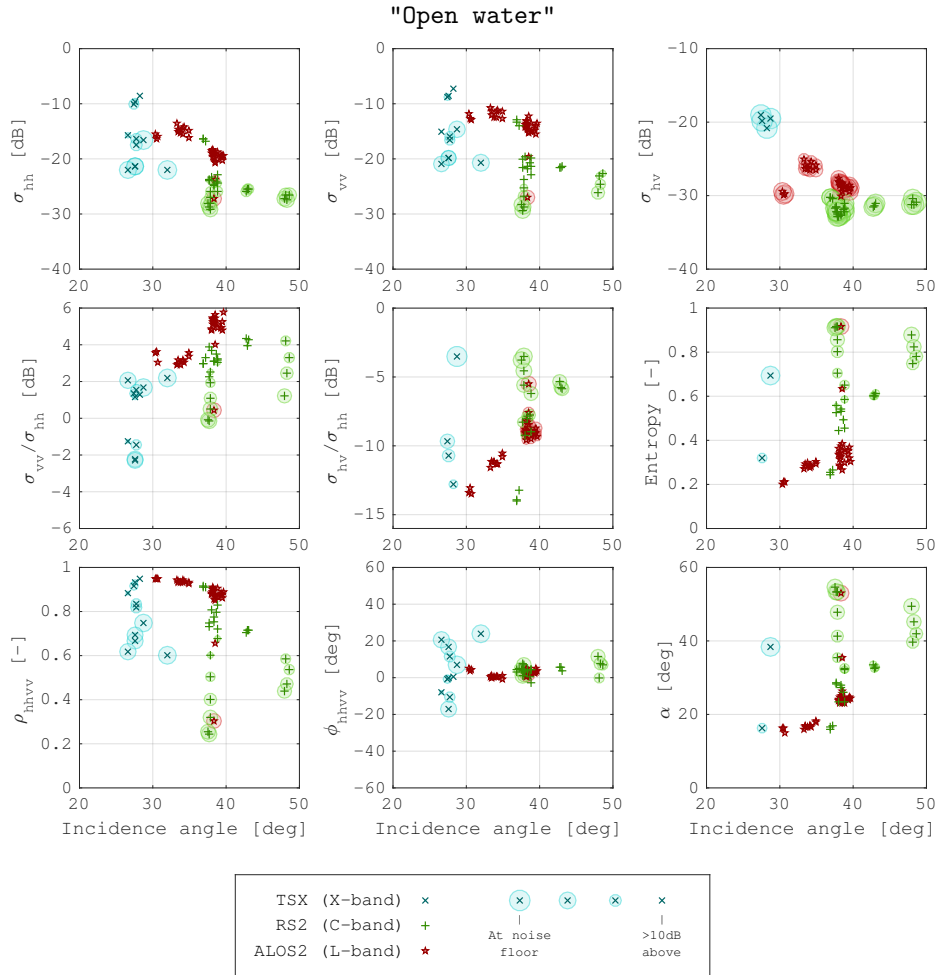
Figure 6.5: The polarimetric data for polygons tagged as "open water". Each marker corresponds to the median value of a polygon. The colours indicate sensor type and the shapes SNR (see legend).
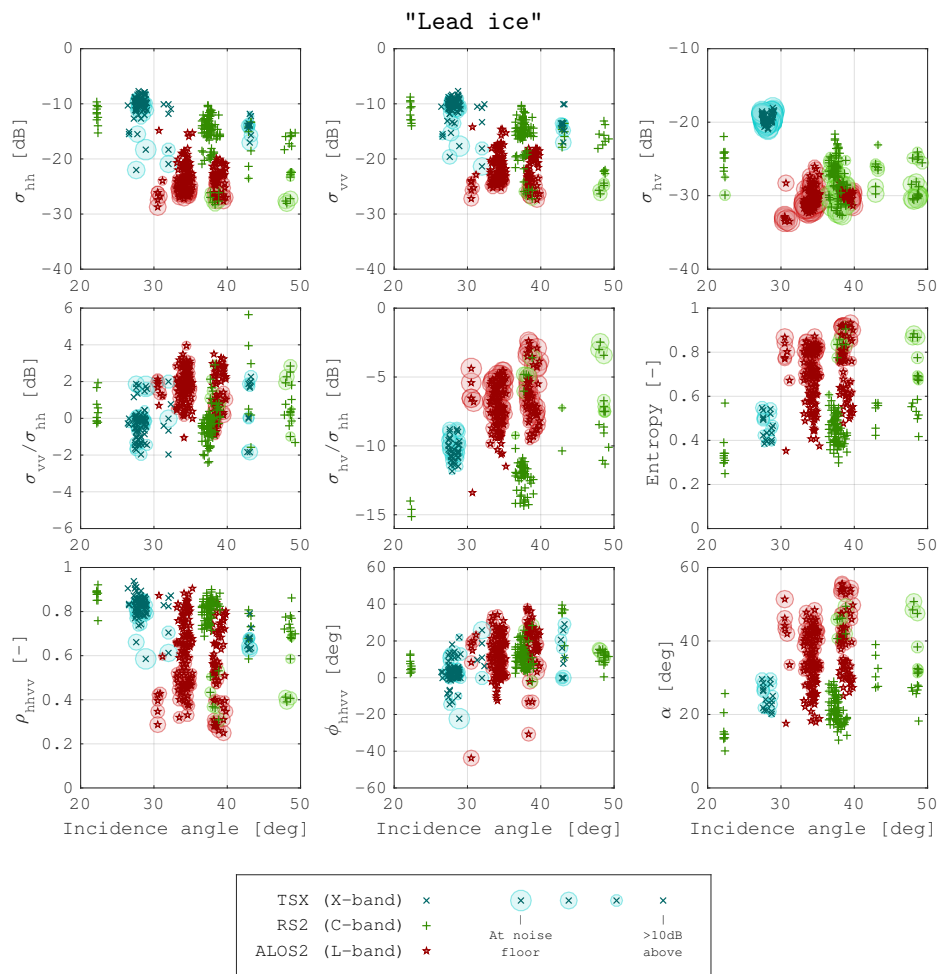
Figure 6.6: The polarimertic data for polygons tagged as "lead ice". Each tick corresponds to the median value of one polygon. The colours indicate sensor type and the shapes SNR (see legend).
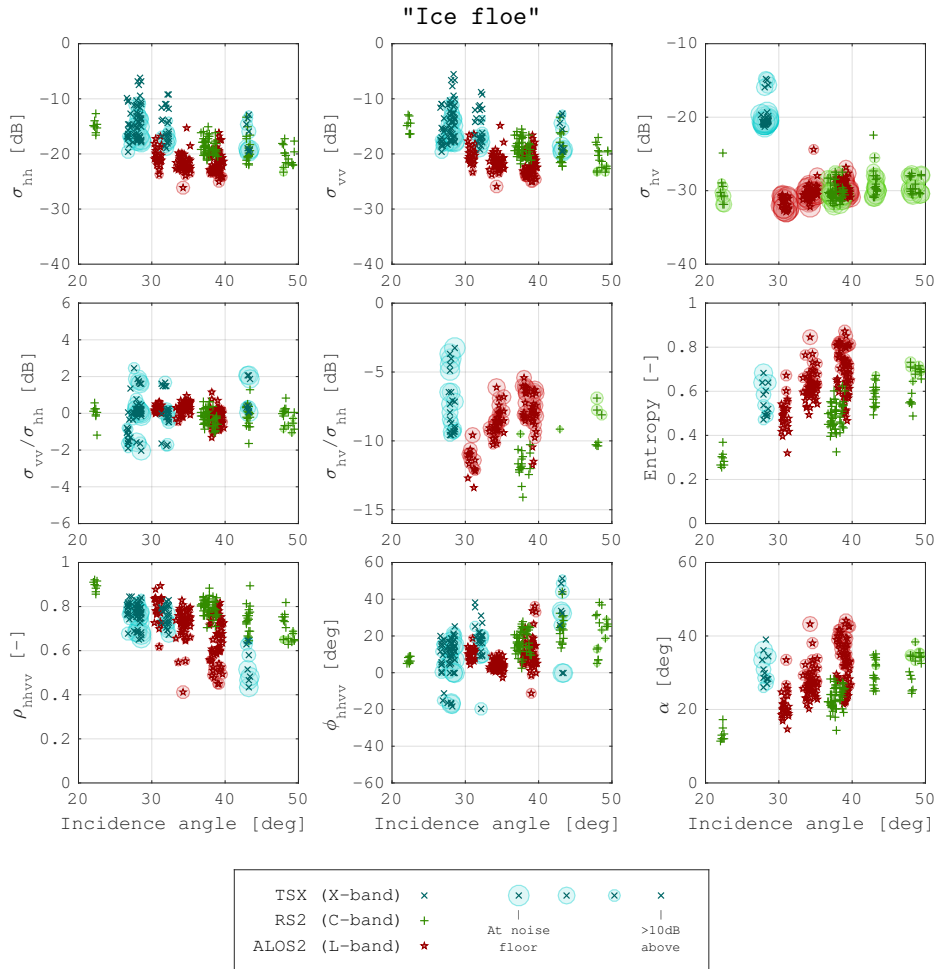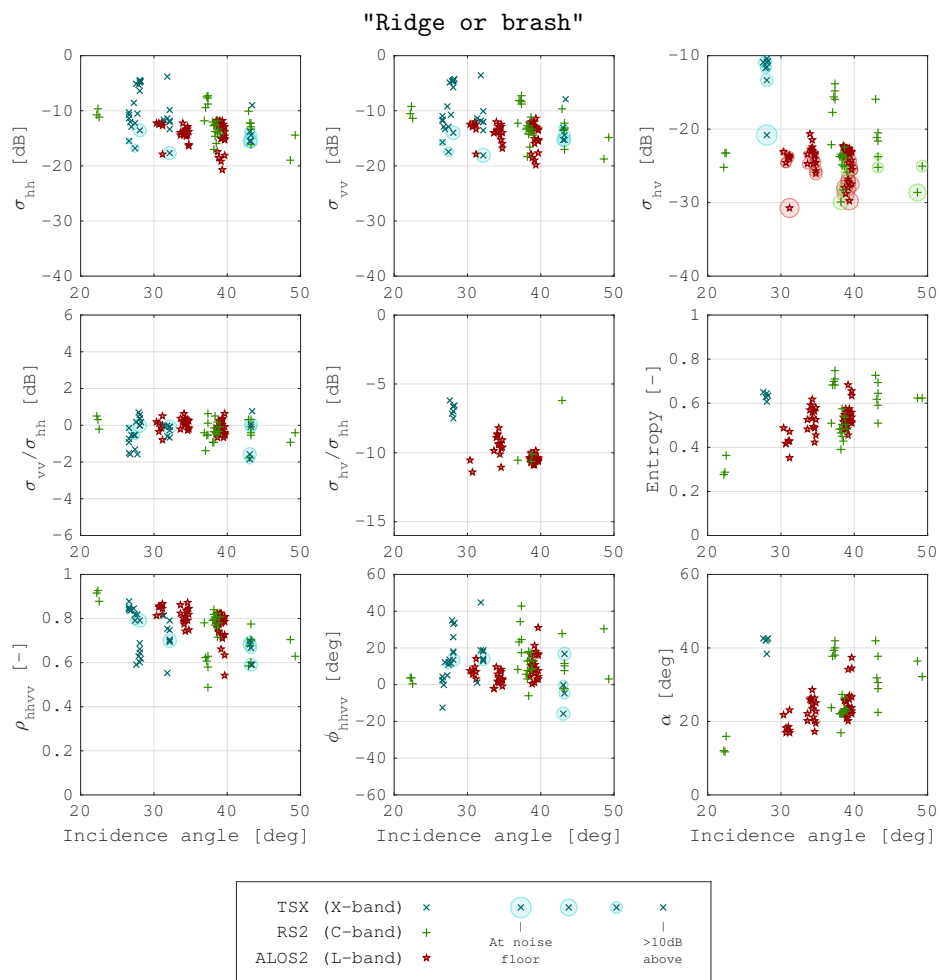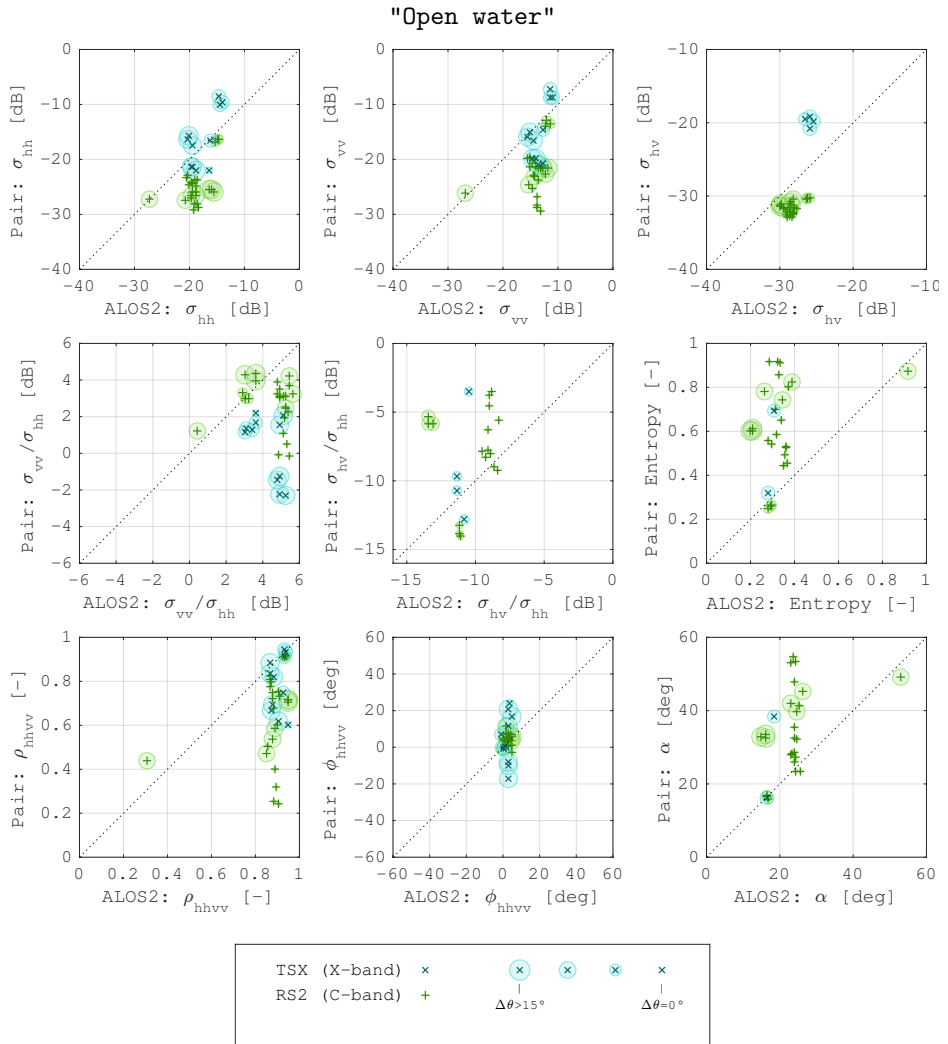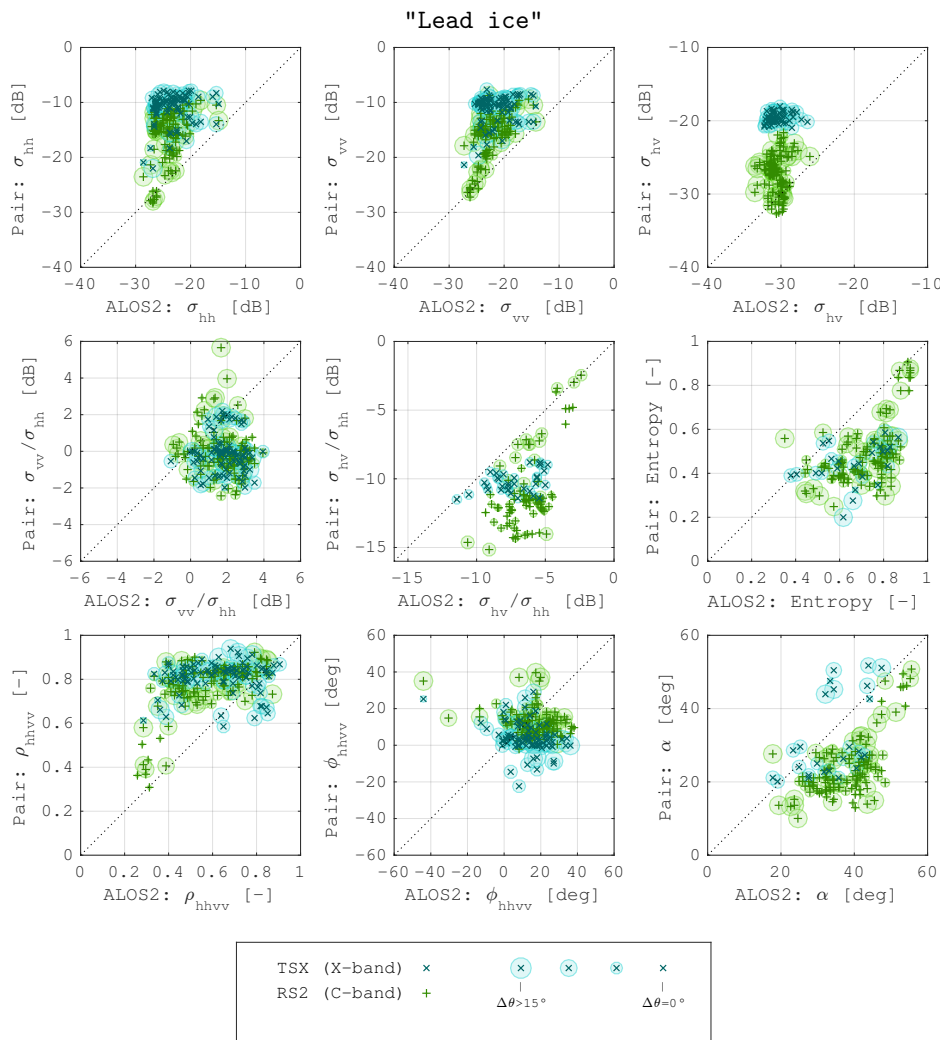
Figure 6.7: The polarimetric data for polygons tagged as "ice floe". Each tick corresponds to the median value of one polygon. The colours indicate sensor type and the shapes SNR (see legend).

Figure 6.8: The polarimetric data for polygons tagged as "ridge or brash". Each tick corresponds to the median value of one polygon. The colours indicate sensor type and the shapes SNR (see legend).

Figure 6.9: The differences between paired polygons tagged as "open water". Each tick corresponds to the median value of one polygon. The colour and size of the markers indicate sensor and incidence angle difference, respectively (see legend).

Figure 6.10: The differences between paired polygons tagged as "lead ice". Each tick corresponds to the median value of one polygon. The colour and size of the markers indicate sensor and incidence angle difference, respectively (see legend).
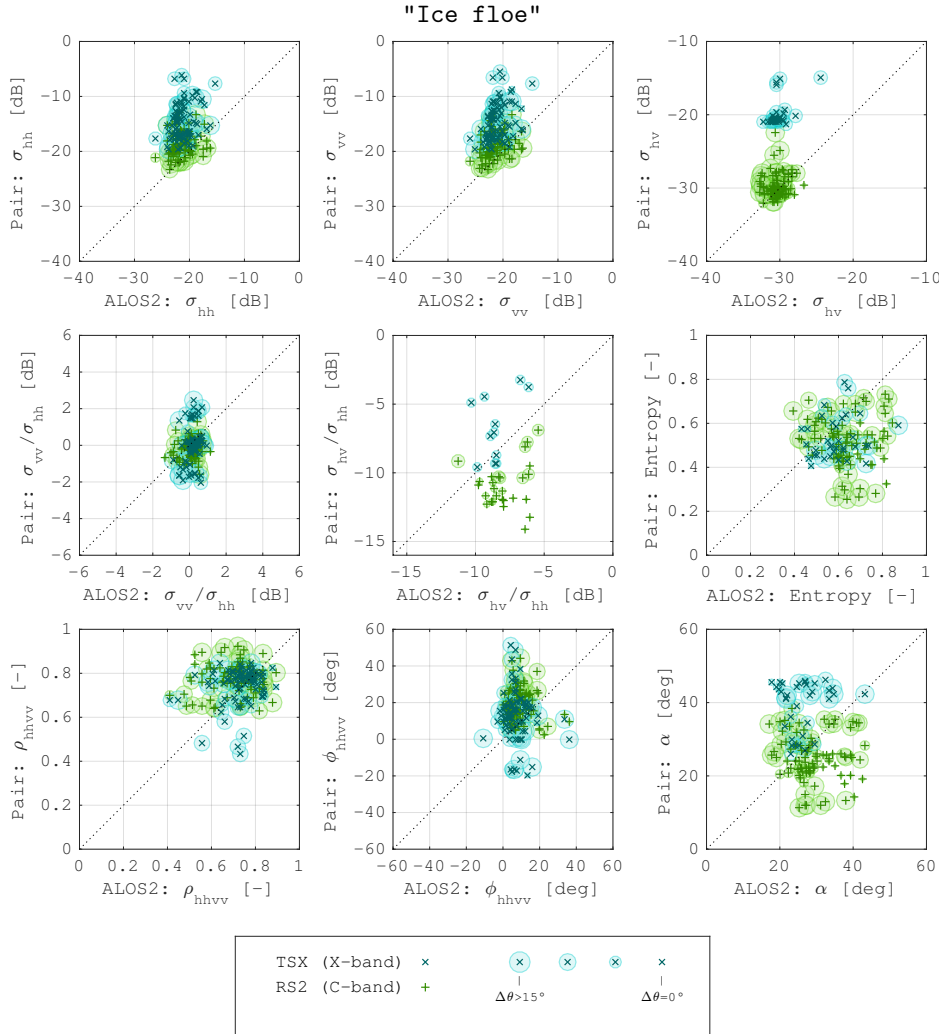
Figure 6.11: The differences between paired polygons tagged as "ice floe". Each tick corresponds to the median value of one polygon. The colour and size of the markers indicate sensor and incidence angle difference, respectively (see legend).
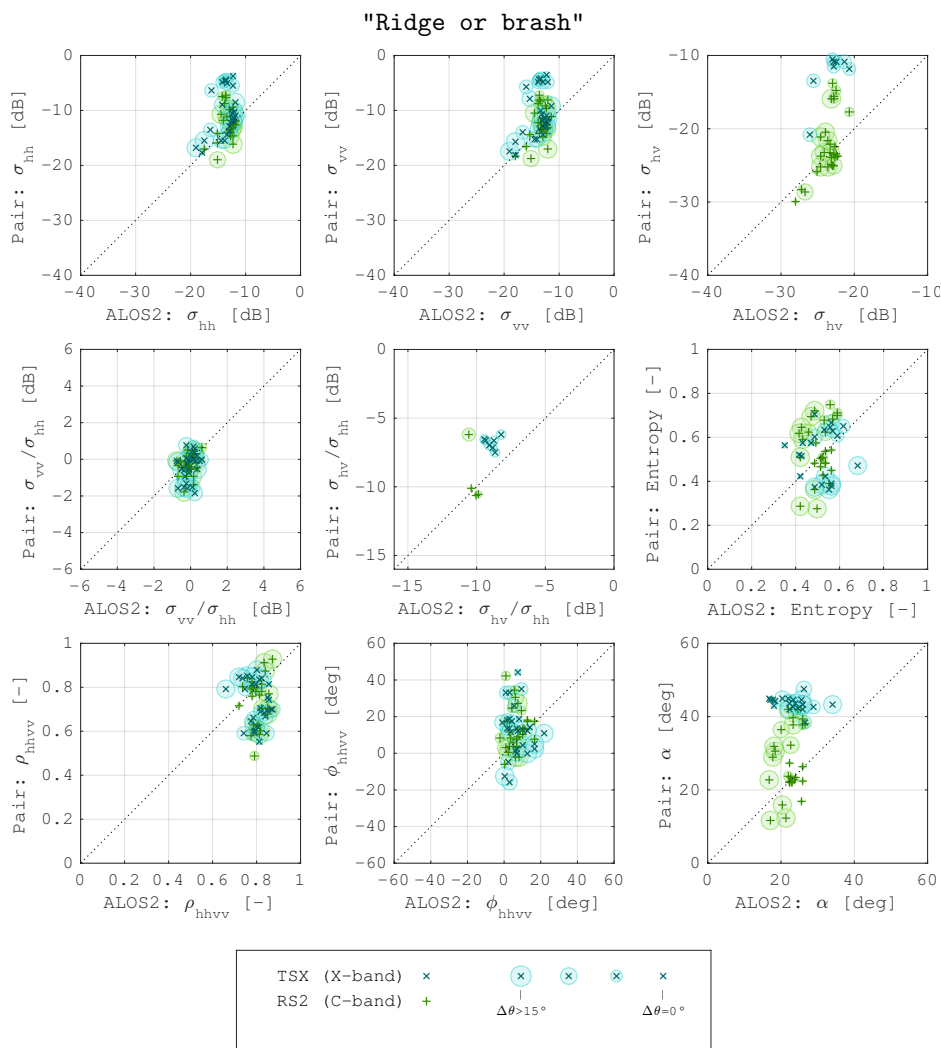
Figure 6.12: The differences between paired polygons tagged as "ridge or brash". Each tick corresponds to the median value of one polygon. The colour and size of the markers indicate sensor and incidence angle difference, respectively (see legend).

be caused by differences in wind conditions, although as seen in figure 6.15, the wind speeds recorded at RV Lance are generally similar at the Radarsat-2 and ALOS-2 acquisitions, except for overlap 2. However, the polygons showing the largest difference between the two sensors originate from overlaps 3 to 5. Another explanation could be that a thin layer of frazil ice in the water suppresses short surface waves and consequently Bragg waves in the C-band wavelength range. This is discussed in more detail in chapter 7.

The co-polariserd ratio is above 0 dB for all polygons except a few from TerraSAR-X. This may indicate dominant Bragg scattering for Radarsat-2 and ALOS-2, which is expected from a wind roughened sea surface. ALOS-2 yield the highest ratios, up to 5.9 dB. The hv-channel is very low for all polygons. It is significantly above the NESZ only for ALOS-2.

The co-polarised phase difference is close to zero for all polygons with a significant SNR. This is expected if surface scattering at the air-water interface dominates. The co-polarised correlation coefficient is large, also as expected if surface scattering dominates. Only the noisy polygons show low correlation.

Considering the scattering entropy and alpha angle, noisy polygons generally show high entropies, as expected. The entropies are relatively low for ALSO-2, below 0.4 in all examples except one. Radarsat-2 show slightly larger entropies, but still below 0.6 for the less noisy polygons. While these values are relatively low, they are not insignificant which could indicate that surface scattering is not the only dominant scattering mechanism, or that the polygons contain large texture variations within the multi-look window (4×4 pixels). Only two quad-polarised examples were found for TerraSAR-X: one close to the NESZ and hence with a large entropy and one less noisy polygon with a lower entropy. The situation is similar for the alpha angles: the largest values are associated to a low SNR, relatively small angles are observed for ALOS-2 and larger ones for Radarsat-2 and TerraSAR-X.

Lead ice

The polygons tagged as "lead ice" are plotted in figure 6.6. As for open water, the range of values of the radar cross sections is wide. The co-polarised channels vary between the NESZ and about -10 dB for Radarsat-2 and TerraSAR-X. The backscatter in the ALOS-2 images are generally lower, but reaches up to -15 dB in some examples. In the difference plots shown in figure 6.10, all pairs have a higher backscatter for Radarsat-2 and TerraSAR-X than for ALOS-2. In some examples, the difference is larger than 15 dB. The co-polarised ratio is however generally larger for ALOS-2 than the other sensors, with up to 6 dB in difference.

The cross-polarised channel is close to the NESZ for most polygons. For TerraSAR-X, which has a relatively high noise floor, all polygons have essentially

zero SNR. The cross-polarised channel is on average higher for Radarsat-2 than for ALOS-2, with a few points as high as about -22 dB.

The co-polarised correlation coefficient is high for most polygons with a high SNR. Some exceptions exist for ALOS-2, with a relatively high SNR yet low coefficient below 0.4. In most polygon pairs, the correlation coefficient is higher for Radarsat-2 and TerraSAR-X compared to ALOS-2 (see figure 6.10).

The co-polarised phase difference varies considerably between the polygons in all sensors, but with a bias towards positive phase shifts. This is interesting, since the model configurations in chapter 5 typically yield negative shifts. For the examples with a relatively high SNR, both Radarsat-2 and ALOS-2 show shifts up to 40°. The shifts for TerraSAR-X are typically lower.

The scattering entropy and alpha angle are highly variable, especially for Radarsat-2 and ALOS-2. For many polygons, the large entropy values can be explained by a low SNR, yet some points have relatively high values despite being significantly above the noise floor. This may indicate that the scattering mechanism is somewhat complicated and not simply the result of a single rough interface or similar. This is in addition indicated by the relatively high values of the alpha angle. Both the entropy and alpha angle is generally higher for ALOS-2 as seen in the difference plot in figure 6.10.

Ice floe

In figure 6.7 the polygons tagged as "ice floe" are shown. Compared to lead ice the variation among polygons is smaller. The co-polarised channels are most variable for TerraSAR-X where the highest are recorded at about -7 dB. Most polygons for TerraSAR-X do however have a steeper incidence angle than for the other sensors. Considering the difference plots in figure 6.11, the backscatter is higher for Radarsat-2 and TerraSAR-X compared to ALOS-2.

The co-polarised ratio is centred around 0 dB for the most part, also for ALOS-2 (in contrast to the lead ice polygons where it was up to 4 dB in some examples). The co-polarised correlation coefficient is generally high. All examples with a coefficient below 0.6 are noisy for TerraSAR-X and Radarsat-2. There are however some ALOS-2 polygons with a coefficient below 0.5 yet with a relatively high SNR.

The co-polarised phase difference varies considerably with a bias towards positive values, as was also seen for the lead ice. All sensors include polygons with positive shifts above 20°, still with a high SNR. The values for the scattering entropy and alpha angle are generally lower compared to the lead ice polygons. The TerraSAR-X polygons are generally noisy.
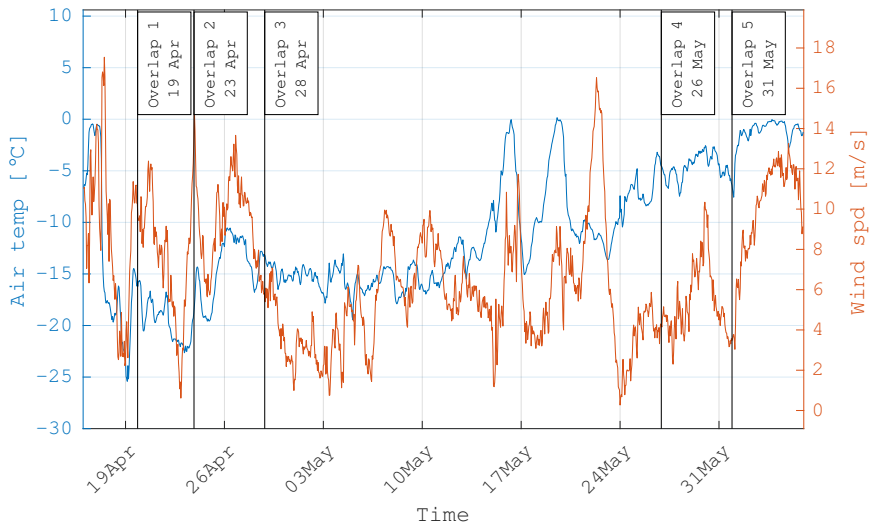
Figure 6.13: Air temperatures and wind speeds recorded at RV Lance. During the plotted time interval, the ship was drifting with the sea ice. The dates for the five overlapping scene sets are indicated by vertical lines. The data is averaged over 1 hour to reduce short term fluctuations.

Ridge or brash

Despite being the least defined polygon type in terms of identifying what type of ice it actually represents, the polygons tagged as "ridge or brash" is the least variable, as seen in figure 6.8. The co-polarised channels are generally very high, up to -3 to -4 dB for TerraSAR-X. All pairs have a higher or similar backscatter for Radarsat-2 and TerraSAR-X compared to ALOS-2, as seen in the difference plot in figure 6.12. The cross polarised channel is also generally high, but lowest for ALOS-2.

The co-polarised ratio is mostly close to 0 dB. The co-polarised correlation coefficient is also high, with only a few cases below 0.6 for TerraSAR-X. The co-polarised phase difference however, varies considerably and most so in X-band. The entropy is generally in the range between 0.4 to 0.7 and similar among the three sensors. The alpha angle is however significantly different between ALOS-2 and TerraSAR-X, where the latter have angles above 40°. Apart from one polygon for Radarsat-2, both the Radarsat-2 and ALOS-2 polygons are around 20°in alpha angle.

6.3   Environmental conditions

During the N-ICE 2015 expedition, large amounts of ground based data of various sorts were collected in addition to the remote sensing data presented in the previous section. Here, the meteorological data recorded at the research vessel RV Lance is presented (Hudson et al. 2015, for details), which will aid in the interpretation of the SAR data.

Specifically, air temperature, air humidity, air pressure, sea water temperature, wind speed and wind direction were recorded continually. While these parameters all are important, the air temperature and wind speed are highlighted here (the other parameters are presented in appendix C). The former affects the ice temperature, which in turn modulates the amount of liquid water and brine in the sea ice. The latter affects the ice formation process (see section 3.3) and also roughens water surfaces, thus increasing the radar backscatter.

The wind speed was recorded every second and the air temperature every 34 seconds. In order to reduce short term fluctuations that are not consistent over larger areas, the data is averaged over 1 hour. In figure 6.13, the air temperature and wind speed are plotted together over a period for which RV Lance was passively drifting with the ice pack (corresponding to drift period 3 in figure 6.1). This period covers all overlapping scenes of table 6.1, which are indicated by vertical lines in the plot. In the following, the air temperature and wind speed will be discussed in more detail for the individual overlaps.

Air temperature

Considering figure 6.13, two warm periods were recorded with temperatures up to $0°C$ that may have caused melting (around the 16th and 19th of May, respectively). Otherwise, freezing degrees were recorded over the entire time interval with a general increasing temperature trend.

In figure 6.14, more detailed plots of the air temperatures are shown individually for the five overlapping SAR scene sets. The acquisition times of the scenes are indicated by vertical lines with corresponding temperatures stated in the plot. The temperatures are generally lower for the scenes from April (overlap 1, 2 and 3), varying from roughly -25°C to -15°C, compared to the scenes from May (overlap 4 and 5), with temperatures around -5°C. The temperatures fluctuate mostly during overlap 1 and 2, with a maximum-minimum difference of 11°C and 8°C, respectively. In overlaps 3 to 5, the temperatures are relatively stable and vary within 5°C.
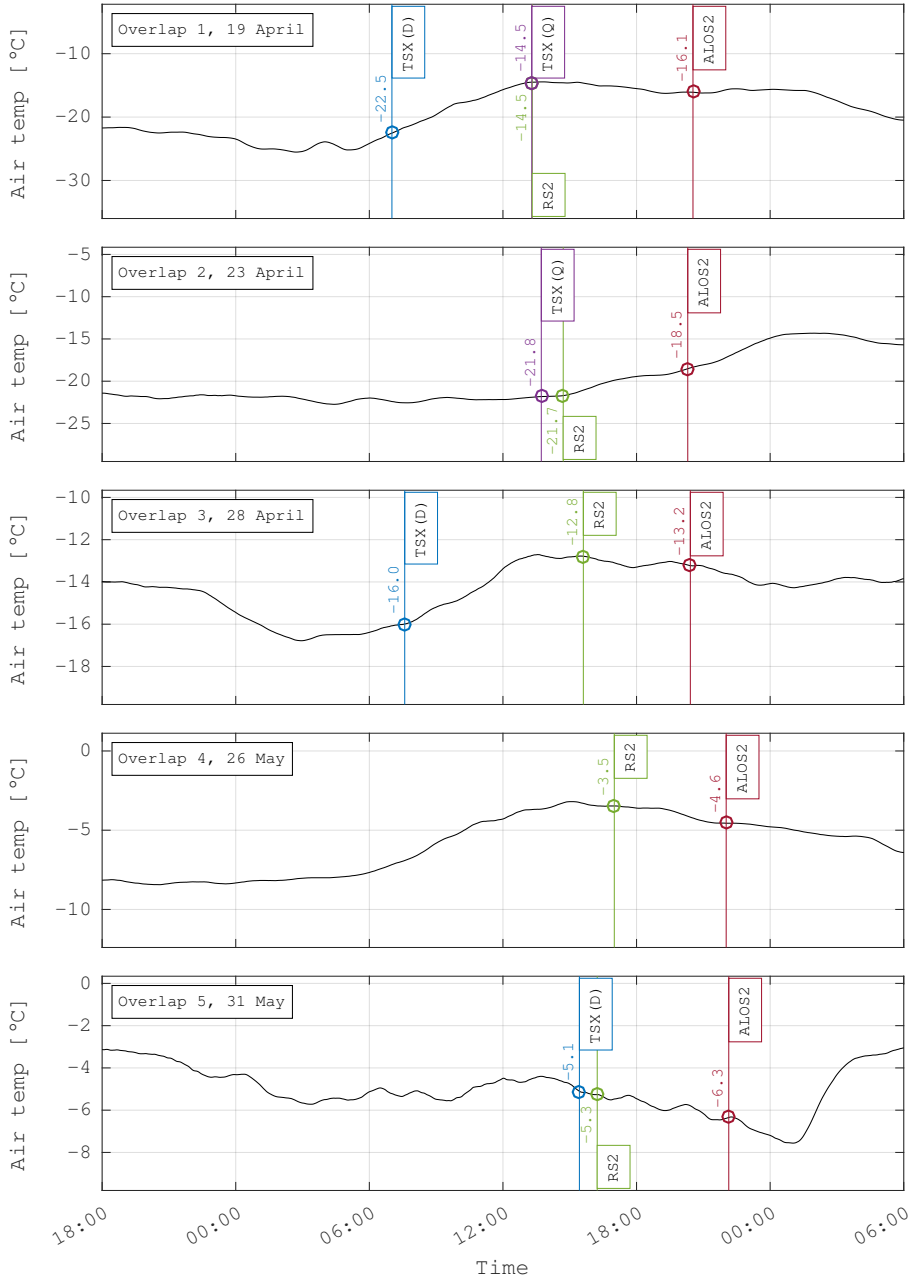
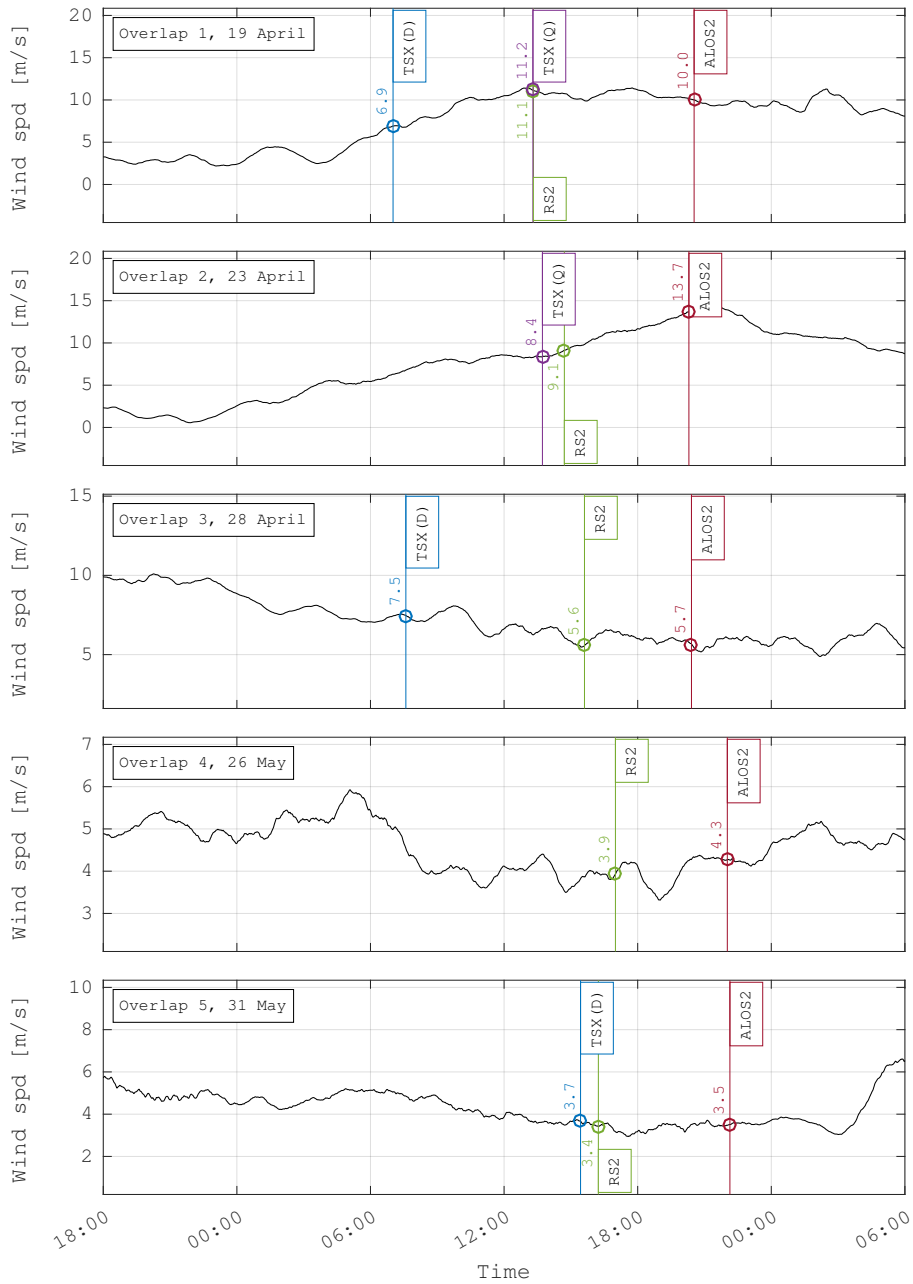Figure 6.14: Air temperatures at RV Lance during the five overlaps of table 6.1. The values are averaged over 1 hour.

Figure 6.15: Wind speed at RV Lance during the five overlaps of table 6.1. The values are averaged over 1 hour.

"Lead ice"

Layer	Effective medium	Top surface correlation	Background medium	Inclusion medium	Inclusion shape
0	Air	-	Air	-	-
1	Brine wetted snow	GPL	Dry snow	Brine	Spherical
2	Sea ice	GPL	Pure ice	Brine	Ellipsoidal
3	Sea water	Gaussian	Sea water	-	-

"Ice floe"

Layer	Effective medium	Top surface correlation	Background medium	Inclusion medium	Inclusion shape
0	Air	-	Air	-	-
1	Dry snow	GPL	Air	Pure ice	Spherical
2	Brine wetted snow	GPL	Dry snow	Brine	Spherical
3	Sea ice	GPL	Pure ice	Brine	Ellipsoidal
4	Sea water	Gaussian	Sea water	-	-

Table 6.2: Above are the considered layer configurations for simulating the data tagged as "lead ice" and "ice floe", respectively. The tables indicate what correlation function is used for characterising the top interface of each layer and what background and inclusion materials are considered (see sections 5.3.1 to 5.3.4 for details about these).

Wind speed

Again considering figure 6.13, the hourly mean wind speed fluctuates considerably over the time interval covering all overlaps, from around 0 to 17 m/s. The wind speeds at the individual overlaps are further shown in figure 6.15. The highest values were recorded in overlap 1 and 2, with mean wind speeds up to 12 to 14 m/s. The values do however vary considerably over the plotted 36 hours, at times down to only a few m/s. Overlaps 3 to 5 show lower wind speeds and also less fluctuations over the plotted 36 hours.

6.4   Polarimetric backscatter simulation

The layer-stacking method described in chapter 5 will now be used to simulate the backscatter and compare it to the polygons described in the previous sections. In summary, the model is built up by an arbitrary number of layers that are stacked incoherently. Each layers may have a rough top surface, described by the

"Lead ice"

Model input parameter	Min.	Max.	Unit
Brine wetted snow:			
Thickness	1	30	cm
Density	300	500	kg/m^3
Salinity	20	60	ppt
Brine droplet cor. length (l_{bs})	0.01	1	mm
RMS height (σ_{zbs})	0.1	10	mm
RMS slope (σ_{sbs})	0	0.3	
Sea ice:			
Thickness	10	40	cm
Salinity	7	15	ppt
Brine pocket cor. length (l_{si})	0.01	1	mm
Brine pocket anisotropy (-)	1	4	-
Brine pocket tilt (ψ_{si})	0	90	$^\circ$
RMS height (σ_{zsi})	0.1	100	mm
Surface slope (σ_{ssi})	0	0.3	
Sea water:			
RMS height (σ_{zsi})	0.1	2	mm
Surface slope (σ_{ssi})	0	0.05	

Table 6.3: The sampling limits for simulating lead ice.

"Ice floe"

Model input parameter	Min.	Max.	Unit
Dry snow:			
Thickness	10	80	cm
Density	200	400	kg/m^3
Snow grain cor. length (l_{ds})	0.1	1	mm
RMS height (σ_{zds})	0.1	10	mm
RMS slope (σ_{sds})	0	0.3	-
Brine wetted snow:			
Thickness	1	10	cm
Density	300	500	kg/m^3
Salinity	10	20	ppt
Brine droplet cor. length (l_{bs})	0.01	1	mm
RMS height (σ_{zbs})	0.1	10	mm
RMS slope (σ_{sbs})	0	0.3	
Sea ice:			
Thickness	20	200	cm
Salinity	1	15	ppt
Brine pocket cor. length (l_{si})	0.01	1	mm
Brine pocket anisotropy (-)	1.5	4	-
Brine pocket tilt (ψ_{si})	0	90	$^\circ$
RMS height (σ_{zsi})	0.1	100	mm
Surface slope (σ_{ssi})	0	0.3	
Sea water:			
RMS height (σ_{zsi})	0.1	20	mm
Surface slope (σ_{ssi})	0	0.3	

Table 6.4: The sampling limits for simulating ice floe.

IIEM or GOM (depending on roughness scale relative to the radar wavelength, see section 4.1 for details) and a volume containing inclusions as described by the N2M (see section 4.2.2). The surface and volume scattering contributions are computed separately and added incoherently. A more detailed description of the layer-stacking method can be found in section 5.2.

6.4.1   Model configurations

Since the model is not intended for deformed ice or open water, the polygons tagged as "ridge or brash" and "open water" are correspondingly disregarded in the comparison, leaving those tagged as "lead ice" and "ice floe" up for consideration. Lead ice is modelled as a thin sea ice layer with a relatively high salinity covered by a thin layer of brine-wetted snow. Such wetted snow layers were frequently observed during N-ICE 2015 (Merkouriadi et al. 2017). The ice floe configuration contains a dry snow layer, a brine wetted snow layer and a sea ice layer. In both configurations, interface roughness is described by the GPL correlation function (with $p = 2.1$), except for the ice-water interface which is believed to have a smoother characteristic and therefore described by the Gaussian correlation function. Details about how the different layers are parametrised can be found in section 5.3, but an overview is shown in table 6.2.

6.4.2   Monte-Carlo sampling

The comparison between the model configurations and the SAR data contained in the polygons is based on Monte Carlo sampling. Specifically, the model input parameters are sampled uniformly between an upper and lower limit and the corresponding model output samples are compared to the data. The sampling limits for the model input parameters are shown in table 6.3 for the lead ice configuration and in table 6.4 for the ice floe configuration. While it is hard to argue for specific input limits without detailed, co-incident and co-located in-situ measurements, observations from the N-ICE 2015 campaign can be used to set plausible limits.

Specifically, the limits on the air temperature are based on data from the ship log of RV Lance, as presented in section 6.3 (Hudson et al. 2015, for details). The limits on ice and snow thickness, sea ice salinity and snow density are based on detailed measurements that were made at the research camp close to the ship. Specifically, ice core, snow pit and magna-probe measurements as well as ground based electromagnetic sounding measurements are considered (Gallet et al. 2017, Merkouriadi et al. 2017, Gerland et al. 2017, Rösel & King 2017). For the ice thickness limits, additional data from an airborne electromagnetic sounding instrument are also taken into account (Rösel et al. 2018), which yield information over considerably larger areas than those from the research camp

around RV Lance. While these in-situ observations were not collected at the specific polygons of consideration, but a few to about a hundred kilometres away (depending on particular polygon), they are extensive and thus believed to yield a good indication on the general ice conditions for the region.

Some input parameters, such as correlation lengths of snow grains and brine pockets, or roughness parameters at the layer interfaces, are notoriously difficult to measure in the field. Indeed, quantitative measurements of small scale roughness, snow grains or brine pockets are limited from N-ICE 2015, thus corresponding limits are based on field and laboratory measurements found in the literature. Specifically, limits on the roughness parameters are based on Fung & Eom (1982) and Johansson (1988) and limits for the correlation lengths of snow grains and brine pockets are based on Perovich & Gow (1991), Nghiem et al. (1990) and Proksch et al. (2015).

6.4.3   Addative noise

In order to realistically simulate the SAR data, system noise cannot be neglected. This is therefore incorporated into the model as an additive term with uncorrelated polarimetric channels, such that the diagonal elements of the total simulated covariance matrix $C_{ppqq}^{(tot)}$ are:

$$C_{ppqq}^{(tot)} = C_{ppqq}^{(model)} + C_{ppqq}^{(noise)} \qquad (6.1)$$

where p and q indicate polarisation, $C_{ppqq}^{(model)}$ is the noise-free model and $C_{ppqq}^{(noise)}$ is the noise term. The noise is chosen according to the sensor specifications for Radarsat-2 and TerraSAR-X but is manually estimated for ALOS-2 (see section 6.2.4).

6.5   Results

The results of the Monte Carlo simulation described in section 6.4 are now presented and analysed. Specifically, the model input limits listed in tables 6.3 and 6.4 are used for uniform random sampling of the model input parameters. In the next two sections, the model output samples are compared to the polygons based on (1) visual comparison and (2) a distance measure between model output samples and polygon data samples.
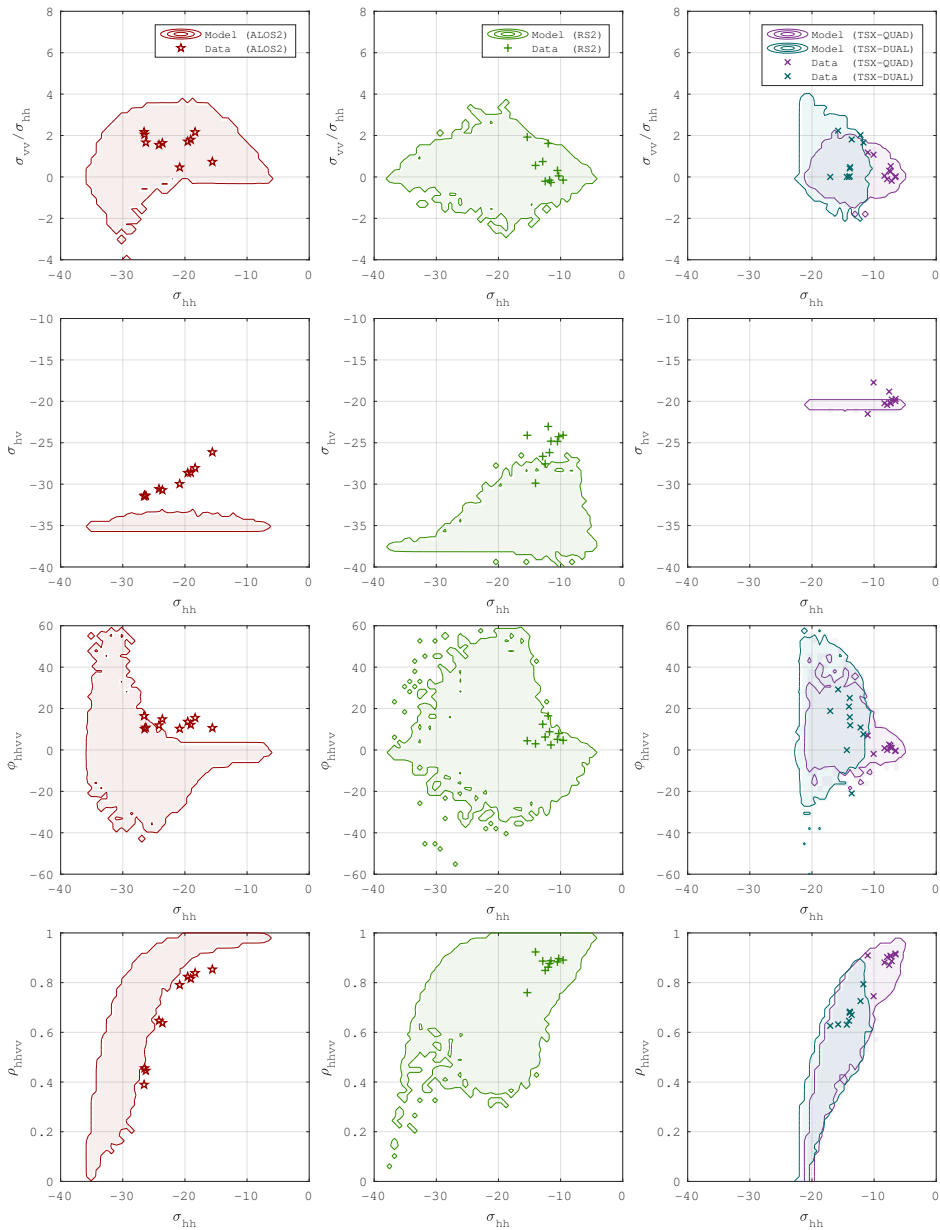
Figure 6.16: Model output and data polygons tagged as "lead ice" in overlap 1 are compared per polarimetric feature. The hh-channel is chosen on the x-axis for all plots.
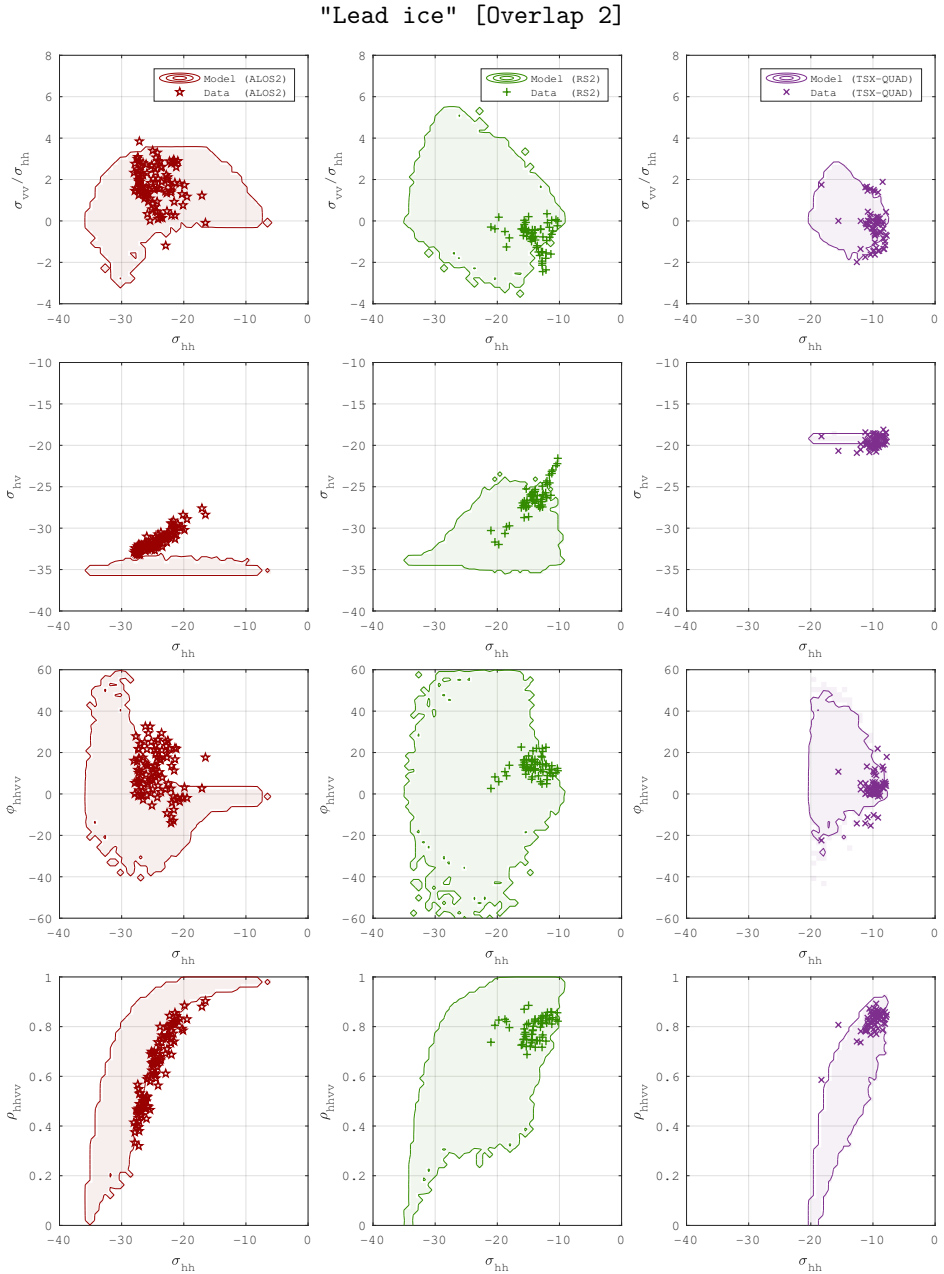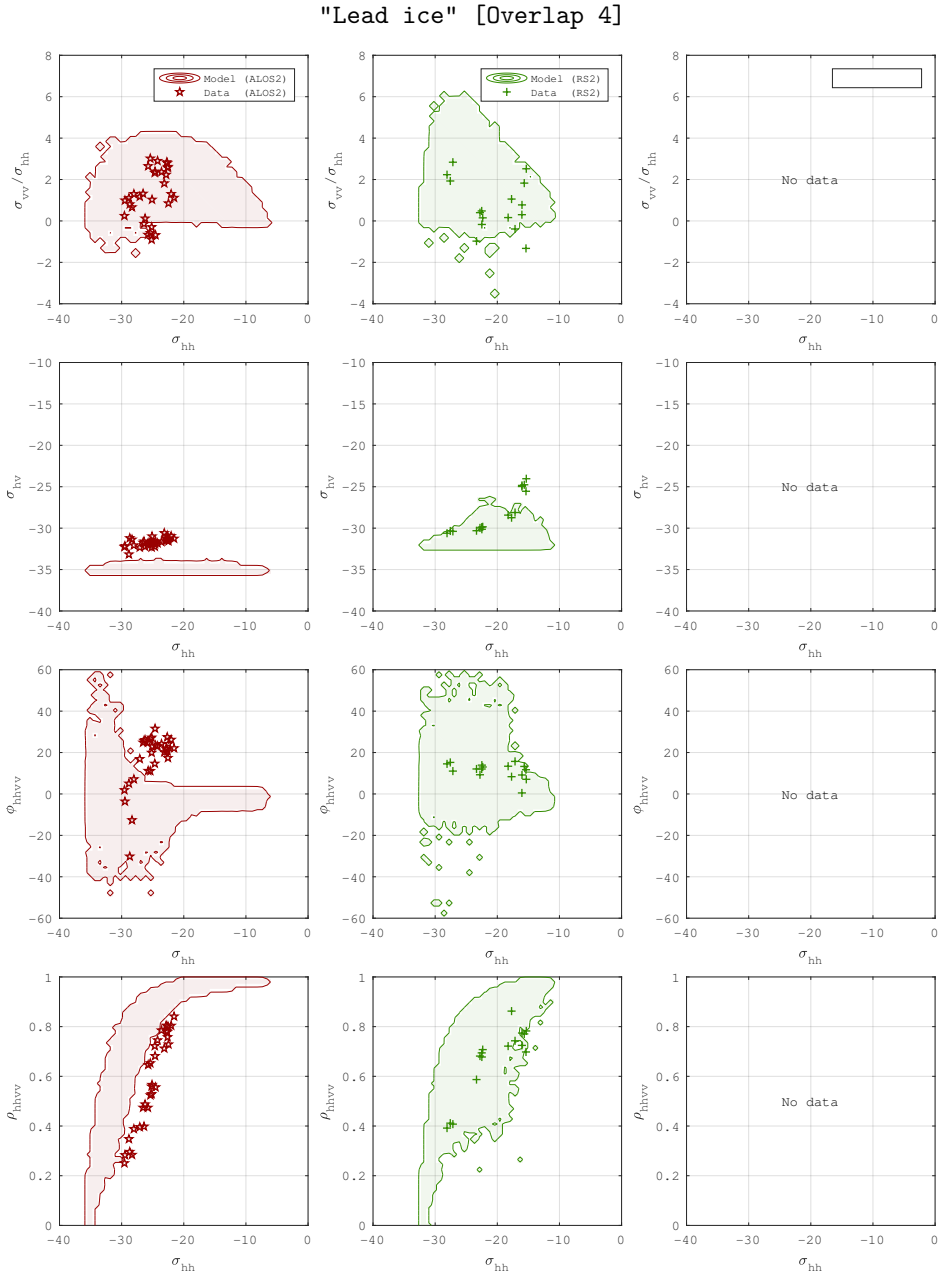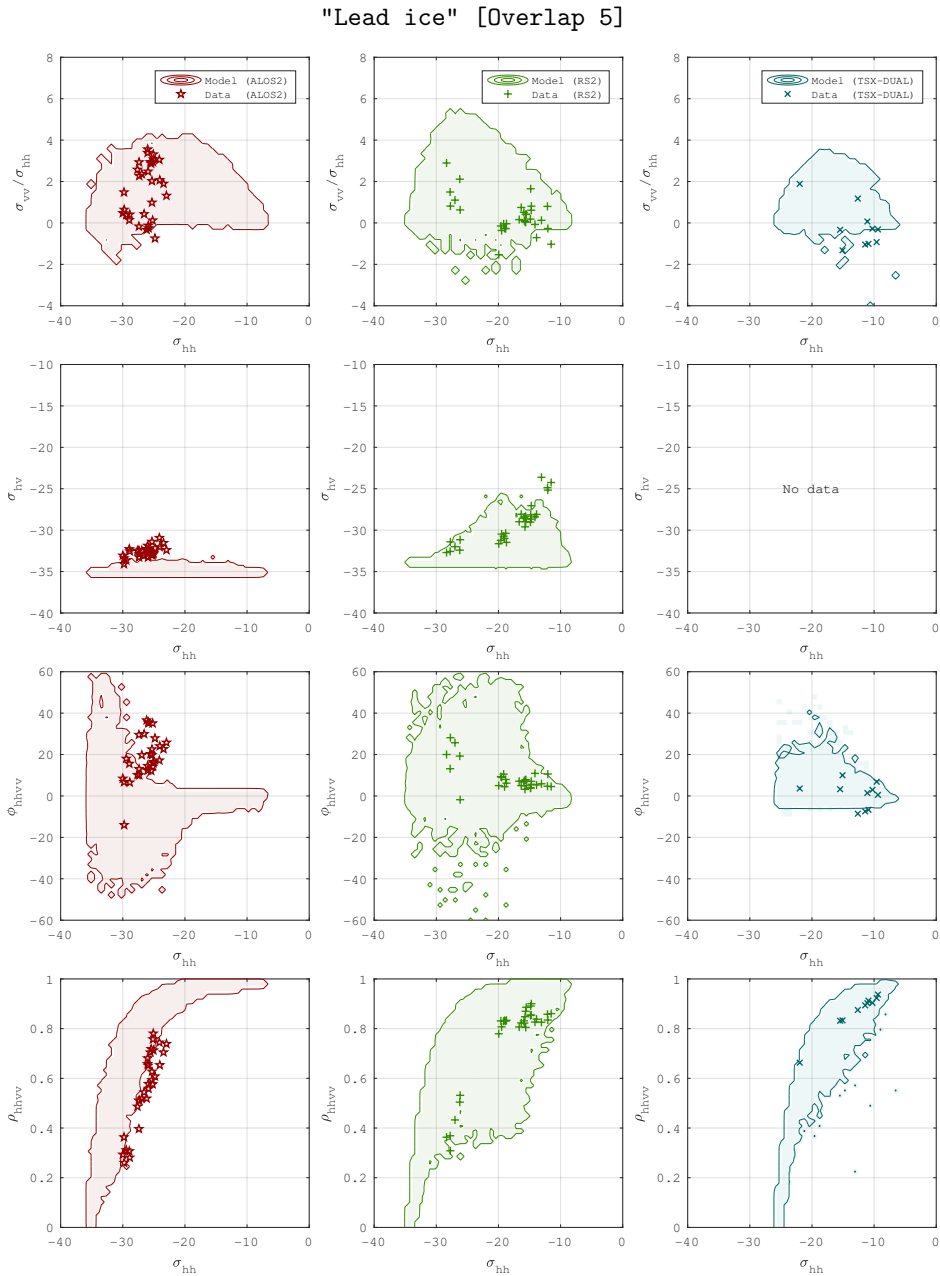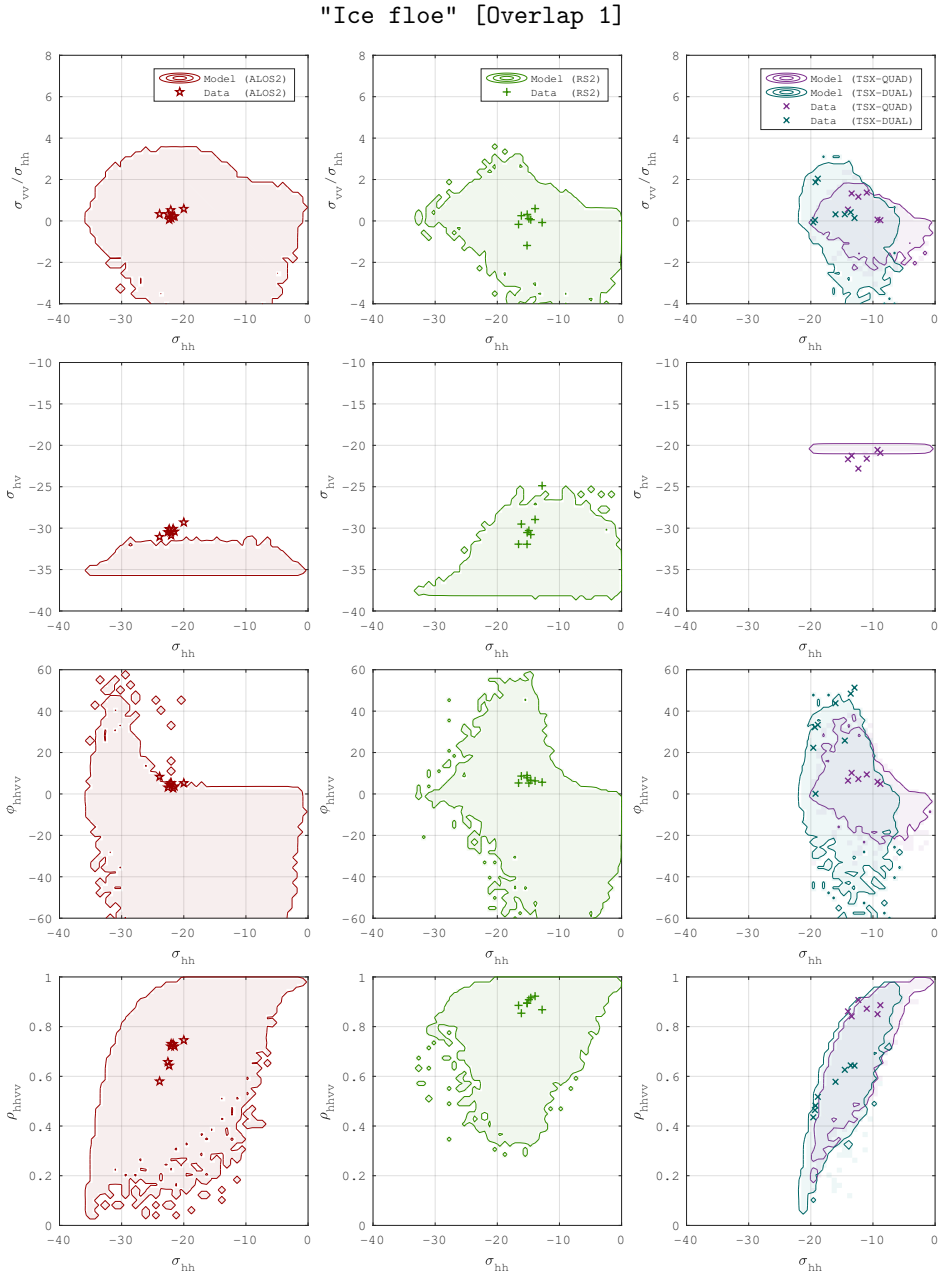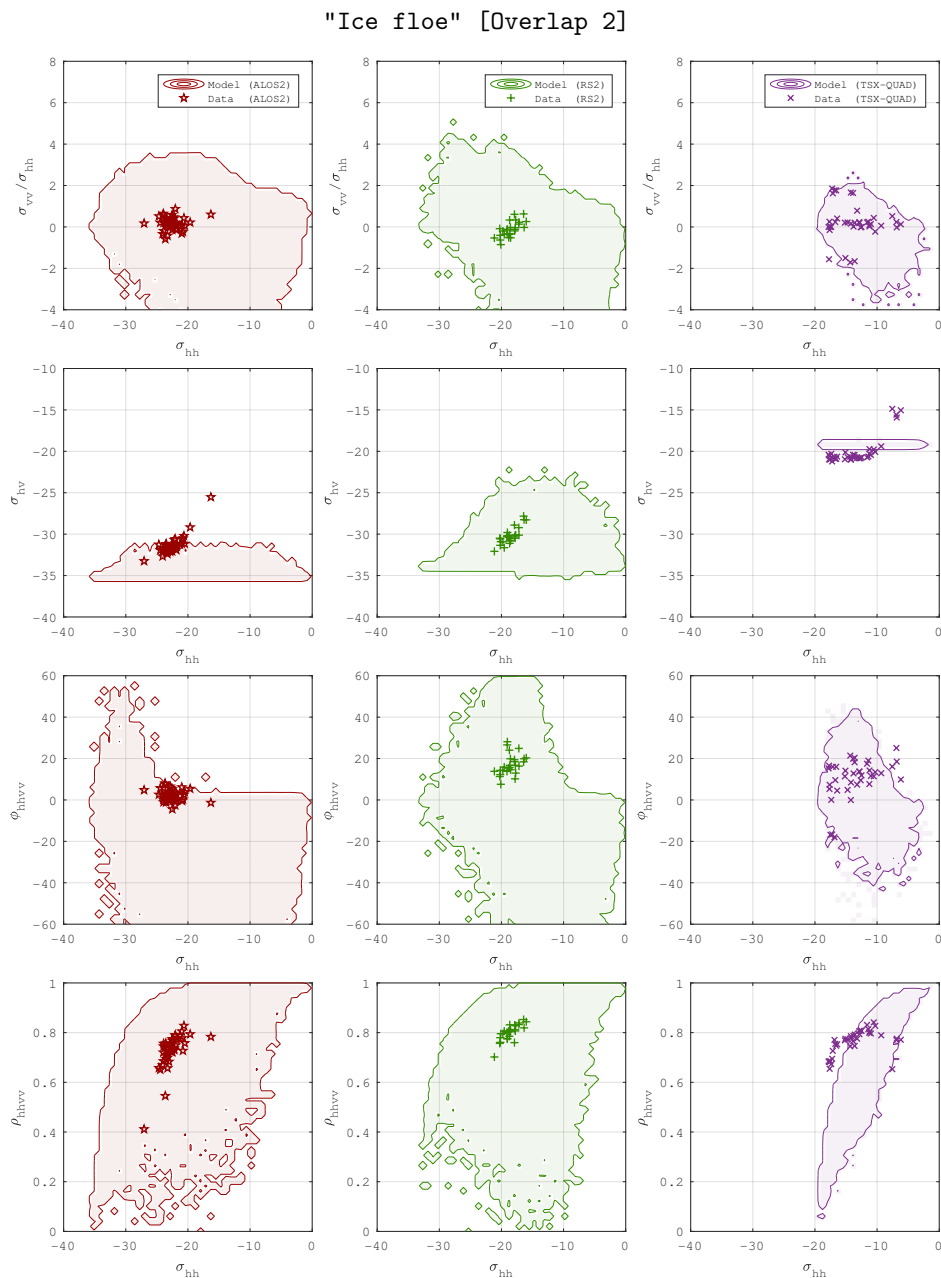
Figure 6.17: Model output and data polygons tagged as "lead ice" in overlap 2 are compared per polarimetric feature. The hh-channel is chosen on the x-axis for all plots.
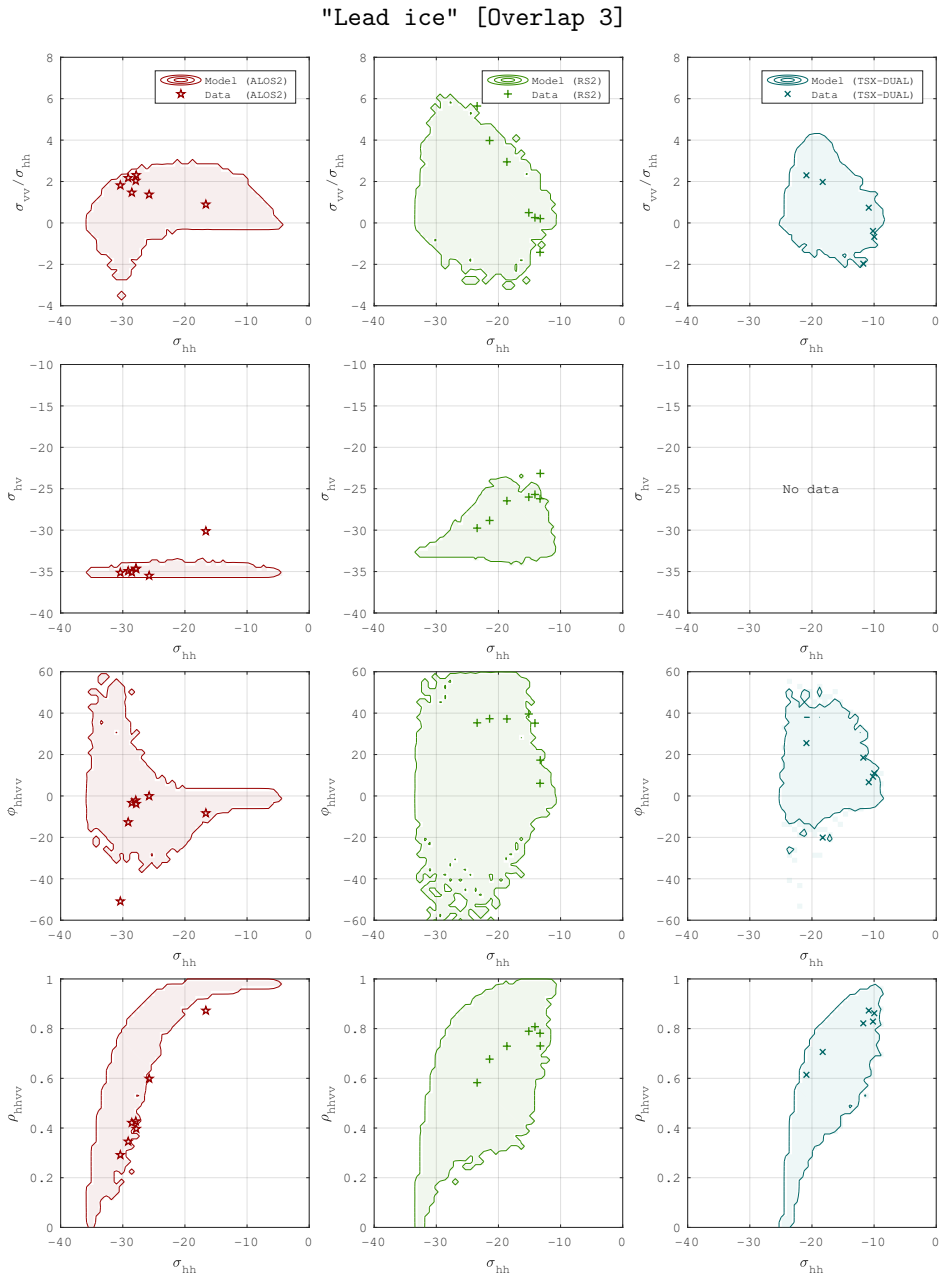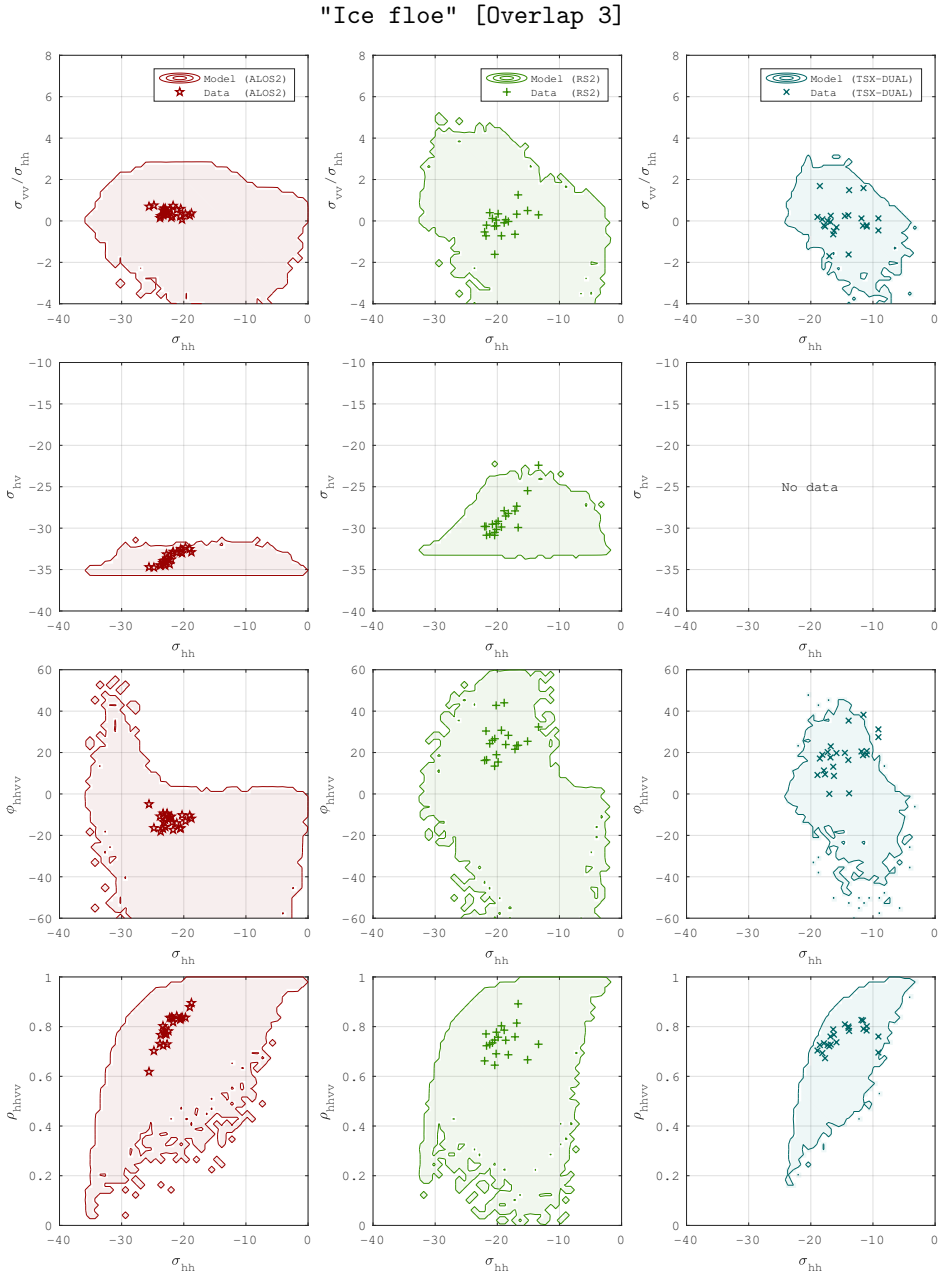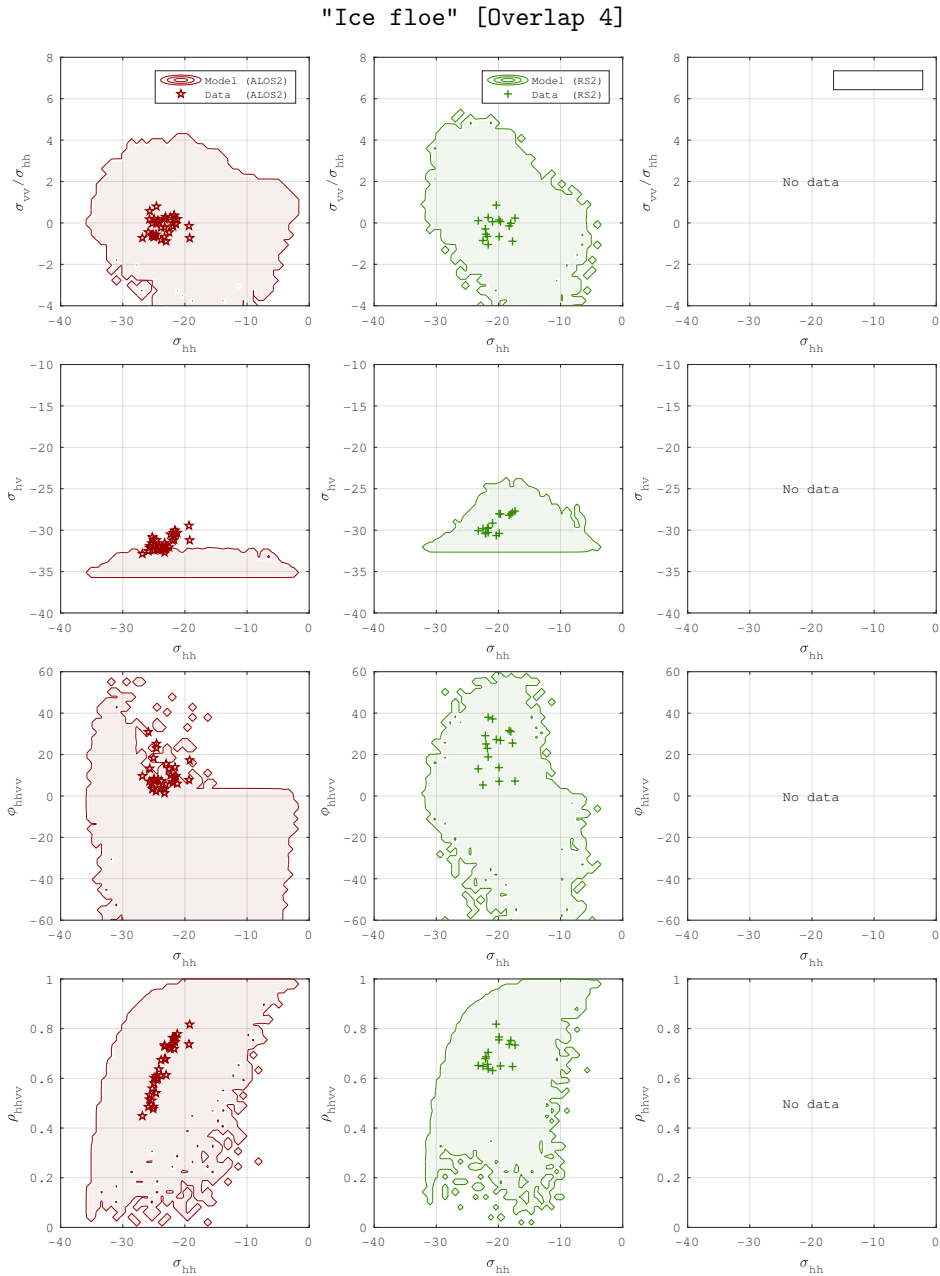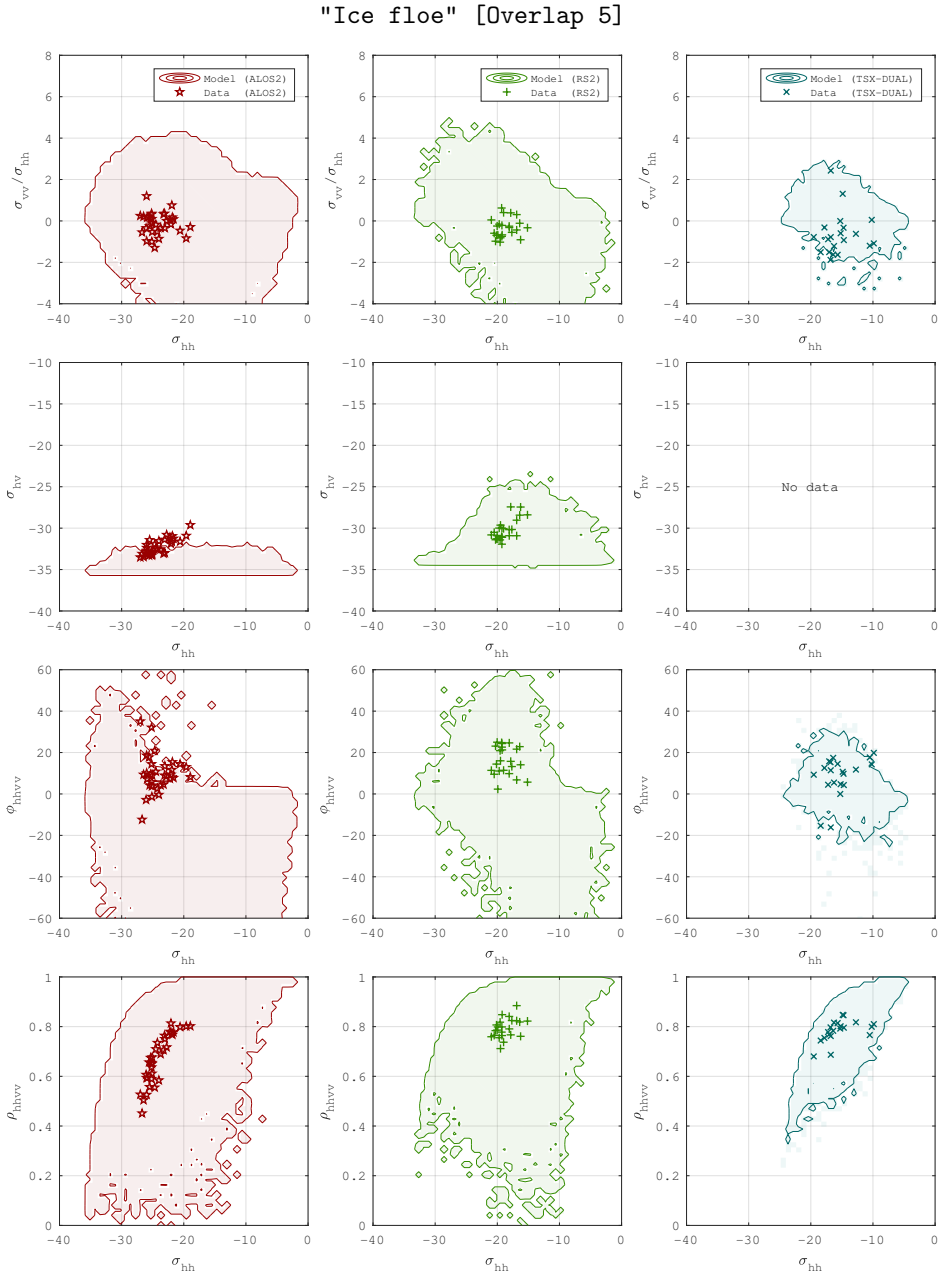
Figure 6.18: Model output and data polygons tagged as "lead ice" in overlap 3 are compared per polarimetric feature. The hh-channel is chosen on the x-axis for all plots.

Figure 6.19: Model output and data polygons tagged as "lead ice" in overlap 4 are compared per polarimetric feature. The hh-channel is chosen on the x-axis for all plots.

Figure 6.20: Model output and data polygons tagged as "lead ice" in overlap 5 are compared per polarimetric feature. The hh-channel is chosen on the x-axis for all plots.

"Ice floe" [Overlap 1]

Figure 6.21: Model output and data polygons tagged as "ice floe" in overlap 1 are compared per polarimetric feature. The hh-channel is chosen on the x-axis for all plots.

Figure 6.22: Model output and data polygons tagged as "ice floe" in overlap 2 are compared per polarimetric feature. The hh-channel is chosen on the x-axis for all plots.

Figure 6.23: Model output and data polygons tagged as "ice floe" in overlap 3 are compared per polarimetric feature. The hh-channel is chosen on the x-axis for all plots.

"Ice floe" [Overlap 4]

Figure 6.24: Model output and data polygons tagged as "ice floe" in overlap 4 are compared per polarimetric feature. The hh-channel is chosen on the x-axis for all plots.

Figure 6.25: Model output and data polygons tagged as "ice floe" in overlap 5 are compared per polarimetric feature. The hh-channel is chosen on the x-axis for all plots.

6.5.1   Visual comparison

For visual comparison, the model output is computed and expressed in terms of the following polarimetric parameters:

$$
Y = \begin{cases}
10\log_{10}(\sigma_{hh}) \\
10\log_{10}(\sigma_{vv}/\sigma_{hh}) \\
10\log_{10}(\sigma_{hv}) \\
\phi_{hhvv} \\
\rho_{hhvv}
\end{cases}
\tag{6.2}
$$

The output parameters in equation 6.2 are considered pairwise to form 2D-histograms of 50×50 bins. Bins containing one or more output sample are highlighted by a colour such that regions in the polarimetric output space are formed, in which the model is able to produce a plausible prediction (given the limits of the input parameters). By default, all 2D-histograms use the hh-channel on the x-axis and one of the other polarimetric parameters of equation 6.2 on the y-axis. By inserting the polygon data samples in the same plot, the overlap between model and data is illustrated.

The plots for the respective overlapping scene sets are shown in figures 6.16 to 6.20 for the lead ice class and in figures 6.21 to 6.25 for the ice floe class. It can be seen that when considering the output parameters pairwise, the models generally overlap well with the data samples. The main exceptions are the cross-polarised channel and the co-polarised phase difference, primarily for ALOS-2 in the lead ice class. Specifically, the simulated hv-channel is generally too low and the simulated phase difference is generally too small or has the wrong sign. It is moreover interesting to note that the modelled output regions generally cover a considerable part of the shown 2D output spaces.

6.5.2   Model-data distance

Note that the (coloured) model regions shown in figures 6.16 to 6.25 represent 5-dimensional regions in the full polarimetric output space (defined by the output parameters in equation 6.2). This means that if all polarimetric parameters are considered at the same time, the data samples may not necessarily be confined in the 5-dimensional regions. To obtain a more quantitative measure of how well the polygon data samples overlap with the model output, a distance measure will now be considered.

A simple distance measure

Denote a polygon data sample in the polarimetric output space by $\mathbf{y}_i^d$ and a model output sample by $\mathbf{y}^m(\mathbf{x}_j)$, where $\mathbf{x}_j$ is the corresponding model input sample (containing all geophysical input parameters of the model). The displacement between the data and model samples is:

$$\mathbf{d}_{ij} = \mathbf{y}_i^d - \mathbf{y}^m(\mathbf{x}_j) \qquad (6.3)$$

Indeed, the Euclidian norm $|\mathbf{d}_{ij}|$ can readily be regarded as a measure of how well the model sample $\mathbf{y}^m(\mathbf{x}_j)$ matches with the data sample $\mathbf{y}_i^d$. However, since the data samples are accompanied with noise and calibration uncertainties, the displacement should be weighed accordingly. Specifically, if say the hh-channel is certain to 1 dB, but the co-polarised phase difference is certain to 5°, a 1° offset in the phase should not be weighed the same as a 1 dB offset in the hh-channel. Consider therefore the distance:

$$D_{ij} = \sqrt{\mathbf{d}_{ij}^{\mathrm{T}} \bar{\boldsymbol{\Sigma}}^{-1} \mathbf{d}_{ij}} \qquad (6.4)$$

where superscript $^{\mathrm{T}}$ denote transpose and scaling is introduced through the matrix $\bar{\boldsymbol{\Sigma}}$. Ideally, the scaling should thus depend on the uncertainty of the data samples, which unfortunately is not provided for all the considered sensors. They are however provided for Radarsat-2 (Slade 2011), for which the radiometric error is specified as 1 dB and the error in polarimetric phase difference as 5°. No information is provided for the co-polarised correlation which was included in the previous section, which therefore will be dropped in the following analysis. This means that a point in the polarimetric output space can be expressed as:

$$\mathbf{y} = \begin{bmatrix} 10\log_{10}(\sigma_{hh}) \\ 10\log_{10}(\sigma_{hv}) \\ 10\log_{10}(\sigma_{vv}) \\ \phi_{hhvv} \end{bmatrix} \qquad (6.5)$$

and the scaling matrix is chosen as:

$$\bar{\boldsymbol{\Sigma}} = \begin{bmatrix} 1 & 0 & 0 & 0 \\ 0 & 1 & 0 & 0 \\ 0 & 0 & 1 & 0 \\ 0 & 0 & 0 & 5 \end{bmatrix}^2 \qquad (6.6)$$

When computing distances according to equation 6.4, deviations in the radar cross sections will thus be measured in units per 1 dB and deviations in co-polarised phase difference in units per 5°.

Next, consider a data sample $\mathbf{y}_i^d$ and denote the distance to the closest model output sample as:

$$D_i = \min_j D_{ij} \qquad (6.7)$$

This minimum distance will be regarded as a measure of how well the model is able to predict the particular data sample $\mathbf{y}_i^d$. Doing so, it should be noted that the model output samples are not distributed uniformly in the output space. Some regions are relatively dense in terms of model output samples, while other regions are relatively sparsely sampled. It should moreover be noted that speckle noise is assumed insignificant in the data samples. Note moreover that even if a data sample is located within a 2D-histogram as shown in figures 6.16 to 6.25, it may have a non-zero distance since the 2D-histograms are discretised into 50×50 bins. Additionally, the polygons from TerraSAR-X are excluded since most of them are acquired in the dual-polarimetric mode and thus lack either one of the co-polarised channels or the cross-polarised channel.

Histograms over the minimum distance according to equation 6.7, considering polygons tagged as lead ice are shown in figure 6.26. Specifically, the top histogram shows the histogram over distances for all polygon pairs, and the lower four plots shows the corresponding deviations per polarimetric parameter. Recall that a distance unit in the top histogram corresponds to a deviation in σ by 1 dB or in co-polarised phase difference by 5°. The green histograms correspond to Radarsat-2 polygons and the red histograms to ALOS-2 polygons.

Considering the top histogram in figure 6.26, it is evident that the ALOS-2 polygons generally deviate more than the Radarsat-2 polygons. In the four lower histograms, it is evident that this is mainly attributed to deviations in the cross-polarised channel and the co-polarised phase difference. For ALOS-2, the former is typically 1-3 dB off, while the latter is up to 25° off. The co-polarised channels are typically well described by the model for both sensors, with most of the deviation being less than 2 dB. For Radarsat-2, the main offsets are in the co-polarised phase difference.

In figure 6.26, the corresponding histograms are shown for polygons tagged as ice floe. Compared to the lead ice class, they are overall very well predicted by the model. The distances are again lower for Radarsat-2. Considering the four lower histograms, it is clear that the deviations are typically larger in the cross-polarised channel, in particular for ALOS-2. The phase shifts are moreover considerably better matched for ALOS-2 in the ice floe class than in the lead ice class.

Combining C- and L-band

For the two types of polygons (lead ice and ice floe) considered above, the models generally agree well with the data when compared per sensor. A valid model
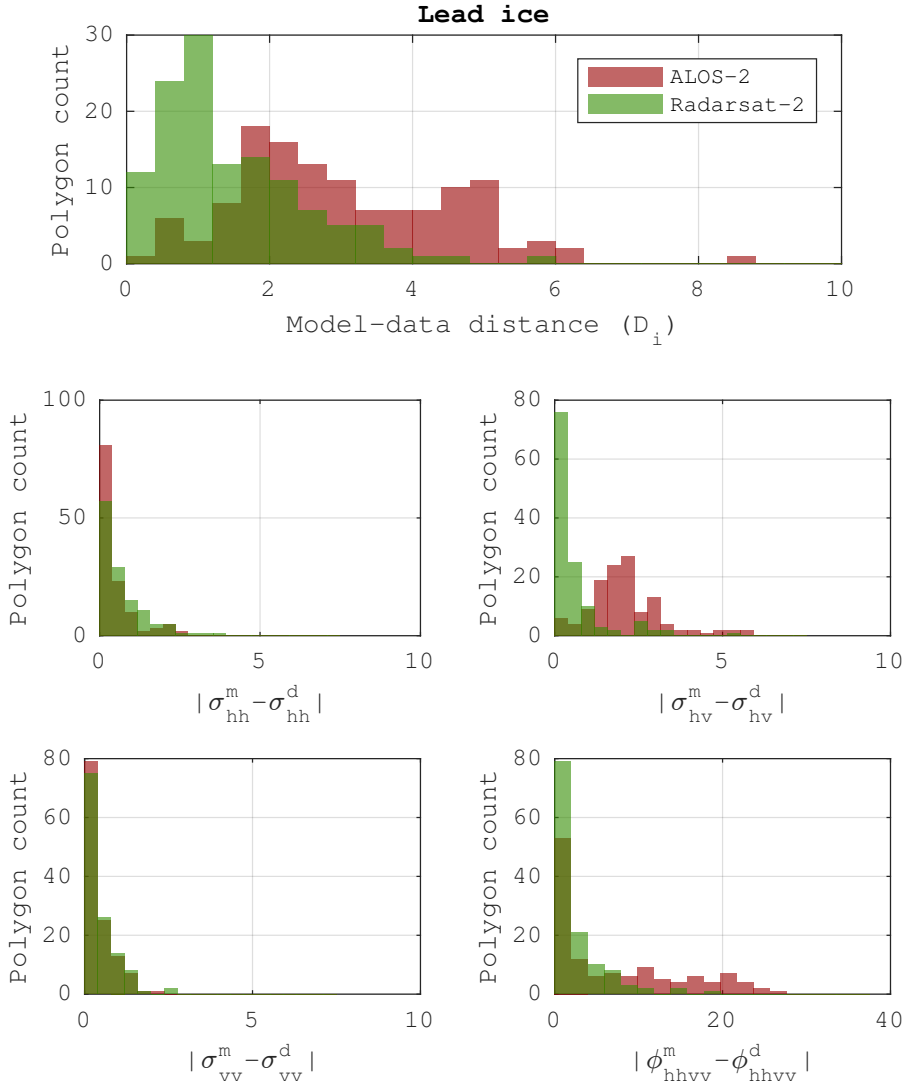
Figure 6.26: Histograms over minimum model-data distances according to equation 6.7 for the lead ice class. 10^5 model samples were used.
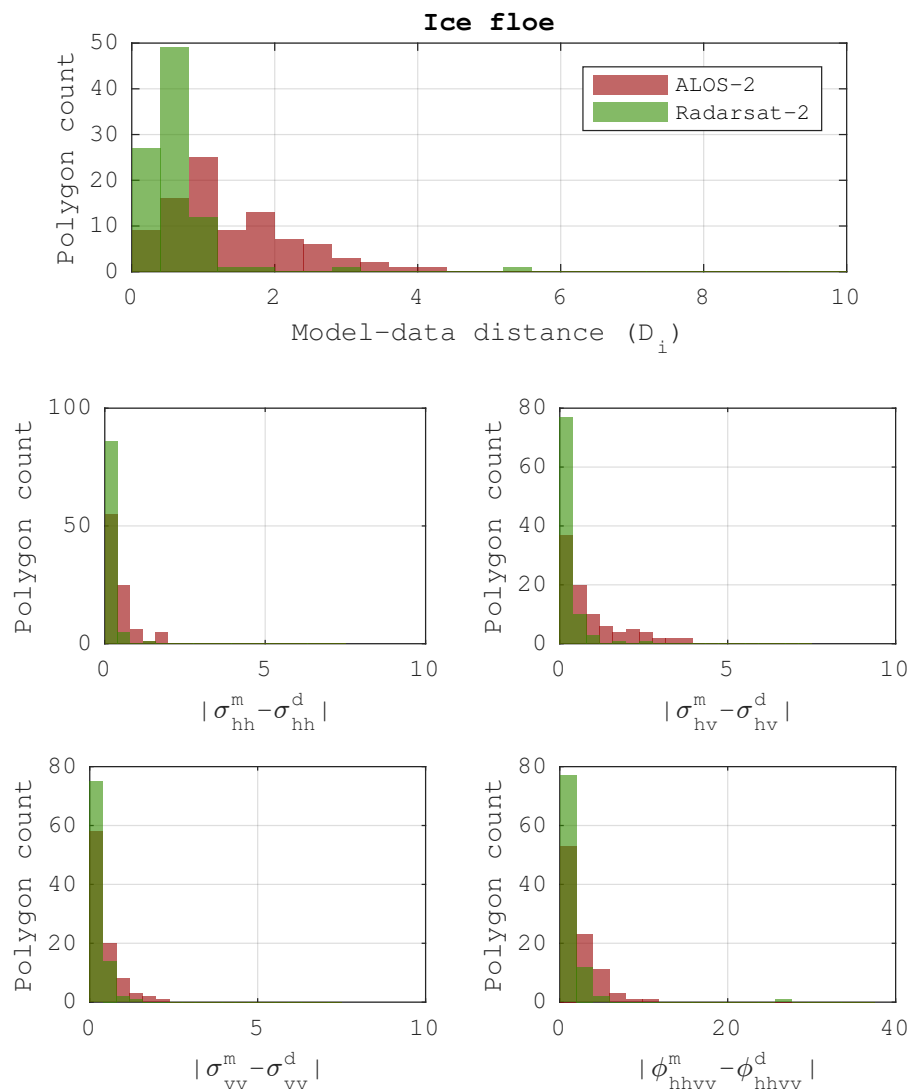
Figure 6.27: Histograms over minimum model-data distances according to equation 6.7 for the ice floe class. 10^5 model samples were used.
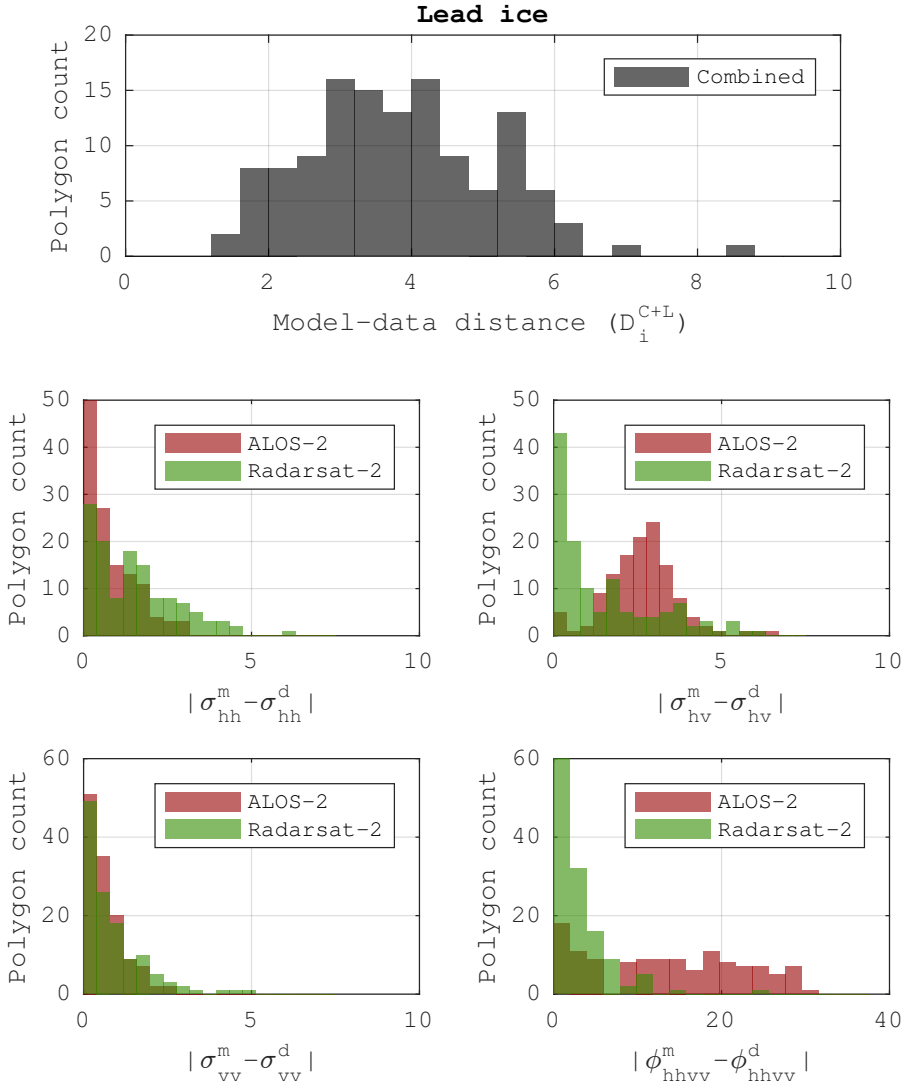
Figure 6.28: Histograms over minimum model-data distances according to equation 6.10 for the lead ice class. 10^5 model samples were used.
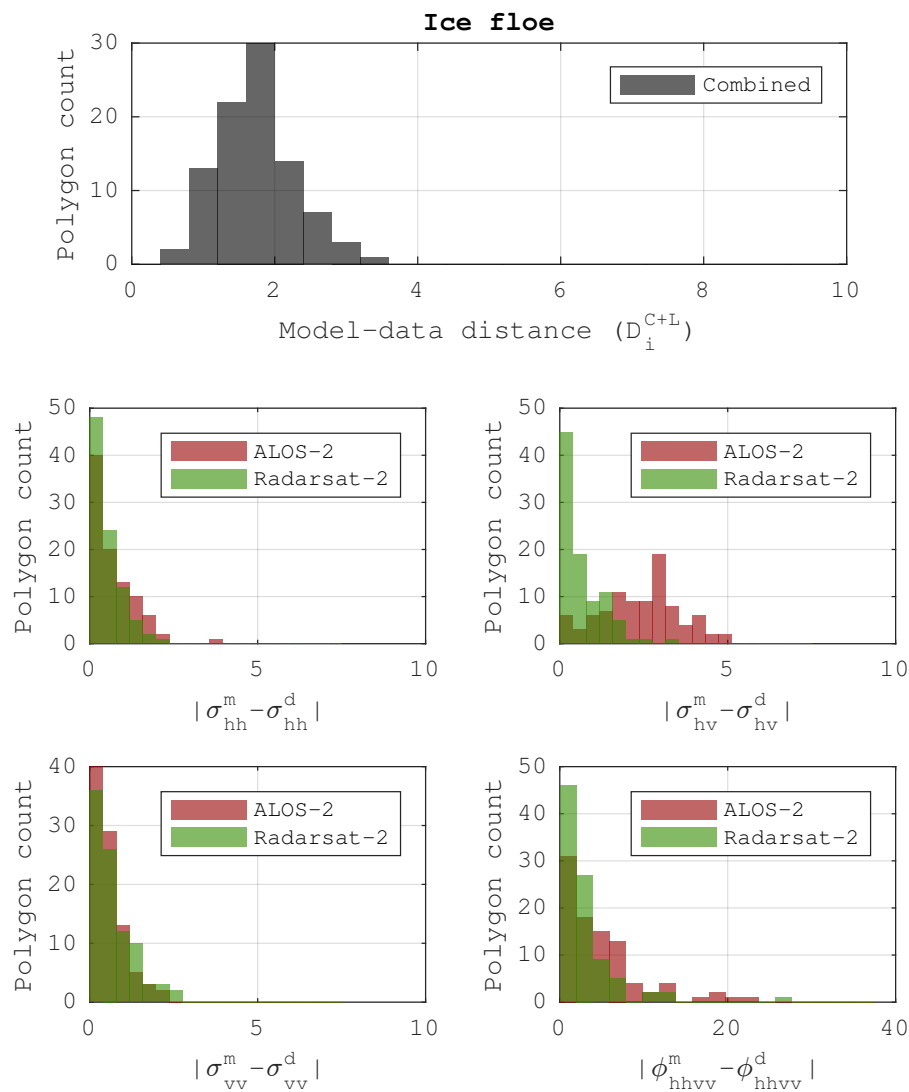
Figure 6.29: Histograms over minimum model-data distances according to equation 6.10 for the ice floe class. 10^5 model samples were used.

should however also agree well when multiple radar configurations are combined. That is, the same geophysical model input parameters should produce realistic predictions for paired polygons, assuming they are co-located. This will be investigated in terms of a combined distance as described next.

Denote two data samples of a polygon pair by $\mathbf{y}_{Ci}^d$ and $\mathbf{y}_{Li}^d$, where the former is the Radarsat-2 data sample and the latter is the paired ALOS-2 data sample. Consider next the two model output samples resulting from the corresponding radar configurations, but with a fixed geophysical configuration, denoted $\mathbf{y}_C^m(\mathbf{x}_j)$ and $\mathbf{y}_L^m(\mathbf{x}_j)$, respectively. Denote the displacements:

$$\mathbf{d}_{ij}^C = \mathbf{y}_{Ci}^d - \mathbf{y}_C^m(\mathbf{x}_j) \tag{6.8a}$$

$$\mathbf{d}_{ij}^L = \mathbf{y}_{Li}^d - \mathbf{y}_L^m(\mathbf{x}_j) \tag{6.8b}$$

and the distances:

$$D_{ij}^C = \sqrt{\mathbf{d}_{ij}^{C\,\mathrm{T}}\bar{\boldsymbol{\Sigma}}^{-1}\mathbf{d}_{ij}^C} \tag{6.9a}$$

$$D_{ij}^L = \sqrt{\mathbf{d}_{ij}^{L\,\mathrm{T}}\bar{\boldsymbol{\Sigma}}^{-1}\mathbf{d}_{ij}^L} \tag{6.9b}$$

By minimising the averaged distance:

$$D_i^{C+L} = \min_j \frac{1}{2}\left(D_{ij}^C + D_{ij}^L\right) \tag{6.10}$$

a measure of the combined match between the polygon pair and the model is obtained. In contrast to the distances previously shown in figures 6.26 and 6.27, where the minimum distance per paired polygon could correspond to different input parameters, the combined distance in equation 6.10 uses the same input parameters for both polygons in a pair. The combined distance may this be larger than simply the sum of the individual distances as shown in figures 6.26 and 6.27.

Histograms over the minimum combined distance according to equation 6.10 are shown in figure 6.28 for lead ice and figure 6.29 for ice floe. As previously, the top plot show the histogram over distances for all polygon pairs, while the lower four plots shows the corresponding deviations per polarimetric parameter. In the lower plots, the green histograms correspond to Radarsat-2 polygons and the red histograms to ALOS-2 polygons.

Considering the lead ice class and comparing the top histogram of the combined distances in figure 6.28, with those computed per band in figure 6.26, it is evident that the model generally deviate more when the bands are combined. The bottom four plots moreover show that the main contribution to deviation comes from the cross-polarised channel and the co-polarised phase shift in ALOS-2. The

deviation in the co-polarised channels are however also increased compared to the distances computed per band (figure 6.26).

Considering the histograms for the ice floe class, the combined distance is generally larger than for the distances computed per band shown in figure 6.27. It is however clear (from the top histogram) that the model generally fits considerably better with the data than for the combined distances in the lead ice class. In fact, the model typically deviates by less than 3 distance units. The deviation is most attributed to cross-polarised channel for ALOS-2. Compared to the lead ice class, the co-polarised phase shifts agree considerably better for ALOS-2.

6.6 Summary and conclusions

In this chapter, SAR images of sea ice acquired with three different satellite sensors, operating at different frequency bands (X-, C- and L-band), are carefully examined and compared to a layered backscatter model. Regions corresponding to open water, lead ice, ice floes and ridges or brash ice are selected in terms of manually drawn polygons. The polygons are processed and averaged into single data samples in a polarimetric feature space. Polygons that are associated to the same sea ice or water area, but are from different sensors, are referred to as polygon pairs.

In section 6.2.5, an overview of all polygons is presented. In summary, those tagged as open water show significant variation at all frequency bands which is expected due to variability in wind conditions and fetch. Generally, the polarimetric parameters indicate dominant Bragg-like scattering (high co-polarised ratios and correlation coefficients as well as small co-polarised phase differences), although the scattering entropies and alpha angles are significant, suggesting that other scattering mechanisms or texture are not negligible. A few polygons are particularly noticeable in that σ_{vv} is considerably lower for Radarsat-2 than for ALOS-2, despite similar incidence angles. The possibility that this is due to thin layers of frazil ice in the water that suppresses short surface waves and consequently Bragg waves at the C-band wavelength range, is discussed in more detail in chapter 7. The polygons tagged as lead ice also show considerable variation. In contrast to the open water class, relatively large co-polarised phase shifts are observed, in particular at L-band. The ice floe and ridge or brash classes are less variable. Also for these classes, significant co-polarised phase shifts are observed.

The polygons tagged as lead ice and ice floes are further compared to a backscatter model. Specifically, the model input parameters are sampled randomly and the corresponding output is compared to the polygon data samples. The sampling limits for model input parameters are chosen carefully, partly based on data from the N-ICE 2015 campaign and partly based on field and laboratory measurements presented in the literature. The model is configured differently

for the two ice classes and generally compares well with the observed data when
sensors are considered separately. Overall, the data from Radarsat-2 agree better
than that from ALOS-2 and the ice floe class agrees better than the lead ice class.
In particular, the cross-polarised channel and the co-polarised phase shift devi-
ate most between the model output and the data. The cross-polarised channel
is typically higher than the model output and the co-polarised phase difference
is typically positive in the data, but negative in the model output (although the
magnitude generally agree relatively well). The deviation in the cross-polarised
channel could result from the fact that the model does neither include multiple
backscattering effects nor large slopes of the layer interfaces.

When paired polygons are combined (excluding X-band) and compared with
the model, such that the same sea ice parameters are used for both polygons
in a pair, the agreement with the model is worse. The deviation is again larger
for the lead ice class than for the ice floe class, which still is relatively well
modelled. For the lead ice class, especially the co-polarised phase difference and
cross-polarised channel are problematic. For the ice floe class, the cross-polarised
channel contribute most to the deviation. The increased combined distances could
moreover be caused by (a) the polygon pairs not being accurately co-located, such
that different areas are compared and/or (b) the model not providing a realistic
representation of the backscatter response. Recalling that the model (1) neglects
higher order backscattering responses at interfaces (by restricting the RMS-slope
to small values) and in the volume (by assuming the DBA) and (2) assumes highly
symmetric inclusions (by describing them with a simplified correlation function),
it is perhaps not surprising that the cross-polarised channel deviates. The reason
for deviations in co-polarised phase shift is however less obvious.

Finally, it should be emphasised that the range of plausible model predic-
tions is quite large, even when the model input parameters are constrained by
the observations from N-ICE 2015. This relates to the results of the sensitivity
analysis in chapter 5, which concluded that the most important parameters in
terms of sensitivity are those describing small scale structures, specifically in-
terface roughness parameters as well as correlation lengths of brine pockets and
snow grains. These parameters are among the most difficult and variable ones to
measure in the field, and information about them is usually very limited. This
illustrates a major issue when applying backscatter models to SAR data. That
is, if complementary and rather detailed information about the sea ice conditions
is lacking, it is relatively easy to configure a model in a way such that it fits with
the data. The question if the model really represents the observed sea ice or not
still remains.

6.7   Acknowledgements

Chapter 7

Backscatter reduction due to damping of gravity waves in frazil or grease ice slicks

It is well known that slicks of frazil or grease ice can cause a low radar backscatter compared to open water roughened by wind or many types of consolidated sea ice. A detailed understanding of this reduction of the radar backscatter is important for characterisation, classification and parameter retrieval of sea ice from radar remote sensing data. It is also critical for interpreting oil spills in ice infested waters, since these also may cause a low radar backscatter and may be misinterpreted as ice slicks (or vice versa). In this chapter, this is examined in more detail. The general approach mimics the one used for slicks of oil presented in, for instance, Alpers & Hühnerfuss (1989) and Gade et al. (1998).

The chapter begins with a brief motivation and background on the ice types of consideration. Wave dispersion is then discussed, specifically for open water and for slicks of ice. The model by Keller (1998) (referred to as the Keller model) is considered for the latter, which treats an ice slick as a viscous layer and provide the corresponding dispersion relation for gravity waves. The model is solved numerically and compared to the well known dispersion relation for open water. Next, the action balance equation is considered for linking the dispersion relation to the wave spectrum. The source terms of the action balance equation are examined. The term for wind input and the one for viscous dissipation are assumed dominant and examined in detail. Lastly, the wave spectrum is coupled with the SPM in order to relate the dispersion relation to a scattering band ratio. The ratio predicts the reduction of the radar cross section (RCS) due to an ice

171

slick, relative to some reference wavelength. Choosing the reference wavelength to correspond to L-band radar waves, the ratio is used to interpret observations from chapter 6.

The analysis concludes that under certain conditions, ice slicks have strong impact on the spectral behaviour of the radar backscatter. According to the numerical solution of the Keller model, the damping due to ice slicks is generally very strong at wavelengths relevant to radar remote sensing. Consequently, the wind speed presumably needs to be high in order to cause significant roughness of the ice slick surface and thus detectable amounts of Bragg scattering.

While the approach presented in this study is essentially the same as the one used for oil slicks in for example Gade et al. (1998), this study provide the first attempt (to my knowledge) to quantitatively describe the spectral backscatter characteristics of frazil or grease ice slicks. It is moreover different from Gade et al. (1998) in that a band ratio (ratio of the RCS from a slick at one wavelength relative to another) is here considered instead of a damping ratio (ratio of the RCS from a slick relative to that of open water) as considered in Gade et al. (1998) among others.

7.1 Motivation and objectives

Frazil and grease ice are under turbulent conditions the earliest ice types in the ice formation process (see section 3.3.1 for further details). Their characteristics and abundances are therefore important to monitor in order to better understand and model sea ice growth and ocean-atmosphere interactions. As an example, Smedsrud & Martin (2015) show that by incorporating grease ice into a basin-scale sea ice-ocean model, the closing of sea ice leads is delayed and the heat loss from the ocean to the atmosphere is significantly increased in fall and winter.

With increasing human activity in the Arctic Ocean in terms of fishing, shipping and petroleum exploration or production, slicks of mineral oil at the sea surface are likely to become much more frequent. Radar remote sensing has proven to be extremely useful in detecting such slicks, since they typically reduces the radar backscatter significantly compared to open water (Brekke & Solberg 2005). It is well known that slicks of frazil or grease ice also can cause a reduction in backscatter. In figure 7.1, an example of a SAR image containing streaks of grease ice is shown as an example (dark stripes perpendicular to the highlighted transect). In ice infested waters, misclassification between slicks of oil and ice is therefore a potential problem, thus a detailed understanding of their characteristics is of great interest.

In this chapter, the reduction of the radar backscatter due to slicks of frazil or grease ice is examined in more detail. In particular, the damping characteristics as a function of radar wavelength is considered. This will also yield insights to

Figure 7.1: Example of grease ice in a SAR image. These can be seen as dark stripes perpendicular to the highlighted transect in the middle of the image. The slicks were validated from co-incident optical data. The image cover the Terra Nova Bay Polynya in Antarctica and is acquired by ALOS PALSAR (L-band) on 10 September in 2009. The image is provided as a processed joint photographic experts group (JPEG) file by Wolfgang Dierking through the ESA project ALO.3545.

observations made for open leads mentioned in the chapter 6, which is discussed at the end of this chapter (section 7.4.5).

7.2   Frazil and grease ice

As mentioned in section 3.3.1, ice formation in turbulent and supercooled water results in small submerged ice spicules and plates, called frazil ice. Accumulated frazil ice is called grease ice. A characteristic property of frazil and grease ice is the damping of short surface waves, which has been attributed to the viscosity of the ice-water mixture (Weber 1987, Newyear & Martin 1997, 1999). Published measurements of the viscosity of frazil or grease ice are however scarce, yet some studies indicate that the kinematic viscosity of grease ice can be up to four orders of magnitude larger than the one of sea water (Newyear & Martin 1997, 1999, Rabault et al. 2017).

In the following, three different viscosities will be considered:

$$\nu^{(i)} = \begin{cases} 10^1 \nu^{(w)} & \text{"Low-viscous case"} \\ 10^2 \nu^{(w)} & \text{"Medium-viscous case"} \\ 10^4 \nu^{(w)} & \text{"High-viscous case"} \end{cases} \tag{7.1}$$

where $\nu^{(w)} = 10^{-6}$ m^2/s is the kinematic viscosity of water (Newyear & Martin 1997). The high-viscous case thus agrees with the measurements of accumulated grease ice in Newyear & Martin (1997, 1999) and Rabault et al. (2017) and may be considered as a "worst case scenario" in terms of wave damping. No studies have been found for less concentrated frazil ice, which is expected in the earliest stage of the ice formation process. It is however arguable that these types of ice will have a lower viscosity compared to the accumulated grease ice and can hence be represented by the medium- and low-viscous cases.

7.3   Dispersion and damping of surface waves

Wave dispersion relates the frequency of a wave to its wavenumber (Crawford 1968). Knowing how these two quantities relate, yield information about the propagation characteristics of the wave, such as its group or phase velocity as well as its attenuation. Formally, the so called dispersion relation couples the wave number k_s (here the subscript s is used to distinguish the wavenumber of surface waves to that of radar waves) and angular frequency ω of a plane wave of the form $\mathrm{e}^{i(k_s x - \omega t)}$ which can be assumed for small amplitude waves. Either the wave number or the frequency can be considered a complex number which

associates to wave damping. Here, ω will be a real number while k_s will be complex valued such that:

$$k_s = k_s' + i k_s'' \tag{7.2}$$

Here, the subscript s is used to distinguish wave number of surface waves to those of the radar waves (these will however later be linked through the SPM). The real part of the wave number relates to the wavelength λ_s as:

$$\lambda_s = \frac{2\pi}{k_s'} \tag{7.3}$$

and the imaginary part relates to wave damping, which can be expressed in terms of the attenuation length l:

$$l = \frac{1}{k_s''} \tag{7.4}$$

A freely propagating wave will thus decay as $\mathrm{e}^{-x/l}$, hence l is the distance the wave needs to propagate before the amplitude is reduced to $1/\mathrm{e} \approx 0.37$ of its initial value. More details about wave dispersion can be found in an introductory book on wave mechanics, fluid dynamics, optics or similar (Crawford 1968, for example).

7.3.1   Waves in open water

For small amplitude waves, the dispersion relation for non-viscous water is:

$$\omega^2 = \left(g k_s + \frac{\gamma^{(w)}}{\rho^{(w)}} k_s^3 \right) \tanh(k_s H) \tag{7.5}$$

where g is the gravitational constant, $\gamma^{(w)}$ is the surface tension of water, $\rho^{(w)}$ is the water density and H is the water depth. The term $g k_s$ is associated to gravitational forces and the term $\frac{\gamma^{(w)}}{\rho^{(w)}} k_s^3$ to capillary forces. It is clear that for long wavelengths (small k_s) the gravitational forces dominate, while for short wavelengths (large k_s) the capillary forces dominate. In numbers, the gravity term typically dominate above 7 cm in wavelength and capillary term below about 4 mm. In between these regimes, both the gravity and capillary forces are important.

The roots to equation 7.5 will yield real valued wave numbers, thus no damping is present. For viscous water however, the wave number will have a non-zero imaginary part which is assumed (the solution to equation 9 with respect to the spatial variable in Lamb 1916, section 948):

$$k_s'' = \frac{2\nu^{(w)} k_s'^{\,2}}{c_g} \tag{7.6}$$

where $k_s{}'$ is the real valued root of equation 7.5, $\nu^{(w)}$ is the kinematic viscosity of water and:

$$c_g = \frac{\mathrm{d}\omega}{\mathrm{d}k_s'} \tag{7.7}$$

is the group velocity.

7.3.2 Waves in frazil and grease ice

The dispersion and damping of gravity waves in grease ice has been studied by several researchers. The main focus has been to understand how open water waves behave as they penetrate into sea ice in the MIZ. Early attempts to model the damping assumed a so called mass loading theory (Wadhams & Holt 1991), which later turned out to be inconsistent with experiments (Newyear & Martin 1997). Models treating the ice as a viscous layer have shown considerably better agreement with observations (Newyear & Martin 1997, 1999, Rabault et al. 2017).

An early attempt to model the viscous damping of grease ice was made by Weber (1987). The model treats the grease ice as a layer on top of infinitely deep water. It is assumed that both the ice and the water are homogeneous, viscous and incompressible fluids. The dispersion relation is found by assuming that the grease ice viscosity is very large and that the ice thickness is much smaller than the wavelength of the surface waves. Since grease ice can be up to some tens to hundred centimetres thick (Smedsrud 2011), the latter assumption makes the model primarily applicable to ocean swell.

Later, Keller (1998) developed a two layer model, where the ice is viscous but the water is not. It does not make explicit assumptions on the wavelength of the waves, but lacks closed form solutions and thus needs to be solved numerically. Approximate solutions on closed form are however found for wavelengths much larger and much smaller than the ice layer thickness, respectively.

Further developments of the model by Keller (1998) were made by De Carolis & Desiderio (2002) and Wang & Shen (2010). De Carolis & Desiderio (2002) treat the case where also the water is viscous, while Wang & Shen (2010) extend it by including elastic effects in order to better describe consolidated ice being mixed with the frazil and grease ice. Both these models are mathematically more involved than those by Weber (1987) and Keller (1998).

While the models mentioned above are mainly aimed at describing dispersion of relatively long waves penetrating into the sea ice, this work needs a description of the damping of relatively short surface waves, comparable to the radar wavelength. This rules out the model by Weber (1987), which assumes long waves. Since additionally ice floes are not considered here, the model by Wang & Shen (2010) is also not suitable. The model by Keller (1998) is moreover mathematically simpler than that of De Carolis & Desiderio (2002) and it has been

successfully used for predicting the dispersion of relatively short waves (about 1-1.5m in wavelength) in laboratory grown grease ice (Newyear & Martin 1999). For this reason, the model by Keller (1998), hereafter referred to as "the Keller model", will be considered in this study.

7.3.3   The Keller model

This section briefly describes the Keller model. For further details please refer to Keller (1998). The model yields the dispersion relation of small amplitude gravity waves. In contrast to the dispersion relation for open water (equation 7.5), it does not account for surface tension and thus not capillary forces.
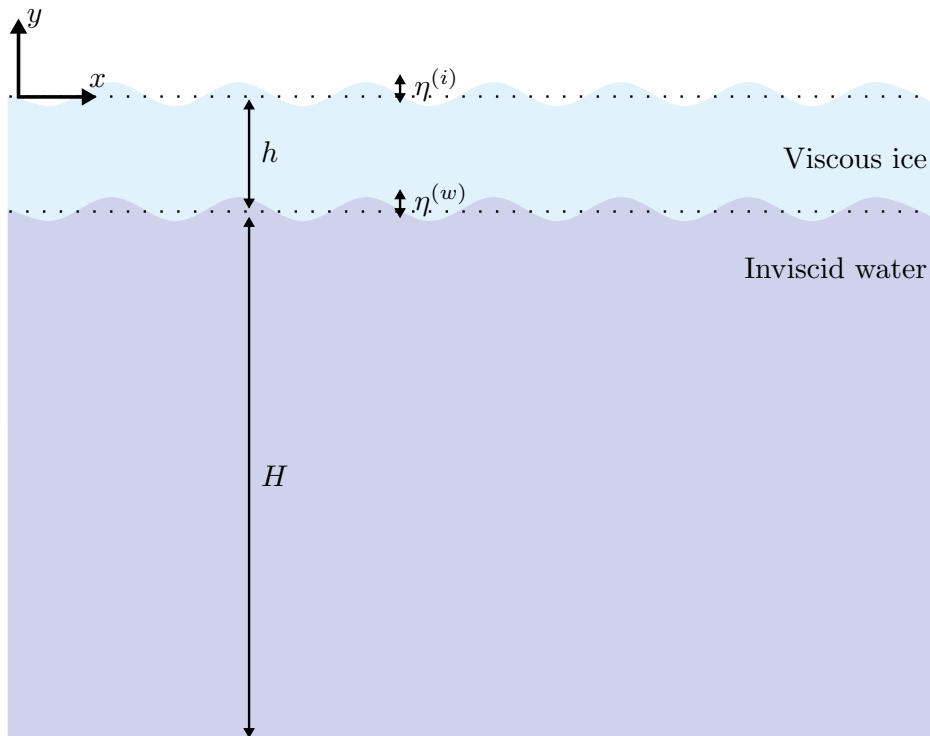
Figure 7.2: The physical setup of the Keller model. An ice slick is represented by a viscous layer of thickness h positioned on top of an inviscid layer of thickness H. The model yields the complex wave number as a function of frequency for a small amplitude harmonic perturbation at the interfaces to the ice layer, with amplitudes $\eta^{(i)}$ and $\eta^{(w)}$ as shown in the figure.

The model represents the ice slick as a viscous layer of thickness h and kinematic viscosity ν, floating on top of an inviscid water layer of thickness H (see figure 7.2). The ice slick is governed by the Navier-Stokes equations for incompressible fluids while the water layer is governed by the Euler equations. The former accounts for a non-zero viscosity while the latter does not. The state of the system is fully described by specifications of the interfaces between the air, ice and water layers as well as the 2D velocity (vector) field $\mathbf{u}(x,y,t) = [U(x,y,t), V(x,y,t)]$ and (scalar) pressure field $P(x,y,t)$ (both being functions of space and time). The system is at rest when the pressure and velocities are in hydrostatic equilibrium and consequently the air-ice, ice-water and water-bottom interfaces are at $y = 0$, $y = -h$ and $y = -H$ for all x, respectively (see figure 7.2). If the state of rest is slightly perturbed however, gravity waves will propagate.

If the air-ice and ice-water interfaces are displaced slightly from their state of rest, say by $\eta^{(i)}(x,t)$ and $\eta^{(w)}(x,t)$, respectively, the governing equations can be linearised and solved analytically assuming a solution of the form:

$$\begin{bmatrix} U(x,y,t) \\ V(x,y,t) \\ P(x,y,t) \\ \eta^{(i)}(x,t) \\ \eta^{(w)}(x,t) \end{bmatrix} = \begin{bmatrix} u(y) \\ v(y) \\ p(y) \\ a \\ b \end{bmatrix} e^{i(k_s x - \omega t)} \qquad (7.8)$$

where k_s is the complex wave number, ω the angular frequency and the vector on the right hand side contains amplitudes. By imposing appropriate boundary conditions, the problem of finding the unique solution can be reduced to that of finding four unknown constants related to the amplitudes of equation 7.8 from four linear equations (Keller 1998, equations (15)-(18)). These equations can be written in matrix form as:

$$\mathbf{M}(k_s, \omega)\mathbf{x} = 0 \qquad (7.9)$$

where $\mathbf{x}$ is a vector of the four unknown constants and $\mathbf{M}(k_s, \omega)$ is a 4×4 coefficient matrix, with elements containing k_s and ω. For this system to have a non-trivial solution, the determinant of the coefficient matrix must be zero, that is:

$$\det(\mathbf{M}(k_s, \omega)) = 0 \qquad (7.10)$$

which yields the dispersion relation. For the full expression see equation A.7 (or equivalently equation (19) in Keller 1998, although this is not written in dimensionless variables as in equation A.7). The equation may have multiple roots which does not have closed form solutions. The roots must therefore be found numerically and here the Levenberg-Marquardt algorithm is used with analytically calculated gradients. If multiple roots are found, the one with the longest attenuation length is considered. Further details on the numerical implementation is found in section A.2.2.
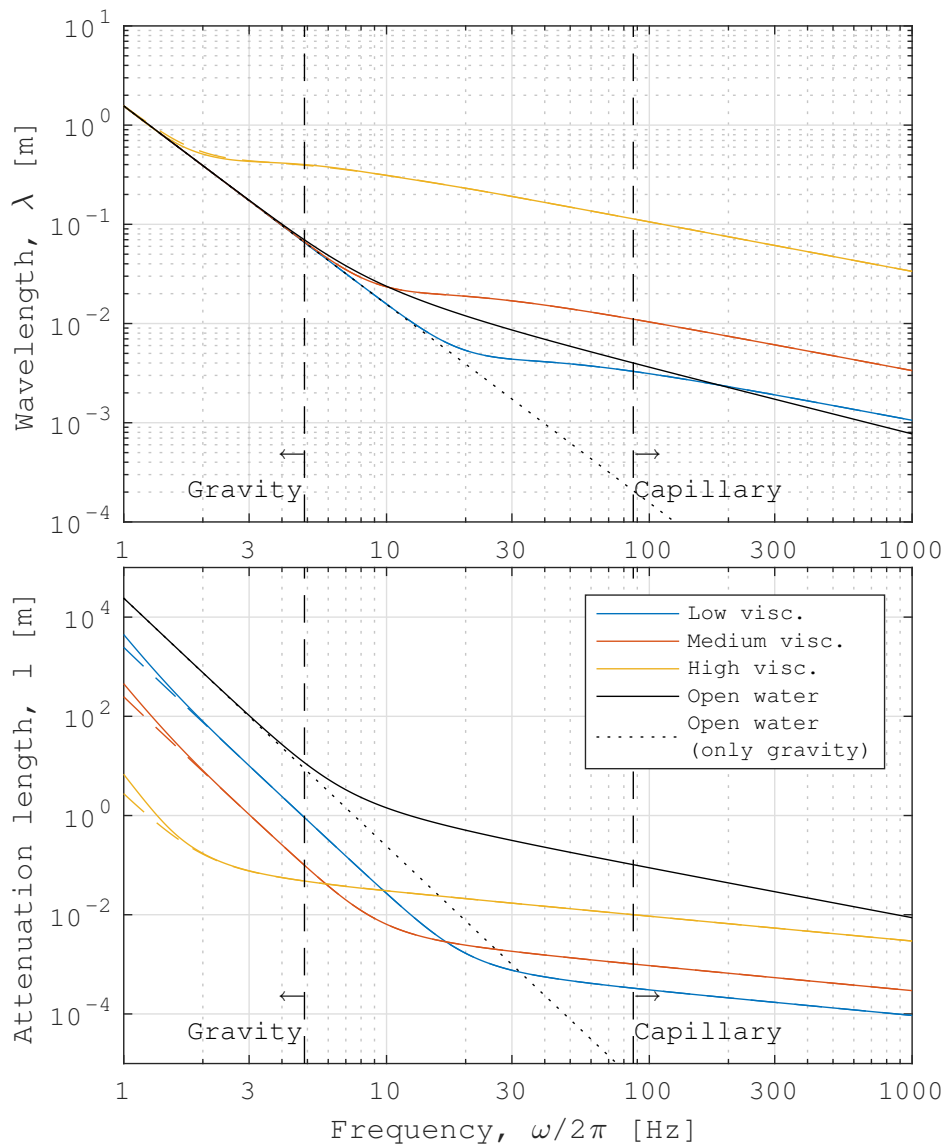
Figure 7.3: The above two plots show the dispersion relations for open water (black line) and water covered by ice slicks (coloured lines) of various viscosities (see legend) and thicknesses (solid = 10 cm and dashed = 50 cm). The water depth H is infinite, the ice slick density $\rho^{(i)} = 969$ kg/m^3, the water density $\rho^{(w)} = 1020$ kg/m^3, the water kinematic viscosity $\nu^{(w)} = 10^{-6}$ m^2/s and the water surface tension $\gamma^{(w)} = 0.0745$ N/m.

7.3.4   Comparing wave dispersion in ice slicks to open water

In figure 7.3, the dispersion of waves in various ice slicks are compared to the dispersion in open water. Specifically, the wavelength and attenuation length is plotted for the frequencies 1 to 1000 Hz. The plotted ice viscosities (distinguished by line colour in the figure) are stated in equation 7.1. The plotted ice thicknesses (distinguished by solid and dashed lines) are 10 and 50 cm, respectively. The frequency regimes where gravity or capillary forces are dominant for open water are indicated by vertical lines. The dispersion for open water, including both capillary and gravity waves is shown as a black solid line and the relation for only gravity waves is shown as a dotted line. Note that the two lines deviate considerably for frequencies in the capillary regime, as anticipated. In particular, as the capillary forces begin to dominate there is a kink in the open water dispersion relation (see top plot in figure 7.3), such that the wavelength is longer than for pure gravity waves.

Considering the slicks, both the wavelength and the attenuation length decrease monotonically with increased frequency. At the lowest frequency (1 Hz), the ice slicks do not affect the wavelength. As the frequency increases, all slicks begin to deviate from the open water gravity waves (dotted black line) in terms of increased wavelength. The effect is stronger for higher viscosities. Specifically, a similar kink as for the open water case that includes capillary forces (solid black line) is observed although the slicks do not account for capillary forces. This is interesting, however for frequencies much higher than those in the gravity regime, the results of the Keller model should be treated with care.

The attenuation length is considerably shorter in the ice slicks compared to open water for all frequencies in the gravity regime. At higher frequencies, the attenuation length becomes longer in the ice slicks than for pure gravity water waves (dotted black line) but are still much shorter than for water waves governed by both capillary and gravity forces (solid black line). Again however, at these frequencies the neglect of capillary forces in the Keller model needs to be remembered.

In figure 7.4 the attenuation length is plotted versus wavelength for open water and ice slicks (with the same settings as in figure 7.3). As before, the onset of the regime for gravity waves is indicated by a vertical line (the capillary regime is outside the plotted wavelength interval). It is clear that the slicks of lowest viscosity (blue lines) have considerably longer attenuation lengths compared to those of highest viscosity (yellow lines). Overall, the attenuation length is 1-4 orders of magnitude shorter for the slicks compared to open water.
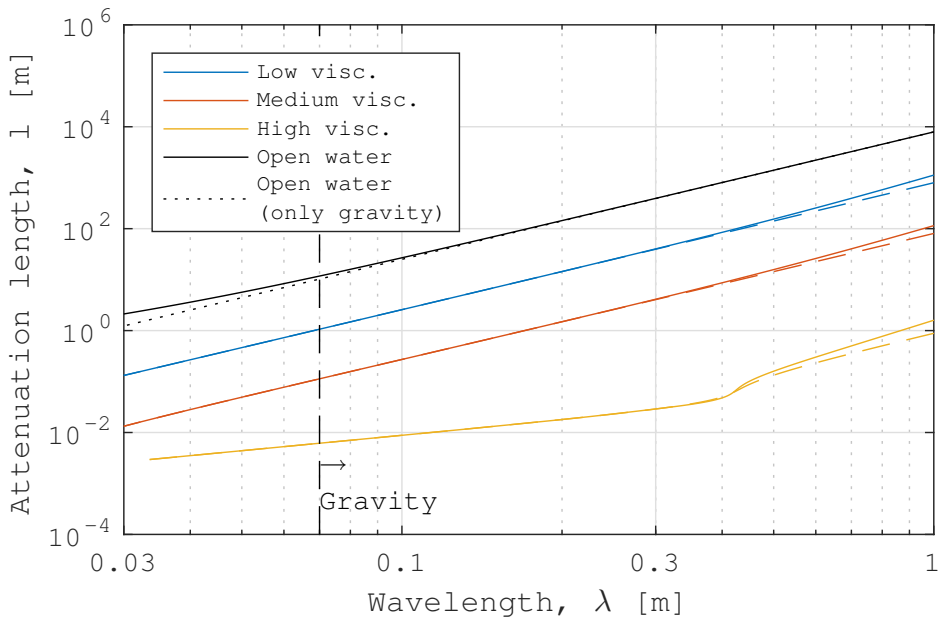
Figure 7.4: The attenuation length plotted versus wavelength for open water (black lines) and water covered by ice slicks (coloured lines) of various viscosities (see legend) and thicknesses (solid = 10 cm and dashed = 50 cm). The water depth H is infinite, the ice slick density $\rho^{(i)} = 969$ kg/m^3, the water density $\rho^{(w)} = 1020$ kg/m^3, the water kinematic viscosity $\nu^{(w)} = 10^{-6}$ m^2/s and the water surface tension $\gamma^{(w)} = 0.0745$ N/m.

7.4   Scattering reduction due to ice slicks

From section 7.3 it is clear that a slick of frazil or grease ice will significantly
change both the wavelength and attenuation of surface waves compared to open
water. It is anticipated that this in turn will result in a reduction of the RCS, as
will be discussed in more detail here.

7.4.1   Bragg scattering

Considering the high permittivity of sea water, surface scattering can generally be
considered the dominant scattering mechanism from the sea surface. Specifically,
the small perturbation model (SPM) (see also section 4.1.2) has been extensively
used in oceanographic applications and will be assumed adequate for the purpose
of this chapter.

The SPM approximates the RCS from a randomly rough surface as (see also
equation 4.10):

$$\sigma_{pp}^0 = 4(k\cos\theta)^4 |\alpha_{pp}|^2 W(k_b) \tag{7.11}$$

where pp indicates polarisation, k is the radar wave number, α_{pp} is defined in
equation 4.11 (being a function of only the incidence angle θ and permittivity ε_r)
and $W(k_b)$ is the surface spectrum evaluated at the so called Bragg wave number:

$$k_b = 2k\sin\theta \tag{7.12}$$

The backscatter is thus proportional to the surface spectrum evaluated at the
Bragg wavenumber k_b, thus if a surface slick reduces the spectrum at the Bragg
wave number, the RCS will be reduced correspondingly. In order to relate this
reduction to wave dispersion and damping, the spectral action balance equation
is considered next.

7.4.2   Spectral action balance equation

The spectral action balance equation dictates how the surface spectrum, or more
precisely, the spectral action density evolves over time. The spectral action den-
sity is defined as (Alpers & Hühnerfuss 1989):

$$N = \frac{g}{\omega} W(k_s) \tag{7.13}$$

where g is the gravitational constant and $W(k_s)$ is the surface wave spectrum.
For small amplitude waves, the rate of change of N is the sum of various sources
and sinks which is expressed in the so called spectral action balance equation
(Phillips 1985):

$$\frac{\mathrm{d}N}{\mathrm{d}t} = S_{wi} + S_{nl} - S_{br} - S_{vd} \tag{7.14}$$

where the right hand side represents the sources and sinks. Specifically, S_{wi} represents input from wind and is the main generator of the waves and is thus positive. The term S_{nl} accounts for non-linear wave-wave interactions that redistribute the action density across wave numbers and can thus be both positive and negative. S_{br} represents wave breaking, also a non-linear effect but purely dissipative and thus negative. The last term S_{vd} represents dissipation due to viscosity.

If the spectral action density and consequently the surface spectrum does not change with time, the sources and sinks balance each other:

$$0 = S_{wi} + S_{nl} - S_{br} - S_{vd} \tag{7.15}$$

If the source terms are known as functions of the action density, equation 7.15 can in principal be solved to yield the surface spectrum through equation 7.13. General theoretical expressions for these terms are however seldom well known, in particular for slicks of frazil or grease ice. However, the wind input and viscous damping terms are likely to be the most important for viscous slicks, such that the wind is the main source and viscous damping the main sink. A comparison of the corresponding source terms could accordingly provide insights to how much the spectrum is suppressed due to the ice slick at certain wave numbers. Specifically, if the wind input at a certain wave number is much smaller than the dissipative output due to viscosity, the spectrum is likely to be strongly reduced at that wave number unless there are other sources, such as the non-linear one in equation 7.15, that compensates the viscous dissipation. This is discussed in more detail next.

7.4.3   Wind input compared to viscous dissipation

For a slick free sea surface, the wind input is typically assumed proportional to the action density as (Plant 1982):

$$S_{wi} = \beta N \tag{7.16}$$

where:

$$\beta = 0.04\omega \left(\frac{u_*}{c_p}\right)^2 \tag{7.17}$$

where the wind and wave directions are assumed to be aligned for simplicity, $c_p = \omega/k_s$ is the wave phase velocity and u_* is the wind friction velocity. For open water, the friction velocity can be assumed 3.5% of the wind speed at 10 m height which is denoted U_{10} (Wu 1975). If a slick is present, the friction velocity is likely lower. For oil slicks, it has been estimated to be as low as 68% of the corresponding slick free friction velocity (Mitsuyasu & Honda 1982). Similar studies have however not been found for ice slicks and therefore the reduction
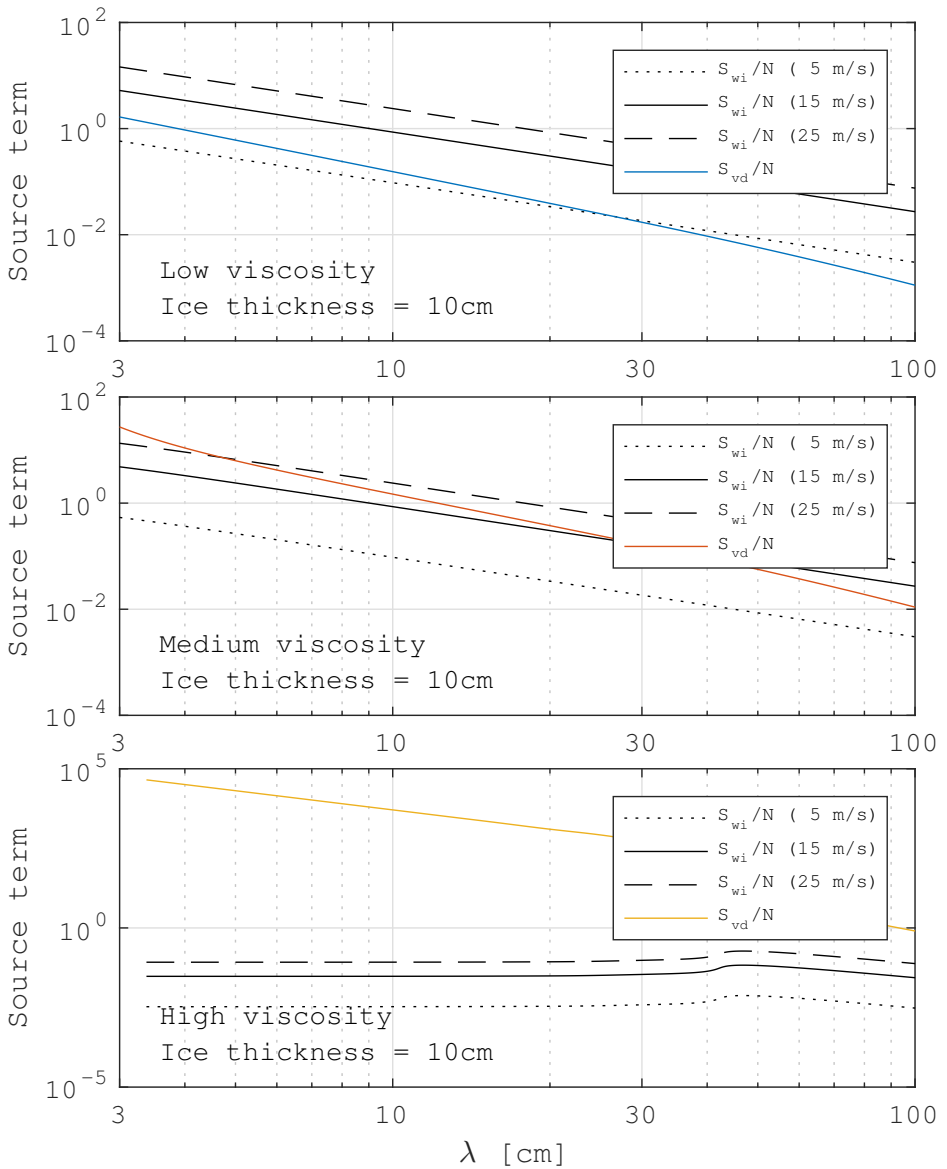
Figure 7.5: The source terms for wind input (with U_{10} set to 5, 15 and 25 m/s) and viscous damping (see equations 7.16 and 7.19, respectively) for ice slicks of different viscosity in the top, middle and bottom plot. The parameters for the Keller model are the same as in figures 7.3 and 7.4 (see figure texts for details).

compared to the slick free case will somewhat arbitrarily be assumed 70%, such that for an ice slick:

$$u_* = 0.7 \times 0.035 \ U_{10} \tag{7.18}$$

Since this velocity will be used qualitatively in the subsequent sections and not be compared to direct measurements, the exact number is not critical as long as the order of magnitude is correct.

If the water is viscous, the term for the resulting viscous damping is (Phillips 1985):

$$S_{vd} = 2k_s'' c_g N \tag{7.19}$$

where $c_g = \mathrm{d}\omega/\mathrm{d}k_s'$ is the group velocity of the surface waves. Equation 7.19 will be assumed valid also when a viscous slick is present (where k_s'' and c_g are computed according to the Keller model).

The terms for the wind input and viscous damping in equations 7.16 and 7.19, respectively, can now be compared to provide insights about the dissipative characteristics of the slick in relation to the input from the wind. Specifically, if equation 7.16 and equation 7.19 are inserted into the spectral action balance equation (equation 7.14) and the terms for non-linear effects and wave-breaking are ignored, it is easy to show that:

$$W(k_s) = \frac{\omega}{g} \mathrm{e}^{\gamma t} \tag{7.20}$$

where equation 7.13 is used to relate the spectral action density to the wave spectrum and:

$$\gamma = \frac{S_{wi}}{N} - \frac{S_{vd}}{N} = \beta - 2k_s'' c_g \tag{7.21}$$

Clearly, whenever $\frac{S_{wi}}{N} < \frac{S_{vd}}{N}$ the spectrum in equation 7.20 will decay exponentially with time, while if $\frac{S_{wi}}{N} > \frac{S_{vd}}{N}$ it will grow exponentially with time. The latter is obviously not realistic over a long enough time scales, since non-linear effects become important as the wave amplitude become large (equation 7.20 will no longer be a valid solution to the action balance equation). It however illustrates that the difference between the normalised source terms in equation 7.21 dictates if the spectrum is likely to be suppressed or not. Small amplitude waves will grow rapidly if the wind input is larger than viscous damping while if smaller, they will quickly dissipate.

The normalised source terms $\frac{S_{wi}}{N} = \beta$ and $\frac{S_{vd}}{N} = 2k_s'' c_g$ are plotted in figure 7.5 as functions of wavelength, where the Keller model is used to compute the wave numbers as functions of the frequency. The same model settings as in figures 7.3 and 7.4 are considered, that is for slicks of low, medium and high viscosity (see equation 7.1). The slick thickness is 10 cm and the wind speed U_{10} is 5, 15 and 25 m/s, respectively, for the wind term plotted as black lines.

In the top plot of figure 7.5, showing the low-viscous slick ($\nu^{(i)} = 10^1 \nu^{(w)}$), the wind input terms for 15 and 25 m/s winds are greater than the viscous damping term for all wavelengths. For 5 m/s winds, only the longest waves have a higher wind input. Small amplitude waves will grow rapidly until non-linear effects become relevant and roughness due to the wind is thus likely if the wind is sufficiently strong.

The middle plot in figure 7.5 shows the source terms for the medium-viscous slick ($\nu^{(i)} = 10^2 \nu^{(w)}$). For the low-wind case (5 m/s), the viscous dissipation is larger than the wind input over the whole wavelength range. For intermediate winds (15 m/s) only the waves longer than about 30 cm have larger wind input than viscous dissipation. For the strong wind case (25 m/s), the input is larger for waves longer than roughly 5 cm. The viscous dissipation is thus quite strong and wind induced roughness at relevant radar wavelengths mainly appears likely for very strong winds in the order of 20-30 m/s.

Considering the high-viscous slick ($\nu^{(i)} = 10^4 \nu^{(w)}$) shown in the bottom plot in figure 7.5, the viscous damping term shown in yellow dominates for wind situations and over the whole wavelength range. Surface roughness due to the wind and consequently Bragg scattering will be significantly reduced in the presence of a high-viscous slick, even in strong wind conditions.

It is evident that gravity waves in the wave length range relevant to radar backscattering are very effectively attenuated by the presence of a viscous ice slick. Unless the wind speed is very high or the viscosity of the slick is relatively low, the surface is unlikely to be significantly roughened by the wind.

7.4.4   Backscatter reduction in low viscous slicks

Now, the damping characteristics of an ice slick will be linked to radar backscattering assuming the SPM. The approach mimics that used for oil slicks in Gade et al. (1998). By combining equations 7.13, 7.15 and 7.19, the surface spectrum can be written as:

$$W(k_s) = \frac{\omega}{g\gamma} \left(S_{nl} - S_{br} \right) \tag{7.22}$$

Note that this is not in general a solution for the spectrum, since S_{nl} and S_{br} will generally depend on $W(k_s)$. Assuming however that wave breaking is negligible compared to non-linear effects, S_{br} may be dropped. Consider then the wave spectrum normalised by its value at an arbitrary reference wavenumber k_{s0} as:

$$\frac{W(k_s)}{W(k_{s0})} = \frac{\omega(k_s)\gamma(k_{s0})}{\omega(k_{s0})\gamma(k_s)} \cdot \frac{S_{nl}(k_s)}{S_{nl}(k_{s0})} \tag{7.23}$$

In the following, the reference wave number is taken to be $k_0 = 25.2$ m^{-1} which corresponds to the centre frequency at L-band. If variations of this ratio, as a

function of the wavenumber k_s, is dominantly governed by the wind input and viscous damping (through $\gamma(k_s)$), then $S_{nl}(k_s)$ is approximately constant and:

$$\frac{S_{nl}(k_s)}{S_{nl}(k_{s0})} \approx 1 \tag{7.24}$$

The normalised spectrum then simplifies to:

$$\frac{W(k_s)}{W(k_{s0})} \approx \frac{\omega(k_s)\gamma(k_{s0})}{\omega(k_{s0})\gamma(k_s)} \tag{7.25}$$

Under the SPM, the ratio between the corresponding RCSs is consequently:

$$\frac{\sigma_{pp}^0(k)}{\sigma_{pp}^0(k_0)} = \frac{W(k_b)}{W(k_{b0})} \cdot \frac{|\alpha_{pp}(k)|^2}{|\alpha_{pp}(k_0)|^2} \approx \frac{\omega(k)\gamma(k_b)}{\omega(k_0)\gamma(k_{b0})} \cdot \frac{|\alpha_{pp}(k)|^2}{|\alpha_{pp}(k_0)|^2} \tag{7.26}$$

where equations 7.11 and 7.25 are used and $k_{b0} = 2k_0 \sin\theta$. Equation 7.26 will be referred to as the band ratio relative to the radar wave number k_0. The factor $\alpha_{pp}(k)$ depends on the radar wave number through the permittivity of the slick. Here, the permittivity is assumed the same as for sea water at -2°C with a salinity of 32 ppt (see equation 3.4).

Note that, while the derivation of the band ratio in equation 7.26 mimics the damping ratio presented in Gade et al. (1998), there is a major difference. Gade et al. (1998) derives the ratio relative to open water, while equation 7.26 is relative to the slick but at another wavenumber. This will enable comparison to data from chapter 6.

A similarity to the damping ratio derived by Gade et al. (1998) is however that the band ratio in equation 7.26 is singular at $\gamma(k) = 0$, that is when the source terms for the wind input and viscous damping are equal. This is not physical and wavenumbers close to, or lower than this singularity should be avoided. In the previous section, it was found that this is avoided in the wavenumber range relevant to radar Bragg scattering, if the wind is very high or the slick viscosity is low (see figure 7.5). Therefore, only the slick of lowest viscosity (see equation 7.1) with relatively high wind speeds is considered in the following analysis.

As an example, the band ratio relative to L-band is plotted as a function of wavelength in figure 7.6. The incidence angle is 30°, the viscosity is $\nu^{(i)} = 10^1 \nu^{(w)}$ and the ice thickness is 10 cm (the results for 50 cm are almost identical). The wind speed is varying from medium to high in order to avoid the singularity, specifically it is 10, 15 and 25 m/s for the respective line. However, the 10 m/s line begins to grow as the wavelength decreases below roughly 4 cm, which is due to the singularity. The wavelengths corresponding to the centre frequencies at X-, C- and L-band are highlighted with vertical lines. Since the band ratio is relative to L-band, it is accordingly 0 dB at the L-band line. At the C-band
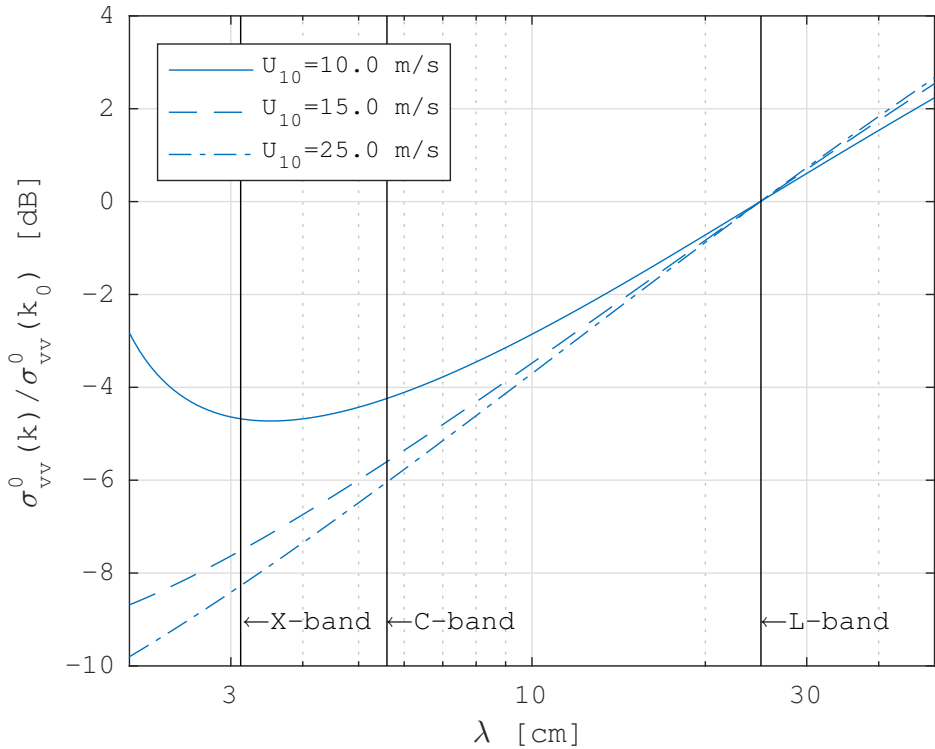
Figure 7.6: Band ratios relative to L-band (at 30° incidence angle) according to equation 7.26. Three different wind speeds are shown as indicated in the legend. The wavelengths corresponding to X-, C- and L-band are highlighted as vertical lines.

line, the band ratio vary from about -4 to -6 dB depending on wind speed and at X-band from about -5 to -8 dB. It should however be noted that the wavelengths at X-band are outside the regime for gravity waves and the results need to be considered with care.

   In summary, the band ratio yields a prediction on the backscatter reduction relative to L-band for low viscous ice slick in medium to high wind speed cases. It can now be used for analysing observations from chapter 6, as discussed in the next section.
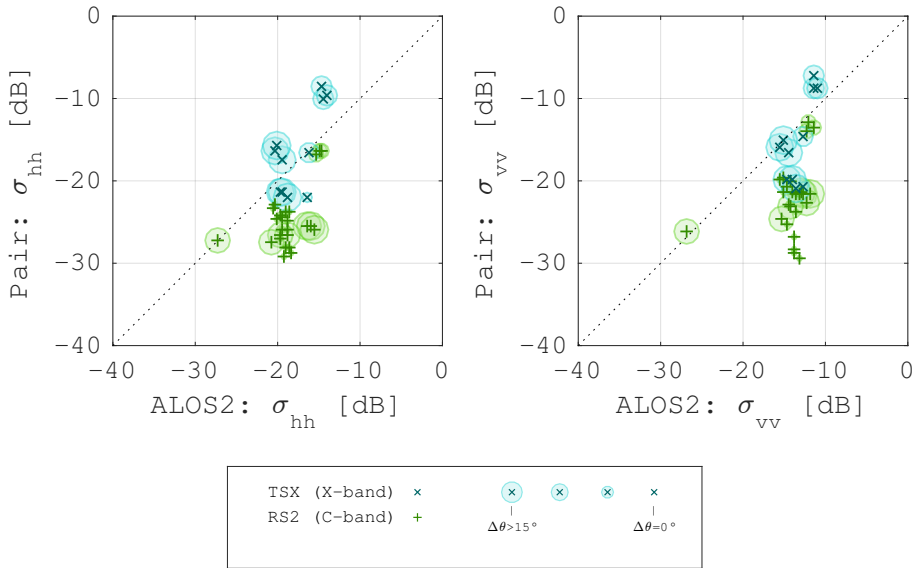
Figure 7.7: The differences between polygons tagged as "open water" from chapter 6. Each tick corresponds to the median value of one polygon. The colour and size of the markers indicate sensor and incidence angle difference, respectively (see legend). Note specifically the green markers showing a significantly lower backscatter for Radarsat-2 (C-band) than ALOS-2 (L-band), with a difference up to 10 dB in the *vv*-channel.

7.4.5 Comparison to observations from chapter 6

Given the results of the previous two sections, a comment on the observations shown in figure 7.7 can now be made. The figure originates from chapter 6 where data from ALOS-2, Radarsat-2 and TerraSAR-X were analysed. Specifically, manually selected polygons over open leads were examined. Figure 7.7 shows the co-polarised RCSs for paired polygons, where the polygons in a pair cover the same ice or water feature in the respective scene (each point in the plot corresponds to the median of one polygon). The signal for ALOS-2 is shown on the x-axis and the corresponding paired signal, either from Radarsat-2 or TerraSAR-X, is shown on the y-axis.

A notable feature in the plots is that some Radarsat-2 polygons yield a significantly lower backscatter than the corresponding ALOS-2 polygons, in particular for the vv-channel (right plot). The same is however not true for the TerraSAR-X

polygons, which could be explained by a steeper incidence angle and possibly also noise saturation due to a considerably lower SNR (with a NESZ at about -24 dB for TerraSAR-X compared to below -30 dB for both ALOS-2 and Radarsat-2). Differences in incidence angle or noise level do not explain the reduced backscatter for Radarsat-2, since they are both similar to the ALOS-2 polygons. A hypothetical cause could therefore be that slicks of frazil or grease ice reduces the backscatter in the C-band observations (Radarsat-2), compared to the L-band observations (ALOS-2).

In section 7.4.3 it was concluded that unless the wind speed is very strong both the medium and high viscous slicks are likely to reduce surface waves very effectively compared to the wind input for wavelengths relevant to Bragg scattering. For the data points being mostly reduced at C-band in figure 7.7, the wind speeds are however relatively low, around 5 m/s (measured at the research vessel RV Lance, see chapter 6 for details). This suggests that a slick most likely also would reduce the L-band signal significantly, which is not observed (the vv-polarised RCS is above -20 dB).

Assuming however, that the wind speeds were higher than those recorded at RV Lance and that the hypothesised slick viscosities were low, the backscatter reduction as predicted by the band ratio in equation 7.26 agrees rather well to the observations. Specifically, the results shown in figure 7.6 suggests that the backscatter reduction relative to L-band (at 30° incidence angle) range roughly from -4 to -6 dB depending on wind speed compared to the observed values in figure 7.7 that ranges from minus a few dB down to -10 dB. Without further in-situ data however, conclusions on the possibility of such high wind speeds or low slick viscosities are difficult to draw. Given the relatively high backscatter values at L-band and low wind speeds at RV Lance, it does however at this point appear unlikely that the reduction is caused by slicks of grease or frazil ice.

7.5   Summary and conclusions

While it is well known that slicks of frazil or grease ice can reduce the radar backscatter compared to wind roughened sea water, a thorough understanding of the reduction is needed for interpreting radar backscatter data from ice slicks. This chapter provide a detailed analysis of the damping characteristics of viscous slicks of frazil or grease ice and their effect on the radar backscatter.

The initial assumption is that viscous damping is the main cause for reducing the backscatter. This is further considered for gravity waves using the dispersion model by Keller (1998), in which the ice slick is treated as a viscous layer floating on top of an inviscid water layer. The model is solved numerically to yield the wavelength and attenuation length of small amplitude gravity waves, as functions of wave frequency.

	Relative ice viscosity, $\nu^{(i)}/\nu^{(w)}$		
	10^1	10^2	10^4
3.1 cm (X-band)	0.143 m	0.015 m	- m
5.5 cm (C-band)	0.586 m	0.062 m	0.005 m
25.0 cm (L-band)	25.253 m	2.603 m	0.023 m
68.0 cm (P-band)	363.000 m	37.036 m	0.455 m

Table 7.1: Attenuation length for an ice slick (in metres), for various wavelengths and viscosities. The wavelengths corresponds to X-, C-, L- and P-band radar wavelengths. The ice thickness is 10 cm. For the highest viscosity and shortest wavelength, a numerical solution to the Keller model was not obtained and therefore the corresponding attenuation length is not stated for that case.

	Wind speed, U_{10}		
	10 m/s	15 m/s	25 m/s
3.1 cm (X-band)	-4.7 dB	-7.5 dB	-8.3 dB
5.5 cm (C-band)	-4.3 dB	-5.7 dB	-6.1 dB
25.0 cm (L-band)		reference	
68.0 cm (P-band)	3.2 dB	3.6 dB	3.8 dB

Table 7.2: Band ratios for the vv-polarisation at different wavelengths relative to L-band at 30° incidence angle and for different wind speeds. The wavelengths corresponds to X-, C-, L- and P-band. The ice thickness is 10 cm and the viscosity of the ice is $\nu^{(i)} = 10^1 \nu^{(w)}$. These values can also be seen in figure 7.6.

The attenuation length describes the distance scale at which small amplitude waves dissipate. In figure 7.4, the attenuation length for various ice slicks was plotted versus wavelength and to summarise, values corresponding to four important wavelengths are highlighted in table 7.1. These wavelengths are: 3.1 cm, 5.5 cm, 25 cm and 68 cm, which roughly corresponds to X-, C-, L- and P-band radar wavelengths. As expected, the attenuation length increases with wavelength and decreases with ice viscosity, which is assumed 1, 2 and 4 orders of magnitude greater than the viscosity of typical sea water (assumed 10^{-6} m^2/s).

For the shortest wavelength (corresponding to X-band), the attenuation length is very short (in the order of a centimetre or less) indicating very strong wave damping even for the slick of low viscosity. For the longest wavelength (corresponding to P-band) which is well in the range of pure gravity waves, the attenuation length is considerably longer and vary from 46 cm up to 363 m, depending on ice viscosity. Note however that both X- and C-band are in the wavelength zone were capillary forces are important for corresponding water waves. This needs to be emphasised since the Keller model only accounts for gravitational forces.

The dispersion relation is further linked to source terms in the action balance equation. In particular, the reduction of spectral action density per unit time due to ice slicks is compared to the input from wind. It is found that the viscous dissipation is stronger than the wind input, unless the slick has a relatively low viscosity or the wind speed is very high (see figure 7.5).

The action balance equation is then used to relate the dispersion relation to the radar backscatter. In particular, a band ration is found which yields the reduction of the RCS relative to a reference wavelength, which here is chosen to the wavelength corresponding to the L-band centre frequency (25.0 cm).

In table 7.2 a set of band ratios corresponding to the wavelengths at X-, C-, L- and P-band are shown. X-band is here reduced relative to L-band by about -5 to -8 dB depending on wind speed, C-band by about -4 to -6 dB and P-band is increased by roughly 3 to 4 dB. The values are dependent on the viscosity of the ice slick which here corresponds to the lowest case, that is $\nu^{(i)} = 10^1 \nu^{(w)}$.

By comparing the theoretically predicted band ratios for the high-wind-low-viscosity scenario to observations from chapter 6, a good agreement is obtained. Specifically, the reduction of radar backscatter at C-band relative to L-band as observed in data, range from a few dB below zero down to -10 dB. The corresponding theoretical predictions range from roughly -4 to -6 dB, depending on wind speed and ice viscosity. While the theoretical values assume high wind speeds, relatively low wind speeds were recorded simultaneous to the data acquisitions. This may suggest that the reduction is not likely a result of ice slicks. The results for X-band are not considered further due to differences in noise level and incidence angle between TerraSAR-X and ALOS-2, in addition to the fact

that X-band waves are well within the wavelength domain where capillary forces are important, which are not accounted for in the model by Keller.

In conclusion, this chapter presents a quantitative analysis of the spectral behaviour of the radar backscatter from frazil or grease ice. The approach provides predictions on the backscatter reduction, as a function of radar wavelength. It is demonstrated that the predictions can readily be compared to data and significantly help interpretation. While the approach mimics that used for oil slicks in previous studies (Alpers & Hühnerfuss 1989, Gade et al. 1998, for example), it is the first (to my knowledge) that provide quantitative predictions with regard to frazil or grease ice, at wavelengths relevant to radar remote sensing.

Chapter 8

Summary and outlooks

The studies presented in the previous three chapters will now be summarised. Note that these chapters specifically address the objectives stated in the introduction of the thesis (section 1.4). Then, concluding remarks will be made that connect to the problem formulation in section 1.3 and lastly, research issues to be considered in the future will be highlighted.

8.1   Summary of studies

Chapter 5 (to my knowledge) presents the first global sensitivity analysis of the fully polarimetric radar backscatter response from snow covered sea ice. The analysis is global in the sense that it takes into account the observed ranges of sea ice properties that are needed as input, and it attributes a quantitative sensitivity measure to each individual input parameter, such that the most influential one(s) can be identified. The considered model is configured with different snow layers and in particular the presence of brine-wetted snow is considered both in comparison and in combination with dry snow. The analysis is performed for X-, C- and L-band radar frequencies.

A general conclusion is that the polarimetric backscatter response of snow covered sea ice is complex. There is no single input parameter that stands out across the considered radar frequencies or snow and ice conditions. Generally it can be concluded that parameters describing roughness of interfaces and dimensions of brine inclusions and snow grains, are more important than parameters describing bulk properties such as salinity, temperature and density. It is moreover found that parameters associated to the snow and upper part of the ice dominate at X- and C-band, while the roughness of the ice-water interface is important at L-band.

The analysis moreover shows that a snow layer that is fully or partially soaked by brine can have a significant impact on the radar signature. The general effect of a brine-wetted snow layer is attributed to (1) the real part of the effective permittivity being closer to that of sea ice, making the permittivity contrast weaker at the snow-ice interface and (2) the imaginary part of the effective permittivity being considerably higher than for dry snow, thus causing significant attenuation at high frequencies (such as at X- or C-band). The effect of brine-wetted snow is strongly dependent on its temperature and salinity, which also couples to the dry snow since this insulates the brine-wetted snow from the air.

Chapter 6 complements the sensitivity analysis of chapter 5 by showing that the composite backscatter model (based on incoherent layer-stacking as considered in chapter 5) can be fitted well to SAR data at both C- and L-band, for ice identified as lead ice and ice floes (which presumably is first year ice). Generally, C-band data compare better than L-band data. Likewise, the ice identified as ice floes is better represented than ice types identified as lead ice. The model primarily deviates from the data in the co-polarised phase shift and the cross-polarised channel. Overall, the variance in model output is very large which can be explained by insufficient constraints on roughness and volumetric structure parameters (which are among the most important ones in terms of model sensitivity, as concluded in chapter 5).

While chapters 5 and 6 are tightly linked to each other (since they mainly deal with snow covered sea ice) chapter 7 focuses on a rather special topic, that is the backscatter from frazil and grease ice. A detailed analysis of the damping characteristics of viscous slicks of frazil or grease ice and their effect on the radar backscatter is presented. This was initially motivated by observations found over open leads (presented in chapter 6), where the co-polarised backscatter at C-band was significantly suppressed compared to that at L-band. A hyppothetical explanation is that slicks of frazil ice can suppress short surface waves and thus the C-band backscatter. In order to provide insights into the observations, a model for the dispersion relation of viscous ice slicks by Keller (1998) (referred to as the Keller model) is considered. An approach similar to the one described in Gade et al. (1998) is then adopted and modified, such that the dispersion relation is linked to a band ratio. This ratio provides the backscatter relative to a reference radar frequency and can readily be compared to data from chapter 6 and significantly help the interpretation.

The analysis concludes that under certain conditions, ice slicks have strong impact on the spectral behaviour of the radar backscatter. According to the numerical solution of the Keller model, the damping due to ice slicks is generally very strong at wavelengths relevant to radar remote sensing. Consequently, the wind speed presumably needs to be high in order to cause significant roughness of the ice slick surface and thus detectable amounts of Bragg scattering.

8.2   Concluding remarks

In the problem formulation of the thesis (section 1.3), the following questions were phrased:

A. What input parameters are most important in a layered backscatter model (based on existing surface and volume scattering models) at X-, C- and L-band radar frequencies?

B. How does brine wetted snow affect model sensitivity?

C. Can a layered backscatter model generally be used to describe typical ice types observed at multiple frequency bands?

D. What is the multi-frequency backscatter characteristic of frazil and grease ice?

So, does this thesis answer them?

Chapter 5 provides important answers to the first two questions, by presenting a unique sensitivity analysis that (as far as I know) has not yet been been done for the radar backscatter from sea ice. It does not simply suggest that certain parameters are important, but it provides quantitative numbers of the relative importance of the model input parameters in terms of Sobol indices. It suggests that the model sensitivity is rather complex. Depending on the snow condition, different input parameters dominate for different radar frequencies. In many situations, multiple parameters are important. This is critical information that should be taken into account when interpreting data and retrieving parameters by means of model inversion.

Chapter 6 addresses the third question. While there are deviations, the analysis clearly shows that the selected model can predict the majority of the considered observations (restricted to what is identified as lead ice and ice floes). While this is quite remarkable, it must be emphasised that without complementary data that can be used to validate the model input parameters, some uncertainty is left that the model actually fully represents the real sea ice configuration. Considering that the model sensitivity is highly dependent on radar frequency (as shown in chapter 5), data acquired at different frequency bands could complement each other. This is acknowledged by combining observations (of the same ice regions) from Radarsat-2 and ALOS-2, and fitting the model to the combined data (assuming the same geophysical input parameters in the model). Compared to treating each frequency independently, the model compares worse to the combined data which indicates that further model tuning is required. The co-location of the combined data is however not perfect (due to ice drift), which complicates the analysis.

Finally, chapter 7 provides the first (to my knowledge) attempt to answer the last question, characterising the multi-frequency backscatter response from frazil and grease ice in a quantitative manner. While there are important simplifications made in the analysis (capillary forces and non-linear effects are neglected), the study provides simulation results that can readily be compared to the data.

8.3   Future outlooks

While previous work on modelling and analysis of the radar backscatter from sea ice is extensive, there are still unresolved or only partly resolved issues remaining. While this thesis provides some new insights, in particular on model sensitivity, the impact of brine-wetted snow and the backscatter characteristics of frazil and grease ice, some important issues to be dealt with in the future are discussed in the following paragraphs.

In chapter 6, it is noted that the considered model primarily deviated from data in the cross-polarised channel and the co-polarised phase shift. For better agreement, other models should be considered. In particular models that account for higher order backscattering mechanisms, irregular inclusion shapes, multiple inclusion types (both air bubbles and brine pockets for instance), coherent layer interactions (especially for thin layers) and a wider range of roughness scales at layer interfaces should be tested or even still need to be developed. These are all aspects that were neglected in the model used here. Regarding volume scattering for instance, approaches that are based on dense medium radiative transfer (DMRT) could potentially provide better agreement to data, since they account for multiple backscattering of inclusions and coherent near range effects. There are moreover a number of numerical approaches that are fully coherent and include higher order scattering effects, for instance the method of moments (MoM), the finite-volume time-domain (FVTD) method and the finite element method (FEM). Such approaches are often regarded as computationally too demanding, but with computational power becoming cheaper, they are attracting more attention (Isleifson et al. 2012, Xu et al. 2016) and could perhaps yield better agreement to data.

Next, an issue that is arguably among the most pressing ones, relates to the lack of validation data. From chapter 5 it was found that parameters describing the small scale structure of interfaces and inclusions are among the most important ones. In chapter 6, it was moreover found that relatively simple scattering models agree quite well with SAR data. In order to validate such results, complementary measurements of small scale structural parameters are thus needed. Such measurements are however extremely difficult to perform.

Consider for example the roughness of a snow covered interface. For a roughness measurement to be feasible (with for example a laser scanner), the snow

needs to be removed without affecting the interface which is extremely difficult in practice. The measurement moreover needs to cover a large area, since (a) the roughness characteristics can be very variable and (b) the measurement should preferably cover multiple pixels in a SAR image to be useful for validation. At the same time, the interface needs to be sampled on sub-wavelength scales in order to provide sufficiently good estimates of the roughness. Instruments being able to resolve the volumetric structure of the snow and sea ice are also needed. For that, radar tomography has proven to be useful for identifying from where in the volume the dominant backscatter is coming (Yitayew et al. 2017a,b). Such information could undoubtably be of great help in validating layered backscatter models.

Regarding chapter 7, validation data are also lacking. There has been a few documented tank experiments with relatively thick grease ice (Newyear & Martin 1997, 1999) aimed at understanding ocean swell. No published measurements of less dense frazil ice, at wavelengths on centimetre to decimetre scales relevant to radar scattering, were available to support this study. Such measurements would be needed for validating the simulations presented in chapter 7. Also, multi-frequency radar data acquired over known locations of frazil or grease ice would be of great help.

Appendices

Appendix A

Expressions and derivations

A.1 Average radius of curvature for the GPL correlation function

If $\sigma_s \ll 1$, the approximate average radius of curvature Γ_c is given in equation 4.8, but restated here for clarity (Ulaby et al. 1982, page 1013):

$$\Gamma_c \approx \frac{1}{\sigma_z} \left(\frac{2}{\pi} \left. \frac{\mathrm{d}^4 \rho(r)}{\mathrm{d}r^4} \right|_{r=0} \right)^{-1/2} \tag{A.1}$$

Moreover, the 4th derivative of the correlation function at the origin can be written in terms of the power spectrum $W_1(k)$ as:

$$\left. \frac{\mathrm{d}^4 \rho(r)}{\mathrm{d}r^4} \right|_{r=0} = \frac{3}{8} \int_0^\infty k^5 W_1(k) \, \mathrm{d}k \tag{A.2}$$

The surface power spectrum for the GPL correlation function is given as (Li et al. 2002, equation 11):

$$W_1(k) = \frac{l^2 (p-1)}{2} \frac{a_p^2}{b_p^2} \left(1 + \frac{a_p^2}{b_p^2} \frac{k^2 l^2}{4} \right)^{-p} \tag{A.3}$$

Inserting equation A.3 and A.2 in equation A.1 and integrating, yields:

$$\Gamma_c \approx \sqrt{\frac{\pi}{6}} \frac{l^2}{2\sigma_z} \frac{a_p^2}{b_p^2} \sqrt{6 - 5p + p^2} \tag{A.4}$$

conditioned that $p > 3$.

A.2   Grease ice dispersion relation

A.2.1   Dispersion relation in dimensionless variables

As outlined in chapter 7, the dispersion relation for small amplitude gravity waves in frazil or grease ice is given by finding the roots of equation 7.10. The full expression of this equation is stated in equation (19) in Keller (1998). However, it is found that if the expression is rewritten in terms of dimensionless variables, numerical root-finding appears more stable. In particular, the following dimensionless variables are considered:

$$
\tilde{\omega} = \frac{\omega}{M} \qquad \tilde{k} = \frac{k}{N}
$$
$$
\tilde{h} = \frac{h}{N} \qquad \tilde{H} = \frac{H}{N} \tag{A.5}
$$
$$
\tilde{\rho} = \frac{\rho_i}{\rho_w}
$$

where the dimensoinal scaling factors are:

$$
N = \left(\frac{g}{\nu^2}\right)^{1/3} \qquad M = \left(\frac{g^2}{\nu}\right)^{1/3} \tag{A.6}
$$

and ρ_i and ρ_w are the densities of frazil or grease ice and water, respectively. Rewriting equation (19) in Keller (1998) in terms of these variables and dividing by $N^4 M^2$, the following expression is found:

$$
\begin{aligned}
f(k) = {} & 2ABCD\left(1 - \operatorname{sech}\left(k\tilde{h}\right)\operatorname{sech}\left(a\tilde{h}\right)\right) - \\
& BC(iA + B)(E + F)\tanh\left(a\tilde{h}\right) + \\
& ((BC)^2 + (AD)^2 + (iA + B)^2 EF)\tanh\left(a\tilde{h}\right)\tanh\left(k\tilde{h}\right) - \\
& AD(iA + B)(E + F)\tanh\left(k\tilde{h}\right) = 0
\end{aligned} \tag{A.7}
$$

where:

$$
A = 2i\tilde{k}^2 \qquad B = a^2 + \tilde{k}^2 \qquad C = 2\tilde{k}^2 - i\tilde{\omega}
$$
$$
D = 2i\tilde{k}a \qquad E = \frac{\tilde{k}}{i\tilde{\omega}} \tag{A.8}
$$
$$
F = \frac{i\tilde{\omega}}{\tilde{\rho}}\left(\coth\left(\tilde{k}\tilde{H}\right) - \frac{(1 - \tilde{\rho})\tilde{k}}{\tilde{\omega}^2}\right) \qquad a = \sqrt{\tilde{k}^2 - i\tilde{\omega}}
$$

Given an angular frequency ω, equation A.7 is solved numerically to yield the complex wave number k. The equation have multiple roots (Keller 1998), but

the root with the smallest value of k'' will however have the longest attenuation length and thus be most relevant here (waves with shorter attenuation lengths may still be excited, but will more quickly disappear and thus contribute less to the surface power spectrum).

A.2.2   Numerical solution to equation 7.10 and A.7

The roots of equations 7.10 and A.7, are found numerically using the Levenberg-Marquardt algorithm. This is a gradient based iterative method which needs to be initialised with a guess of the true root.

Gradient

Since the unknown k of equation A.7 is a complex number, the respective real and imaginary parts k' and k'' are treated as separate real valued variables. Correspondingly, the gradient will be a 2×2 matrix defined as:

$$\nabla f(k', k'') = \begin{bmatrix} \mathrm{Re}\left\{\frac{\partial f}{\partial k}\right\} & -\mathrm{Im}\left\{\frac{\partial f}{\partial k}\right\} \\ \mathrm{Im}\left\{\frac{\partial f}{\partial k}\right\} & \mathrm{Re}\left\{\frac{\partial f}{\partial k}\right\} \end{bmatrix} \tag{A.9}$$

where $\frac{\partial f}{\partial k}$ is given by differentiating equation A.7 with respect to k, as if it would be a real valued variable. The full analytic expression is quite involved and is therefore not stated in this document.

Initialisation

Since equation A.7 has multiple roots, the initialisation of the Levenberg-Marquardt algorithm, call it k_0, needs to be chosen carefully. Generally, the closer k_0 is to the true root, the higher is the likelihood that it will be found. Here two different initialisations are used, as described below.

It is arguable that low frequency waves are little affected by the viscous ice layer and therefore have a wave number close to that of gravity waves in an inviscid fluid, given by the root of:

$$\omega^2 = gk\tanh(kH) \tag{A.10}$$

As a first initialisation, k_0 is therefore chosen to be the root of this equation. If $H = \infty$, the root is simply:

$$k_0' = \frac{\omega^2}{g} \qquad k_0'' = 0 \tag{A.11}$$

For higher frequencies, the roots may deviate considerably from equation A.11. Therefore, a second initialisation is made by fitting a spline to the low frequency roots and extrapolating to higher frequencies. The initialisation that yields the root of smallest k'' is then selected.

Validation

Based on the above mentioned numerical scheme, all figures of Keller (1998) have been reproduced, apart from Figure 1 with the parameter setting $R = 1000$ and $h = 0.1$ (see parameter definitions in Keller (1998)). The above mentioned scheme yields a slightly lower k' for $\hat{\omega}$ higher than about 3.5. However, since Figure 2 in Keller (1998) does not deviate for the same parameter setting, the deviation of Figure 1 in Keller (1998) may be due to a misprint.

Appendix B

Coefficients

B.1 Fresnel coefficients

Boundary conditions... Fresnel reflection coefficients:

$$r_v = \frac{\varepsilon_r \cos\theta - q}{\varepsilon_r \cos\theta + q} \tag{B.1}$$

$$r_h = \frac{\mu_r \cos\theta - q}{\mu_r \cos\theta + q} \tag{B.2}$$

where

$$q = \sqrt{\mu_r \varepsilon_r - \sin^2\theta} \tag{B.3}$$

Fresnel reflectivities:

$$R_v = |r_v|^2 \tag{B.4}$$

$$R_h = |r_h|^2 \tag{B.5}$$

B.2 Debye relaxation coefficients

This section contains expressions for the coefficients entering the Debye relaxation equations 3.3 and 3.4.

B.2.1 Debye relaxation of brine

Below are the expressions for the coefficients for brine, that enter the Debye relaxation equation 3.3. That is; the static and high frequency limit of permittivity (ε_s and ε_∞), the relaxation time (τ_r) and conductivity (σ_c).

Permittivity limits of brine (ε_s and ε_∞)

For brine, the static and high frequency limits of the relative permittivity are found to be temperature dependent (Stogryn & Desargant 1985):

$$\varepsilon_s(T) = \frac{939.66 - 19.068T}{10.737 - T} \tag{B.6a}$$

$$\varepsilon_\infty(T) = \frac{82.79 + 8.19T^2}{15.68 + T^2} \tag{B.6b}$$

Relaxation time of brine (τ_r)

The relaxation time (in seconds) of brine is found to be approximated as (Stogryn & Desargant 1985):

$$
\begin{aligned}
\tau_r(T) = \frac{1}{2\pi}(& 0.10990 \times 10^{-9} \\
& + 0.13603 \times 10^{-11}\ T \\
& + 0.20894 \times 10^{-12}\ T^2 \\
& + 0.28167 \times 10^{-14}\ T^3)
\end{aligned}
\tag{B.7}
$$

Conductivity of brine (σ_c)

The conductivity of brine is found as (Stogryn & Desargant 1985):

$$\sigma_c(T) = \begin{cases} -T\mathrm{e}^{0.5193+0.08755T} & \text{if } T \geq -22.9°\mathrm{C} \\ -T\mathrm{e}^{1.0334+0.1100T} & \text{if } T < -22.9°\mathrm{C} \end{cases} \tag{B.8}$$

B.2.2   Debye relaxation of sea water

Below are the expressions for the coefficients for sea water, that enter the double Debye relaxation equation 3.4. That is; the static, intermediate and high frequency limit of permittivity (ε_s, ε_1 and ε_∞), the first and second relaxation time ($\tau_r^{(1)}$ and $\tau_r^{(2)}$) and the conductivity (σ_c).

Permittivity limits of sea water (ε_s, ε_1 and ε_∞)

Static, intermediate and high frequency limit (Meissner & Wentz 2004):

$$\varepsilon_s(T, S) = \varepsilon_s(T, 0)\ \mathrm{e}^{d_0 S + d_1 S^2 + d_2 TS} \tag{B.9a}$$

$$\varepsilon_1(T, S) = \varepsilon_1(T, 0)\ \mathrm{e}^{d_6 S + d_7 S^2 + d_8 TS} \tag{B.9b}$$

$$\varepsilon_\infty(T, S) = \varepsilon_\infty(T, 0)\ (1 + S(d_{11} + d_{12}T)) \tag{B.9c}$$

where:

$$\varepsilon_s(T,0) = \frac{37088.6 - 82.168T}{421.854 + T} \tag{B.10a}$$

$$\varepsilon_1(T,0) = c_0 + c_1 T + c_2 T^2 \tag{B.10b}$$

$$\varepsilon_\infty(T,0) = c_6 + c_7 T \tag{B.10c}$$

The coefficients c_i and d_i are found in table B.1.

Relaxation times of sea water ($\tau_r^{(1)}$ and $\tau_r^{(2)}$)

$$\tau_r^{(1)}(T,S) = \tau_r^{(1)}(T,0)\ (1 + S(d_3 + d_4 T + d_5 T^2))^{-1} \tag{B.11a}$$

$$\tau_r^{(2)}(T,S) = \tau_r^{(2)}(T,0)\ (1 + S(d_9 + d_{10} T))^{-1} \tag{B.11b}$$

where:

$$\tau_r^{(1)}(T,0) = \frac{c_3 + c_4 T + c_5 T^2}{45 + T} \times \frac{10^{-9}}{2\pi} \tag{B.12a}$$

$$\tau_r^{(2)}(T,0) = \frac{c_8 + c_9 T + c_{10} T^2}{45 + T} \times \frac{10^{-9}}{2\pi} \tag{B.12b}$$

The coefficients c_i and d_i are found in table B.1.

Conductivity of sea water (σ_c)

$$\sigma_c(T,S) = \sigma_c((T,35)) R_{15} R_{T/15} \times \frac{2\pi}{10^{-9}} \tag{B.13}$$

where:

$$\begin{aligned}
\sigma_c(T,35) =\ & 2.903602 \\
& + 8.607 \times 10^{-2}\ T \\
& + 4.738817 \times 10^{-4}\ T^2 \\
& - 2.991 \times 10^{-6}\ T^3 \\
& + 4.3047 \times 10^{-9}\ T^4
\end{aligned} \tag{B.14}$$

and:

$$R_{15} = S \frac{37.5109 + 5.45216S + 1.4409 \times 10^{-2} S^2}{1004.75 + 182.283S + S^2} \tag{B.15}$$

and:

$$R_{T/15} = 1 + \frac{A(T - 15)}{B + T} \tag{B.16}$$

c_0	5.7230	
c_1	2.2379	$\times 10^{-2}$
c_2	-7.1237	$\times 10^{-4}$
c_3	5.0478	
c_4	-7.0315	$\times 10^{-2}$
c_5	6.0059	$\times 10^{-4}$
c_6	3.6143	
c_7	2.8841	$\times 10^{-2}$
c_8	1.3652	$\times 10^{-1}$
c_9	1.4825	$\times 10^{-3}$
c_{10}	2.4166	$\times 10^{-4}$

d_0	-3.56417	$\times 10^{-3}$
d_1	4.74868	$\times 10^{-6}$
d_2	1.15574	$\times 10^{-5}$
d_3	2.39357	$\times 10^{-3}$
d_4	-3.13530	$\times 10^{-5}$
d_5	2.52477	$\times 10^{-7}$
d_6	-6.28908	$\times 10^{-3}$
d_7	1.76032	$\times 10^{-4}$
d_8	-9.22144	$\times 10^{-5}$
d_9	-1.99723	$\times 10^{-2}$
d_{10}	1.81176	$\times 10^{-4}$
d_{11}	-2.04265	$\times 10^{-3}$
d_{12}	1.57883	$\times 10^{-4}$

Table B.1: Polynomial coefficients for equations B.9, B.10, B.11 and B.12.

where:

$$A = \frac{6.9432 + 3.2841S - 9.9486 \times 10^{-2}S^2}{84.850 + 69.024S + S^2} \tag{B.17a}$$

$$B = 49.843 - 0.2276S + 0.198 \times 10^{-2}S^2 \tag{B.17b}$$

The coefficients c_i and d_i are found in table B.1.

B.3   Brine volume fraction coefficients

The functions F_1 and F_2 of equation 3.6, for calculating the volume fraction of brine (see Cox & Weeks 1983, for details):

$$F_1 = (f_0^{(1)} + f_1^{(1)}T + f_2^{(1)}T^2 + f_3^{(1)}T^3) \times 10^3 \tag{B.18a}$$

$$F_2 = f_0^{(2)} + f_1^{(2)}T + f_2^{(2)}T^2 + f_3^{(2)}T^3 \tag{B.18b}$$

where the coefficients $f_i^{(1)}$ and $f_i^{(2)}$ for $i = 0, ..., 3$ are stated in table B.2

Para-	Temperature (°C)		
meter	$0 \geq T > -2$	$-2 \geq T \geq -22.9$	$-22.9 > T \geq -30$
$f_0^{(1)}$	-4.1221×10^{-2}	-4.732	9.899×10^3
$f_1^{(1)}$	-1.8407×10^1	-2.245×10^1	1.309×10^3
$f_2^{(1)}$	5.8402×10^{-1}	-6.397×10^{-1}	5.527×10^1
$f_3^{(1)}$	2.1454×10^{-1}	-1.074×10^{-2}	7.160×10^{-1}
$f_0^{(2)}$	9.0312×10^{-2}	8.903×10^{-2}	8.547
$f_1^{(2)}$	-1.6111×10^{-2}	-1.763×10^{-2}	1.089
$f_2^{(2)}$	1.2291×10^{-4}	-5.33×10^{-4}	4.518×10^{-2}
$f_3^{(2)}$	1.3603×10^{-4}	-8.801×10^{-6}	5.819×10^{-4}

Table B.2: Coefficients for equation B.18, which enter equation 3.6 used to calculate the volume fraction of brine in "standard" sea ice. The coefficients are taken from Cox & Weeks (1983).

B.4   Sea ice bulk permittivity coefficients

The coefficients a_0, a_1, b_0 and b_1 used for calculating sea ice permittivity in equation 5.20 are listed in table B.3. The tabulated coefficients are take from Vant et al. (1978).

B.5   GPL coefficients

For the GPL correlation function defined in equation 4.3c, and it's corresponding spectrum and RMS slope in equations 4.5c and 4.7c, respectively, the coefficient a_p is defined as:

$$a_p = \frac{\Gamma(p - 0.5)}{\Gamma(p)} \tag{B.19}$$

where $\Gamma(\cdot)$ is the Gamma function. The coefficient b_p is not defined on closed form, but obtained numerically by solving the equation:

$$\left(\frac{2b_p}{a_p}\right)^{p-1} K_{p-1}\left(\frac{2b_p}{a_p}\right) = 2^{p-2}\Gamma(p-1)\mathrm{e}^{-1}; \tag{B.20}$$

Parameter	f (GHz)	FYI		MYI	
		a_0	a_1	a_0	a_1
ε'	0.100	3.22	20.6		
	0.200	3.23	14.5		
	0.400	3.26	12.3		
	0.800	3.12	9.9		
	1.000	3.12	9.0		
	2.000	3.07	7.6		
	4.000	3.05	7.2		
		b_0	b_1	b_0	b_1
ε''	0.100	0.161	13.24	0.022	6.66
	0.200	0.043	8.95	-	-
	0.400	0.043	7.15	-0.058	12.01
	0.800	0.048	5.34	0.000	4.74
	1.000	0.039	6.04	-0.004	4.36
	2.000	0.034	3.56	0.013	4.35
	4.000	0.024	3.29	-0.007	2.99
	7.500	0.032	3.53	-	-

Table B.3: Coefficients used in equation 5.20 for calculating sea ice permittivity for FYI and MYI. The coefficients are taken from Vant et al. (1978).

where $K_\nu(\cdot)$ is the modified Bessel function of the second kind of order ν. For the spectrum in equation 4.5c, the coefficient f_p is further defined as:

$$f_p = \frac{1}{2} \left(1 + \left(\frac{3}{2p} \right)^2 \right) \tag{B.21}$$

Appendix C

Tables and figures

216

Overlap	Date	UTC	Satellite	Open water	Lead ice	Ice floe	Ridge or brash
1	2015-04-19	20:32	ALOS-2	0	10	8	5
		13:19	RS-2	0	10	8	5
		13:18	TS-X (Q)	0	10	6	3
		07:01	TS-X (D)	0	10	8	5
		08:02	S-1A	-	-	-	-
2	2015-04-23	20:18	ALOS-2	9	100	43	10
		14:42	RS-2	4	62	30	7
		13:43	TS-X (Q)	5	67	39	8
3	2015-04-28	20:25	ALOS-2	3	7	23	8
		15:37	RS-2	3	7	20	8
		07:35	TS-X (D)	1	6	23	8
4	2015-05-26	22:02	ALOS-2	6	31	33	14
		17:00	RS-2	4	16	24	2
5	2015-05-31	22:08	ALOS-2	15	31	33	14
		16:14	RS-2	15	31	33	14
		15:26	TS-X (D)	6	10	20	10
Total polygon count:				71	408	351	121

Table C.1: An overview of the number of polygons per sensor and overlap. See table 6.1 for further details on radar configurations. As an example, the polygons for overlap number 1 are shown in figure 6.4.
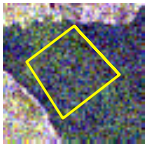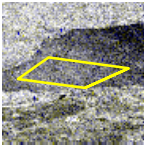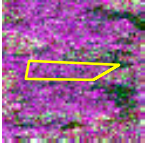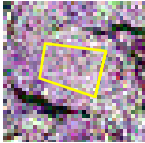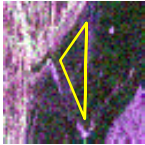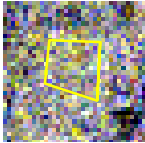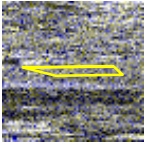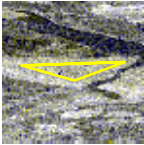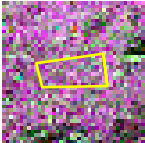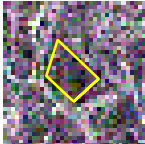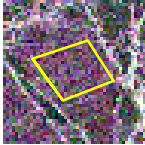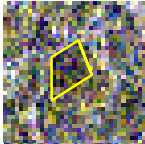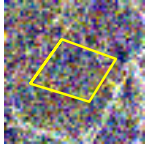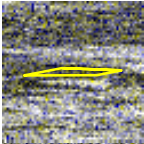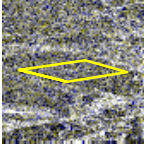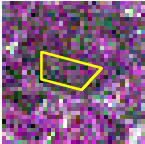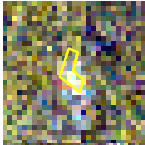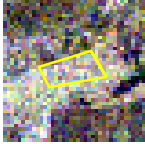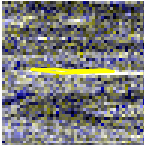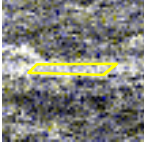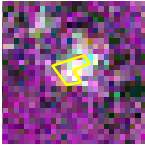
Figure C.1: Example polygons shown in the radar geometry (slant range on the horizontal and azimuth on the vertical) after coherent and incoherent multi looking.
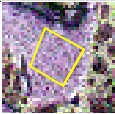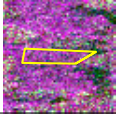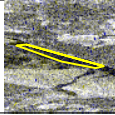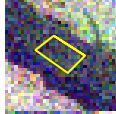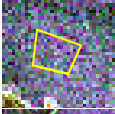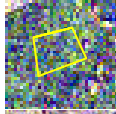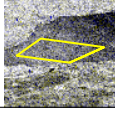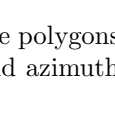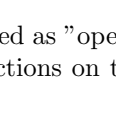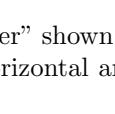
Figure C.2: Example polygons tagged as "open water" shown in the radar geometry (slant range and azimuth directions on the horizontal and vertical, respectively).
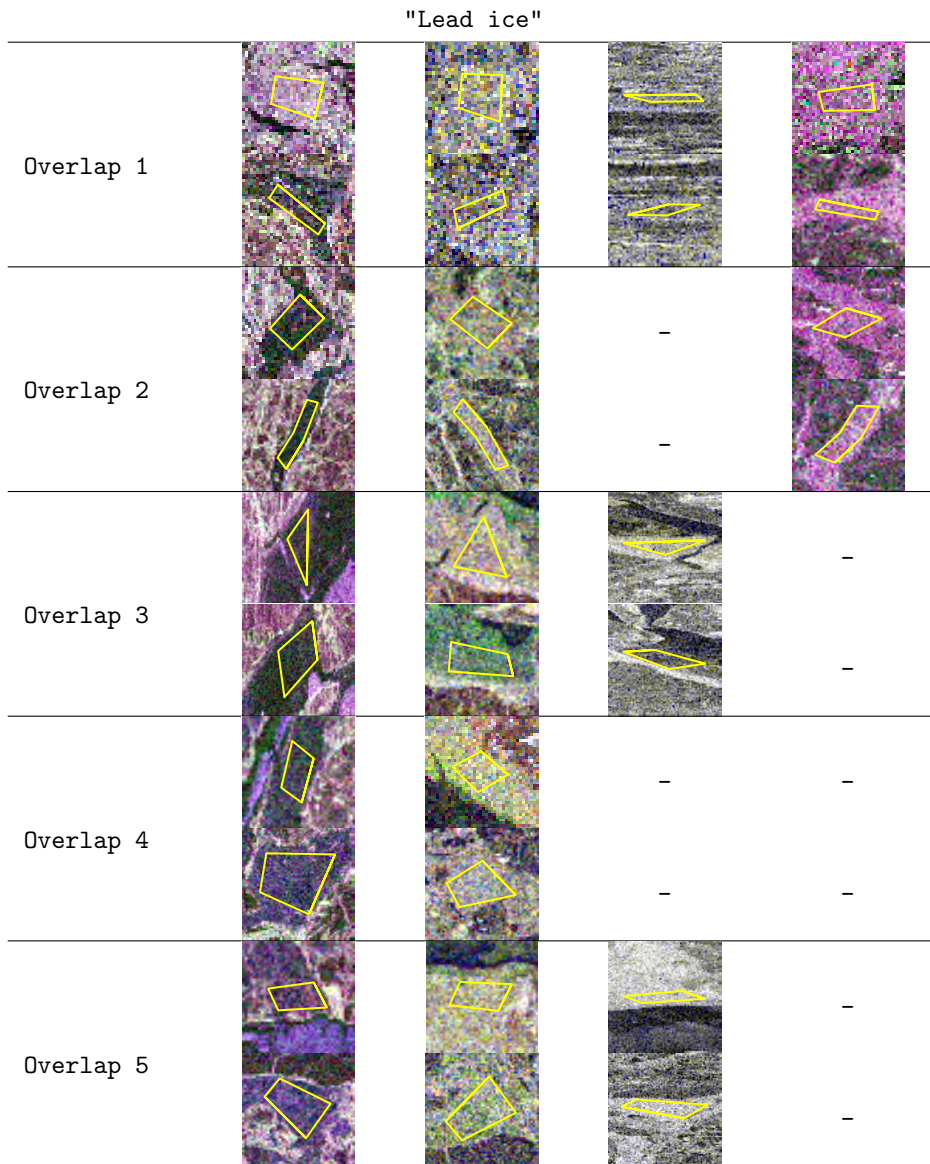
Figure C.3: Example polygons tagged as "lead ice" shown in the radar geometry (slant range and azimuth directions on the horizontal and vertical, respectively).
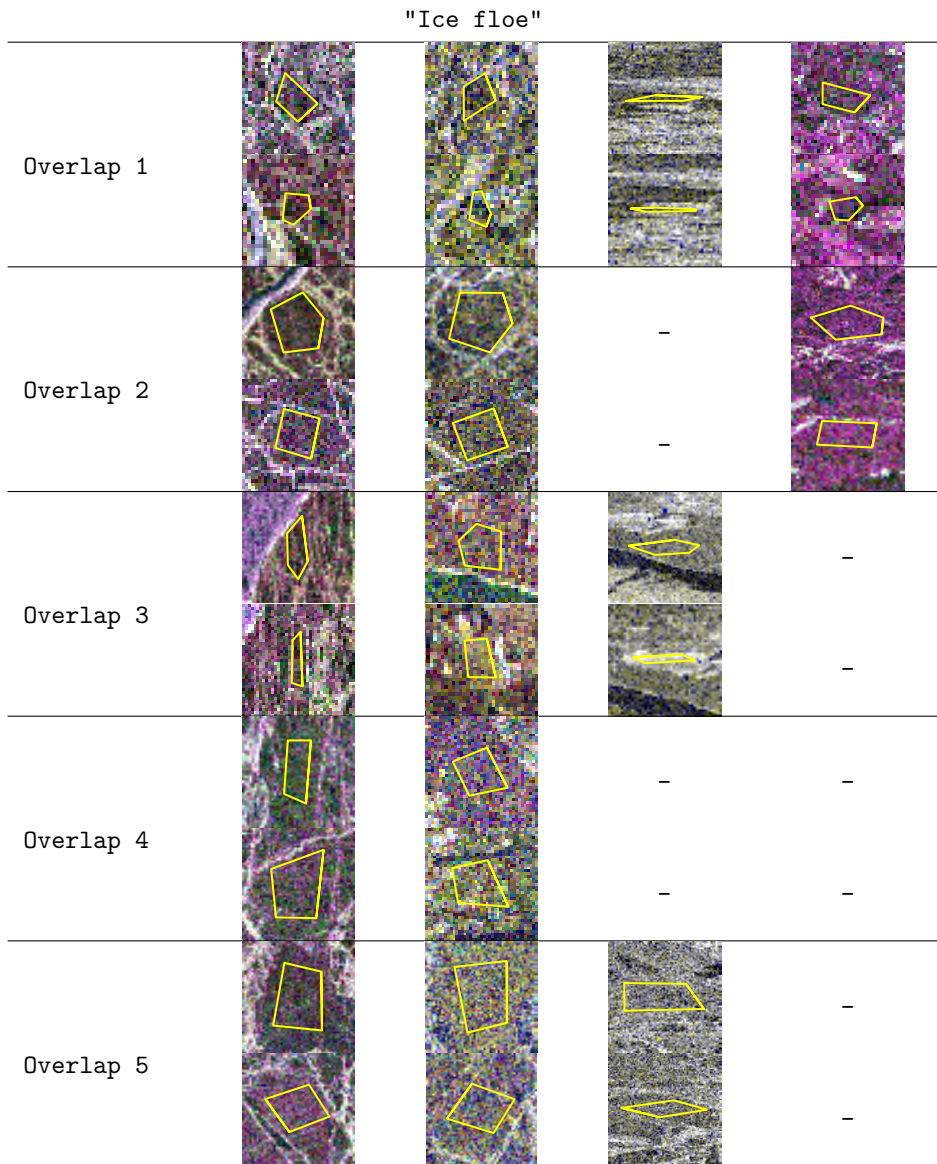
Figure C.4: Example polygons tagged as "ice floe" shown in the radar geometry (slant range and azimuth directions on the horizontal and vertical, respectively).
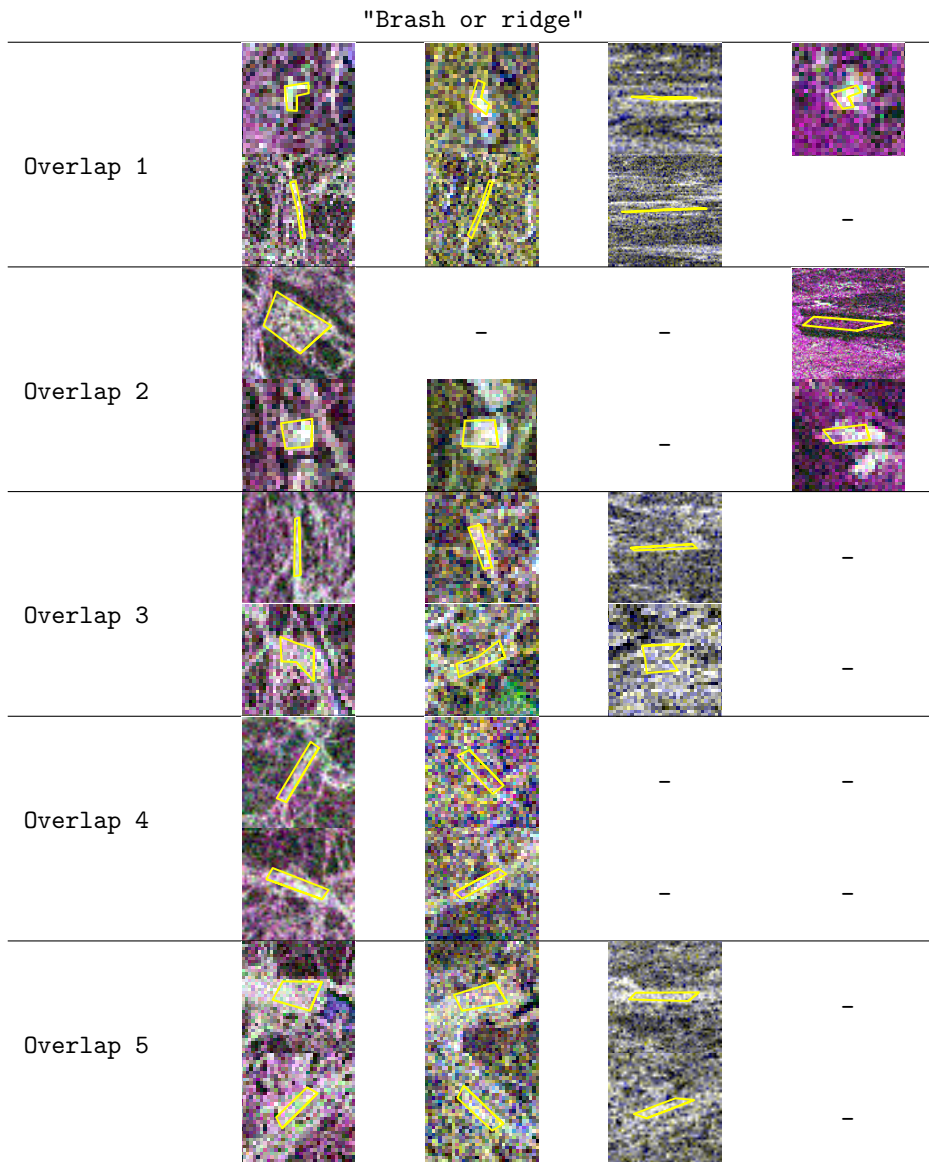
"Brash or ridge"

Figure C.5: Example polygons tagged as "brash or ridge" shown in the radar geometry (slant range and azimuth directions on the horizontal and vertical, respectively).
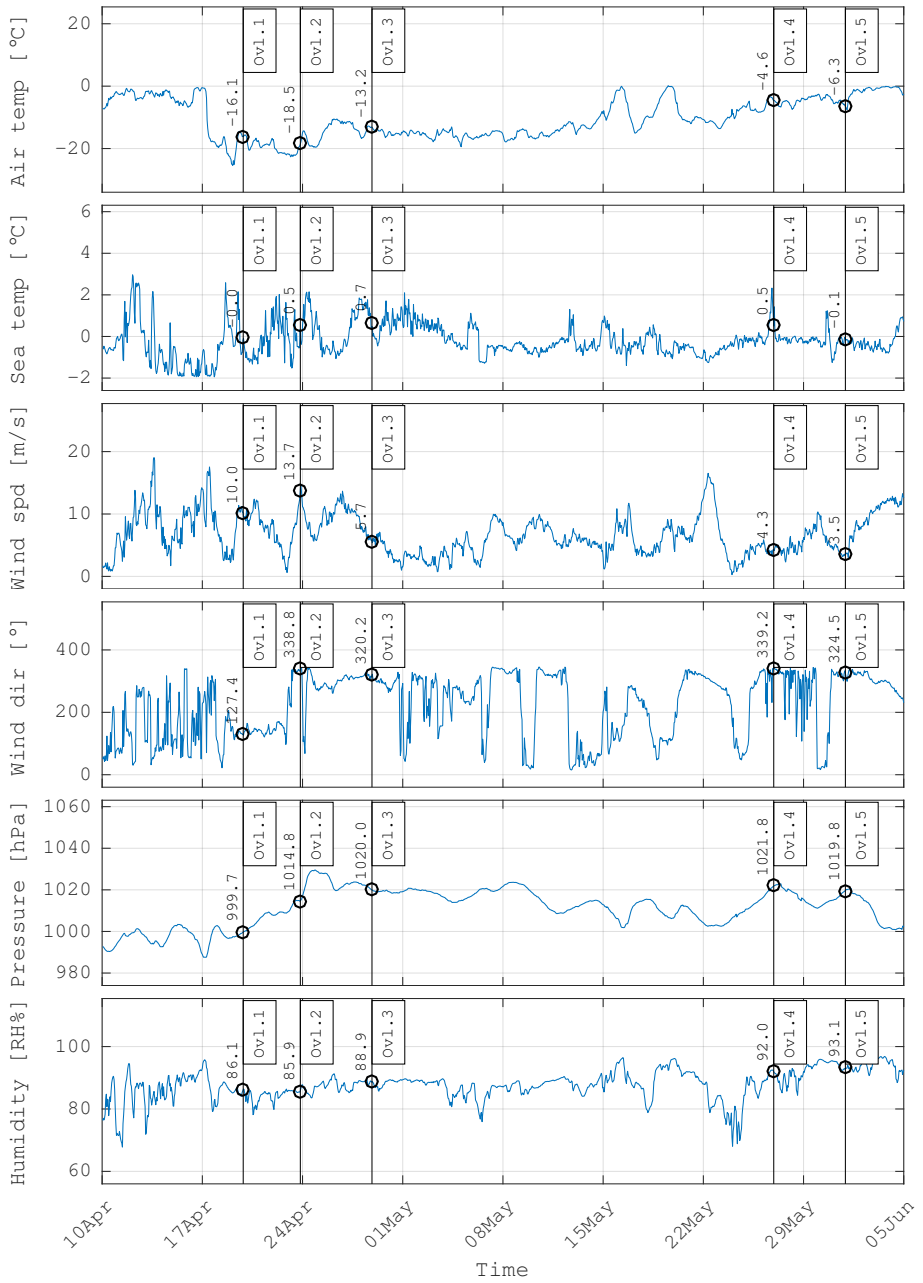
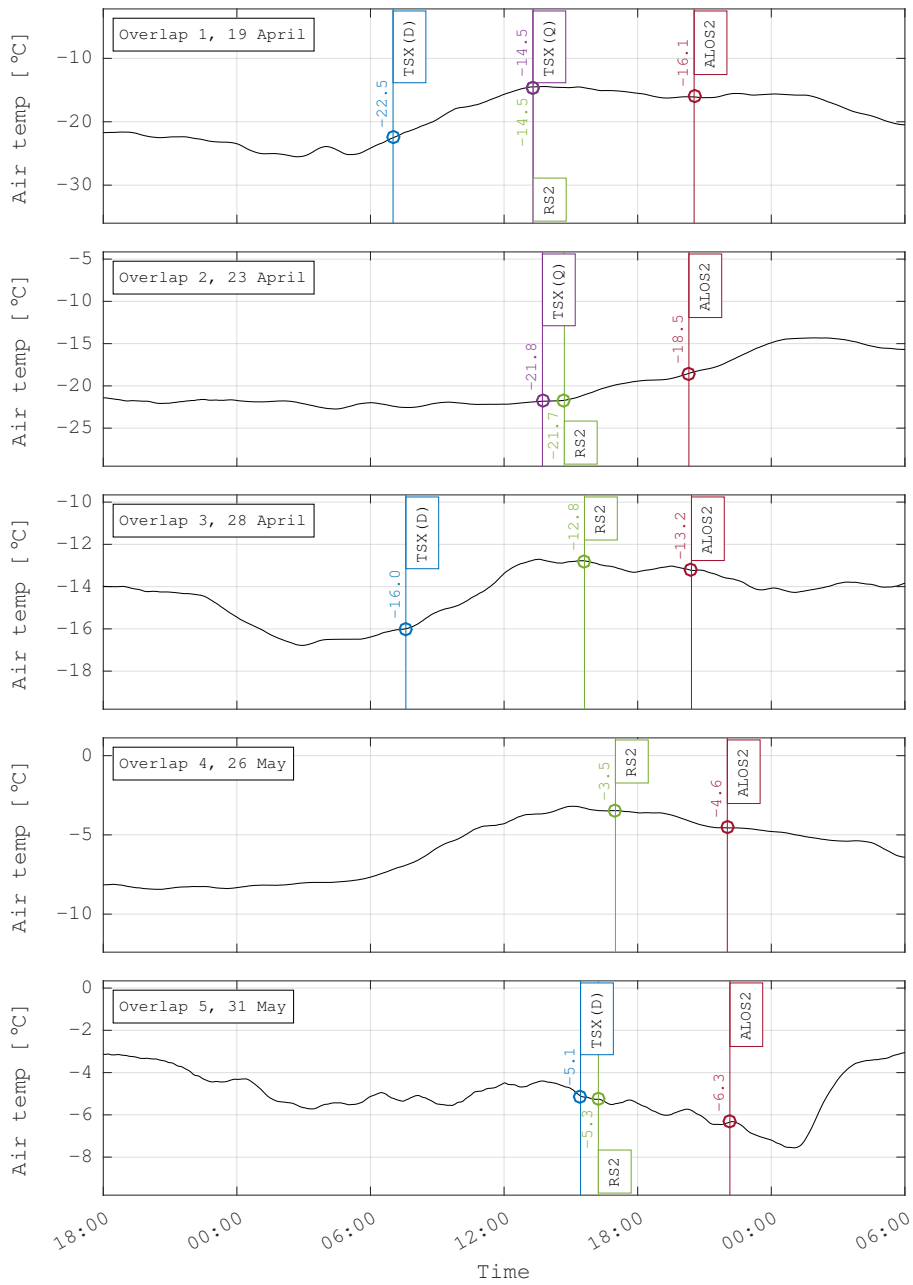Figure C.6: Meteorological parameters averaged over 1 hour.

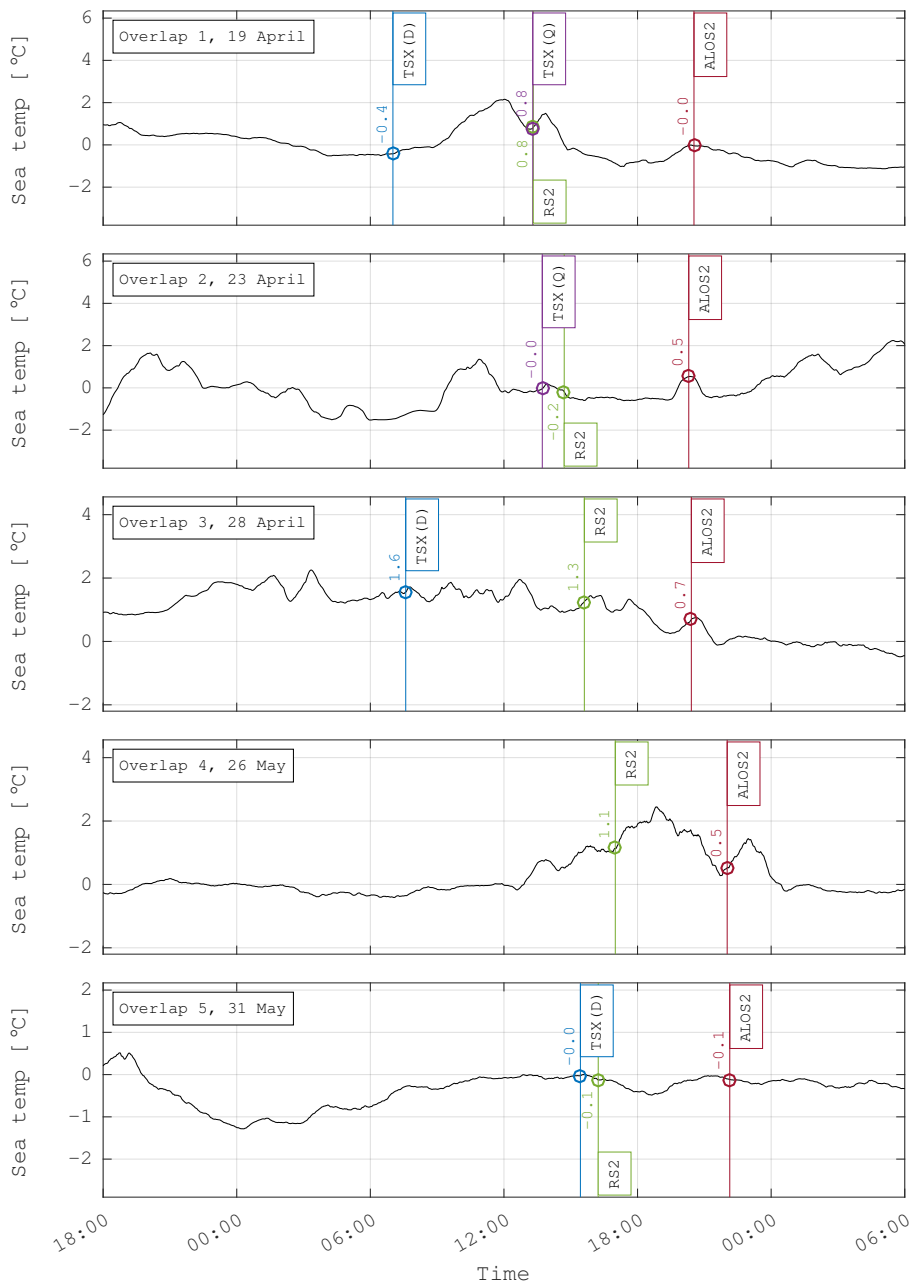Figure C.7: Air temperature averaged over 1 hour.

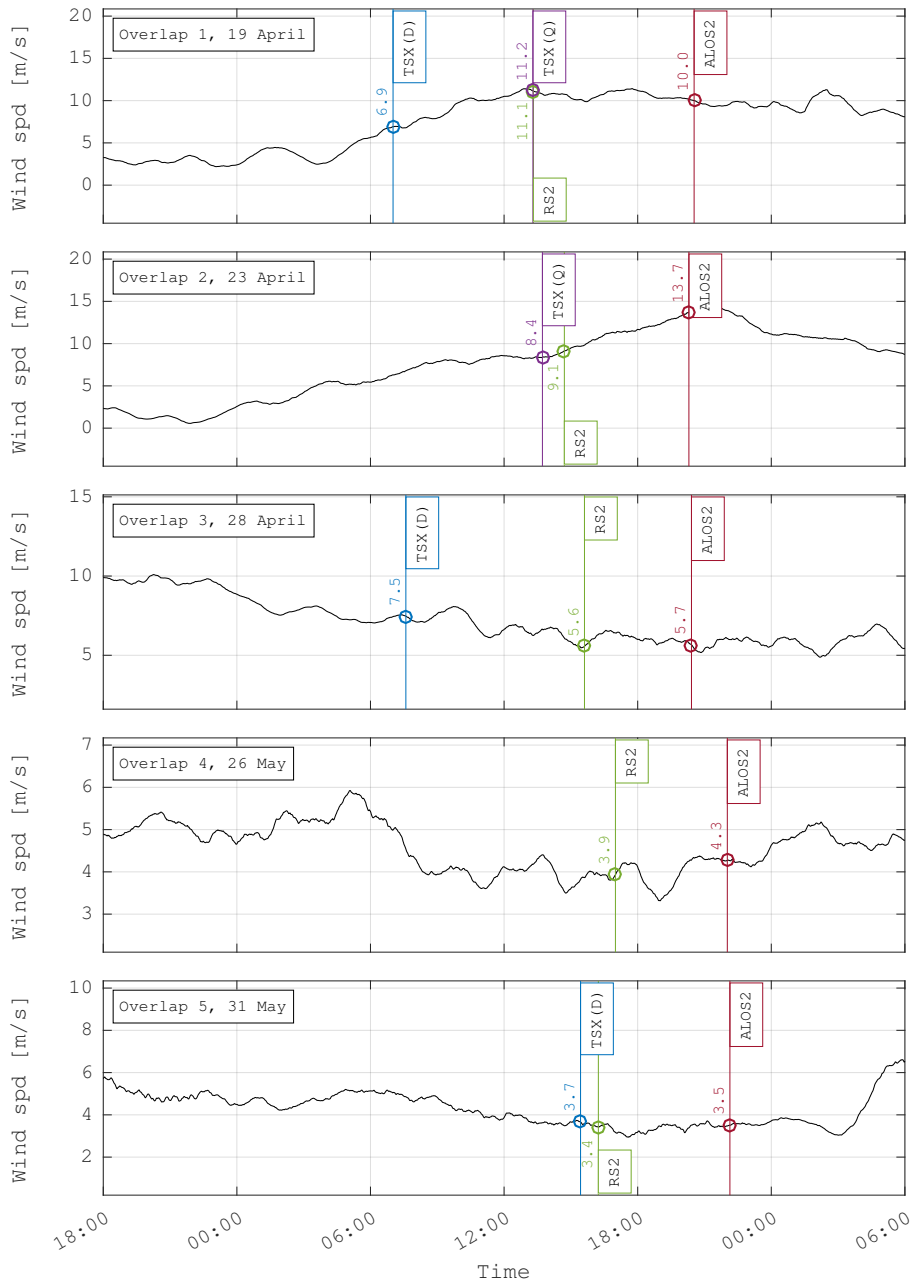Figure C.8: Sea water temperature averaged over 1 hour.

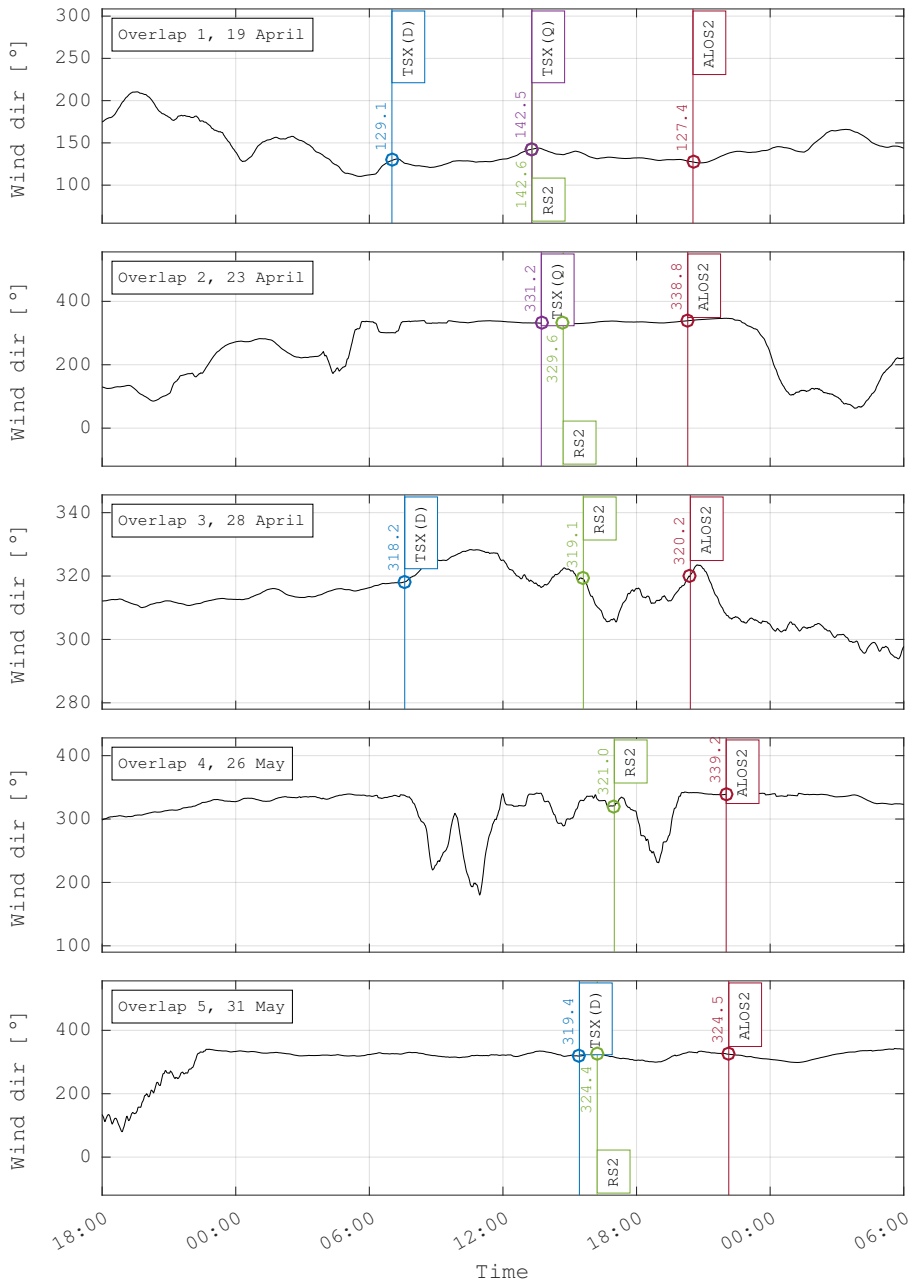Figure C.9: Wind speed averaged over 1 hour.

226
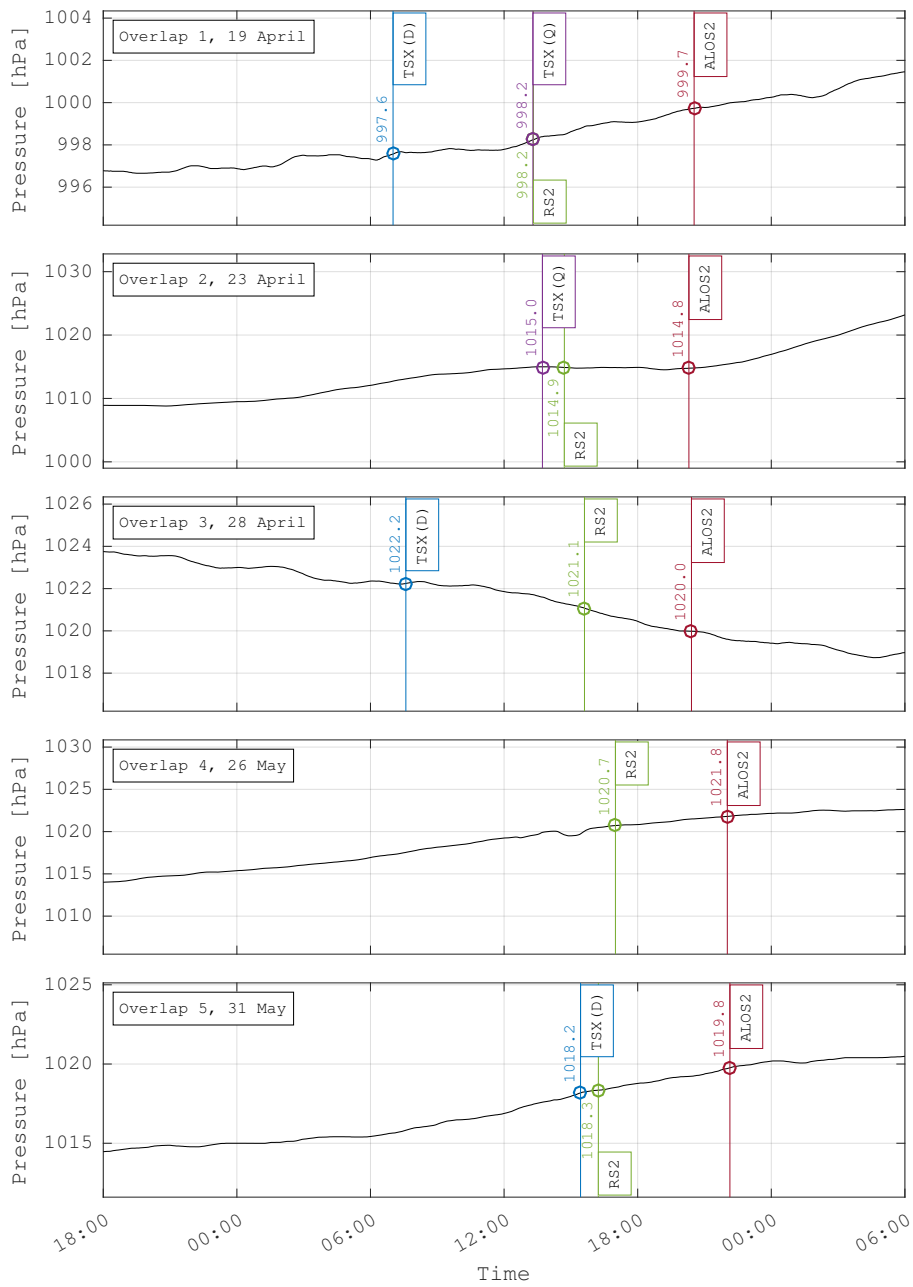

Figure C.10: Wind direction averaged over 1 hour.

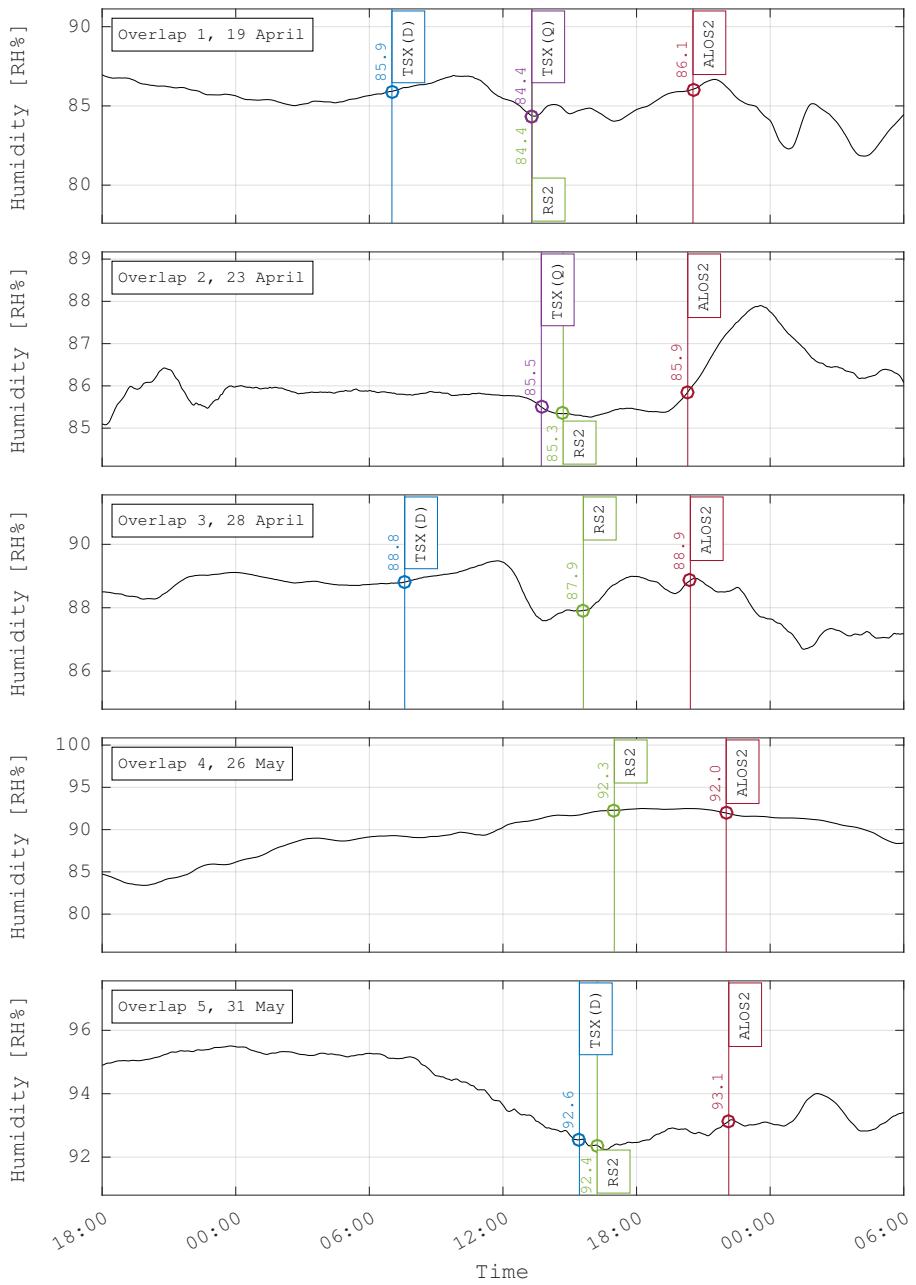Figure C.11: Air pressure averaged over 1 hour.

Figure C.12: Relative humidity averaged over 1 hour.

Bibliography

Aksenov, Y., Popova, E. E., Yool, A., Nurser, A. G., Williams, T. D., Bertino, L. & Bergh, J. (2017), 'On the future navigability of arctic sea routes: High-resolution projections of the arctic ocean and sea ice', *Marine Policy* **75**, 300 – 317.
URL: *http://www.sciencedirect.com/science/article/pii/S0308597X16000038*

Albert, M. D., Lee, Y. J., Ewe, H.-T. & Chuah, H.-T. (2012), 'Multilayer model formulation and analysis of radar backscattering from sea ice', *Progress In Electromagnetics Research* **128**, 267–290.

Alpers, W. & Hühnerfuss, H. (1989), 'The damping of ocean waves by surface films: A new look at an old problem', *Journal of Geophysical Research: Oceans* **94**(C5), 6251–6265.

Álvarez-Pérez, J. L. (2001), 'An extension of the iem/iemm surface scattering model', *Waves in Random Media* **11**(3), 307–329.
URL: *http://dx.doi.org/10.1080/13616670109409787*

Anderson, V. (1966), 'High altitude, side-looking radar images of sea ice in the arctic(high altitude side-looking radar images of sea ice patterns in arctic ocean)', *1966.* pp. 845–857.

Arcone, S. A., Gow, A. J. & McGrew, S. (1986), 'Structure and dielectric properties at 4.8 and 9.5 ghz of saline ice', *Journal of Geophysical Research: Oceans* **91**(C12), 14281–14303.

Assmy, P., Fernández-Méndez, M., Duarte, P., Meyer, A., Randelhoff, A., Mundy, C. J., Olsen, L. M., Kauko, H. M., Bailey, A., Chierici, M. et al. (2017), 'Leads in arctic pack ice enable early phytoplankton blooms below snow-covered sea ice', *Scientific reports* **7**, 40850.

Assur, A. (1958), 'Composition of sea ice and its tensile strength', *Arctic sea ice* **598**, 106–138.

Barber, D. G. & Nghiem, S. V. (1999), 'The role of snow on the thermal dependence of microwave backscatter over sea ice', *Journal of Geophysical Research: Oceans (1978–2012)* **104**(C11), 25789–25803.

Brekke, C. & Solberg, A. H. (2005), 'Oil spill detection by satellite remote sensing', *Remote sensing of environment* **95**(1), 1–13.

Brubaker, R. D. & Ragner, C. L. (2010), 'A review of the international northern sea route program (insrop)–10 years on', *Polar Geography* **33**(1-2), 15–38.

Carlström, A. (1997), 'A microwave backscattering model for deformed first-year sea ice and comparisons with sar data', *Geoscience and Remote Sensing, IEEE Transactions on* **35**(2), 378–391.

Cavalieri, D. & Parkinson, C. (2012), 'Arctic sea ice variability and trends, 1979-2010', *The Cryosphere* **6**(4), 881.

Chen, K.-S., Wu, T.-D., Tsay, M.-K. & Fung, A. K. (2000), 'Note on the multiple scattering in an iem model', *Geoscience and Remote Sensing, IEEE Transactions on* **38**(1), 249–256.

Chew, W. C. (1995), *Waves and fields in inhomogeneous media*, IEEE press New York.

Cloude, S. (2010), *Polarisation: applications in remote sensing*, Oxford University Press.

Cox, G. F. & Weeks, W. F. (1983), 'Equations for determining the gas and brine volumes in sea-ice samples', *Journal of Glaciology* **29**(102), 306–316.

Crawford, F. S. (1968), *Waves*, Vol. 3, Tata McGraw-Hill Education.

De Carolis, G. & Desiderio, D. (2002), 'Dispersion and attenuation of gravity waves in ice: a two-layer viscous fluid model with experimental data validation', *Physics Letters A* **305**(6), 399–412.

Dierking, W. (1992), 'Sensitivity studies of selected theoretical scattering models with applications to radar remote sensing of sea ice', *Report, Physics Department, Alfred Wegener Institute, Bremerhaven, No. 33* .

Dierking, W. (1999), 'Multifrequency scatterometer measurements of baltic sea ice during emac-95', *International Journal of Remote Sensing* **20**(2), 349–372.

Dierking, W. & Busche, T. (2006), 'Sea ice monitoring by l-band sar: An assessment based on literature and comparisons of jers-1 and ers-1 imagery', *Geoscience and Remote Sensing, IEEE Transactions on* **44**(4), 957–970.

Dierking, W., Lang, O. & Busche, T. (2017), 'Sea ice local surface topography from single-pass satellite insar measurements: a feasibility study', *The Cryosphere* **11**(4), 1967.

Drinkwater, M. (1989), 'Limex '87 ice surface characteristics: implications for c-band sar backscatter signatures', *Geoscience and Remote Sensing, IEEE Transactions on* **27**(5), 501–513.

Drinkwater, M. R. & Crocker, G. (1988), 'Modelling changes in scattering properties of the dielectric and young snow-covered sea ice at gh z requencies', *Journal of Glaciology* **34**(118), 274–282.

Dubois, P. C., van Zyl, J. & Engman, T. (1995), 'Measuring soil moisture with imaging radars', *IEEE Transactions on Geoscience and Remote Sensing* **33**(4), 915–926.

Eicken, H., Bock, C., Wittig, R., Miller, H. & Poertner, H.-O. (2000), 'Magnetic resonance imaging of sea-ice pore fluids: methods and thermal evolution of pore microstructure', *Cold Regions Science and Technology* **31**(3), 207–225.

Elfouhaily, T. M., Guérin, C.-A. et al. (2004), 'A critical survey of approximate scattering wave theories from random rough surfaces', *Waves in Random Media* **14**(4), R1–R40.

Fetterer, F., Knowles, K., Meier, W., Savoie, M. & Windnagel, A. K. (2018), 'Sea ice index, version 3', doi: http://dx.doi.org/10.7265/N5K072F8.

Frankenstein, G. & Garner, R. (1967), 'Equations for determining the brine volume of sea ice from -0.5 c to -22.9 c', *Journal of Glaciology* **6**(48), 943–44.

Fukusako, S. (1990), 'Thermophysical properties of ice, snow, and sea ice', *International Journal of Thermophysics* **11**(2), 353–372.

Fung, A. K. (1994), *Microwave scattering and emission models and their applications*, Artech house.

Fung, A. K. & Chen, K.-S. (2010), *Microwave scattering and emission models for users*, Artech house.

Fung, A. K. & Eom, H. J. (1982), 'Application of a combined rough surface and volume scattering theory to sea ice and snow backscatter', *Geoscience and Remote Sensing, IEEE Transactions on* (4), 528–536.

Fung, A. K. & Eom, H. J. (1985), 'A study of backscattering and emission from closely packed inhomogeneous media', *Geoscience and Remote Sensing, IEEE Transactions on* (5), 761–767.

Fung, A. K., Li, Z. & Chen, K.-S. (1992), 'Backscattering from a randomly rough dielectric surface', *IEEE Transactions on Geoscience and remote sensing* **30**(2), 356–369.

Fung, A., Liu, W., Chen, K. & Tsay, M. (2002), 'An improved iem model for bistatic scattering from rough surfaces', *Journal of Electromagnetic Waves and Applications* **16**(5), 689–702.

Gade, M., Alpers, W., Hühnerfuss, H., Wismann, V. R. & Lange, P. A. (1998), 'On the reduction of the radar backscatter by oceanic surface films: Scatterometer measurements and their theoretical interpretation', *Remote Sensing of Environment* **66**(1), 52–70.

Gallet, J.-C., Merkouriadi, I., Liston, G. E., Polashenski, C., Hudson, S., Rösel, A. & Gerland, S. (2017), 'Spring snow conditions on arctic sea ice north of svalbard, during the norwegian young sea ice (n-ice2015) expedition', *Journal of Geophysical Research: Atmospheres* .

Galley, R., Else, B., Geilfus, N.-X., Hare, A., Isleifson, D., Barber, D. & Rysgaard, S. (2015), 'Imaged brine inclusions in young sea ice—shape, distribution and formation timing', *Cold Regions Science and Technology* **111**, 39–48.

Garbrecht, T., Lüpkes, C., Hartmann, J. & Wolff, M. (2002), 'Atmospheric drag coefficients over sea ice—validation of a parameterisation concept', *Tellus A* **54**(2), 205–219.

Gautier, D. L., Bird, K. J., Charpentier, R. R., Grantz, A., Houseknecht, D. W., Klett, T. R., Moore, T. E., Pitman, J. K., Schenk, C. J., Schuenemeyer, J. H., Sørensen, K., Tennyson, M. E., Valin, Z. C. & Wandrey, C. J. (2009), 'Assessment of undiscovered oil and gas in the arctic', *Science* **324**(5931), 1175–1179.
URL: *http://dx.doi.org/10.1126/science.1169467*

Gerland, S., Granskog, M. A., King, J. & Rösel, A. (2017), 'N-ice2015 ice core physics: temperature, salinity and density'.
URL: *https://doi.org/10.21334/npolar.2017.c3db82e3*

Golden, K. M., Eicken, H., Heaton, A., Miner, J., Pringle, D. & Zhu, J. (2007), 'Thermal evolution of permeability and microstructure in sea ice', *Geophysical Research Letters* **34**(16).

Griffiths, D. J. (2005), 'Introduction to electrodynamics'.

Guest, P. & Davidson, K. (1987), 'The effect of observed ice conditions on the drag coefficient in the summer east greenland sea marginal ice zone', *Journal of Geophysical Research: Oceans* **92**(C7), 6943–6954.

Hallikainen, M., Ulaby, F. & Abdelrazik, M. (1986), 'Dielectric properties of snow in the 3 to 37 ghz range', *IEEE transactions on Antennas and Propagation* **34**(11), 1329–1340.

Herman, A. (2010), 'Sea-ice floe-size distribution in the context of spontaneous scaling emergence in stochastic systems', *Physical Review E* **81**(6), 066123.

Hsieh, C.-Y., Fung, A., Nesti, G., Sieber, A. & Coppo, P. (1997), 'A further study of the iem surface scattering model', *Geoscience and Remote Sensing, IEEE Transactions on* **35**(4), 901–909.

Hudson, S. R., Cohen, L. & Walden, V. (2015), 'N-ice2015 surface meteorology'.
URL: *https://doi.org/10.21334/npolar.2015.056a61d1*

Isleifson, D., Galley, R. J., Barber, D. G., Landy, J. C., Komarov, A. S. & Shafai, L. (2014), 'A study on the c-band polarimetric scattering and physical characteristics of frost flowers on experimental sea ice', *IEEE Transactions on Geoscience and Remote Sensing* **52**(3), 1787–1798.

Isleifson, D., Jeffrey, I., Shafai, L., LoVetri, J. & Barber, D. G. (2012), 'A monte carlo method for simulating scattering from sea ice using fvtd', *IEEE Transactions on Geoscience and Remote Sensing* **50**(7), 2658–2668.

Johansson, R. (1988), 'Laser based surface roughness measurements of snow and sea ice on the centimeter scale', *Res. Rep. 162Chalmers Univ. of Technol., Goteborg, Sweden* .

Katsaros, K. B. (1973), 'Supercooling at the surface of an arctic lead', *Journal of Physical Oceanography* **3**(4), 482–486.

Katsaros, K. B. & Liu, W. T. (1974), 'Supercooling at a free salt water surface in the laboratory', *Journal of Physical Oceanography* **4**(4), 654–658.

Keller, J. B. (1998), 'Gravity waves on ice-covered water', *Journal of Geophysical Research: Oceans* **103**(C4), 7663–7669.

Kim, Y., Moore, R., Onstott, R. & Gogineni, S. (1985), 'Towards identification of optimum radar parameters for sea-ice monitoring', *Journal of Glaciology* **31**(109), 214–219.

Komarov, A. S., Shafai, L. & Barber, D. G. (2014), 'Electromagnetic wave scattering from rough boundaries interfacing inhomogeneous media and application to snow-covered sea ice', *Progress In Electromagnetics Research* **144**, 201–219.

Krishfield, R. A. & Perovich, D. K. (2005), 'Spatial and temporal variability of oceanic heat flux to the arctic ice pack', *Journal of Geophysical Research: Oceans* **110**(C7).

Kumar, A., Perlwitz, J., Eischeid, J., Quan, X., Xu, T., Zhang, T., Hoerling, M., Jha, B. & Wang, W. (2010), 'Contribution of sea ice loss to arctic amplification', *Geophysical Research Letters* **37**(21), n/a–n/a. L21701.
   URL: *http://dx.doi.org/10.1029/2010GL045022*

Kwok, R., Nghiem, S., Yueh, S. & Huynh, D. (1995), 'Retrieval of thin ice thickness from multifrequency polarimetric sar data', *Remote sensing of environment* **51**(3), 361–374.

Lamb, H. (1916), *Hydrodynamics*, 4th edn, Cambridge university press.

Landy, J. C., Isleifson, D., Komarov, A. S. & Barber, D. G. (2015), 'Parameterization of centimeter-scale sea ice surface roughness using terrestrial lidar', *IEEE Transactions on Geoscience and Remote Sensing* **53**(3), 1271–1286.

Lee, J. K. & Kong, J. A. (1985), 'Active microwave remote sensing of an anisotropic random medium layer', *Geoscience and Remote Sensing, IEEE Transactions on* **GE-23**(6), 910–923.

Lee, J. & Kong, J. (1988), 'Modified radiative transfer theory for a two-layer anisotropic random medium', *Journal of electromagnetic waves and applications* **2**(3-4), 391–424.

Lee, J.-S. & Pottier, E. (2009), *Polarimetric radar imaging: from basics to applications*, Vol. 142, CRC PressI Llc.

Li, Q., Shi, J. & Chen, K.-S. (2002), 'A generalized power law spectrum and its applications to the backscattering of soil surfaces based on the integral equation model', *IEEE Transactions on Geoscience and Remote Sensing* **40**(2), 271–280.

Liu, W., Chen, K., Tsay, M. & Wu, T. (2003), 'A reexamination of the iem model for microwave scattering from randomly rough boundary', *Journal of the Chinese Institute of Engineers* **26**(3), 271–277.
   URL: *http://dx.doi.org/10.1080/02533839.2003.9670779*

Lytle, V., Massom, R., Bindoff, N., Worby, A. & Allison, I. (2000), 'Wintertime heat flux to the underside of east antarctic pack ice', *Journal of Geophysical Research: Oceans* **105**(C12), 28759–28769.

Matzler, C. & Wegmuller, U. (1987), 'Dielectric properties of freshwater ice at microwave frequencies', *Journal of Physics D: Applied Physics* **20**(12), 1623.

Maus, S., Müller, S., Büttner, J., Brütsch, S., Huthwelker, T., Schwikowski, M., Enzmann, F. & Vähätolo, A. (2011), 'Ion fractionation in young sea ice from kongsfjorden, svalbard', *Annals of glaciology* **52**(57), 301–310.

Maykut, G. A. (1978), 'Energy exchange over young sea ice in the central arctic', *Journal of Geophysical Research* **83**(C7), 3646–3658.

McDougall, T. J., Jackett, D. R., Wright, D. G. & Feistel, R. (2003), 'Accurate and computationally efficient algorithms for potential temperature and density of seawater', *Journal of Atmospheric and Oceanic Technology* **20**(5), 730–741.

Meissner, T. & Wentz, F. J. (2004), 'The complex dielectric constant of pure and sea water from microwave satellite observations', *IEEE Transactions on Geoscience and remote Sensing* **42**(9), 1836–1849.

Melia, N., Haines, K. & Hawkins, E. (2016), 'Sea ice decline and 21st century trans-arctic shipping routes', *Geophysical Research Letters* **43**(18), 9720–9728.

Merkouriadi, I., Gallet, J.-C., Liston, G. E., Polashenski, C., Graham, R. M., Rösel, A. & Gerland, S. (2017), 'Winter snow conditions on arctic sea ice north of svalbard during the norwegian young sea ice (n-ice2015) expedition', *Journal of Geophysical Research: Atmospheres* .

Mishchenko, M. I. (2008), 'Multiple scattering, radiative transfer, and weak localization in discrete random media: unified microphysical approach', *Reviews of Geophysics* **46**(2).

Mitsuyasu, H. & Honda, T. (1982), 'Wind-induced growth of water waves', *Journal of Fluid Mechanics* **123**, 425–442.

Mittermayer, J., Younis, M., Metzig, R., Wollstadt, S., Martínez, J. M. & Meta, A. (2010), 'Terrasar-x system performance characterization and verification', *IEEE Transactions on Geoscience and Remote Sensing* **48**(2), 660–676.

Nakamura, K., Wakabayashi, H., Naoki, K., Nishio, F., Moriyama, T. & Uratsuka, S. (2005), 'Observation of sea-ice thickness in the sea of okhotsk by using dual-frequency and fully polarimetric airborne sar (pi-sar) data', *Geoscience and Remote Sensing, IEEE Transactions on* **43**(11), 2460–2469.

Nakawo, M. & Sinha, N. K. (1984), 'A note on brine layer spacing of first-year sea ice', *Atmosphere-ocean* **22**(2), 193–206.

Nandan, V., Geldsetzer, T., Yackel, J. J., Islam, T., Gill, J. P. & Mahmud, M. (2017), 'Multifrequency microwave backscatter from a highly saline snow cover on smooth first-year sea ice: First-order theoretical modeling', *IEEE Transactions on Geoscience and Remote Sensing* **55**(4), 2177–2190.

Nelson, K. H. & Thompson, T. G. (1954), Deposition of salts from sea water by frigid concentration, Technical report, DTIC Document.

Newyear, K. & Martin, S. (1997), 'A comparison of theory and laboratory measurements of wave propagation and attenuation in grease ice', *Journal of Geophysical Research: Oceans* **102**(C11), 25091–25099.

Newyear, K. & Martin, S. (1999), 'Comparison of laboratory data with a viscous two-layer model of wave propagation in grease ice', *Journal of Geophysical Research: Oceans* **104**(C4), 7837–7840.
URL: *http://dx.doi.org/10.1029/1999JC900002*

Nghiem, S., Borgeaud, M., Kong, J. & Shin, R. (1990), 'Polarimetric remote sensing of geophysical media with layer random medium model', *Progress In Electromagnetics Research* **3**, 1–73.

Nghiem, S., Kwok, R., Kong, J. A. & Shin, R. (1993), 'A model with ellipsoidal scatterers for polarimetric remote sensing of anisotropic layered media', *Radio science* **28**(5), 687–703.

Nghiem, S., Kwok, R., Yueh, S. & Drinkwater, M. (1995*a*), 'Polarimetric signatures of sea ice 2. experimental observations', *Oceanographic Literature Review* **2**(43), 204.

Nghiem, S., Martin, S., Perovich, D., Kwok, R., Drucker, R. & Gow, A. (1997), 'A laboratory study of the effect of frost flowers on c band radar backscatter from sea ice', *Journal of Geophysical Research: Oceans* **102**(C2), 3357–3370.

Nghiem, S. V., Kwok, R., Yueh, S. H. & Drinkwater, M. R. (1995*b*), 'Polarimetric signatures of sea ice: 1. theoretical model', *Journal of Geophysical Research: Oceans* **100**(C7), 13665–13679.
URL: *http://dx.doi.org/10.1029/95JC00937*

Oh, Y., Sarabandi, K. & Ulaby, F. T. (1992), 'An empirical model and an inversion technique for radar scattering from bare soil surfaces', *IEEE Transactions on Geoscience and Remote Sensing* **30**(2), 370–381.

Onstott, R. G. (1992), 'Sar and scatterometer signatures of sea ice', *Microwave remote sensing of sea ice* pp. 73–104.

Overland, J. E. & Wang, M. (2013), 'When will the summer arctic be nearly sea ice free?', *Geophysical Research Letters* **40**(10), 2097–2101.

Parkinson, C. L. (2014), 'Global sea ice coverage from satellite data: annual cycle and 35-yr trends', *Journal of Climate* **27**(24), 9377–9382.

Partington, K. & Hanna, M. (1994), 'Modelling radar sea ice backscatter in support of ers-1 sar', *EARSeL Advances in Remote sensing* **3**(2), 42–53.

Paterson, J., Brisco, B., Argus, S. & Jones, G. (1991), 'In situ measurements of micro-scale surface roughness of sea ice', *Arctic* pp. 140–146.

Perey, F. & Pounder, E. (1958), 'Crystal orientation in ice sheets', *Canadian Journal of Physics* **36**(4), 494–502.

Perovich, D. K. & Gow, A. J. (1991), 'A statistical description of the microstructure of young sea ice', *Journal of Geophysical Research: Oceans* **96**(C9), 16943–16953.

Perovich, D. K. & Gow, A. J. (1996), 'A quantitative description of sea ice inclusions', *Journal of Geophysical Research: Oceans* **101**(C8), 18327–18343.

Phillips, O. (1985), 'Spectral and statistical properties of the equilibrium range in wind-generated gravity waves', *Journal of Fluid Mechanics* **156**, 505–531.

Pianosi, F., Sarrazin, F. & Wagener, T. (2015), 'A matlab toolbox for global sensitivity analysis', *Environmental Modelling & Software* **70**, 80–85.

Pianosi, F. & Wagener, T. (2015), 'A simple and efficient method for global sensitivity analysis based on cumulative distribution functions', *Environmental Modelling and Software* **67**(Supplement C), 1 – 11.
URL: *http://www.sciencedirect.com/science/article/pii/S1364815215000237*

Plant, W. J. (1982), 'A relationship between wind stress and wave slope', *Journal of Geophysical Research: Oceans* **87**(C3), 1961–1967.

Polyakov, I. V., Walsh, J. E. & Kwok, R. (2012), 'Recent changes of arctic multiyear sea ice coverage and the likely causes', *Bulletin of the American Meteorological Society* **93**(2), 145–151.

Proksch, M., Löwe, H. & Schneebeli, M. (2015), 'Density, specific surface area, and correlation length of snow measured by high-resolution penetrometry', *Journal of Geophysical Research: Earth Surface* **120**(2), 346–362.

Rabault, J., Sutherland, G., Gundersen, O. & Jensen, A. (2017), 'Measurements of wave damping by a grease ice slick in svalbard using off-the-shelf sensors and open-source electronics', *Journal of Glaciology* pp. 1–10.

Rankin, A. M., Wolff, E. W. & Martin, S. (2002), 'Frost flowers: Implications for tropospheric chemistry and ice core interpretation', *Journal of Geophysical Research: Atmospheres* **107**(D23).

Rice, S. O. (1951), 'Reflection of electromagnetic waves from slightly rough surfaces', *Communications on pure and applied mathematics* **4**(2-3), 351–378.

Rigor, I. G. & Wallace, J. M. (2004), 'Variations in the age of arctic sea-ice and summer sea-ice extent', *Geophysical Research Letters* **31**(9).

Ringer, W. E. (1928), 'Uber die veränderungen in der zusammensetzung des meereswassersalzes beim ausfrieres', *Conseil Permanent International pour l'Exploration de la Mer* **47**, 226–31.

Rösel, A., Itkin, P., King, J., Divine, D., Wang, C., Granskog, M. A., Krumpen, T. & Gerland, S. (2018), 'Thin sea ice, thick snow, and widespread negative freeboard observed during n-ice2015 north of svalbard', *Journal of Geophysical Research: Oceans* .
    URL: *http://dx.doi.org/10.1002/2017JC012865*

Rösel, A. & King, J. (2017), 'N-ice2015 ice thickness, snow thickness, and freeboard from thickness drillings'.
    URL: *https://doi.org/10.21334/npolar.2017.25f70db1*

Rouse, J. (1969), 'Arctic ice type identification by radar', *Proceedings of the IEEE* **57**(4), 605–611.

Saltelli, A., Ratto, M., Andres, T., Campolongo, F., Cariboni, J., Gatelli, D., Saisana, M. & Tarantola, S. (2008), *Global sensitivity analysis: the primer*, John Wiley & Sons.

Schweiger, A. J. (2004), 'Changes in seasonal cloud cover over the arctic seas from satellite and surface observations', *Geophysical Research Letters* **31**(12).

Screen, J. A. & Francis, J. A. (2016), 'Contribution of sea-ice loss to arctic amplification is regulated by pacific ocean decadal variability', *Nature Climate Change* .

Screen, J. A. & Simmonds, I. (2010), 'The central role of diminishing sea ice in recent arctic temperature amplification', *Nature* **464**(7293), 1334–1337.

Serreze, M. C., Holland, M. M. & Stroeve, J. (2007), 'Perspectives on the arctic's shrinking sea-ice cover', *science* **315**(5818), 1533–1536.

Slade, B. (2011), Radarsat-2 product description, Technical Report 1/8, MDA.

Smedsrud, L. H. (2011), 'Grease-ice thickness parameterization', *Annals of Glaciology* **52**(57), 77–82.

Smedsrud, L. H. & Martin, T. (2015), 'Grease ice in basin-scale sea-ice ocean models', *Annals of Glaciology* **56**(69), 295–306.

Smith, T. G. & Stirling, I. (1975), 'The breeding habitat of the ringed seal (phoca hispida). the birth lair and associated structures', *Canadian Journal of Zoology* **53**(9), 1297–1305.

Sobol, I. M. (1993), 'Sensitivity estimates for nonlinear mathematical models', *Mathematical Modelling and Computational Experiments* **1**(4), 407–414.

Soulis, E., Lennox, W. & Sykes, J. (1989), Estimation of the thickness of undeformed first year ice using radar backscatter, *in* 'Geoscience and Remote Sensing Symposium, 1989. IGARSS'89. 12th Canadian Symposium on Remote Sensing., 1989 International', Vol. 4, IEEE, pp. 2366–2369.

Stogryn, A. (1983), 'The bilocal approximation for the electric field in strong fluctuation theory', *IEEE transactions on antennas and propagation* **31**, 985.

Stogryn, A. & Desargant, G. (1985), 'The dielectric properties of brine in sea ice at microwave frequencies', *Antennas and Propagation, IEEE Transactions on* **33**(5), 523–532.

Style, R. W. & Worster, M. G. (2009), 'Frost flower formation on sea ice and lake ice', *Geophysical Research Letters* **36**(11).

Thomas, D. N. & Dieckmann, G. S. (2009), *Sea ice*, John Wiley & Sons.

Tiuri, M., Sihvola, A., Nyfors, E. & Hallikaiken, M. (1984), 'The complex dielectric constant of snow at microwave frequencies', *IEEE Journal of Oceanic Engineering* **9**(5), 377–382.

Tjuatja, S., Fung, A. & Bredow, J. (1992), 'A scattering model for snow-covered sea ice', *Geoscience and Remote Sensing, IEEE Transactions on* **30**(4), 804–810.

Tonboe, R. T., Dybkjær, G. & Høyer, J. L. (2011), 'Simulations of the snow covered sea ice surface temperature and microwave effective temperature', *Tellus A* **63**(5), 1028–1037.
URL: *http://dx.doi.org/10.1111/j.1600-0870.2011.00530.x*

Tsang, G., Hanley, T. O. et al. (1985), 'Frazil formation in water of different salinities and supercoolings', *Journal of Glaciology* **31**(108), 74–85.

Tsang, L. & Kong, J. A. (1981), 'Scattering of electromagnetic waves from random media with strong permittivity fluctuations', *Radio Science* **16**(3), 303–320.
URL: *http://dx.doi.org/10.1029/RS016i003p00303*

Tsang, L. & Kong, J. A. (2004), *Scattering of electromagnetic waves, advanced topics*, Vol. 26, John Wiley & Sons.

Tsang, L., Kong, J. A. & Ding, K.-H. (2004), *Scattering of Electromagnetic Waves, Theories and Applications*, Vol. 27, John Wiley & Sons.

Ulaby, F. T., Moore, R. K. & Fung, A. K. (1982), 'Microwave remote sensing active and passive-volume ii: Radar remote sensing and surface scattering and enission theory'.

Ushio, S. & Wakatsuchi, M. (1993), 'A laboratory study on supercooling and frazil ice production processes in winter coastal polynyas', *Journal of Geophysical Research: Oceans* **98**(C11), 20321–20328.

Valenzuela, G. (1967), 'Depolarization of em waves by slightly rough surfaces', *IEEE Transactions on Antennas and Propagation* **15**(4), 552–557.

Vancoppenolle, M., Fichefet, T. & Goosse, H. (2009), 'Simulating the mass balance and salinity of arctic and antarctic sea ice. 2. importance of sea ice salinity variations', *Ocean Modelling* **27**(1-2), 54–69.

Vant, M., Ramseier, R. & Makios, V. (1978), 'The complex-dielectric constant of sea ice at frequencies in the range 0.1–40 ghz', *Journal of Applied Physics* **49**(3), 1264–1280.

Vihma, T. (2014), 'Effects of arctic sea ice decline on weather and climate: a review', *Surveys in Geophysics* **35**(5), 1175–1214.

Wadhams, P. & Holt, B. (1991), 'Waves in frazil and pancake ice and their detection in seasat synthetic aperture radar imagery', *Journal of Geophysical Research: Oceans* **96**(C5), 8835–8852.

Wakabayashi, H., Matsuoka, T., Nakamura, K. & Nishio, F. (2004), 'Polarimetric characteristics of sea ice in the sea of okhotsk observed by airborne l-band sar', *Geoscience and Remote Sensing, IEEE Transactions on* **42**(11), 2412–2425.

Walsh, J. E., Fetterer, F., Scott Stewart, J. & Chapman, W. L. (2017), 'A database for depicting arctic sea ice variations back to 1850', *Geographical Review* **107**(1), 89–107.

Wang, R. & Shen, H. H. (2010), 'Gravity waves propagating into an ice-covered ocean: A viscoelastic model', *Journal of Geophysical Research: Oceans* **115**(C6).

Weber, J. E. (1987), 'Wave attenuation and wave drift in the marginal ice zone', *Journal of physical oceanography* **17**(12), 2351–2361.

Weeks, W. F. & Ackley, S. F. (1986), The growth, structure, and properties of sea ice, *in* 'The geophysics of sea ice', Springer, pp. 9–164.

Weeks, W. F. & Gow, A. J. (1978), 'Preferred crystal orientations in the fast ice along the margins of the arctic ocean', *Journal of Geophysical Research: Oceans* **83**(C10), 5105–5121.

Winebrenner, D., Farmer, L. & Joughin, I. (1995), 'On the response of polarimetric synthetic aperture radar signatures at 24-cm wavelength to sea ice thickness in arctic leads', *Radio Science* **30**(2), 373–402.

Winebrenner, D. P., Bredow, J., Fung, A. K., Drinkwater, M. R., Nghiem, S., Gow, A. J., Perovich, D. K., Grenfell, T. C., Han, H. C., Kong, J. A. et al. (1992), 'Microwave sea ice signature modeling', *Microwave remote sensing of sea ice* pp. 137–175.

Wu, J. (1975), 'Wind-induced drift currents', *Journal of Fluid Mechanics* **68**(01), 49–70.

Wu, T.-D., Chen, K.-S., Shi, J. & Fung, A. K. (2001), 'A transition model for the reflection coefficient in surface scattering', *Geoscience and Remote Sensing, IEEE Transactions on* **39**(9), 2040–2050.

Wu, T.-D., Chen, K.-S., Shi, J., Lee, H.-W. & Fung, A. K. (2008), 'A study of an aiem model for bistatic scattering from randomly rough surfaces', *Geoscience and Remote Sensing, IEEE Transactions on* **46**(9), 2584–2598.

Xu, X., Doulgeris, A. P., Melandsø, F. & Brekke, C. (2016), Numerical simulation of microwave scattering from sea ice based on the finite element method, *in* 'Geoscience and Remote Sensing Symposium (IGARSS), 2016 IEEE International', IEEE, pp. 4846–4849.

Yitayew, T. G., Dierking, W., Divine, D. V., Eltoft, T., Ferro-Famil, L., Rösel, A. & Negre, J. (2018), 'Validation of sea ice topographic heights derived from tandem-x interferometric sar data with results from laser profiler and photogrammetry', *IEEE Transactions on Geoscience and Remote Sensing (in review)* .

Yitayew, T. G., Ferro-Famil, L., Eltoft, T. & Tebaldini, S. (2017*a*), 'Lake and fjord ice imaging using a multifrequency ground-based tomographic sar system', *IEEE Journal of Selected Topics in Applied Earth Observations and Remote Sensing* **10**(10), 4457–4468.

Yitayew, T. G., Ferro-Famil, L., Eltoft, T. & Tebaldini, S. (2017*b*), 'Tomographic imaging of fjord ice using a very high resolution ground-based sar system', *IEEE Transactions on Geoscience and Remote Sensing* **55**(2), 698–714.

Zhang, J., Schweiger, A., Steele, M. & Stern, H. (2015), 'Sea ice floe size distri-
    bution in the marginal ice zone: Theory and numerical experiments', *Journal
    of Geophysical Research: Oceans* **120**(5), 3484–3498.